

Electronic Thesis and Dissertation Repository

5-1-2014 12:00 AM


Tip-Enhances Raman Spectroscopy, Enabling Spectroscopy at the Nanoscale

Nastaran Kazemi Zanjani
The University of Western Ontario

Supervisor
Dr. François Lagugné-Labarthe
The University of Western Ontario

Graduate Program in Chemistry
A thesis submitted in partial fulfillment of the requirements for the degree in Doctor of
Philosophy
© Nastaran Kazemi Zanjani 2014

Follow this and additional works at: <https://ir.lib.uwo.ca/etd>

 Part of the [Analytical Chemistry Commons](#), [Materials Chemistry Commons](#), and the [Physical Chemistry Commons](#)

Recommended Citation

Kazemi Zanjani, Nastaran, "Tip-Enhances Raman Spectroscopy, Enabling Spectroscopy at the Nanoscale" (2014). *Electronic Thesis and Dissertation Repository*. 2079.
<https://ir.lib.uwo.ca/etd/2079>

This Dissertation/Thesis is brought to you for free and open access by Scholarship@Western. It has been accepted for inclusion in Electronic Thesis and Dissertation Repository by an authorized administrator of Scholarship@Western. For more information, please contact wlsadmin@uwo.ca.

TIP-ENHANCED RAMAN SPECTROSCOPY, ENABLING SPECTROSCOPY AT
THE NANOSCALE
(Thesis Format: Integrated Article)

by

Nastaran Kazemi-Zanjani

Graduate Program in Chemistry

A thesis submitted in partial fulfillment
of the requirements for the degree of
Doctor of Philosophy

The School of Graduate and Postdoctoral Studies
The University of Western Ontario
London, Ontario, Canada

©Nastaran Kazemi-Zanjani 2014

Abstract

The knowledge on the chemical and the structural properties of substances benefits strongly from characterization methods that can provide access to the sample's nanoscale building blocks. Not only should the sensitivity of these methods approach a low detection limit up to single molecule, but also the accessible spatial resolution must enable chemical imaging of individual nanoscale features of the substances. High resolution imaging is often provided by electron microscopes through methods such as transmission electron microscopy (TEM) and scanning electron microscopy (SEM); nevertheless, these methods do not offer chemical information. Surface-enhanced spectroscopy (SERS) was developed to improve the sensitivity of the chemical measurements through placing the sample onto rough silver or gold surfaces. However, in SERS, spatially resolved measurements are not possible since an ensemble of nanoscale features give birth to the SERS effect. The challenge of the simultaneous improvement of the spatial resolution and sensitivity was addressed indeed through combining high resolution optical microscopy with high sensitivity of surface-enhanced spectroscopy and was termed as tip-enhanced Raman spectroscopy (TERS).

In this thesis, the confined electric field in proximity of the nanoscale apex of the metallic TERS tip is first investigated theoretically through finite-difference time-domain (FDTD) calculations. The results were employed in optimization of the experimental TERS setup which is utilized in this thesis. The power of TERS in high resolution detection of nanoscale substances is then evaluated through TERS study of isolated single walled carbon nanotubes. The accessible high resolution is also used to acquire insight into the impact of structural strains on the molecular vibrations in silicon nanowires. The large surface sensitivity and specificity of TERS is also evaluated through TERS mapping of the adsorption sites of osteopontin phosphoproteins on the surface of calcium oxalate microcrystal which are responsible for the formation of kidney stones in human body.

Keywords

tip-enhanced Raman spectroscopy, atomic force microscopy, localized surface plasmon resonances, spatial resolution, surface specificity, detection sensitivity, enhancement factor,

near-field measurements, radial and linear polarization, finite-difference time-domain calculations, carbon nanotubes, silicon nanowires, calcium oxalate microcrystals.

Dedication

To my husband and my family

Co-Authorship Statement

The following thesis contains material from previously published manuscripts. Dr. François Lagugné-Labarthet was the corresponding author on the presented papers and was responsible for the supervision of Nastaran Kazemi-Zanjani over the course of her studies.

Nastaran Kazemi-Zanjani was the primary author of the published papers presented in Chapters 4, 6 and 7. She was responsible for the majority of the experimental work in these papers as well as the writing and revision for all drafts, including final manuscripts. Some data were jointly acquired and analyzed by co-authors as summarized below:

In Chapter 4, Dr. Sylvain Vedraïne was involved in some technical aspects regarding the optimization of the FDTD simulations. In Chapter 5, the purification of single walled carbon nanotubes as well as the TEM characterization of the purified product was done by Pierangelo Gobbo and Ziyang Zhu in the research laboratory of Dr. Mark S. Workentin in chemistry department at Western university. Silicon nanowires in Chapter 6 were synthesized by Erwan Kergrene and Dr. Lijia Liu in research laboratory of Dr. Tsun-Kong Sham in chemistry department at Western university. In Chapter 7, the crystallization of the calcium oxalate monohydrate microcrystals and the adsorption of osteopontin phosphoprotein onto their faces were done by Dr. Bernd Grohe, Honghong Chen, and Harvey A. Goldberg in research laboratory of Dr. Graeme K. Hunter in Schulich school of medicine and dentistry at Western university. Additional collaborations were done with Dr. Alexandre Merlen and Alexandre Sangar in the field of FDTD simulation and with Farshid Pashaei in the field of TERS which resulted in publications that are not the direct subject of this thesis. Nastaran is appreciative of their experimental assistance and useful discussions.

Acknowledgments

I acknowledge, with gratitude, my supervisor: Dr. François Lagugné-Labarthet for his advice and encouragement and also to the staff from Nanofabrication facility at the University of Western Ontario, Todd Simpson and Tim Goldhawk and my colleagues Shabila Fayyaz, Renjie Hou, Gregory Wallace and Mohammadali Tabatabaei for their technical support in preparation of my TERS probes.

Table of Contents

Abstract.....	ii
Dedication.....	iv
Co-Authorship Statement.....	v
Table of Contents.....	vii
List of Tables.....	xii
List of Figures.....	xiii
List of Abbreviations, Symbols and Nomenclature.....	xxii
List of Appendices.....	xxv
Chapter 1.....	1
1 General Introduction.....	1
1.1 Overview.....	1
1.2 Application of TERS in Material and Life Sciences.....	3
1.3 Scope of the Thesis.....	6
1.4 References.....	8
Chapter 2.....	12
2 Principles and Theory of Tip-enhanced Raman Spectroscopy.....	12
2.1 Raman Spectroscopy: Theory and Selection Rules.....	12
2.2 Resonance Raman.....	18
2.3 Plasmonic Resonances in Metal.....	19
2.3.1 Plasmon.....	20
2.3.2 Surface Plasmon.....	21
2.3.3 Localized surface Plasmon.....	24
2.4 The Near-Field Concept.....	26
2.5 Diffraction Limit in Optical Measurements.....	28

2.6	Tip-enhanced Raman spectroscopy	32
2.6.1	SERS and TERS Enhancement Mechanism	33
2.7	Thermal Degradation of the Samples in TERS.....	37
2.8	Summary	38
2.9	References.....	39
Chapter 3.....		44
3	Experimental Design and Technical Aspects for Tip-enhanced Raman Spectroscopy	44
3.1	Technical Aspects	44
3.1.1	Methods for Controlling the TERS Probe Position	44
3.1.2	TERS Optical Configuration.....	48
3.1.3	TERS Experimental Setup	52
3.2	Fabrication of TERS Probes	54
3.2.1	Tip Material of TERS Probes	54
3.2.2	TERS Tip Geometry	57
3.2.3	Fabrication Methods	58
3.2.4	Reproducibility and Lifetime of TERS tip.....	66
3.3	Laser Polarization	68
3.3.1	Experimental Setup to Generate Radial Polarization.....	69
3.3.2	Polarization Sensitive Raman Spectroscopy Experiment.....	73
3.4	TERS Experimental Procedure	75
3.4.1	Alignment of the TERS Tip to the Laser Focal Region.....	75
3.4.2	TERS Spectra Acquisition	78
3.4.3	General Considerations.....	79
3.5	Estimation of the Enhancement Factors in TERS.....	80
3.6	Determination of the Spatial Resolution.....	82
3.7	TERS Peak Assignment.....	83

3.7.1	Polarization Considerations	83
3.7.2	Tip Contamination	83
3.7.3	Local Annealing and Heating	84
3.7.4	Other Sources of Misleading Peaks	84
3.8	Conclusion	84
3.9	References.....	85
Chapter 4	92
4	Localized Enhancement of Electric Field in Tip-enhanced Raman Spectroscopy Using Radially and Linearly Polarized Light	92
4.1	Introduction.....	92
4.2	Finite-Difference Time-Domain Method.....	93
4.3	Results and Discussion	98
4.3.1	Polarization Modulation for FDTD Simulations	98
4.3.2	Normalization of the Electric Field Intensity.....	101
4.3.3	FDTD Calculation of the Electric Field.....	102
4.4	Conclusion	109
4.5	References.....	109
Chapter 5	112
5	Tip-enhanced Raman Spectroscopy of Single Walled Carbon Nanotubes; Imaging beyond the Diffraction Limit	112
5.1	Introduction.....	112
5.2	Experimental Section.....	115
5.2.1	Sample Preparation	115
5.2.2	TERS Experimental Details.....	117
5.3	Results and Discussion	118
5.3.1	Estimation of Lateral Resolution	118
5.3.2	Near-Field Origin of the Enhanced Raman Signals.....	123

5.3.3	Estimation of the Enhancement Factor	124
5.4	Conclusion	125
5.5	References.....	126
Chapter 6	129
6	Tip-enhanced Raman Imaging and Nanospectroscopy of Etched Silicon Nanowires	129
6.1	Introduction.....	129
6.2	Experimental Section	131
6.2.1	Sample Preparation	131
6.2.2	TERS Setup.....	133
6.3	Results and Discussion	133
6.3.1	Raman Characterization of Silicon Nanowires.....	133
6.3.2	TERS Tip Alignment	135
6.3.3	TERS Imaging of Silicon Nanowires	136
6.3.4	Estimation of Accessible Spatial Resolution	138
6.3.5	Estimation of Enhancement Factor	140
6.3.6	Lattice Strain Influence on Spectral Fingerprints of Nanowires	141
6.4	Conclusion	143
Chapter 7	145
7	Label-free Mapping of Osteopontin Adsorption to Calcium Oxalate Monohydrate Crystals by Tip-enhanced Raman Spectroscopy.....	145
7.1	Introduction.....	145
7.2	Experimental Section	148
7.2.1	Chemicals and Solution Preparation.....	148
7.2.2	Crystallization and Adsorption Experiments	148
7.2.3	TERS Experimental Details.....	150
7.3	Results and Discussion	150

7.4 Conclusion	157
7.5 References.....	157
Chapter 8.....	160
8 Conclusion and Outlook.....	160
8.1 References.....	165
Appendix A.....	167
Curriculum Vitae	190

List of Tables

Table 4.1 Comparison of the electric field enhancement at the apex of silver or gold tip in 1 nm distance from thin gold or silver substrate.....	107
Table 7.1 Preliminary structure of OPN	147
Table 7.2 Raman peak assignment for p-OPN and COM Crystals.....	151

List of Figures

Figure 1.1 Examples of recently published TERS studies (a) STM morphology of insulin fibrils, TERS scanning along the dashed line has revealed α -helix and β -sheet domains. The image is adapted from reference 43 with permission from American Chemical Society.⁴³ (b) AFM image of β -amyloid nanotapes (left bottom corner inset) along with TERS image corresponding to the ring breathing mode. The images are adapted from reference 51 with permission from American Chemical Society.⁵¹ (c) AFM image of malaria-infected and non-infected cells (d) AFM image of the highlighted area in (c) showing hemozoin crystals inside the infected cell along with TERS spectra acquired with tip approached to or retracted from the cell surface. Images in (c) and (d) are adapted from reference 49 with permission from American Chemical Society.⁴⁹ (e) confocal Raman image of carbon nanotubes corresponding to the G band (f) TERS image of the highlighted area in (e). The images in (e) and (f) are adapted from reference 56 with permission from American Physical Society.⁵⁶ (g) STM topographic image taken simultaneously with TERS image of carbon nanotubes with 1.7 nm resolution. Images are adapted from reference 57 with permission from Nature publications.⁵⁷ 5

Figure 2.1 Jablonski Diagram for various light-matter interactions..... 13

Figure 2.2 Illustration of propagating surface plasmon at the interface between metal surface and a dielectric 21

Figure 2.3 Complex dielectric constants of (a) gold and silver (b) copper and aluminum according to the Drude model..... 22

Figure 2.4 Dispersion relation (solid line) and the propagating length (dashed line) of a surface plasmon on (a) gold-air (b) silver-air (c) copper-air and (d) aluminum air interface according to the Drude model. The propagation of light in free space is shown by dotted lines in each case. 23

Figure 2.5 Illustration of localized surface plasmon in metal nanostructures (a) SEM image of hexagonal arrays of gold nanopillars created by nanolithography over the glass surface (b) FDTD simulation of a single hexagonal array showing the confinement of the electric field at

the surface of the nanopylramids and inside the gaps between the neighboring pyramids. The images are adapted from reference 34 with permission from American Chemical Society.³⁴ 25

Figure 2.6 Illustration of the near-field concept in TERS setup. The TERS tip is kept at around 1 nm distance above the surface by means of the feedback system. When the apex of the TERS tip is placed inside the focal region of an incident laser beam, the electric field gets confined in close proximity of the apex with 10-20 nm diameters. The Raman scattering of a molecule which is placed inside this intensified electric field will be enhanced..... 27

Figure 2.7 Illustration of the diffraction limit problem and its dependence on the relative positions of neighboring Airy patterns (a) shows the top and side view of Airy pattern (b) demonstrates the diffraction limit (Δx) to be the distance between the center of the two Airy patterns when the first intensity minimum of each Airy pattern is aligned with the intensity maximum of the neighboring one (c) For center-to-center distances larger than Δx the neighboring objects will be completely resolved..... 29

Figure 2.8 Schematic of various SNOM configurations (a) Principle of SNOM using a small aperture on an opaque substrate (b) aperture SNOM with a coated optical fiber attached to a tuning fork. The tip is shown in excitation mode but can also be used for light collection purpose. (c) aperture SNOM provided through making hollow AFM probes (d) apertureless metallic tip, in close proximity of sample surface. 32

Figure 2.9 Illustration of different enhancement mechanism (a)-(c) demonstrate three types of chemical mechanism while (d) shows electromagnetic mechanism..... 35

Figure 3.1 Illustration of different SPM feedback systems (a) AFM feedback with tip oscillating vertically with respect to the sample surface (b) STM feedback with tip oscillating laterally with respect to the sample surface (c) shear force feedback with tuning fork mounted vertically and the tip moving laterally with respect to the surface (d) feedback mechanism with tuning fork mounted horizontally and the tip oscillating vertically with respect to the sample surface..... 45

Figure 3.2 TERS optical configurations (a) side illumination, the back-scattered light can be collected either by the illuminating microscope objective or a different one in transmission

geometry. The two objectives are depicted in grey and green respectively (b) top illumination, the back-scattered light can be collected either by the illuminating microscope objective or by a different one in transmission geometry The two objectives are depicted in grey and green respectively (c) illustration of parabolic mirror-based top illumination configuration. Radially polarized laser is focused by a parabolic mirror onto an etched gold tip connected to tuning fork (d) bottom illumination geometry where both incident and back-scattered light is collected by the same microscope objective (e) plasmonic TERS tip nanofabricated through creating waveguides on the tip cantilever (f) etched gold tip with FIB fabricated grating on its shaft. The tip is mounted on the tuning fork of a shear force AFM. 49

Figure 3.3 (a) SEM image of a trapped waveguide on Si₃N₄ AFM cantilever. The radius of the tip apex is 5 nm. The image is obtained from reference 34 with permission from Nature publications.³⁴ (b) SEM image of an electrochemically etched gold tip with FIB-cut grating on its shaft. The image is adapted from reference 45 with permission from American Chemical Society.⁴⁵ 52

Figure 3.4 Scheme of the TERS setup used in this thesis. The linearly polarized laser passes through a spatial filter to yield a homogeneous Gaussian spatial distribution and then gets converted into a radially polarized light by a liquid crystal (LC) polarization converter. The diameter of the radially polarized laser gets minimized by means of a pair of convex-concave lenses before entering the microscope objective. Next, the radially polarized laser gets focused onto the apex of the TERS tip to excite the Raman scattering of the sample in proximity of the TERS tip. The backscattered light from the sample gets collected using the same microscope objective, passes through the notch filter to reject the incident wavelength and then enters the spectrometer. Inside the spectrometer, a diffraction grating disperses the light spatially, separating the distinct wavelengths. The dispersed light is then detected by a CCD detector. A signal will be sent from the CCD to computer software where the Raman spectrum is created..... 53

Figure 3.5 (a) Real and (b) imaginary part of complex dielectric function for some noble metals. The two charts are plotted based on the dielectric constant values reported by Johnson & Christy for gold, silver and copper.⁵¹ Dielectric constants of aluminum matches the values reported by Rakie.⁵² 55

Figure 3.6 SEM images of (a) silicon NCL tapping mode AFM tip (b) ND-DTIRL nanocrystalline all diamond AFM tips.....	58
Figure 3.7 The schematic diagram of the etching process for fabricating the gold tips. The gold wire is immersed through a floating cathode ring into the etching solution of HCl and ethanol. The anode (gold wire) and the cathode ring are connected to an AC/DC current supply.....	59
Figure 3.8 SEM image of gold tip etched inside the etching solution of (1:1 V/V) HCl and ethanol using (a) DC and (b) AC voltage	62
Figure 3.9 SEM images of silver coated silicon tips (NCL tapping mode tips, NanoWorld™). The coated layer includes 5 nm of titanium and 30 nm of silver. (a)-(d) present different magnification of the same image. A metal island of around 30 nm diameters is formed at the tip apex as presented in (d).	63
Figure 3.10 (a) Top view SEM image of bow-tie optical antenna at the apex of an AFM tip. The image is obtained from reference 89 with permission from American Physical Society. ⁸⁸ (b) Side view SEM image of a tip-on aperture nanoantenna. The image is obtained from reference 92 with permission from American Chemical Society. ⁹¹	64
Figure 3.11 (a) SEM image of a TERS gold tip fabricated by focused ion beam (FIB) method. The image is obtained from reference 95 with permission from Annual Reviews. ⁹⁴ (b) SEM image of a template-stripped gold tip. The image is obtained from reference 97 with permission from American Chemical Society. ⁹⁶	65
Figure 3.12 Mechanical damage of the silver coating layer after several scans with non-optimized feedback parameters.....	67
Figure 3.13 (a) Interaction between a metalized tip and Gaussian transverse polarized mode creates no component along the tip axis (b) interaction between a metalized tip and radially polarized mode generates a field component along the tip axis	68
Figure 3.14 Liquid crystal polarization modulator configurations. Linearly polarized light enters from the left first into the phase compensator. The electric field vectors might be	

rotated by the nematic cell and the light will exit with a radially or azimuthally polarization from the θ -cell.....	70
Figure 3.15 (a) radially (b) azimuthally polarized light generated by θ -cell.....	71
Figure 3.16 Radially polarized (a) 632.8 nm laser projected at a CCD camera before reaching the microscope objective(b) 532 nm laser projected at a CCD camera before reaching the microscope objective(c) 632.8 nm laser focused by a x100 oil immersion objective with $N.A.=1.4$ (d) 532 nm laser focused by a x100 oil immersion objective with $N.A.=1.4$	72
Figure 3.17 (a) Raman spectra of the α -quartz obtained with radially and azimuthally polarized laser (b) z component of α -quartz Raman spectra.....	75
Figure 3.18 Tip alignment based on the collection of the Rayleigh scattering from the cantilever. (a) and(b) are images of an area around the tip apex proximity recorded with different zoom.....	76
Figure 3.19 Tip alignment by Raman spectra collection (a) image of the cantilever generated by light reflection caused by vertical deflection of the tip upon interacting with the laser (b) Raman map generated by integrating the Raman intensity in the $[515-525]\text{cm}^{-1}$ spectral range. The pixel with the larger intensity indicates the tip location (indicated by a dashed circle in (b)).....	77
Figure 3.20 Illustration of TERS mapping process. After the AFM image of the sample is collected, an area over the surface will be mapped. The mapping area is divided into small pixels and a Raman spectrum will be collected from each pixel as it moves to the close proximity of the TERS tip apex. The mapped area is shown by a white dashed mesh in this figure.....	79
Figure 4.1 Illustration of standard Cartesian Yee cell used for FDTD. The electric (E_x, E_y, E_z) and magnetic (H_x, H_y, H_z) field components are distributed about this cell. The electric field components originate from the edges of the cube and the magnetic field components come out of the faces.....	97

Figure 4.2 (a) Transverse component of a focused radially polarized beam (b) longitudinal component of a focused radially polarized beam in 3D and 2D presentations.....	99
Figure 4.3 Electric energy density of the total field of a focused linearly x polarized light in (a) top and (b) side view (c) longitudinal field of a linearly x polarized light in top and (d) side view.	101
Figure 4.4 Electric field distribution at the 10 nm apex of (a) a silver tip illuminated at 532 nm by linearly polarized light along the tip axis (b) a silver tip illuminated at 532 nm by linearly polarized light perpendicular to the tip axis (c) a silver tip illuminated at 532 nm by radially polarized light along the tip axis (d) gold tip illuminated at 632.8 nm by linearly polarized light along the tip axis (e) gold tip illuminated at 632.8 nm by linearly polarized light perpendicular to the tip axis (f) gold tip illuminated at 632.8 nm by radially polarized light along the tip axis.....	103
Figure 4.5 Electric field distribution at the 10 nm apex of a silver or gold tip illuminated at 532 or 632.8 nm, respectively, (a)-(d) by linearly polarized light along the tip axis in 1 nm separation from a gold or silver substrate (e)-(h) by linearly polarized light perpendicular to the tip axis in 1 nm separation from a gold or silver substrate (I)-(L) by radially polarized light along the tip axis in 1 nm separation from a gold or silver substrate.....	105
Figure 4.6 Electric field distribution at the 10 nm apex of a silver tip protected with 1nm Al_2O_3 layer and illuminated at 532 nm by (a) linearly polarized light along the tip axis (b) linearly polarized light perpendicular to the tip axis (d) radially polarized light along the tip axis, in 1 nm separation from a gold substrate.....	108
Figure 5.1 Illustration of the unit cell in single layer graphene. There are two sp^2 carbons in each unit cell and the overall structure consists of unsaturated hexagonal carbon cycles with carbon-carbon double bonds. \mathbf{a}_1 and \mathbf{a}_2 are the unit vectors.....	113
Figure 5.2 Correlation between the n and m integers and the structure of carbon nanotube. Rolling of the single layer graphene in the direction of X or any combination of the two integers results in unique structural and physical properties	113

Figure 5.3 (a) AFM image of carbon nanotubes on glass cover slip. Evidenced by the inset cross-section curve, carbon nanotubes with sub-15 nm diameter are perfectly resolved (b) Raman spectrum of carbon nanotubes in far-field configuration	118
Figure 5.4 (a) Near-field Raman intensity map of SWCNT (b) TERS spectra of three arbitrary points on the TERS map (c) AFM topographic image of the SWCNT (d) averaged Raman cross-section obtained from the Raman map in (a), (d) topographic cross section obtained over the dashed line in (c)	119
Figure 5.5 (a) AFM image of an isolated carbon nanotube with 15 nm diameter as shown in the inset topographic cross-section curve (b) Raman intensity profile along the dash line in orthogonal direction to the SWCNT's main axis while the tip is approached to (TIP-IN) and retracted from (TIP-OUT) the sample. The lateral resolution is estimated to be around 20 nm according to the fitted curve.	121
Figure 5.6 (a) AFM image of a nearly isolated carbon nanotube with 10 nm diameter as shown in the inset topographic cross-section curve (b) Raman intensity cross-section along the dash line in orthogonal direction to the SWCNT's main axis while the tip is approached to (TIP-IN) and retracted from (TIP-OUT) the sample. The lateral resolution is estimated to be around 20 nm according to the fitted curve.	122
Figure 5.7 Dependence of the Raman intensity of the G band on the longitudinal tip-sample separation. The squared points show the experimental data and the dashed line shows a fitted line over these data.....	124
Figure 6.1 First order optical phonon Raman peak of silicon nanowire and (100) silicon wafer	134
Figure 6.2 (a) Vertical deflection image of the nanocrystalline diamond tip and cantilever coated with 5 nm titanium and 20 nm silver (b) Raman intensity map of the same tip. The three edges of the tetrahedral pyramid can clearly be distinguished (c) Raman spectra of a nanocrystalline diamond tip (d) Geometry of the nanocrystalline tetrahedral diamond tip, $\alpha = 125.24^\circ$ and $\alpha' = 79.34^\circ$	135

Figure 6.3 (a) AFM image and topographic cross-section of the studied silicon nanowire. The AFM image was recorded with a non-coated tip after the TERS experiments. The lateral resolution of the AFM cross-section is poor compared to the height resolution presumably due to the wide opening angle of the tip apex shown in Figure 6.2d (b) near-field (TIP-IN) Raman intensity map of the silicon nanowire showing the variation of the silicon Raman signal intensity (c) far-field (TIP-OUT) Raman intensity map of the silicon nanowire. For (b) and (c) the spectra were integrated over the 511-534 cm^{-1} spectral range.....	137
Figure 6.4 (a) AFM image of a single silicon nanowire and the topography cross-section of the same nanowire (b) total Raman signal when the metal tip approaches the sample. The full width at half maximum indicates a spatial resolution of ~ 450 nm as compared to a topographical cross-section of ~ 300 nm provided by the AFM. (c) the optical cross-section obtained in far-field measurements provides a full width at half maximum of 1200 nm and significantly lower Raman intensities.....	139
Figure 6.5 Raman spectra with metalized tip positioned in the optical near-field and in the optical far-field of the sample. The difference of the two spectra indicates the enhancement induced by the metallic tip.....	140
Figure 6.6 (a) AFM image of a bent silicon nanowire (b) TERS spectra collected along the nanowire in position 1-4	141
Figure 6.7 (a) AFM image of two crossed silicon nanowires (b) TERS spectra measured on points 1-3	142
Figure 7.1 Perspective view of a faceted COM penetration twin depicting the main crystal faces of calcium oxalate monohydrate.....	146
Figure 7.2 Schematic (not to scale) of a reaction well-containing Teflon block for the growth of COM crystals.....	149
Figure 7.3 Raman spectra of the phosphoprotein p-OPN and COM crystals. The acquisition times were 120 sec for p-OPN and 20 sec for the COM crystal using similar irradiation conditions. The spectrum of the protein is multiplied by a factor of 10.....	150

Figure 7.4 TERS maps of p-OPN adsorbed to {100} and {010} crystal faces. The color bars represent Raman intensity. Blue and white colors indicate weak and strong Raman signals, respectively. (a and d) Integration area used to generate the maps in (b and c) and (e and f), respectively. (b and c) Maps resulting from the integration of the 1465 cm⁻¹ peak on {100} and {010} faces (signal of COM and p-OPN), respectively. (e and f) Raman intensity maps resulting from the integration of the 1487 cm⁻¹ peak of {100} and {010} faces (COM only), respectively. (g and h) Raman spectra of four spots (see (b) and (c)) selected from maps on {100} and {010} faces, respectively..... 152

Figure 7.5 (a) Raman spectra of adsorbed p-OPN on COM faces along with (b) AFM images of {010} face of COM. The green, red, and blue spectra correspond to the near-field, far-field, and TERS spectra, respectively. 155

Figure 7.6 (a,d) AFM images of {100} and {010} faces. Raman intensity maps of p-OPN adsorbed to an {100} face: (b) in TERS, (c) in standard Raman mode. Raman intensity maps of OPN adsorbed to an {010} face (e) in TERS and (f) in Raman mode. For both modes, the scanned area was set to be 20×5 μm², using 330 nm steps along both directions. This results in a total of 900 measuring points..... 156

Figure 8.1 (a) STM image of sub-monolayer of H₂TBPP molecules on Ag(111). Two isolated single molecules on the right, three-molecule cluster at the center and a densely packed monolayer island on the left are observed. The blue area in this image shows the Ag(111) surface (b) Experimental TERS mapping of single molecule generated through intensity variation of the 817 cm⁻¹ Raman peak (c) Height profile of a line trace in the inset STM image (d) TERS intensity profile of the same line trace in the inset TERS map (e) TERS spectra of different spots on the STM image presented in (a). The acquisition time was 3sec for all the recorded spectra. The images are adapted from reference 1 with permission from Nature publications. 163

List of Abbreviations, Symbols and Nomenclature

$\bar{\alpha}$	polarizability of a molecule
α	maximum focusing angle of a microscope objective
β_0	ratio of the pupil radius to the beam waist
χ	shape factor of a nanoparticle
Δ	tip-sample separation
Δx	optical diffraction limit
ϵ_0	dielectric constant of free-space
ϵ_d	dielectric constant of a dielectric
ϵ_m	complex dielectric constant of a metal
$\epsilon(\omega)$	dielectric function of the TERS tip
γ_k	anisotropic polarizability for Raman mode k
λ	wavelength of light
μ	permeability or magnetic constant of a medium
$\bar{\mu}$	dipole moment
ν_0	wavenumber of incident laser
ν_k	wavenumber of vibrational mode k
ν	wavenumber
θ	indicator angle of points in polar coordinate
ρ	transverse size of a beam
$\rho(t,r)$	volume density of electric charge
$\sigma_{\text{ext/sca/abs}}$	extinction/scattering/absorption cross-section
ω	laser frequency
ω_p	plasmon frequency
Ω	two dimensional solid angle
0D	zero dimensional
1D	one dimensional
2D	two dimensional
3D	three dimensional
$\nabla \cdot$	divergence function
$\nabla \times$	curl operator
\mathbf{a}_1 and \mathbf{a}_2	in plane unit vectors of graphene unit cell
a_k	isotropic polarizability for Raman mode k
AC	alternating current
AFM	atomic force microscope
APD	avalanche photodiode
A_{farfield}	illuminated area in far-field measurements
$A_{\text{nearfield}}$	illuminated area in near-field measurements
B	radius of illumination aperture in Airy pattern equation
\bar{B}	magnetic flux density in Maxwell equation
c	speed of light
C	spectroscopic contrast
CCD	charge-coupled device
COM	calcium oxalate monohydrate

d	diameter of a nanosphere
\vec{D}	electric displacement in Maxwell equations
DC	direct current
DDA	discrete dipole approximation
DFT	density function theory
e	charge of electron
\vec{E}	electric field
$\vec{E}_{in/out}$	incoming/emitted electric field in near-field optics
$E_{tip/0}$	electric field magnitude in presence/absence of the TERS tip
$ E ^2$	total electric field density
$ E_{x/y/z} ^2$	intensity of the $x/y/z$ electric field component
EF	enhancement factor
EFGR	electric field gradient in Raman
F-C	Frank-Condon (overlap/factor)
FDTD	finite-difference time-domain
FE	finite element
FIB	focused ion beam
FWHM	full width at half maximum
GPMM	generalized point matching method
h	Planck's constant
\vec{H}	magnetic field
HOMO	highest occupied molecular orbital
I	light intensity
$I_{nearfield/TIP-IN}$	near-field Raman intensity
$I_{farfield/TIP-OUT}$	far-field Raman intensity
J_0	Bessel function of the first kind of order zero
J_1	Bessel function of the first kind of order one
$\vec{J}(t,r)$	volume density of electric current
\vec{k}	wavevector
k_B	Boltzmann constant
k_{sp}	dispersion of surface plasmon along the interface
k_z	dispersion of surface plasmon normal to the interface
LC	liquid crystal
LO	longitudinal optical mode
l_{sp}	propagation length of surface plasmon
LSPR	localized surface plasmon resonance
LUMO	lowest unoccupied molecular orbital
m_e	effective mass of electron
MALDI-TOF	matrix-assisted laser desorption/ionization time-of-flight mass
MS	spectroscopy
MMP	multiple multipole program
n	index of refraction
n_e	number of electrons
(n,m)	geometrical integers in carbon nanotube
$N.A.$	numerical aperture of an microscope objective
OPO	optical parametric oscillator

OPN	osteopontin
\bar{P}	microscopic polarization
$P(\theta)$	pupil function of a Bessel Gaussian beam
PECVD	plasma enhanced chemical vapor deposition
PML	perfectly matched layer
PMT	photomultiplier tube
pOPN	phosphorylated osteopontin
\bar{Q}_k	normal coordinate of the vibrational mode k
\bar{r}	electron displacement inside an incident electromagnetic field
r_{laser}	radius of the laser cross-section
r_{tip}	radius of the TERS tip apex
\vec{R}	radius vector of a point position in space
RBM	ring breathing mode
recOPN	recombinant osteopontin
s_0	incident photon density
S_1, S_2	singlet energy state
SEM	scanning electron microscopy
SERS	surface-enhanced Raman spectroscopy
SF	sheer force
SiNW	silicon nanowire
SNOM	scanning near-field microscopy
SPM	scanning probe microscopy
SP	surface plasmon
STM	scanning tunneling microscope
SWCNT	single walled carbon nanotube
t	time
T	temperature
T_1	triplet energy state
TEM	transmission electron microscopy
TERS	tip-enhanced Raman spectroscopy
TFSF	total field scattered field
THP	Tamm-Horsefall protein
TO	transverse optical mode
Trp	tryptophan
UHV	ultrahigh vacuum

List of Appendices

Appendix A.: Copyrights

167

Chapter 1

1 General Introduction

1.1 Overview

The discovery of Raman scattering resulted from extensive studies of inelastic scattering of light in liquids and solids by Indian scientist C. V. Raman in the early 1920's. Also, in 1923, Adolf Smekal suggested that light could get scattered inelastically with wavelengths shorter or longer than the original excitation wavelength.^{1,2} In 1928, C. V. Raman presented the first Raman spectra and the resulting seminal manuscript reporting this effect.³ He was honored by a Nobel Prize in Physics in 1930. Further development of Raman spectroscopy was however marginal for years mainly because the Raman scattering was typically too weak to be detected in absence of powerful light sources and efficient detectors.⁴ Much later, the discovery of laser in 1960 as well as the progress in optical detection stimulated the continuous development of Raman spectroscopy.

Raman spectroscopy is an analytical method that reveals knowledge about structure,^{5,6} symmetry,⁷ bonding in molecules or crystals⁸⁻¹⁰ and also the electronic environment¹¹ of material through their vibrational fingerprints. Currently, Raman spectroscopy is inclusively employed in various fields such as chemical analysis,^{12,13} material sciences,^{14,15} biomedical applications^{16,17} and even art-related investigations.^{18,19} Noticeably, the inherent low efficiency of the inelastic scattering in Raman can be counter-balanced using plasmonic platforms that enable enhancement of the signal by several orders of magnitude. In this context, the use of localized surface plasmon resonances is of particular interest with the goal to concentrate the light in the vicinity of sharp metal structures that act as near-field of light.^{20,21} Plasmon resonances originate from the optical response of the free conduction electron in noble metals to incoming electromagnetic field. Consequently, a confined electric field will be generated within the near-field of the metal surface. When a molecule is located inside this confined and intensified electric field its Raman signal will get intensified since it roughly scales with the forth power of the excitation electric field.^{22,23} The discovery of this phenomenon

gave rise to a revolutionary sensitive analytical method which was termed as surface-enhanced Raman spectroscopy (SERS) in the early 1970s.^{24,25}

In SERS, the Raman scattering is typically enhanced up to a factor of 10^6 to 10^{12} through locating the sample in close proximity to plasmonic metal nanostructures.²⁶⁻²⁸ SERS has emerged as a powerful technique with applications within multidisciplinary fields and with detection limits down to single molecule.²⁹⁻³¹ Beyond the increased sensitivity of molecules adsorbed onto a metallic surface, the use of plasmonic structures is also very useful to improve the spatial resolution in optical microscopy and spectroscopy measurements inherently limited by the diffraction limit of light.³² This limit, known as the Rayleigh criterion, is a function of the excitation wavelength, λ , and the focusing properties of the utilized microscopic objective.³³ This dependence implies that the smallest distance that could be resolved in far-field measurement, including SERS, is in the range of $\lambda/2$, which is typically about 200-300 nm under the ideal experimental conditions.³⁴ For this reason, many research groups have been developing new approaches to use efficiently plasmonic nanostructures with the goal to improve the lateral resolution of the surface-enhanced Raman measurements.

As early as 1928, Synge introduced the concept of illuminating the sample through a sub-wavelength aperture in a metallic film which is brought into a few nanometers above the sample surface with the goal to probe the near-field of the sample.³⁵ In this new configuration, the lateral resolution will no longer be dictated by classical optics laws but by the dimension of the aperture. After the invention of the scanning probe microscopy techniques such as scanning tunneling microscopy (STM) and atomic force microscopy (AFM) in the 1980's and the development of micro and nanofabrication techniques, Synge's ideas found new implications into the development of methods termed as scanning near-field optical microscopy (SNOM) which allowed for microscopy and spectroscopy measurements with lateral resolutions surpassing the Rayleigh's diffraction limit.³⁶⁻³⁹ Tip-enhanced Raman spectroscopy (TERS) was indeed developed on the basis of scanning near-field optical microscopy in combination with near-field optics and plasmonic effects.

In TERS, a metallic tip (usually silver or gold) with a tip radius of 10-20 nm is brought into feedback with the surface of a sample using a typical atomic force or scanning tunneling microscope setup. The power of TERS originates from the excitation of the localized surface plasmon that is confined at the sharp apex of this metallic tip located inside the focal region of a tightly focused laser beam.⁴⁰ The localized surface plasmon resonances intensify the electric field in a small volume around the apex. The tip apex, hence, acts as a nanoantenna that receives, intensifies and emits the excitation light. This local confinement of the electric field enhances the Raman process and allows for specifically investigating surfaces and interfaces and collecting Raman intensity map of very small features with sub-20 nm lateral resolution.⁴¹ In TERS, the accessible resolution is mainly determined by the size of the tip apex. In addition to the improvement of the lateral resolution, TERS allows for sensitive analyses of very small domains in the absence of any label (isotopes, fluorophores, etc.). Labeling could lead to undesirable artifacts and misleading information in the Raman spectra of the sample, and sometimes it requires the synthesis of exogenous fluorophores, which could perturb the native organization of the biosystem of interest.⁴² Therefore, the nature of TERS to be label-free is specifically of interest for the study of biological samples.

1.2 Application of TERS in Material and Life Sciences

At present, there are limited alternatives to TERS measurements when simultaneous structural and chemical analysis of nanoscale features and/or sensitive detection of very low concentrations are needed. In life sciences, TERS abilities have been evaluated for characterizing a large variety of samples by several leading research groups. Among many examples where TERS is key to understand intimate processes in material and biomaterials science, Deckert⁴³ showed that TERS is a powerful tool for characterizing the surface structure of individual amyloid fibrils that are associated with many neurodegenerative diseases. Using TERS they located α -helix and β -sheets along the microscale fibrils as shown in **Figure 1.1a**. Deckert's TERS measurements extend to individual RNA strands,⁴⁴ isolated mitochondria of yeast cells,⁴⁵ various nucleobases,⁴⁶ the lipids and protein domains of human cells,⁴⁷ viruses⁴⁸ and malaria-infected cells.⁴⁹ An example of a malaria-infected cell along with its corresponding TERS spectra are

presented in **Figure 1.1c** and **Figure 1.1d**. Through scanning the surfaces of each of these samples by the TERS tip, Deckert and his coworkers found valuable structural details on the composition and the organization of proteins and nucleobases located on the surfaces at the sub-micrometer scale. Meixner *et al.*⁵⁰ investigated monolayer of calf thymus DNA and improved the detection limit to a single DNA strand, opening an innovative spectroscopic technique for the investigation of DNA-drug interactions. Zenobi *et al.*⁵¹ studied a single nanotape formed from β -amyloid peptide fragments by TERS. Despite the weak scattering of these biological species, high sensitivity of TERS enabled generating high resolution TERS images that match simultaneously obtained STM topographic images as shown in **Figure 1.1b**. In a different study, they demonstrated that TERS is the method of choice in investigating lipid monolayer on gold surfaces, while emphasizing the non-destructive nature of TERS combined with a spatial resolution better than 50 nm.⁵² Wood and his coworkers⁵³ employed TERS to detect DNA double strand breaks and provide information on the molecular events that occur at each individual break site.

TERS has also found applications in interfacial and surface sciences. Deckert *et al.*⁵⁴ showed that TERS is capable of dynamic monitoring photo-catalytic reactions onto functionalized surfaces. In their study, a silver coated tip was used to enhance the Raman process and to catalyze the photo-catalytic reduction of self-assembled monolayer of p-nitrothiophenol molecules adsorbed on transparent gold nanoplates. In surface science, Rzenicka *et al.*⁵⁵ used TERS to investigate the molecular arrangement of 4,4'-bipyridine and 4,4'-bipyridine N,N'-dioxide adsorbed on gold(111) thin film. They concluded that 4,4'-bipyridine adsorbs upright to the gold surface while it stabilizes the attachment by coordinating one of the N atoms of the pyridyl ring with gold. They also concluded that 4,4'-bipyridine N,N'-dioxide adsorbs in a vertical configuration with the molecular longitudinal axis parallel to the surface.

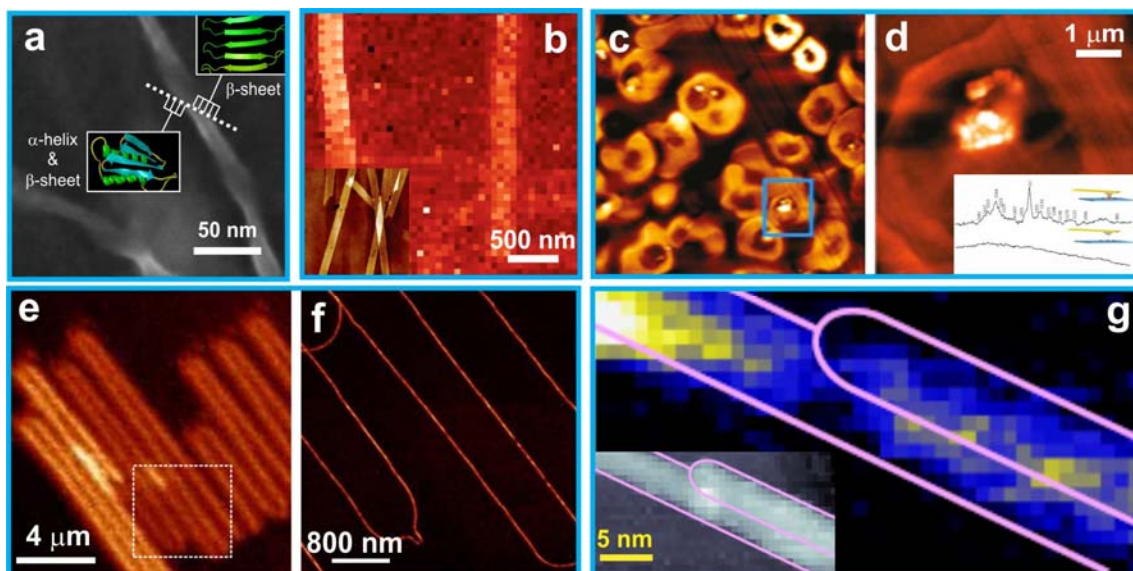


Figure 1.1 Examples of recently published TERS studies (a) STM morphology of insulin fibrils, TERS scanning along the dashed line has revealed α -helix and β -sheet domains. The image is adapted from reference 43 with permission from American Chemical Society.⁴³ (b) AFM image of β -amyloid nanotapes (left bottom corner inset) along with TERS image corresponding to the ring breathing mode. The images are adapted from reference 51 with permission from American Chemical Society.⁵¹ (c) AFM image of malaria-infected and non-infected cells (d) AFM image of the highlighted area in (c) showing hemozoin crystals inside the infected cell along with TERS spectra acquired with tip approached to or retracted from the cell surface. Images in (c) and (d) are adapted from reference 49 with permission from American Chemical Society.⁴⁹ (e) confocal Raman image of carbon nanotubes corresponding to the G band (f) TERS image of the highlighted area in (e). The images in (e) and (f) are adapted from reference 56 with permission from American Physical Society.⁵⁶ (g) STM topographic image taken simultaneously with TERS image of carbon nanotubes with 1.7 nm resolution. Images are adapted from reference 57 with permission from Nature publications.⁵⁷

In the field of material science, TERS has been widely used to characterize one-dimensional structure such as CdSe,⁵⁸ GaN⁵⁹ and Ge nanowires.⁶⁰ Novotny,^{56,61,62} Hartschuh,^{34,41,58,63-65} Maultzsch,⁶⁶⁻⁶⁸ Williams⁶⁹ and Kawata⁷⁰⁻⁷³ have made significant efforts in TERS investigation of carbon nanotubes, initiating extensive and ongoing contributions in this area.⁷⁴⁻⁷⁶ The work of Novotny in large scale TERS mapping of a self-organized carbon nanotube serpentine⁵⁶ is a great illustration of the high lateral resolution of the method as presented in **Figure 1.1e** and **Figure 1.1f**. The near-field map is obtained by integrating the intensity of the C-C stretching G band at 1580 cm^{-1} which resulted in resolution of 25 nm defined by the TERS tip radius. Recently, Kawata⁵⁷ reached 1.7 nm resolution in TERS mapping of carbon nanotubes through simultaneous chemical and structural analysis by STM-TERS. The measurements are conducted at room temperature and inside a dry nitrogen environment inside an enclosure and the gold tip is illuminated in side illumination configuration by a 632.8 nm wavelength laser which is polarized along the tip axis. In their work a strong plasmonic enhancement is generated inside the nanogap between a clean gold tip and a gold substrate. STM image of carbon nanotubes along with the corresponding TERS image are presented in **Figure 1.1g**. Other than one dimensional samples, TERS has been used successfully as a nanocrystallographic technique for the study of a variety of crystalline nanomaterials including GaAs and BaTiO₃ single crystals,^{77,78} and silicon/silicon oxide structures.⁷⁹

1.3 Scope of the Thesis

The present thesis is organized as follows:

In Chapter 2, the theoretical background that is essential for thorough understanding of the TERS underlying principles is developed. The principles of Raman spectroscopy are first presented. Plasmonic properties of noble metals along with near-field optics are described theoretically. Principles of TERS have also been approached theoretically followed by a discussion concerning the enhancement phenomenon and the mechanisms that are proposed to explain it.

The experimental aspects of tip-enhanced Raman spectroscopy are described in Chapter 3 providing technical details of the TERS setup and information on fabrication of the TERS probes. The Chapter includes practical information about the laser polarization consideration. The TERS experimental procedure used in this thesis and a section on calculation of the enhancement factor in TERS are also included.

In Chapter 4 a series of numerical calculation are presented that were performed by finite-difference time-domain (FDTD) method. Intensity and distribution of the electric field around the apex of the TERS tip has been investigated for various illumination configurations and different laser polarizations. Radially polarized light has been created and integrated into FDTD software to account for longitudinal polarizations. The effect of a transparent metal substrate as well as a tip-protection layer on the enhancement of the electric field in TERS have been also covered.

Chapter 5 of this thesis focuses on the limit of spatial resolution that is accessible in the utilized TERS configuration. For this purpose, isolated carbon nanotubes have been mapped and the acquired dimensions for the nanotubes in TERS maps have been compared to the high resolution AFM images of the same carbon nanotubes. The near-field nature of the enhanced Raman signals is also investigated in this Chapter.

Chapter 6 contains the results for TERS study of isolated silicon nanowires on glass substrate. High resolution of TERS has been employed to track the morphological changes along single nanowires. The observed variations have been related to spectral changes and optical responses in terms of the magnitude of the Raman shifts and the broadening effect that it might cause to the spectra. Single straight and bent nanowires as well as crossing wires have been studied in this Chapter.

Tip-enhanced Raman mapping of the surface of calcium oxalate monohydrate microcrystals is another example of valuable information obtained by TERS and is discussed in Chapter 7. The surface specificity and high sensitivity of TERS has been used to map the specific adsorption sites of osteopontin phosphoproteins over the distinct facets of single crystals. This Chapter emphasizes that beyond the improvement of the

spatial resolution, the interaction of a metallic tip with a surface provides high surface sensitivity and specificity.

In the conclusion Chapter, we give a critical view of the emerging fields where TERS can be of interest as well as the possible technical improvements yielding better reproducibility and better sensitivity of the TERS setup.

1.4 References

- (1) Long, D. A. *The Raman Effect: A Unified Treatment of the Theory of Raman Scattering by Molecules*; John Wiley & Sons, Inc.: Chichester, 2002.
- (2) Smekal, A. *Naturwissenschaften* **(1923)**, *11*, 873.
- (3) Raman, C. V.; Krishnan, R. S. *Nature* **(1928)**, *121*, 501.
- (4) Hibben, J. H. *The Raman Effect and Its Chemical Applications*; Reinhold Publishing Corp.: New York, 1939.
- (5) Acharya, S. A.; Maheshwari, N.; Tatikondewar, L.; Kshirsagar, A.; Kulkarni, S. K. *Cryst. Growth Des.* **(2013)**, *13*, 1369.
- (6) Fu, Q.; Lu, J.; Lin, N.; Zheng, S. *Rom. Biotechnol. Lett.* **(2012)**, *17*, 7557.
- (7) Heckel, J. C.; Weisman, A. L.; Schneebeli, S. T.; Hall, M. L.; Sherry, L. J.; Stranahan, S. M.; DuBay, K. H.; Friesner, R. A.; Willets, K. A. *J. Phys. Chem. A* **(2012)**, *116*, 6804.
- (8) Matz, K. G.; Mtei, R. P.; Leung, B.; Nieter-Burgmayer, S. J.; Kirk, M. L. *J. Am. Chem. Soc.* **(2010)**, *132*, 7830.
- (9) Nurulhuda, I.; Johari, M. A.; Mazatulikhma, M. Z.; Rusop, M. *Adv. Mater. Res.* **(2013)**, *667*, 464.
- (10) Zalamova, K.; Georgiev, M. D.; Georgiev, G. K. *Proc. SPIE-Int. Soc. Opt. Eng.* **(2003)**, *5226*, 179.
- (11) Schatschneider, B.; Monaco, S.; Tkatchenko, A.; Liang, J.-J. *J. Phys. Chem. A* **(2013)**, *117*, 8323.
- (12) Stair, P. C. *Adv. Catal.* **(2007)**, *51*, 75.
- (13) Chen, Y.; Jin, Z.; Pan, Z. *J. Supercrit. Fluids* **(2012)**, *72*, 22.
- (14) Dresselhaus, M. S.; Dresselhaus, G.; Saito, R.; Jorio, A. *Phys. Rep.* **(2005)**, *409*, 47.
- (15) Torres, A.; Martin-Martin, A.; Martinez, O.; Prieto, A. C.; Hortelano, V.; Jimenez, J.; Rodriguez, A.; Sangrador, J.; Rodriguez, T. *Appl. Phys. Lett.* **(2010)**, *96*, 0119041.
- (16) Choo-Smith, L. P.; Edwards, H. G. M.; Endtz, H. P.; Kros, J. M.; Heule, F.; Barr, H.; Robinson, J. S.; Bruining, H. A.; Puppels, G. J. *Biopolymers* **(2002)**, *67*, 1.
- (17) Thomas, G. J., Jr. *Annu. Rev. Biophys. Biomol. Struct.* **(1999)**, *28*, 1.

- (18) Madariaga, J. M.; Bersani, D.; Editors *Raman Spectroscopy in Art and Archaeology*. [In: *J. Raman Spectrosc.*, 2012; 43(11)]; John Wiley & Sons Ltd., 2012.
- (19) Tournie, A.; Prinsloo, L. C.; Paris, C.; Colomban, P.; Smith, B. *J. Raman Spectrosc.* (2011), 42, 399.
- (20) Kawata, S. *Appl. Spectrosc.* (2013), 67, 117.
- (21) Kawata, S.; Inouye, Y.; Verma, P. *Nat. Photonics* (2009), 3, 388.
- (22) Morton, S. M.; Silverstein, D. W.; Jensen, L. *Chem. Rev.* (2011), 111, 3962.
- (23) Novotny, L.; Hecht, B. *Principles of nano-optics*; 1st ed.; Cambridge University Press: Cambridge, England, 2006.
- (24) Haynes, C. L.; Yonzon, C. R.; Zhang, X.; Van, D. R. P. *J. Raman Spectrosc.* (2005), 36, 471.
- (25) Van Duyne, R. P. In *Chemical and Biochemical Applications of Lasers*; Moore, C. B., Ed.; Academic Press: New York, 1979; Vol. 4.
- (26) Albrecht, M. G.; Creighton, J. A. *J. Am. Chem. Soc.* (1977), 99, 5215.
- (27) Fleischmann, M.; Hendra, P. J.; McQuillan, A. J. *Chem. Phys. Lett.* (1974), 26, 163.
- (28) Jeanmaire, D. L.; Van Duyne, R. P. *Electroanal. Chem.* (1977), 84, 1.
- (29) Dieringer, J. A.; Lettan, R. B., II; Scheidt, K. A.; Van, D. R. P. *J. Am. Chem. Soc.* (2007), 129, 16249.
- (30) Kneipp, K.; Wang, Y.; Kneipp, H.; Perelman, L. T.; Itzkan, I.; Dasari, R. R.; Feld, M. S. *Phys. Rev. Lett.* (1997), 78, 1667.
- (31) Xu, H.; Bjerneld, E. J.; Kall, M.; Borjesson, L. *Phys. Rev. Lett.* (1999), 83, 4357.
- (32) Rayleigh, L. *Philos. Mag.* (1879), 8, 261.
- (33) Abbe, E. *Archiv für mikroskopische Anatomie* (1873), 9, 413.
- (34) Hartschuh, A.; Sanchez, E. J.; Xie, X. S.; Novotny, L. *Phys. Rev. Lett.* (2003), 90, 0955031.
- (35) Synge, E. H. *Philos. Mag.* (1928), 6, 356.
- (36) Bachelot, R.; Gleyzes, P.; Boccara, A. C. *Opt. Lett.* (1995), 20, 1924.
- (37) Inouye, Y.; Kawata, S. *Opt. Lett.* (1994), 19, 159.
- (38) Specht, M.; Pedarnig, J. D.; Heckl, W. M.; Haensch, T. W. *Phys. Rev. Lett.* (1992), 68, 476.
- (39) Zenhausern, F.; O'Boyle, M. P.; Wickramasinghe, H. K. *Appl. Phys. Lett.* (1994), 65, 1623.
- (40) Novotny, L. *Nature* (2008), 455, 887.
- (41) Cancado, L. G.; Hartschuh, A.; Novotny, L. *J. Raman Spectrosc.* (2009), 40, 1420.
- (42) Deckert-Gaudig, T.; Deckert, V. *Phys. Chem. Chem. Phys.* (2010), 12, 12040.

- (43) Kurouski, D.; Deckert-Gaudig, T.; Deckert, V.; Lednev, I. K. *J. Am. Chem. Soc.* **(2012)**, *134*, 13323.
- (44) Bailo, E.; Deckert, V. *Angew. Chem., Int. Ed.* **(2008)**, *47*, 1658.
- (45) Boehme, R.; Mkandawire, M.; Krause-Buchholz, U.; Roesch, P.; Roedel, G.; Popp, J.; Deckert, V. *Chem. Commun.* **(2010)**, *47*, 11453.
- (46) Treffer, R.; Bailo, E.; Deckert-Gaudig, T.; Deckert, V. *Beilstein J. Nanotechnol.* **(2011)**, *2*, 628.
- (47) Richter, M.; Hedegaard, M.; Deckert-Gaudig, T.; Lampen, P.; Deckert, V. *Small* **(2011)**, *7*, 209.
- (48) Cialla, D.; Deckert-Gaudig, T.; Budich, C.; Laue, M.; Moeller, R.; Naumann, D.; Deckert, V.; Popp, J. *J. Raman Spectrosc.* **(2009)**, *40*, 240.
- (49) Wood Bayden, R.; Bailo, E.; Khiavi Mehdi, A.; Tilley, L.; Deed, S.; Deckert-Gaudig, T.; McNaughton, D.; Deckert, V. *Nano Lett.* **(2011)**, *11*, 1868.
- (50) Hennemann, L. E.; Meixner, A. J.; Zhang, D. *Spectroscopy* **(2010)**, *24*, 119.
- (51) Paulite, M.; Blum, C.; Schmid, T.; Opilik, L.; Eyer, K.; Walker, G. C.; Zenobi, R. *ACS Nano* **(2013)**, *7*, 911.
- (52) Opilik, L.; Bauer, T.; Schmid, T.; Stadler, J.; Zenobi, R. *Phys. Chem. Chem. Phys.* **(2011)**, *13*, 9978.
- (53) Lipiec, E.; Sekine, R.; Bielecki, J.; Kwiatek, W. M.; Wood, B. R. *Angew. Chem., Int. Ed.* **(2014)**, *53*, 169.
- (54) van Schrojenstein Lantman, E. M.; Deckert-Gaudig, T.; Mank, A. J. G.; Deckert, V.; Weckhuysen, B. M. *Nat. Nanotechnol.* **(2012)**, *7*, 583.
- (55) Rzeznicka, I. I.; Horino, H.; Kikkawa, N.; Sakaguchi, S.; Morita, A.; Takahashi, S.; Komeda, T.; Fukumura, H.; Yamada, T.; Kawai, M. *Surf. Sci.* **(2013)**, *617*, 1.
- (56) Cancado, L. G.; Jorio, A.; Ismach, A.; Joselevich, E.; Hartschuh, A.; Novotny, L. *Phys. Rev. Lett.* **(2009)**, *103*, 1861011.
- (57) Chen, C.; Hayazawa, N.; Kawata, S. *Nat. Commun.* **(2014)**, *5*, 43121.
- (58) Boehmler, M.; Hartschuh, A. *Chem. Phys. Chem.* **(2012)**, *13*, 927.
- (59) Marquestaut, N.; Talaga, D.; Servant, L.; Yang, P.; Pauzauskie, P.; Lagugné-Labarthe, F. *J. Raman Spectrosc.* **(2009)**, *40*, 1441.
- (60) Ogawa, Y.; Yuasa, Y.; Minami, F.; Oda, S. *Appl. Phys. Lett.* **(2011)**, *99*, 0531121.
- (61) Anderson, N.; Hartschuh, A.; Novotny, L. *Nano Lett.* **(2007)**, *7*, 577.
- (62) Hartschuh, A.; Qian, H.; Georgi, C.; Boehmler, M.; Novotny, L. *Anal. Bioanal. Chem.* **(2009)**, *394*, 1787.
- (63) Boehmler, M.; Wang, Z.; Myalitsin, A.; Mews, A.; Hartschuh, A. *Angew. Chem., Int. Ed.* **(2011)**, *50*, 11536.
- (64) Georgi, C.; Hartschuh, A. *Appl. Phys. Lett.* **(2010)**, *97*, 1431171.

- (65) Hartschuh, A.; Anderson, N.; Novotny, L. *J. Microsc.* **(2003)**, *210*, 234.
- (66) Goss, K.; Peica, N.; Thomsen, C.; Maultzsch, J.; Schneider, C. M.; Meyer, C. *Phys. Status Solidi B* **(2011)**, *248*, 2577.
- (67) Peica, N.; Roehrig, S.; Ruediger, A.; Brose, K.; Thomsen, C.; Maultzsch, J. *Phys. Status Solidi B* **(2009)**, *246*, 2708.
- (68) Peica, N.; Thomsen, C.; Maultzsch, J. *Phys. Status Solidi B* **(2010)**, *247*, 2818.
- (69) Roy, D.; Williams, C. *J. Vac. Sci. Technol., A* **(2010)**, *28*, 472.
- (70) Okuno, Y.; Saito, Y.; Kawata, S.; Verma, P. *Phys. Rev. Lett.* **(2013)**, *111*, 2161011.
- (71) Tarun, A.; Hayazawa, N.; Yano, T.-A.; Kawata, S. *J. Raman Spectrosc.* **(2011)**, *42*, 992.
- (72) Yano, T.-a.; Ichimura, T.; Kuwahara, S.; H'Dhili, F.; Uetsuki, K.; Okuno, Y.; Verma, P.; Kawata, S. *Nat. Commun.* **(2013)**, *4*, 3592.
- (73) Yano, T.-a.; Verma, P.; Saito, Y.; Ichimura, T.; Kawata, S. *Nat. Photonics* **(2009)**, *3*, 473.
- (74) Nicklaus, M.; Nauenheim, C.; Krayev, A.; Gavriluk, V.; Belyaev, A.; Ruediger, A. *Rev. Sci. Instrum.* **(2012)**, *83*, 0661021.
- (75) Suzuki, T.; Yan, X.; Kitahama, Y.; Sato, H.; Itoh, T.; Miura, T.; Ozaki, Y. *J. Phys. Chem. C* **(2013)**, *117*, 1436.
- (76) Yan, X.; Suzuki, T.; Kitahama, Y.; Sato, H.; Itoh, T.; Ozaki, Y. *Phys. Chem. Chem. Phys.* **(2013)**, *15*, 20618.
- (77) Berweger, S.; Neacsu, C. C.; Mao, Y.; Zhou, H.; Wong, S. S.; Raschke, M. B. *Nat. Nanotechnol.* **(2009)**, *4*, 496.
- (78) Gucciardi, P. G.; Valmalette, J.-C. *Appl. Phys. Lett.* **(2010)**, *97*, 2631041.
- (79) Lee, N.; Hartschuh, R. D.; Mehtani, D.; Kisliuk, A.; Maguire, J. F.; Green, M.; Foster, M. D.; Sokolov, A. P. *J. Raman Spectrosc.* **(2007)**, *38*, 789.

Chapter 2

2 Principles and Theory of Tip-enhanced Raman Spectroscopy

The design and development of an efficient setup for tip-enhanced Raman spectroscopy (TERS) requires a thorough understanding of Raman spectroscopy and associated enhancement processes that yield high sensitivity and high spatial resolution of Raman measurements. The optical and spectroscopic principles of TERS are therefore presented in this Chapter as a basis to support the research work that follows in this thesis.

2.1 Raman Spectroscopy: Theory and Selection Rules

The nature of the light-matter interaction is dictated by the correspondence between the light wavelength and the energy required for vibrational or electronic transitions in the molecule as depicted in Jablonski diagram in **Figure 2.1**. Absorption of infrared light (IR) in the mid-infrared range (4-20 μm wavelengths) excites molecular vibrations within the ground electronic state. UV-visible light (280-700 nm) promotes electrons to higher energy levels followed by decaying through distinct pathways such as non-radiative relaxation or fluorescence and phosphorescence emission.¹ When the wavelength of incoming light does not match the energy of an electronic transition, light gets scattered by the illuminated molecules. The majority of the scattered photons are elastically scattered with energies equal to the energy of the incident light. This scattering process is called Rayleigh scattering. Meanwhile, a small number of photons (one out of 10^6 to 10^8 photons approximately)^{2,3} are scattered inelastically with optical frequencies different from the incident light. The inelastic light scattering caused by molecular vibrations is referred to as Raman scattering.²

In Raman scattering, the incident light interacts with quantized energy states of the scattering molecules in two different ways. The incident photons can either lose or gain energy upon Raman scattering. When the scattered light has lower energy as compared to the incident light, the process is called Stokes Raman scattering while the radiation with

higher energy is called anti-Stokes Raman scattering.⁴ Anti-Stokes Raman peaks are however less intense compared to the Stokes ones.² Upon Stokes Raman scattering, the photons undergo a transition from lower energy level to a higher one. On the contrary, in anti-Stokes Raman, energy transfers from the system to the incident light during a transition from a higher energy level to a lower one. According to the Boltzmann distribution, excited vibrational energy levels are less populated than the ground state. Hence, anti-Stokes is less intense because the scattering occurs from less populated state. The three forms of Raman scattering are depicted in **Figure 2.1**.

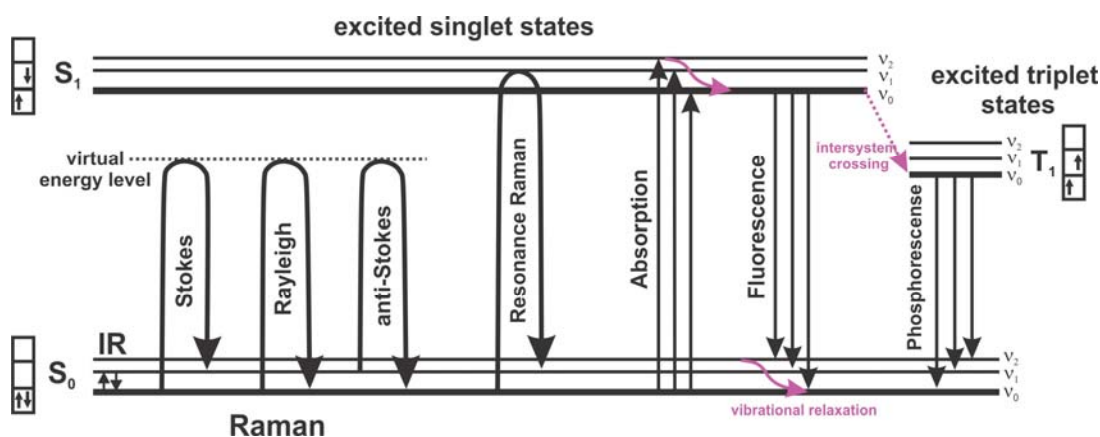


Figure 2.1 Jablonski Diagram for various light-matter interactions

For Stokes and anti-Stokes scattering, the absorption and the scattering process happens to and from an intermediate state which is a time-dependent superposition of molecular electronic states and is usually termed as virtual state. Virtual states have energies that do not match the energy of the existing electronic levels in the scattering system. It is only in the particular case of resonance Raman scattering that the energy of the incoming source of irradiation matches an existing electronic transition which will be discussed later in this Chapter.

Theory of Raman spectroscopy is extended from classical view to fully quantum mechanical approach.^{3,5-8} The presented theory of Raman in this section is however, adjusted to the level of knowledge which is required to understand the work in this thesis.

In Raman spectroscopy, the quantity to be considered is the polarizability represented by a second rank tensor ($\vec{\alpha}$).

$$\vec{\alpha} = \begin{bmatrix} \alpha_{xx} & \alpha_{xy} & \alpha_{xz} \\ \alpha_{yx} & \alpha_{yy} & \alpha_{yz} \\ \alpha_{zx} & \alpha_{zy} & \alpha_{zz} \end{bmatrix} \quad (2.1)$$

Upon irradiation, the molecules that are promoted to a virtual state experience a change of polarizability and, at the same time, a change in the relative position of their atoms. The Raman effect can therefore be described as a function of the frequency of the excitation light and its impact on the polarizability tensor. The time-dependent (t) amplitude of the electric field of a laser at frequency ν_0 has the following form:

$$\vec{E} = \vec{E}_0 \cos(2\pi\nu_0 t) \quad (2.2)$$

The linear optical response of the scattering molecules to this incident electric field leads to molecular vibrations at frequency ν_k . The time-dependent polarizability changes due to these vibrations have the following form:

$$\vec{\alpha} = \vec{\alpha}_0 + \vec{\alpha}_k \cos(2\pi\nu_k t) \quad (2.3)$$

$\vec{\alpha}_0$ is the polarizability at the equilibrium nuclear geometry. Consequently, a dipole moment ($\vec{\mu}$) is induced in the molecules through:

$$\vec{\mu} = \vec{\alpha}\vec{E} \quad (2.4)$$

Combining equations (2.2) to (2.4) leads to the following description of the induced dipole moment:

$$\begin{aligned} \vec{\mu} &= \vec{\alpha}_0 \vec{E}_0 (1 + \cos 2\pi\nu_k t) (\cos 2\pi\nu_0 t) \\ &= \vec{\alpha}_0 \vec{E}_0 \cos 2\pi\nu_0 t + (1/2)\vec{\alpha}_0 \vec{E}_0 \cos 2\pi(\nu_0 + \nu_k)t + (1/2)\vec{\alpha}_0 \vec{E}_0 \cos(\nu_0 - \nu_k)t \end{aligned} \quad (2.5)$$

Equation (2.5) explains the origin of the bands that appear in a Raman spectrum. The first term is the Rayleigh scattering at frequency ν_0 which matches the frequency of the incident laser. The second term is anti-Stokes Raman scattering with blue shifted frequency of $\nu_0 + \nu_k$. The third term is Stokes Raman scattering with reduced frequency of $\nu_0 - \nu_k$. Since the molecular vibration alters the relative position of the atoms, the perturbation induced upon Raman scattering should be expressed in terms of deformation of the polarizability with respect to a normal coordinate similar to:

$$\bar{Q}_k = \bar{Q}_k^0 \cos 2\pi\nu_k t \quad (2.6)$$

\bar{Q}_k is normal coordinate of vibrational mode at frequency ν_k with amplitude \bar{Q}_k^0 . For vibrational mode k , the polarizability alterations with respect to the normal coordinate can be expressed through expanding $\bar{\alpha}$ over the normal coordinate in a Taylor series:

$$\bar{\alpha} = \bar{\alpha}_0 + \left(\frac{\partial \bar{\alpha}}{\partial \bar{Q}_k} \right)_{\bar{Q}_k=0} \bar{Q}_k + \frac{1}{2} \left(\frac{\partial^2 \bar{\alpha}}{\partial \bar{Q}_k^2} \right)_{\bar{Q}_k=0} \bar{Q}_k^2 + \dots \quad (2.7)$$

The first term in this expansion represents unperturbed linear optical polarizability; the second and third terms are first and second order perturbations. This equation demonstrates an essential selection rule for Raman: *a vibrational mode is Raman active only if there is a change of the polarizability of the molecule with respect to the normal coordinates upon irradiation:*

$$\frac{\partial \bar{\alpha}}{\partial \bar{Q}} \neq 0 \quad (2.8)$$

According to this selection rule, the change in polarizability, arising from a group of atoms in molecule, should not get cancelled out by symmetric identical atoms in the same molecule.

The polarizability tensor is symmetric because of the fact that the potential energy of the system remains constant when two orthogonal fields are applied. In other words:

$$U = E_x \cdot \alpha_{xy} \cdot E_y = E_y \cdot \alpha_{yx} \cdot E_x \Rightarrow \alpha_{xy} = \alpha_{yx} \quad (2.9)$$

If a proper principal axis system is found, the polarizability tensor can be diagonalized (off-diagonal elements become zero). In this case $\alpha_{xx}, \alpha_{yy}, \alpha_{zz}$ will be the equivalent of the three semi axes of an ellipsoid. The polarizability ellipsoid will have the following mathematical form:

$$\left(x^2/\alpha_{xx}\right) + \left(y^2/\alpha_{yy}\right) + \left(z^2/\alpha_{zz}\right) = 1 \quad (2.10)$$

Here the more polarizable direction in the molecular geometry corresponds to longer axes. If the molecule has cylindrical symmetry two of these values would be equal. For molecules of tetrahedral or higher symmetry, the three principal values are equal and the ellipsoid becomes a sphere. During molecular vibrations, the shape of the polarizability ellipsoid, its size and also its orientation in space might change. For Raman active totally symmetric vibrations, the size of the ellipsoid should change and all off-diagonal elements of the polarizability tensor should remain zero. For non-totally symmetric Raman active vibrations though, the shape or orientation of the ellipsoid changes and hence off-diagonal elements will appear in the polarization tensor.

Raman scattering efficiency can be evaluated by a parameter known as scattering cross-section, σ_{sca} . Classically the Raman cross-section is expressed as the ratio of intensity of the scattered light to the incident photon density. The intensity of the scattered light is proportional to the number of photons that get scattered per unit time. However, to acquire a more accurate definition for Raman cross-section, the direction of the scattered light which is dictated by the collection configuration of the experimental setup must be considered. For this reason a differential version of the cross-section which is corrected with respect to the collection angle is usually used:

$$\frac{d\sigma_{sca}}{d\Omega} \left(m^2/sr\right) \quad (2.11)$$

Ω denotes the two dimensional solid angle expressed in steradian (sr). This deformation of the Raman cross-section is useful for calculating the intensity of the scattered light (I). For a given Raman mode, averaged over all orientations of the molecule in space, the intensity can be estimated through:⁹

$$I = \frac{d\sigma_{sca}}{d\Omega} s_0 \delta\Omega \quad (2.12)$$

$\delta\Omega$ denotes a small solid angle of collection which is related to the numerical aperture of the collection microscope objective and s_0 shows the incident photon density with W/m^2 units. In equation (2.12), the estimation of the Raman intensity requires a definition for Raman cross-section. Technically classical approaches are unable to predict the intensity of the mode and for these reason quantum mechanical approaches such as density function theory (DFT) can be of interest.³ In DFT the Schrödinger equation is solved for a system of coupled electrons to give the wavefunction and therefore the electronic structure of electrons for certain atomic position in a molecule.¹⁰ For Raman scattering, the deformation of the electron density within an electric field along x , y and z direction can be calculated by DFT. The output suggests the following equation for a given Raman mode with frequency ν_k and excited by laser frequency of ν_0 :¹¹

$$\frac{d\sigma}{d\Omega} = \left(\frac{\pi^2}{45\epsilon_0^2} \right) \left(\frac{h}{8\pi^2 c \nu_k} \right) \left(\frac{45a_k^2 + 7\gamma_k^2}{45} \right) (\nu_0 - \nu_k)^4 \left(1 - \exp\left(\frac{-hc\nu_k}{k_B T} \right) \right)^{-1} \quad (2.13)$$

ϵ_0 is the dielectric constant of free space which has the value of 8.8542×10^{-12} F/m. h is the Planck's constant with the value of 6.6261×10^{-34} m² kg/s and k_B is the Boltzmann constant with value of 1.38065×10^{-23} m² kg s⁻² K⁻¹. The second bracket has the units of kg m² and stands for zero-point amplitude of the Raman mode in reduced mass coordinates. The third bracket shows the Raman scattering activity with units of $C^4 s^4 m^{-2} kg^{-2}$ with C indicating coulomb electrical charge unit. (a) and (γ) are the isotropic and the anisotropic contributions of the polarizability:

$$a = \frac{1}{3}(\alpha_{xx} + \alpha_{yy} + \alpha_{zz}) \quad (2.14)$$

$$\gamma^2 = \frac{1}{2}[(\alpha_{xx} - \alpha_{yy})^2 + (\alpha_{yy} - \alpha_{zz})^2 + (\alpha_{zz} - \alpha_{xx})^2] \quad (2.15)$$

The fourth bracket denotes the thermal population of the vibrational state. Substituting equation (2.13) to (2.15) into (2.12) provides an equation for estimating the intensity of different Raman scattering mode.

2.2 Resonance Raman

In resonance Raman scattering, the virtual energy level, to which the molecule is brought upon excitation, is resonant with an existing excited electronic state. Such matching between the energy of the incident excitation and an existing electronic excited state leads to an increase of Raman signal from 3 to 6 orders of magnitude.¹² The theory behind resonance Raman is available in text books⁷ and in previously published reviews.^{13,14} Modern theories of resonance Raman are mostly based on the work of Albrecht *et al.*¹⁵ who treats resonance Raman as vibronic (vibrational and electronic) spectroscopy. He proposed Frank-Condon (F-C) overlap and Herzberg-Teller vibronic coupling as two mechanisms that explain the scattering intensity in resonance Raman.

In F-C approximation, because the nucleus is much heavier than an electron, the electronic transitions occur without causing any change in the nuclear position in molecule.¹⁶ For F-C overlap to be non-zero two conditions must be met.^{17,18} First the transition dipole moment of the resonant electronic transition should be non-zero. For this to happen, the excitation wavelength should be about the wavelength of an intense charge transfer or π - π^* type absorption band.¹⁹ Second, the overlap integral (F-C factor) between the vibrational wavefunctions of the ground and electronic states be non-zero. This happens when the potential energy minimum experiences a displacement along the normal coordinate between the two electronic states.¹⁶

Herzberg-Teller vibronic coupling mechanism however, is influenced by interactions of electrons with nuclear motions.²⁰ The Herzberg-Teller mechanism plays a smaller role in intensity of resonance Raman scattering and is observed only if F-C overlap is close to zero.²¹

From the empirical observation point of view, the molecules that undergo resonance Raman upon changing the excitation wavelength, experience a change of equilibrium conformation as they go from ground state to excited state. This phenomenon was formulated by Hirakawa and Tsuboi and is valid for totally symmetric, asymmetric and degenerate Raman bands.^{22,23} As an example NH_3 goes from pyramidal shape in ground state to plane in its lowest excited electronic state. The molecule undergoes an umbrella motion upon this transition. It has been observed that the Raman band that corresponds to this motion gets enhanced much more than the other Raman bands when proper wavelength (351 nm wavelength) is used to excite the resonance conditions.

For single molecule Raman spectroscopy or tip-enhanced Raman scattering, resonance Raman can be beneficial through providing additional enhancement of the Raman signal. For example, TERS of isolated dyes molecules (Rhodamine, malachite green) dispersed onto a surface are generally selected with the desire to probe single molecule.^{24,25} For non-resonant molecules, only the localized surface plasmon resonances of the metalized tip are responsible for the enhancement of the Raman scattering.

2.3 Plasmonic Resonances in Metal

The enhancement of the Raman scattering in near-field techniques such as surface and tip-enhanced Raman spectroscopy constitutes a research field which belongs to a more general theme of plasmonics. To acquire better understanding of TERS-related discussions in this thesis, plasmon resonances in metal surfaces are introduced in the following sections.

2.3.1 Plasmon

The interaction of electromagnetic radiation with metallic nanostructures excites the oscillation of the free conduction electrons of the metal out of phase relative to the driving electric field.²⁶ The oscillation causes a displacement of the free electrons with respect to the positively charged lattice in metal, therefore, at certain optical frequencies; the free electrons can sustain surface and volume charge density oscillations which are known as plasmons. The physical process involved in plasmon resonance includes the free motion of the metal conduction electrons within the bulk of the metal. Upon irradiation by a laser with angular frequency of ω , the free conduction electrons undergo a displacement \vec{r} ($\vec{r}(t) = \vec{r}_0 e^{-i\omega t}$) that generates a dipole moment $\vec{\mu}$ through $\vec{\mu} = e\vec{r}$ where e denotes the electron charge and \vec{r}_0 denotes the electron position in absence of an incident electromagnetic field. The generated dipole moment leads to a macroscopic polarization $\vec{P} = n_e \vec{\mu}$ where n_e is the number of electrons per unit volume. Oscillation of the metal free electrons occur at a certain frequency, ω_p , which is termed as plasmon frequency and is defined as:²⁷

$$\omega_p = \frac{1}{2\pi} \sqrt{\frac{n_e e^2}{m_e \epsilon_0}} \quad (2.16)$$

With ϵ_0 being the dielectric constant of free space and m_e being the effective mass of an electron.

The complete characterization of the electron oscillation requires solving the equation of motion for electrons under the incident electromagnetic field which is outside the scope of this thesis and has been studied in detail in the literature.^{26,28,29} The equations that are presented in the following sections to characterize plasmonic resonances are however derived from these studies.

2.3.2 Surface Plasmon

At the interface between a metal surface and a dielectric material such as air or glass, plasmon takes the form of surface plasmon (SPs).²⁷ More precisely, surface plasmons refer to collective oscillations of the electron density at the metal surface. Surface plasmon is excited by the oscillating electric field of the incident light, therefore, higher angles of incidence (wavevector \vec{k} nearly parallel to the surface) couple most efficiently.²⁷ Plasmonic oscillations at the interface between a metal nanostructure and a dielectric can significantly enhance the optical near-field in close proximity of the metal surface. As illustrated in **Figure 2.2**, surface plasmon appears as a combination of an electromagnetic wave and surface charges.³⁰

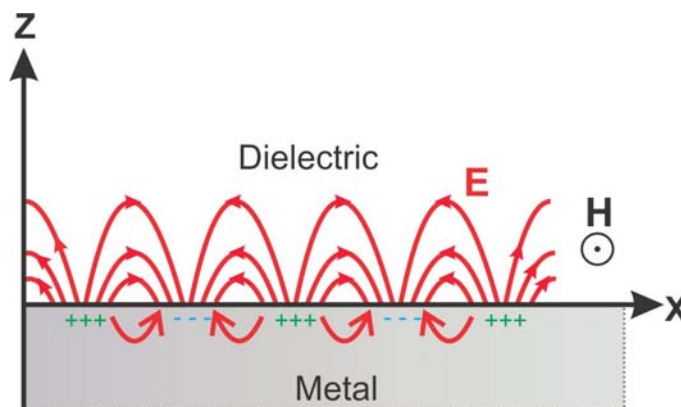


Figure 2.2 Illustration of propagating surface plasmon at the interface between metal surface and a dielectric

The electromagnetic field present at the metal surface includes a transverse magnetic field parallel to the interface. In addition the generation of the surface charge requires the presence of an electric field normal to the surface. As a result, there will be an evanescent surface plasmon field component perpendicular to the surface which gets enhanced near the interface and decays rapidly with distance away from it into the two mediums.³⁰ For surface plasmon to be detectable at the interface between a metal and a dielectric, the complex dielectric constant of the metal has to have a negative real and a positive imaginary part, which is the case for noble metals.^{31,32} The dielectric function of four noble metals, gold, silver, aluminum and copper are shown in **Figure 2.3**. Here the

dielectric constants are calculated through the Drude model which is widely used to characterize the motion of the free electrons inside an electromagnetic field.²⁶ Among the metals illustrated in **Figure 2.3**, silver and gold are more common choices for exciting surface plasmon in the UV-visible region.

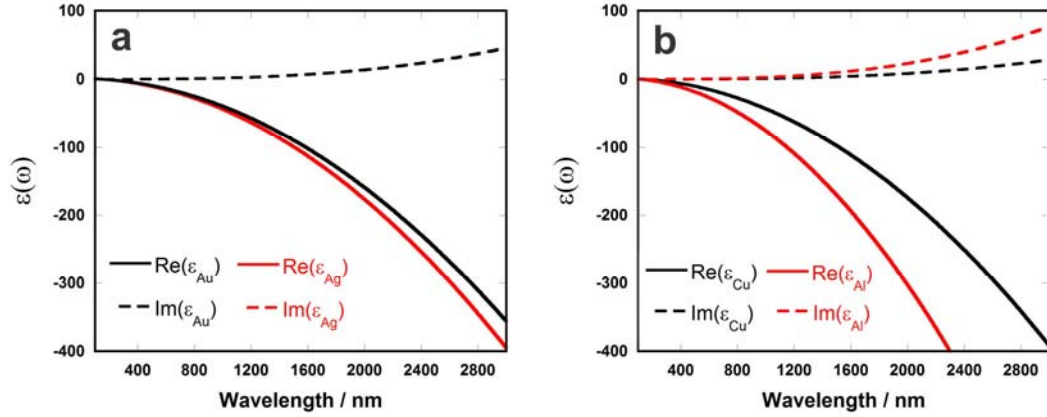


Figure 2.3 Complex dielectric constants of (a) gold and silver (b) copper and aluminum according to the Drude model

In **Figure 2.3a** the imaginary part of the dielectric constant for gold and silver are quite similar, however, small differences between these values at each wavelength results a significant differences in the plasmonic behavior of the two metals.

propagation of the surface plasmon can be characterized by two wavevectors, one describes its dispersion along the interface (k_{sp}) and the other one accounts for dispersion normal to the interface on either side (k_z):³⁰

$$k_{sp} = \frac{2\pi}{\lambda} \sqrt{\frac{\epsilon_d \epsilon_m}{\epsilon_d + \epsilon_m}} \quad (2.17)$$

$$\left(k_z^{d,m}\right)^2 = \epsilon_{d,m} \left(\frac{2\pi}{\lambda}\right)^2 - k_{sp}^2 \quad (2.18)$$

λ is the light wavelength and ϵ_d and ϵ_m are the dielectric constants of the dielectric and the metal.²⁶ Dielectric constant of a metal is a complex function with general form of

$\varepsilon_m = \text{Re}(\varepsilon_m) + i\text{Im}(\varepsilon_m)$ which implies that both k_{sp} and k_z of the metal are complex. The dielectric constant of the dielectric material is a real function while k_z of it remains complex according to equation (2.18).

The decay length of the plasmon field into the dielectric medium above the metal is of the order of half of the excitation wavelength. The decay length in metal is however smaller due to the screening effect of the free charges³³ and is determined by the metal skin depth.³⁰ The real part of k_{sp} contains the evanescent nature of the plasmon field. If the dispersion of the plasmon is plotted, a momentum mismatch will be observed between the surface plasmon (solid line) and the free space photons (dotted lines), as illustrated in **Figure 2.4** for the gold-air, silver-air, copper-air and aluminum-air interfaces.

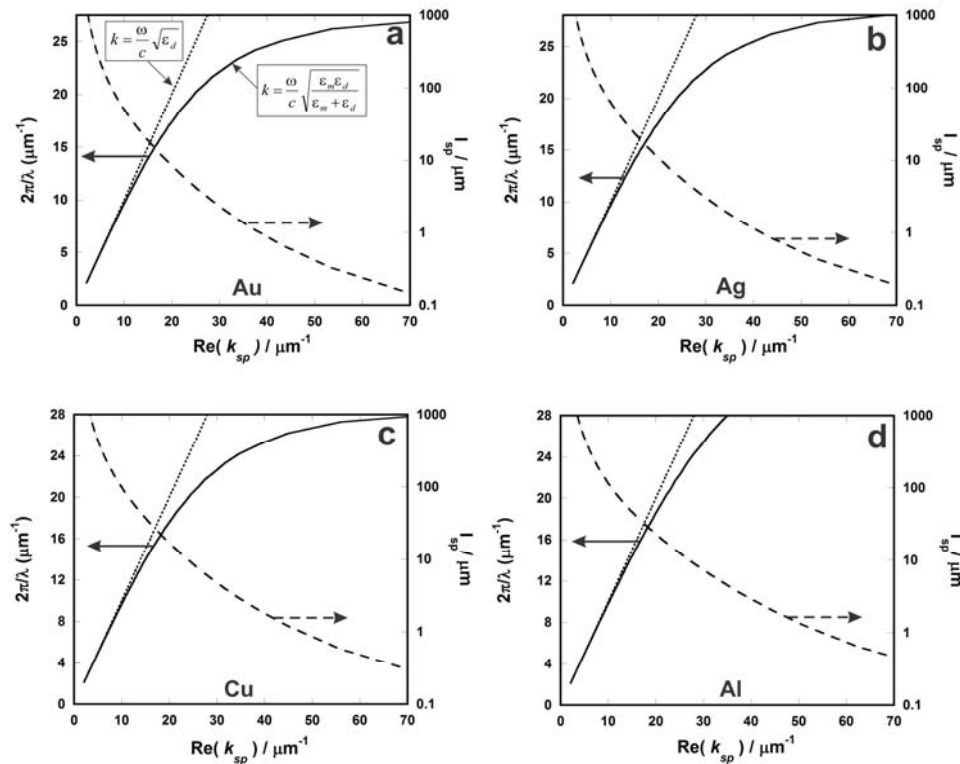


Figure 2.4 Dispersion relation (solid line) and the propagating length (dashed line) of a surface plasmon on (a) gold-air (b) silver-air (c) copper-air and (d) aluminum air interface according to the Drude model. The propagation of light in free space is shown by dotted lines in each case.

The momentum mismatch in these plots is compensated by the additional momentum created through the evanescence nature of the surface plasmon. Evanescent waves are standing waves that exponentially decay in space. The propagation length of these evanescent waves along the interface is expressed as l_{sp} in **Figure 2.4** and can be measured through the following equation:³³

$$l_{sp} = \frac{1}{2 \operatorname{Im}(k_{sp})} = \frac{2}{[\operatorname{Re}(k_{sp})]^3} \times \frac{[2\pi \operatorname{Re}(\epsilon_m)]^2}{\lambda^2 \operatorname{Im}(\epsilon_m)} \quad (2.19)$$

By definition, the propagation length describes the distance along the interface over which the surface plasmon gets dissipated due to damping of electron oscillation. According to equation (2.19) and Figure 2.4, when $\operatorname{Re}(k_{sp})$ decreases, the surface plasmon is less confined and decouples easily from the interface and turns into freely propagating light. When $\operatorname{Re}(k_{sp})$ increases, the surface plasmon becomes more localized and the propagation length decreases due to resistive damping of the oscillation inside the metal.³³

2.3.3 Localized surface Plasmon

Localized surface plasmon resonance (LSPR) gets excited when a surface plasmon is confined to a nanostructure with sizes comparable to the wavelength of the light.²⁷ Incident light will promote the free electrons of the metal nanostructure to oscillate collectively with respect to the incident electric field upon which they experience a change in their momentum. The collective oscillations create charge accumulation at the surface. In addition, when these oscillations couple between neighboring nanostructures, the electric field gets locally intensified inside the interparticle gaps. An example of localized surface plasmon resonance generated within the gaps between gold nanopillars in hexagonal arrays is illustrated in **Figure 2.5**.³⁴

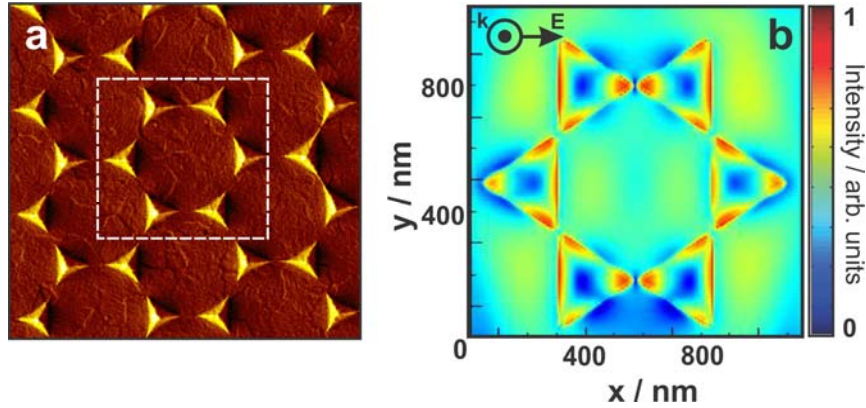


Figure 2.5 Illustration of localized surface plasmon in metal nanostructures (a) SEM image of hexagonal arrays of gold nanopillars created by nanolithography over the glass surface (b) FDTD simulation of a single hexagonal array showing the confinement of the electric field at the surface of the nanopillars and inside the gaps between the neighboring pillars. The images are adapted from reference 34 with permission from American Chemical Society.³⁴

There are two major effects associated with localized surface plasmons; *i.* the electric field is strongly enhanced near sharp features of a metallic nanostructure yielding hot spots and decays rapidly with distance, *ii.* the optical excitation is optimum at a certain optical frequency which is typically in the visible-near IR region for noble metals.^{27,32,35}

Similar to propagating surface plasmon, the localized surface plasmon resonances are dependent on the chemical nature of the metal, the dielectric constant of the surrounding environment along with the optogeometric parameters of the particles or ensemble of particles such as size, shape or interparticle distance.^{27,32} Mie's analytical solution to Maxwell's equations in the scattering and absorption of light by spherical particles is usually utilized for the characterization of LSPR.³⁶ According to the Mie theory, if the particles are very small ($d \ll \lambda$ with d being the diameter of the nanosphere), total scattering (σ_{sca}), extinction (σ_{ext}) and absorption (σ_{abs}) cross-section of a nanosphere can be defined as:^{27,28,32,37}

$$\sigma_{ext} = \frac{18\pi\epsilon_d^{3/2}V}{\lambda^4} \frac{\text{Im}(\epsilon_m)}{[\text{Re}(\epsilon_m)\chi\epsilon_d]^2 + [\text{Im}(\epsilon_m)]^2} \quad (2.20)$$

$$\sigma_{sca} = \frac{32\pi^4 \varepsilon_d^2 V^2}{\lambda^4} \frac{[\text{Re}(\varepsilon_m) - \varepsilon_d]^2 + [\text{Im}(\varepsilon_m)]^2}{[\text{Re}(\varepsilon_m) \chi \varepsilon_d]^2 + [\text{Im}(\varepsilon_m)]^2} \quad (2.21)$$

$$\sigma_{abs} = \sigma_{ext} - \sigma_{sca} \quad (2.22)$$

According to the equations above, optical properties of metal nanoparticles are a function of the dielectric constants of the metal and the dielectric environment as well as the geometrical parameters such as the shape factor (χ) and volume (V) of the nanoparticles. These equations are typically used for estimating the optical response of systems with LSPR. In addition, LSPR can be accumulatively increased when the interparticle distance between the nanoparticles is small enough to allow for coupling of the neighboring hot spots.^{37,38}

This description of the photo-induced electromagnetic field singularity over a metal surface or in the vicinity of nanoparticles is essential to understand the enhancement process in tip-enhanced Raman spectroscopy. The enhancement of Raman scattering in TERS arises from the local confinement of the electromagnetic field at the TERS tip apex. The apex of the TERS tip acts as a single nanoparticle and hence, the presented equations in this section are valid for characterizing LSPR in TERS. Theoretical investigations of TERS along with the parameters that alter the magnitude of LSPR in TERS are presented in Chapter 4 of this thesis.

In summary, thorough understanding of plasmon and more particularly localized surface plasmon is essential for the fabrication of active TERS probes in order to improve the resolution and sensitivity of Raman scattering. Any controlled way to confine a plasmon with defined characteristics (frequency, amplitude and phase of the field) at the extremity of a sharp structure will be of tremendous interest for many applications in high resolution optical microscopy.

2.4 The Near-Field Concept

In conventional microscopy and spectroscopy, an object is illuminated by an incident light and the scattered or emitted light is then collected by a detector. Upon illumination

the incident field \vec{E}_{in} induces a polarization current in the object which in turn gives rise to an emitted field \vec{E}_{out} .³⁹ In near-field optics however, two objects are considered, one is referred to as the probe and the other part as the sample as illustrated in **Figure 2.6** for a TERS setup.

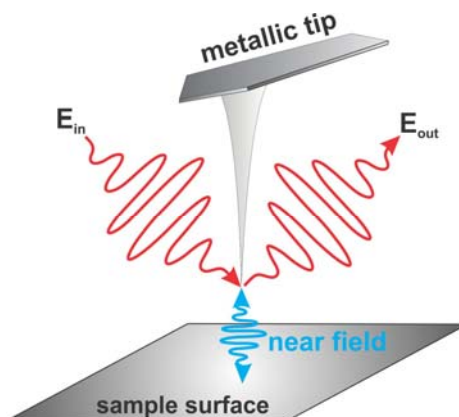


Figure 2.6 Illustration of the near-field concept in TERS setup. The TERS tip is kept at around 1 nm distance above the surface by means of the feedback system. When the apex of the TERS tip is placed inside the focal region of an incident laser beam, the electric field gets confined in close proximity of the apex with 10-20 nm diameters. The Raman scattering of a molecule which is placed inside this intensified electric field will be enhanced.

In near-field microscopy, the probe is designed to have unique properties of metal nanostructures at optical frequencies to exhibit a localized surface plasmon resonance. When the light is incident on the probe, the incoming electric field periodically displaces the probes electrons with respect to the positively charged metal ion lattice. Near resonance, that charge oscillation gives rise to a greatly amplified electric field just outside the probe where it is termed as near-field. In near-field measurements involving a metallic tip, the probe acts as a nanoantenna which converts non-propagating field components confined on the sample surface into propagating radiation.⁴⁰ This nanoscale antennae acts as a receiver for the input light and an emitter for the output light to be detected. \vec{E}_{out} emitted by the combined system contains information about the sample properties. As a result, near-field measurements enable the retrieving of the small details

of a sample through the localized light-sample interaction within the first 10 nm above the surface.

Similar phenomenon is responsible for the enhancement of the Raman scattering in TERS. The TERS tip acts as receiving and emitting antenna which localizes the radiation on the sample and intensifies the molecule response as Raman scattering. High resolution capacities of TERS can be therefore explained based on the principles of near-field optics and more specifically evanescent waves that exist close to the tip apex. In TERS, the non-propagating evanescent wave gets converted into propagating waves that are detectable in far-field.⁴¹

The mechanism of enhancement involved in TERS investigation of the near-field of zero, one and two dimensional samples has been theoretically studied by Novotny *et al.*⁴² and Cançado *et al.*⁴³ Generally in these studies, the electric field near the metal tip is assumed to be axially symmetric⁴⁴ and locally interacts with the sample at a certain frequency. The laser irradiated metal tip generates a local surface plasmon field which gives rise to a screened Raman excitation field to generate a Raman dipole in the sample structure. Estimation of the electric field magnitude caused by the tip at a certain spot on sample surface leads to calculation of the enhanced Raman intensity through the ensemble average of the square modulus of the local field intensity. One important relation obtained from these theoretical studies is the distance dependence for near-field Raman intensity that scales with $(\Delta+r_{tip})^{-12}$, $(\Delta+r_{tip})^{-10}$ and $(\Delta+r_{tip})^{-8}$ for 0D, 1D and 2D samples. Δ and r_{tip} denote the tip-sample separation and the tip radius respectively. These findings have been utilized extensively to evaluate the near-field nature of the enhanced Raman signal in TERS measurements.^{42,45,46} A sample of which is presented in Chapter 5 of this thesis for TERS study of single walled carbon nanotubes.

2.5 Diffraction Limit in Optical Measurements

Optical diffraction implies the limit that restricts the lateral resolution of optical measurements.⁴⁷ The origin of diffraction limit in optical microscopy can be understood through an overview of the interferences of Airy patterns.⁴⁸ An Airy pattern presents the

distribution of a best focused spot of light made by a perfect lens with a circular apex. Mathematically, an Airy diffraction pattern has the following definition:

$$I = I_0 \left(\frac{2J_1(vb \sin \alpha)}{vb \sin \alpha} \right)^2 \quad (2.23)$$

I_0 is the maximum intensity of the pattern at the Airy disc center, J_1 is the Bessel function of the first kind of order one, $v = 2\pi/\lambda$, b is the radius of the aperture and α is the angle of observation. The dark rings in Airy pattern are produced at zeros of the Bessel function. An illustration of an Airy pattern is presented in **Figure 2.7a**.

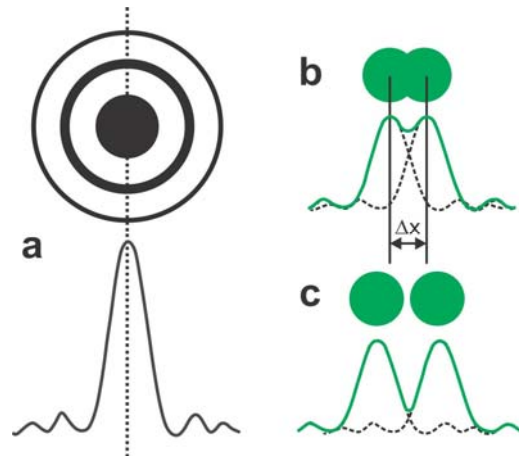


Figure 2.7 Illustration of the diffraction limit problem and its dependence on the relative positions of neighboring Airy patterns (a) shows the top and side view of Airy pattern (b) demonstrates the diffraction limit (Δx) to be the distance between the center of the two Airy patterns when the first intensity minimum of each Airy pattern is aligned with the intensity maximum of the neighboring one (c) For center-to-center distances larger than Δx the neighboring objects will be completely resolved.

The diffraction pattern created by illumination of a circular aperture shows a bright area in the middle which corresponds to maximum intensity and a series of concentric bright rings with decreasing intensity at farther distances from the center. As it is illustrated in **Figure 2.7b**, adjacent points are just resolved when the centers of their Airy patterns are

separated by a minimum distance equal to the radius of the central disk in the Airy pattern. This minimum distance is referred to as Δx in **Figure 2.7b** and also in the next paragraph. The minimum value of Δx , required for two neighboring objects to be resolved, corresponds to a situation where the first minimum in Airy pattern of one of the objects is aligned with the maximum intensity in Airy pattern of the other object.

The diffraction-limited resolution theory was refined by Ernst Rayleigh⁴⁹ in 1873 and refined by Lord Rayleigh⁵⁰ in 1896. The theory was used to estimate the smallest distance between two objects to be distinguished as separate entities in an optical measurement. In Rayleigh criterion the lateral resolution (Δx) is estimated by the following equation:

$$\Delta x = \frac{1.22\lambda}{2n\sin\alpha} \quad (2.24)$$

This equation suggests that at each wavelength, Δx can be improved by changing the surrounding media into one with larger index of refraction (n) and by choosing a focusing lens with larger collection angle (α). The denominator in equation (2.24) is known as the numerical aperture ($N.A.$) of the objective lens which indicates the focusing properties of the lens. Microscope objectives with larger $N.A.$ values focus light more tightly and efficiently. However, there is a limit for improving the diffraction limit in conventional microscopy and spectroscopy. Ideal experimental conditions lead to roughly 200-300 nm resolution in visible light region provided that a microscope objective with $N.A.=1.4$ (oil immersion objective) is used. This limit is clearly not suitable for studying smaller features are of interest.

In the last century, surpassing the diffraction limit of light to acquire higher lateral resolution in microscopic and spectroscopic investigations has been the subject of many researches. In 1928 Synge suggested scanning the surface of the sample by an opaque metal screen with an aperture smaller than the wavelength of light which is illuminated from the back.⁵¹ If the aperture is located within the near-field of the sample, a few nanometers away from it, the resolution of the measurement is no longer limited by the diffraction limit. The size of the aperture will indeed determine the limits of resolution in

this case. This hypothesis built the basis for the realization of scanning near-field optical microscopy (SNOM) in 1984 due to the progresses in nanoscale motion control provided in scanning tunneling microscopy and atomic force microscopy.^{52,53}

Aperture SNOM was the first generation of near-field optical microscopy. In aperture SNOM an optical fiber with sharpened end is used as light source to scan the near-field of the sample.⁵⁴ The fiber is generally coated with a thin metal film, everywhere except at the apex of the tip.^{55,56} However, the low throughput of SNOM and specially fiber probe in combination with the low cross-section of the scattered Raman signal and the tedious fabrication and thin film coating procedure delayed the development of SNOM-Raman until 1994.⁵⁷ Clearly, the coupling of an intense light source was not a proper solution to the low throughput problem since it would lead to local thermal effects that could damage the integrity and subsequent resolution of the tip. The dimension of the uncoated part of the apex determines the spatial resolution of aperture SNOM and since the fiber tips have flatted apex, the optical resolution of the method was limited to about 60 nm.^{58,59}

Nowadays, hollow aperture probes are made using commercial AFM tips through creating a hole at their apex by using advanced nanofabrication techniques such as focused ion beam (FIB). Alpha300 S AFM tips fabricated by WITecTM are an example of these tips where an aperture (100 nm) is created at the apex of a hollow pyramid. Nevertheless this type of approach is marginal and is rarely used for Raman spectroscopy purposes.

It was later proposed that localized surface plasmon be employed through illuminating the metallic tip of scanning tunneling microscopes (STM). In such a case, the tip would act as a nanosource with light confined at its extremity. The idea was to enhance the Raman scattering and to surpass the diffraction limit within the confined electric field at the STM tip apex. This combination of SERS and near-field microscopy was first named *apertureless Raman near-field*⁶⁰ and later, on the same principle, *tip-enhanced Raman spectroscopy (TERS)*. First spectroscopic applications of apertureless SNOM was performed in 1999 in a two photon fluorescence study⁶¹ and in 2000 for tip-enhanced Raman spectroscopy.⁶²⁻⁶⁴ Nowadays, it is also common to use atomic force microscope (AFM) tips in conjunction with an AFM feedback mechanism. As opposed to STM based

TERS setups, AFM feedback does not require the use of conductive samples, a feature that makes TERS accessible for a larger variety of samples. Various TERS configurations will be discussed in detail in Chapter 3 of this thesis. The different SNOM methods that are mentioned above are however summarized in **Figure 2.8**:

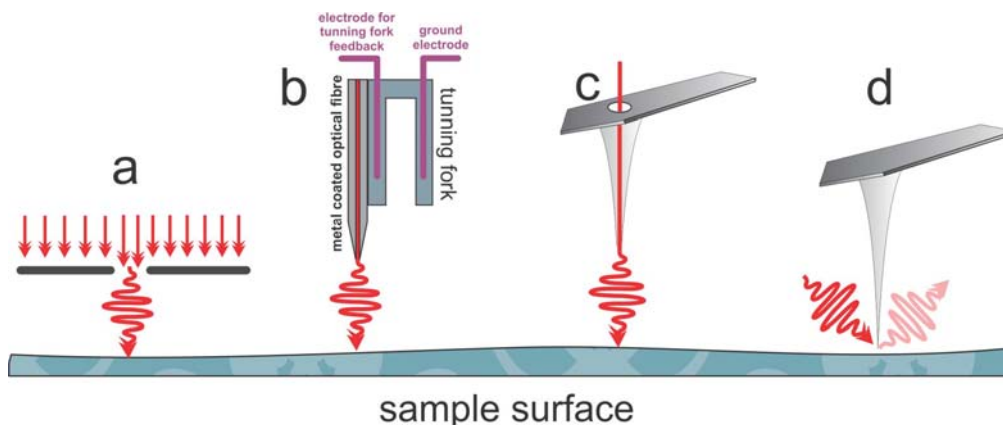


Figure 2.8 Schematic of various SNOM configurations (a) Principle of SNOM using a small aperture on an opaque substrate (b) aperture SNOM with a coated optical fiber attached to a tuning fork. The tip is shown in excitation mode but can also be used for light collection purpose. (c) aperture SNOM provided through making hollow AFM probes (d) apertureless metallic tip, in close proximity of sample surface.

2.6 Tip-enhanced Raman spectroscopy

In TERS measurements, a metalized (gold or silver) AFM or STM tip with a tip radius of 10-20 nm is brought in feedback with the surface of a sample.^{41,45,65} A laser source, aligned to and focused on the tip, induces a locally resonant excitation of the surface plasmons at the apex of the metal coated tip, which in turn provides an enhanced Raman signal of the sample in proximity to the tip apex.⁶⁶ The sample is then scanned point-by-point over a surface providing a TERS map of that surface. The experimental and technical aspects of the TERS setup are discussed in more details in Chapter 3. The enhancement of Raman signal in TERS is usually discussed on the basis of surface-enhanced Raman scattering (SERS). In both techniques, surface plasmon resonances in a metal nanostructure give rise to an enhanced electric field in close proximity of the metal

nanostructure which increases the sensitivity of Raman spectroscopy significantly.⁶⁷ The surface enhancement effect in TERS is a characteristic of the metal grains on the tip. Proper laser photons are absorbed by these grains and excite surface plasmon by making the surface electrons of the metal oscillate. If this plasmon excitation couples with the sample which is located in close proximity of the tip, an efficient pathway to transfer energy to the molecules vibrational modes would be formed.⁶² However, despite the similarities, TERS has an important advantage over SERS since it combines high sensitivity and molecular fingerprinting of SERS with nanometer resolution of scanning probe microscopy (SPM). With TERS it is possible to directly get chemical information about the sample without any need for special substrates. The enhanced Raman signals originate from a few molecules that are located very close to the tip apex.^{68,69} The TERS tip moves laterally on top of the sample; therefore, it would be possible to bring the enhancing tip to any desirable spots on the sample and image the surface with a lateral resolution which is limited only by the size of the tip apex and the confined electric field dimensions consequently.⁶⁶

2.6.1 SERS and TERS Enhancement Mechanism

The localized enhancement of electric field, which is essential for intensifying the weak inelastic scatterings in Raman process and increasing the sensitivity of Raman spectroscopy, originates from different sources such as the magnification of the incident light, enforcement of the Raman scattering and modification of the scattering process. The first two mechanisms are known to have an electromagnetic origin^{67,70-78} while the third factor is usually categorized as chemical mechanism.⁷⁹⁻⁸² These mechanisms, involved in both SERS and TERS methods, are very well described in several review publications by Moskovits and other researchers and will be briefly reviewed in the following sections.^{12,27,37,67,74,75}

2.6.1.1 Electromagnetic Mechanism

Electromagnetic mechanism originates from the plasmon resonance of metal nanostructure with the incident laser.^{83,84} This mechanism has the most significant

contribution to enhancement factor (yields 10^4 to 10^8 enhancement).¹² The metallic TERS tip acts as optical nanoantenna that converts freely propagating optical radiation into localized energy and vice versa.⁴⁰ For the sample in close proximity of nanoantenna, both incident light and Raman scattering are enhanced the same way. Therefore the incident and scattered light are increased about equally and the Raman signal increases roughly by the fourth power of local electric field. The maximum enhancement would occur if the incident and scattered light are in resonance with the antenna. In larger distances from the antenna the resonance would be broken.⁸⁵ The enhancement of the electric field in TERS is therefore, a combination of three different effects: the lightning rod effect, the excitation of localized surface plasmon and the antenna resonance effect.

The lightning rod effect is related to the influence of the shape of the tip. The very sharp apex of the metallic tip generates highly localized surface charge densities that enhance the electric field locally at the sharp end of the metallic tip. The incident light drives the metal free electrons along the polarization direction. Because the charge density is zero inside a metal at any instant of time, charges accumulate on the surface of the metal.⁴⁸

As emphasized earlier in section 2.2.2, the surface plasmon is efficiently excited if the wavelength of the laser matches the plasmon resonance(s) of the metal. Such plasmon resonances depend on the material property and the shape of the tip. Sharper objects with a higher aspect ratio generate stronger confined fields.^{86,87}

Excitation of the antenna resonance depends on wavelength of the incident laser and would be initiated if the size of the tip apex is approximately equal to the half of the radiation wavelength. In this case highly localized and enhanced electric field is observed at the tip apex.⁴⁰

As a combination of these effects is responsible for TERS effect, the material properties of the tip and surrounding medium (including the choice of the substrate), tip shape and size should be optimized in order to guarantee better results.⁴⁶ A detailed description of these parameters would be reviewed in Chapter 3. From the theoretical point of view, since the electromagnetic mechanism arises from the plasmon resonance of the metal surface, it is independent of the molecules that are probed by the metal tip, Therefore;

classical electrodynamics methods such as Mie theory,³⁶ discrete dipole approximation (DDA)⁸⁸⁻⁹⁰ finite-difference time-domain calculations (FDTD)^{91,92} can be utilized to investigate the electromagnetic mechanism. In particular, FDTD has been used in this thesis for investigating the distribution of the electric field around the TERS tip apex, which is presented in Chapter 4 of this thesis.

2.6.1.2 Chemical Mechanism

The presence of the chemical mechanism was evidenced when enhancement of the Raman scattering was observed even without using metals with plasmonic properties in the wavelength region of interest⁹³ or when utilizing flat metal surfaces.⁹⁴ Under these conditions no electromagnetic enhancement is expected to be observed, therefore, a different mechanism has to be responsible for the enhancement of the Raman scattering. These mechanisms are typically categorized under chemical mechanisms and induce $10-10^4$ units of enhancement. Chemical mechanism consists in three different types of sub-mechanisms as depicted in **Figure 2.9a-c**. Electromagnetic mechanism is also depicted in this Figure for the purpose of comparison.⁹⁵

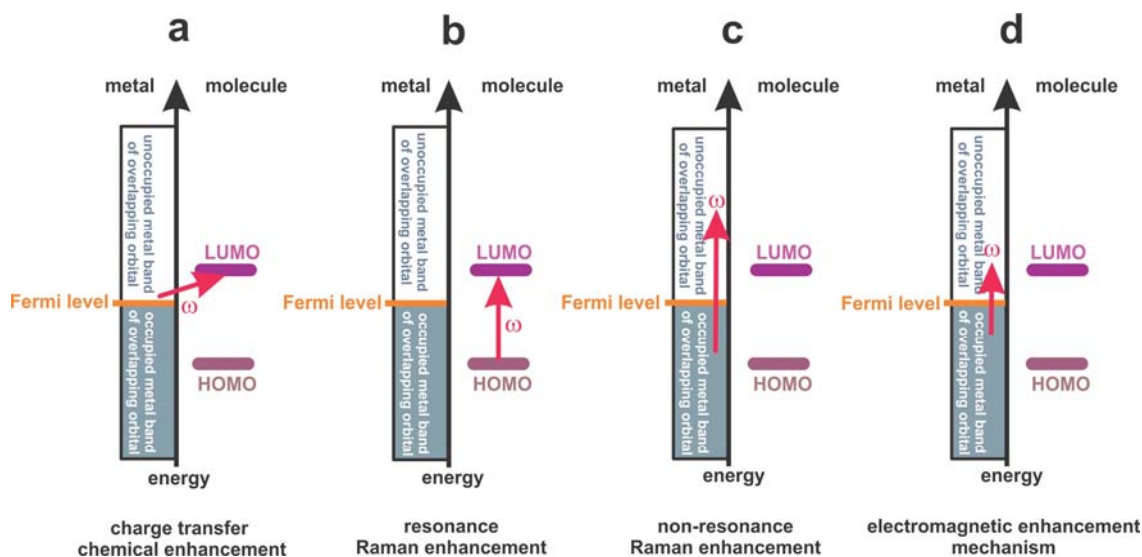


Figure 2.9 Illustration of different enhancement mechanism (a)-(c) demonstrate three types of chemical mechanism while (d) shows electromagnetic mechanism

Studies on non-electromagnetic enhancement mechanisms suggested that the resonance between the incident laser and the metal nanostructure can induce a charge transfer between the sample molecules and the metal nanostructure.^{80,96} For charge transfer to happen, the metal and the sample molecule should be in direct contact. In other words, charge transfer occurs only when the metal and the molecule are close enough for the corresponding wave functions to overlap. The exact mechanism of charge transfer is not fully understood. One of the suggested mechanisms was proposed by Pettinger.⁹⁷ He suggested that radiation excites plasmon resonances in the metal through which an electron-hole pair is generated. The resonant metal transfers its energy to a molecule to promote it to an excited state. The molecule inelastically sends the energy back to the metal after it relaxes back to the ground state. At this point a photon will be emitted by the excited surface plasmon. To explain the charge transfer HOMO and LUMO energy states of the metal and the adsorbent should be considered. Originally, the energy difference between HOMO and LUMO of the sample molecule is too high to be reached upon illumination by laser. HOMO and LUMO of the metal however are at the same Fermi energy level. It is believed that a sample-metal complex is formed when the sample is in direct contact with the metal surface.^{98,99} Formation of the sample-metal complex facilitates a charge transfer from HOMO of the molecule to the LUMO of metal and from there to LUMO in the molecule eventually as depicted in **figure 2.9a**. Hereby, the Raman scattering cross-section is enhanced through lowering the energy gaps between the bands and enabling an electronic transition of the molecule.

Beside the charge transfer phenomenon, resonance Raman is another source for chemical mechanism.^{95,100} The molecular resonance mechanism is very similar to resonance Raman with the difference that the presence of a metal tip induces the resonance by altering the excitation energy of the molecule and consequently through the tip altering the resonance conditions. Therefore, although the resonance Raman is not a surface effect, it should be considered due to the impact of the metallic tip on resonance Raman enhancement.¹² Resonance effects could create 10^3 - 10^6 of the total enhancement under proper conditions.¹²

As a third source for chemical enhancement, 10^2 or less contribution to total enhancement is believed to arise from a phenomenon known as non-resonant chemical mechanism. Non-resonant chemical mechanism is due to interaction between the ground state of the sample molecules and the metal upon placing the sample in close proximity of a noble metal. Quantum mechanical calculations suggest that this phenomenon is very sensitive to size, charge, binding site and the molecule's orientation with respect to the metal cluster and also the separation between the two.^{95,101,102} In the special case of TERS, depending on the relative orientation of the molecule and the tip, certain Raman modes could or could not be excited while charge transfer or resonance conditions are absent.

It is noteworthy that charge transfer has only been observed in previously published TERS study of adenine nucleobases¹⁰³ and C_{60} ^{64,104} and not been detected for other nucleobases such as cytosine and thymine.¹⁰⁵ The effect is typically much more pronounced in SERS measurements.¹⁰⁶ Chemical enhancement is excluded from the work in this thesis because of two main reasons. First, it is very dependent on the sample; second, it requires that the sample is in direct contact with the metallic tip. The TERS studies that are reported in this thesis are performed in non-contact AFM mode, which naturally does not allow for the chemical effect to alter the enhanced Raman scattering. All the results presented in future Chapters are interpreted based on pure electromagnetic enhancement. It is however noteworthy that the chemical and electromagnetic mechanisms work together to produce the overall enhancement of the Raman scattering. The contribution of each mechanism varies in various molecules.¹²

2.7 Thermal Degradation of the Samples in TERS

The enhancement of the electric field within a very small area in vicinity of the tip apex might generate heating upon TERS measurements and could cause morphologic changes in the sample. Theoretical^{107,108} studies have estimated an increase of several tens of Kelvin for TERS measurements. Experimental studies also have been performed by measuring the ratio of Stokes and anti-Stokes Raman signals. For TERS study of a 50 nm thick conductive polymer deposited on aluminum mirror, up to 100 K temperature increase at laser power of 1 mW is measured.¹⁰⁹ The study has revealed the dependence

of the heating magnitude on the wavelength of the light and the optical response of the tip consequently. Higher plasmon resonances of the tip cause higher confinement of the electric field and more significant heating of the sample. In addition, they mention that heating could be higher for samples that absorb larger amounts of the excitation light. Nevertheless, many TERS studies on sensitive samples as well as cells,¹¹⁰⁻¹¹² bacteria^{113,114} and viruses¹¹⁵ are successfully done by using several hundred microwatts without sample destruction and without significant thermal damages. This can be explained based on the lower absorption of light by transparent or semitransparent biological species compared to the larger light absorption by a polymer film deposited on aluminum mirror. Therefore a correspondence between the laser power and the temperature increase cannot be established based on the results of reference 109 and the heating effect has to be measured for each experiment separately. Meanwhile, thermal effects should be carefully watched in TERS experiments and control tests should be performed to evaluate the light induced damage after the TERS measurements are performed.

2.8 Summary

The underlying principles of TERS were reviewed in this Chapter. In brief, Raman scattering was defined as the inelastic scattering of light caused by laser induced molecular vibrations in a medium. The low cross-section of this inelastic scattering can be improved within plasmonic fields created at the surface of the noble metals upon illumination by proper laser wavelengths. The phenomenon constitutes the basis for surface-enhanced Raman spectroscopy, which provides a highly sensitive analytical method to detect very low concentration of a large variety of samples. It was discussed that the complex dielectric function of noble metals along with the dimension and size of the metal nanostructures play key roles in excitation of their plasmon resonances. TERS was then introduced as a revolutionary method that was formed on the basis of surface-enhancement in an effort to surpass the diffraction limit in conventional microscopy and spectroscopy. The confined electric field at the nanoscale apex of the metallic TERS tip functions as a secondary nanosource of light, which enables the direct analysis of few nanometer domains on the surface of the sample. The enhancement of the Raman

scattering in SERS and TERS was analyzed on the basis of two mechanisms termed as the electromagnetic enhancement and chemical enhancement. The former is believed to play a dominant role in the accessible enhancement in TERS while the later is more pronounced in surface-enhanced method where the molecules come to direct contact with the metal surface. The TERS technique will be detailed from a more experimental and technical point of view in the following Chapter.

2.9 References

- (1) Schrader, B.; Editor *Infrared and Raman Spectroscopy: Methods and Applications*; John Wiley & Sons: Verlag, 1995.
- (2) Petry, R.; Schmitt, M.; Popp, J. *Chem. Phys. Chem.* (2003), 4, 14.
- (3) Yates, J. T., Jr.; Madey, T. E.; Editors *Vibrational Spectroscopy of Molecules on Surfaces*; Plenum Press: New York, 1987.
- (4) Popp, J., Kiefer, W. In *Encyclopedia of Analytical Chemistry*; Meyers, R. A., Ed.; John Wiley & Sons: New York, 2000; Vol. 21.
- (5) Ferraro, J. R.; Nakamoto, K.; Brown, C. W. *Introductory Raman Spectroscopy*; 2nd ed.; Academic Press, 2003.
- (6) Long, D. A. *Raman Spectroscopy*; McGraw-Hill: New York, 1977.
- (7) Long, D. A. *The Raman Effect: A Unified Treatment of the Theory of Raman Scattering by Molecules*; John Wiley & Sons, Inc.: Chichester, 2002.
- (8) Matthaus, C.; Chernenko, T.; Newmark, J. A.; Warner, C. M.; Diem, M. *Biophys. J.* (2007), 93, 668.
- (9) Schrader, B.; Moore, D. S. *Pure Appl. Chem.* (1997), 69, 1451.
- (10) Fiolhais, C.; Nogueira, F.; Marques, M.; Editors *A Primer in Density Functional Theory*; Springer: Verlag, 2003.
- (11) Neugebauer, J.; Reiher, M.; Kind, C.; Hess, B. A. *J. Computational Chem.* (2002), 23, 895.
- (12) Morton, S. M.; Silverstein, D. W.; Jensen, L. *Chem. Rev.* (2011), 111, 3962.
- (13) Myers, K. A. *J. Phys. Chem. A* (2008), 112, 11975.
- (14) Neugebauer, J. *Phys. Rep.* (2010), 489, 1.
- (15) Albrecht, A. C. *J. Chem. Phys.* (1961), 34, 1476.
- (16) Kim, H.; Kosuda, K. M.; Van Duyne, R. P.; Stair, P. C. *Chem. Soc. Rev.* (2010), 39, 4820.
- (17) Clark, R. J. H.; Dines, T. J. *Angew. Chem., Int. Ed.* (1986), 98, 131.

- (18) Long, D. A. *The Raman Effect: A Unified Treatment of the Theory of Raman Scattering by Molecules*; John Wiley & Sons: Chichester, 2001.
- (19) Nishimura, Y.; Hirakawa, A. Y.; Tsuboi, M. *Advances in Infrared and Raman Spectroscopy*; Heyden & Son: London, 1978; Vol. 5.
- (20) Tang, J.; Albrecht, A. C. In *Raman Spectroscopy*; Szymanski, H., Ed.; Plenum: New York, 1970; Vol. 2.
- (21) Clark, R. H.; Stewart, B. In *Inorganic Chemistry and Spectroscopy*; Springer Berlin Heidelberg: 1979; Vol. 36.
- (22) Hirakawa, A. Y.; Tsuboi, M. *Science* (1975), 188, 359.
- (23) Tsuboi, M.; Hirakawa, A. Y. *J. Raman Spectrosc.* (1976), 5, 75.
- (24) Hayazawa, N.; Inouye, Y.; Sekkat, Z.; Kawata, S. *Chem. Phys. Lett.* (2001), 335, 369.
- (25) Domke, K. F.; Zhang, D.; Pettinger, B. *J. Am. Chem. Soc.* (2006), 128, 14721.
- (26) Novotny, L.; Hecht, B. *Principles of nano-optics*; 1st ed.; Cambridge University Press: Cambridge, England, 2006.
- (27) Mayer, K. M.; Hafner, J. H. *Chem. Rev.* (2011), 111, 3828.
- (28) Bohren, C. F.; Huffman, D. R. *Absorption and Scattering of Light by Small Particles*; John Wiley & Sons: New York, 1983.
- (29) Born, M.; Wolf, E. *Principles of Optics*; 6th ed.; Cambridge University Press: Cambridge, England, 1980.
- (30) Barnes, W. L.; Dereux, A.; Ebbesen, T. W. *Nature* (2003), 424, 824.
- (31) Banholzer, M. J.; Millstone, J. E.; Qin, L.; Mirkin, C. A. *Chem. Soc. Rev.* (2008), 37, 885.
- (32) Willets, K. A.; Van Duyne, R. P. *Annu. Rev. Phys. Chem.* (2007), 58, 267.
- (33) Ebbesen, T. W.; Genet, C.; Bozhevolnyi, S. I. *Phys. Today* (2008), 61, 44.
- (34) Tabatabaei, M.; Sangar, A.; Kazemi-Zanjani, N.; Torchio, P.; Merlen, A.; Lagugné-Labarthe, F. *J. Phys. Chem. C* (2013), 117, 14778.
- (35) Konstantatos, G.; Sargent, E. H. *Nat. Nanotechnol.* (2010), 5, 391.
- (36) Mie, G. *Ann. Phys.* (1908), 25, 377.
- (37) Moskovits, M. *J. Raman Spectrosc.* (2005), 36, 485.
- (38) Hohenau, A.; Leitner, A.; Aussenegg, F. R. *Springer Ser. Opt. Sci.* (2007), 131, 11.
- (39) Novotny, L. *Phys. Today* (2011), 64, 47.
- (40) Novotny, L.; van Hulst, N. *Nat. Photonics* (2011), 5, 83.
- (41) Bailo, E.; Deckert, V. *Chem. Soc. Rev.* (2008), 37, 921.
- (42) Cancado, L. G.; Jorio, A.; Ismach, A.; Joselevich, E.; Hartschuh, A.; Novotny, L. *Phys. Rev. Lett.* (2009), 103, 1861011.

- (43) Maximiano, R. V.; Beams, R.; Novotny, L.; Jorio, A.; Cançado, L. G. *Phys. Rev. B* **(2012)**, *85*, 235434.
- (44) Novotny, L.; Stranick, S. J. *Annu. Rev. Phys. Chem.* **(2006)**, *57*, 303.
- (45) Hartschuh, A. *Angew. Chem., Int. Ed.* **(2008)**, *47*, 8178.
- (46) Hartschuh, A.; Sanchez, E. J.; Xie, X. S.; Novotny, L. *Phys. Rev. Lett.* **(2003)**, *90*, 0955031.
- (47) Cancado, L. G.; Hartschuh, A.; Novotny, L. *J. Raman Spectrosc.* **(2009)**, *40*, 1420.
- (48) Hartschuh, A.; Qian, H.; Meixner, A. J.; Anderson, N.; Novotny, L. *Surf. Interface Anal.* **(2006)**, *38*, 1472.
- (49) Abbe, E. *Archiv für mikroskopische Anatomie* **(1873)**, *9*, 413.
- (50) Rayleigh, L. *Philos. Mag.* **(1879)**, *8*, 261.
- (51) Synge, E. H. *Philos. Mag.* **(1928)**, *6*, 356.
- (52) Lewis, A.; Isaacson, M.; Harootunian, A.; Muray, A. *Ultramicroscopy* **(1984)**, *13*, 227.
- (53) Pohl, D. W.; Denk, W.; Lanz, M. *Appl. Phys. Lett.* **(1984)**, *44*, 651.
- (54) Dunn, R. C. *Chem. Rev.* **(1999)**, *99*, 2891.
- (55) Uebel, P.; Bauerschmidt, S. T.; Schmidt, M. A.; St. J. Russell, P. *Appl. Phys. Lett.* **(2013)**, *103*, 0211011.
- (56) Wang, R.; Wang, J.; Hao, F.; Zhang, M.; Tian, Q. *Appl. Opt.* **(2010)**, *49*, 1845.
- (57) Tsai, D. P.; Othonos, A.; Moskovits, M.; Uttamchandani, D. *Appl. Phys. Lett.* **(1994)**, *64*, 1768.
- (58) Hoepfner, C.; Siebrasse, J. P.; Peters, R.; Kubitscheck, U.; Naber, A. *Biophys. J.* **(2005)**, *88*, 3681.
- (59) Ianoul, A.; Street, M.; Grant, D.; Pezacki, J.; Taylor, R. S.; Johnston, L. J. *Biophys. J.* **(2004)**, *87*, 3525.
- (60) Wessel, J. *J. Opt. Soc. Am. B Opt. Phys.* **(1985)**, *2*, 1538.
- (61) Sánchez, E. J.; Novotny, L.; Xie, X. S. *Phys. Rev. Lett.* **(1999)**, *82*, 4014.
- (62) Anderson, M. S. *Appl. Phys. Lett.* **(2000)**, *76*, 3130.
- (63) Hayazawa, N.; Inouye, Y.; Sekkat, Z.; Kawata, S. *Opt. Commun.* **(2000)**, *183*, 333.
- (64) Stöckle, R. M.; Suh, Y. D.; Deckert, V.; Zenobi, R. *Chem. Phys. Lett.* **(2000)**, *318*, 131.
- (65) Schmid, T.; Yeo, B.-S.; Leong, G.; Stadler, J.; Zenobi, R. *J. Raman Spectrosc.* **(2009)**, *40*, 1392.
- (66) Stadler, J.; Schmid, T.; Zenobi, R. *Nanoscale* **(2012)**, *4*, 1856.
- (67) Moskovits, M. *Rev. Mod. Phys.* **(1985)**, *57*, 783.

- (68) Sonntag, M. D.; Klingsporn, J. M.; Garibay, L. K.; Roberts, J. M.; Dieringer, J. A.; Seideman, T.; Scheidt, K. A.; Jensen, L.; Schatz, G. C.; Van, D. R. P. *J. Phys. Chem. C* **(2012)**, *116*, 478.
- (69) Zhang, W.; Yeo, B. S.; Schmid, T.; Zenobi, R. *J. Phys. Chem. C* **(2007)**, *111*, 1733.
- (70) Gersten, J.; Nitzan, A. *J. Chem. Phys.* **(1980)**, *73*, 3023.
- (71) Gersten, J. I. *J. Chem. Phys.* **(1980)**, *72*, 5779.
- (72) McCall, S. L.; Platzman, P. M. *Phys. Rev. B* **(1980)**, *22*, 1660.
- (73) McCall, S. L.; Platzman, P. M.; Wolff, P. A. *Phys. Lett. A* **(1980)**, *77A*, 381.
- (74) Moskovits, M. *J. Chem. Phys.* **(1978)**, *69*, 4159.
- (75) Moskovits, M. *Solid State Commun.* **(1979)**, *32*, 59.
- (76) Schatz, G. C. *Acc. Chem. Res.* **(1984)**, *17*, 370.
- (77) Schatz, G. C.; Van, D. R. P. *Surf. Sci.* **(1980)**, *101*, 425.
- (78) Weitz, D. A.; Garoff, S.; Gersten, J. I.; Nitzan, A. *J. Chem. Phys.* **(1983)**, *78*, 5324.
- (79) Adrian, F. J. *J. Chem. Phys.* **(1982)**, *77*, 5302.
- (80) Billmann, J.; Otto, A. *Solid State Commun.* **(1982)**, *44*, 105.
- (81) Burstein, E.; Chen, Y. J.; Chen, C. Y.; Lundquist, S.; Tosatti, E. *Solid State Commun.* **(1979)**, *29*, 567.
- (82) Lombardi, J. R.; Birke, R. L.; Lu, T.; Xu, J. *J. Chem. Phys.* **(1986)**, *84*, 4174.
- (83) Kelly, K. L.; Coronado, E.; Zhao, L. L.; Schatz, G. C. *J. Phys. Chem. B* **(2003)**, *107*, 668.
- (84) McCall, S. L.; Platzman, P. M. *Phys. Rev. B: Condens. Matter* **(1980)**, *22*, 1660.
- (85) Woods, D. A.; Bain, C. D. *Analyst* **(2012)**, *137*, 35.
- (86) Krug Ii, J. T.; Sanchez, E. J.; Xie, X. S. *J. Chem. Phys.* **(2002)**, *116*, 10895.
- (87) Orendorff, C. J.; Gole, A.; Sau, T. K.; Murphy, C. J. *Anal. Chem.* **(2005)**, *77*, 3261.
- (88) Draine, B. T.; Flatau, P. J. *J. Opt. Soc. Am. A* **(1994)**, *11*, 1491.
- (89) Rycenga, M.; Kim, M. H.; Camargo, P. H. C.; Cobley, C.; Li, Z.-Y.; Xia, Y. *J. Phys. Chem. A* **(2009)**, *113*, 3932.
- (90) Yang, W.-H.; Schatz, G. C.; Van, D. R. P. *J. Chem. Phys.* **(1995)**, *103*, 869.
- (91) Bian, R. X.; Dunn, R. C.; Xie, X. S.; Leung, P. T. *Phys. Rev. Lett.* **(1995)**, *75*, 4772.
- (92) Taflove, A.; Hagness, S. C. *Computational Electrodynamics: The Finite - Difference Time - Domain Method*; Artech House: Boston, MA, 2005.
- (93) Jiang, X.; Campion, A. *Chem. Phys. Lett.* **(1987)**, *140*, 95.
- (94) Udagawa, M.; Chou, C.-C.; Hemminger, J. C.; Ushioda, S. *Phys. Rev. B: Condens. Matter* **(1981)**, *23*, 6843.
- (95) Jensen, L.; Aikens, C. M.; Schatz, G. C. *Chem. Soc. Rev.* **(2008)**, *37*, 1061.

- (96) Otto, A. *J. Raman Spectrosc.* **(2005)**, *36*, 497.
- (97) Pettinger, B. *J. Chem. Phys.* **(1986)**, *85*, 7442.
- (98) Kambhampati, P.; Child, C. M.; Foster, M. C.; Campion, A. *J. Chem. Phys.* **(1998)**, *108*, 5013.
- (99) Kneipp, K.; Kneipp, H.; Itzkan, I.; Dasari, R. R.; Feld, M. S. *J. Phys.: Condens. Matter* **(2002)**, *14*, R597.
- (100) Lombardi, J. R.; Birke, R. L. *Acc. Chem. Res.* **(2009)**, *42*, 734.
- (101) Morton, S. M.; Ewusi-Annan, E.; Jensen, L. *Phys. Chem. Chem. Phys.* **(2009)**, *11*, 7424.
- (102) Saikin, S. K.; Olivares-Amaya, R.; Rappoport, D.; Stopa, M.; Aspuru-Guzik, A. *Phys. Chem. Chem. Phys.* **(2009)**, *11*, 9401.
- (103) Watanabe, H.; Ishida, Y.; Hayazawa, N.; Inouye, Y.; Kawata, S. *Phys. Rev. B Condens. Matter Mater. Phys.* **(2004)**, *69*, 1554181.
- (104) Verma, P.; Yamada, K.; Watanabe, H.; Inouye, Y.; Kawata, S. *Phys. Rev. B Condens. Matter Mater. Phys.* **(2006)**, *73*, 0454161.
- (105) Rasmussen, A.; Deckert, V. *J. Raman Spectrosc.* **(2006)**, *37*, 311.
- (106) Fromm, D. P.; Sundaramurthy, A.; Kinkhabwala, A.; Schuck, P. J.; Kino, G. S.; Moerner, W. E. *J. Chem. Phys.* **(2006)**, *124*, 0611011.
- (107) Downes, A.; Salter, D.; Elfick, A. *Opt. Express* **(2006)**, *14*, 5216.
- (108) Zhang, W.; Schmid, T.; Yeo, B.-S.; Zenobi, R. *J. Phys. Chem. C* **(2008)**, *112*, 2104.
- (109) Malkovskiy, A. V.; Malkovsky, V. I.; Kisliuk, A. M.; Barrios, C. A.; Foster, M. D.; Sokolov, A. P. *J. Raman Spectrosc.* **(2009)**, *40*, 1349.
- (110) Boehme, R.; Richter, M.; Cialla, D.; Roesch, P.; Deckert, V.; Popp, J. *J. Raman Spectrosc.* **(2009)**, *40*, 1452.
- (111) Budich, C.; Neugebauer, U.; Popp, J.; Deckert, V. *J. Microsc.* **(2008)**, *229*, 533.
- (112) Schmid, T.; Burkhard, J.; Yeo, B.-S.; Zhang, W.; Zenobi, R. *Anal. Bioanal. Chem.* **(2008)**, *391*, 1899.
- (113) Neugebauer, U.; Schmid, U.; Baumann, K.; Ziebuhr, W.; Kozitskaya, S.; Deckert, V.; Schmitt, M.; Popp, J. *Chem. Phys. Chem.* **(2007)**, *8*, 124.
- (114) Schmid, T.; Schmitz, T. A.; Setz, P. D.; Yeo, B.-S.; Zhang, W.; Zenobi, R. *Chimia* **(2006)**, *60*, 783.
- (115) Cialla, D.; Deckert-Gaudig, T.; Budich, C.; Laue, M.; Moeller, R.; Naumann, D.; Deckert, V.; Popp, J. *J. Raman Spectrosc.* **(2009)**, *40*, 240.

Chapter 3

3 Experimental Design and Technical Aspects for Tip-enhanced Raman Spectroscopy

Tip-enhanced Raman spectroscopy is a promising technique for chemical analysis and surface characterization offering a nanometer scale spatial resolution. Nevertheless, several challenges prevent the widespread application of this technique. Fabrication of efficient TERS probes is indeed one of the most critical challenges. The nanometer spatial resolution in TERS measurements is mainly limited by the size and the shape of the TERS probe. An optimized fabrication method is thus the key to prepare efficient and reproducible tips. Moreover, the polarization of the incident light is an important factor to optimize the enhancement in TERS measurements. The efficient excitation of the plasmonic resonances occurs when the incident light has a component along the tip axis. This can be achieved more easily in reflection TERS configuration by rotating the input polarization in the plane of incidence. However, it becomes more complex when using a transmission TERS scheme. In such case a radially polarized light source can be used to create a longitudinally polarized component oriented along the tip axis.

This Chapter reviews the key components and technical aspects involved in development of an optimized TERS setup. The Chapter summarizes the optimal parameters to achieve high sensitivity and high spatial resolution in TERS experiments.

3.1 Technical Aspects

3.1.1 Methods for Controlling the TERS Probe Position

The enhancement of the electric field in TERS is confined in close proximity of the tip apex. The dimension of the confined area ranges from few to tens of nanometers. However, it has been theoretically^{1,2} and experimentally³⁻⁵ evidenced that the tip-enhanced signal decays quite rapidly as the tip-sample distance increases. Owing to its near-field nature, the intensity of the Raman signals decrease rapidly by extension of the tip-surface distance.⁶⁻⁹ Consequently, it is essential to precisely control the position of the

tip with respect to the sample surface. To fulfill this purpose, the precise control over the tip position (feedback mechanism) provided by scanning probe microscopy (SPM), is ideal. Atomic force microscopy (AFM),^{6,8} scanning tunneling microscopy (STM)^{7,9} and shear force (SF)^{10,11} feedback controls are the three SPM methods that have mainly been utilized in TERS. The feedback system, along with a piezoelectric sample scanner, enables the scanning of the tip and its positioning on a particular region of the sample with sub-nanometer resolution.

3.1.1.1 AFM Feedback

In AFM, the reflection of a laser beam from the cantilever backside is used as the feedback parameter. The reflection of this laser allows one to monitor the tip-sample distance and to maintain a constant interaction using a feedback loop. The feedback loop is equipped by a piezoelectric tube that controls the tip position in *xyz* directions as illustrated in **Figure 3.1a**.

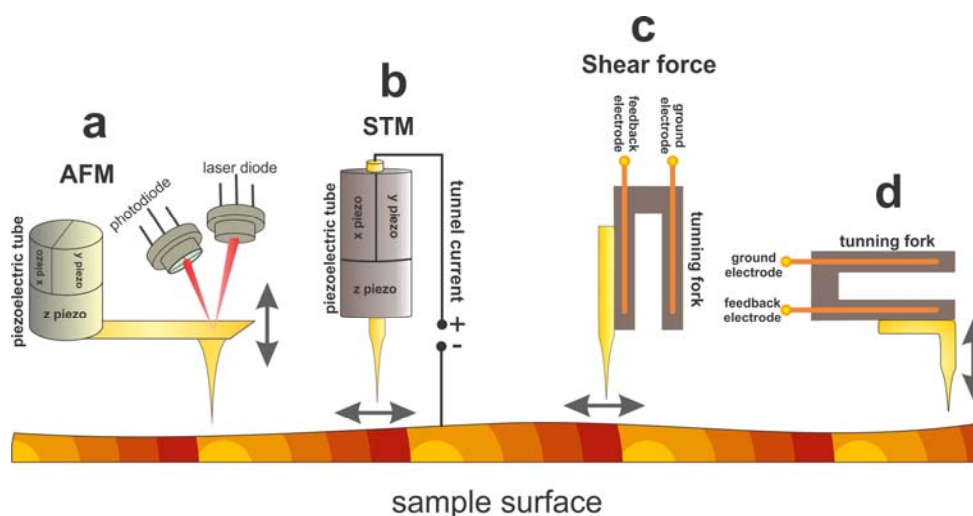


Figure 3.1 Illustration of different SPM feedback systems (a) AFM feedback with tip oscillating vertically with respect to the sample surface (b) STM feedback with tip oscillating laterally with respect to the sample surface (c) shear force feedback with tuning fork mounted vertically and the tip moving laterally with respect to the surface (d) feedback mechanism with tuning fork mounted horizontally and the tip oscillating vertically with respect to the sample surface

The tip-sample interaction is enabled through various AFM modes such as contact and non-contact (intermittent contact or tapping mode). Both contact and non-contact modes are applicable for TERS measurements. The advantage of contact over non-contact mode is the constant distance between the tip and the sample which results in a consistent enhancement over the surface. On the contrary, in tapping mode the tip oscillates and its distance from the surface changes constantly.¹² However, upon each Raman acquisition the tip oscillates several times during which the tip-sample distance ranges from a few to tens of nanometers. As a result, the Raman signal is an average of contact and non-contact signals. In general, lower interaction between the tip and the sample is expected in non-contact mode, which is an advantage specially when working with delicate samples and/or probes that are coated with a thin layer of noble metal. The time during which the tip is in closer proximity (near-field) of the sample can be controlled by optimizing the oscillation amplitude. In addition, near-field contributions can be separately detected by synchronizing the laser with the time duration when tip is in near-field of the sample and using a shutter to collect the signal only when the tip is in sample's close proximity.¹³ In addition, by using fast detectors such as avalanche photodiodes (APD) and a lock-in amplifier, optimization of the signal/noise ratio becomes possible through discriminating the far-field from the near-field contribution.¹⁴

There is however one important limitation involved with AFM based TERS setups arising from the use of an internal laser diode located inside the AFM head and with wavelength usually in the near-IR range. This light source used to maintain the feedback between the surface and the tip restricts the choice of Raman excitation wavelength to UV-visible due to the possible interference of the AFM laser with the detector of the spectrometer. Nevertheless, the addition of filters can be useful to eliminate parasitic wavelength of the AFM laser.

3.1.1.2 STM Feedback

In STM, the tip-sample distance is controlled through keeping a constant tunneling current between a conductive tip and a conductive sample, as illustrated in **Figure 3.1b**. The tip-sample separation in STM setups is in the sub-nanometer range, which is

generally smaller compared to AFM feedback.¹⁵ Metal tips obtained by electrochemical etching of gold or silver wires are generally employed. The fact that the substrate has to be conductive restricts the choices of TERS optical configuration and the samples. Nevertheless, the need for a conductive sample could be resolved by utilizing conductive substrates which are typically metallic or carbon thin plates. Top or side illuminations configuration is generally combined with STM feedback to be compatible with opaque substrates.¹⁴ TERS optical configurations including top and side illuminations will be discussed in detail in section 3.1.2 of this Chapter.

3.1.1.3 Shear Force Feedback

In shear force feedback systems, etched TERS metallic tip is mounted to a tuning fork which usually oscillates horizontally with respect to the sample surface as illustrated in **Figure 3.1c**. In such cases the feedback system holds relatively constant distance between the tip and the sample which resembles contact AFM modes. This configuration is mostly applicable for samples with low roughness and horizontal features. The tuning fork is usually made from quartz crystals and resonates at a frequency in the range of 30-100 kHz.¹⁰ The oscillation occurs in the plane parallel to the sample surface and the feedback is maintained by monitoring the change of the current induced to the tuning fork by the tip-sample shear force interactions. The tuning fork itself is attached to a piezoelectric tube as a part of the feedback loop.

It is also possible that the tuning fork is mounted horizontally with respect to the sample surface (**Figure 3.1d**). Instead of shear forces, tip-sample interactions will be mainly induced by Van der waals and electrostatic interactions in this setup.

An advantage of using a tuning fork scheme compared to standard contact AFM comes from the fact that the choice of Raman excitation laser is not limited to UV-visible due to the absence of feedback laser diode. In shear force setups however, the tip has to be glued to the tuning fork where the quality of the gluing could result in a less stable and reproducible feedback response with tip-sample separation in 5-30 nm range.^{16,17}

3.1.2 TERS Optical Configuration

TERS setup is typically a combination of an AFM/STM microscope and a Raman spectrometer together with selected irradiation wavelength. In TERS, a part of the focused light gets localized at the tip apex and excites the Raman scattering of the sample molecules in close proximity to the tip apex. The back-scattered light has to be collected efficiently and analyzed with a spectrometer prior to detection with detector such as charged-coupled device (CCD),^{18,19} avalanche photodiode (APD)^{20,21} or photomultiplier detector (PMT).^{22,23} Within the TERS setup however, different optical configurations, can be utilized for illuminating the tip and the sample. The choice of the illumination configuration might limit the type of samples that could be studied by a particular TERS setup, as will be discussed in the following section.

3.1.2.1 Side Illumination

Side illumination is a strategy of choice for opaque samples or when the AFM system does not offer access to optical component to irradiate or collect light.²⁴ In side illumination, the laser is focused on the tip from the side and by using microscope objectives with long working distance at an angle in 45-70° range relative to the tip axis.²⁵⁻²⁷ This angle guarantees a laser polarization component along the tip axis as required in TERS measurements. The collection is insured using the same objective in a back-scattered geometry^{26,28-31} or using a different objective on the reflected path^{25,32} or from bottom using a different objective.³³ Because the illumination is performed at a defined angle, the laser focal point on the sample surface is not totally symmetric and spread over a larger surface. Therefore, higher laser powers of 5-10 mW are usually used to compensate the energy loss due to larger laser spot size.¹⁴ The low numerical aperture of long working distance objectives (N.A. ~ 0.7) is a disadvantage to the efficiency of the collection of the tip-enhanced photons. Metal surfaces have been successfully employed as substrate to benefit from the further enhancements produced between two dipoles formed by metal tip and a mirror dipole in metal substrate.^{2,32} Side illumination configuration is illustrated in **Figure 3.2a**.

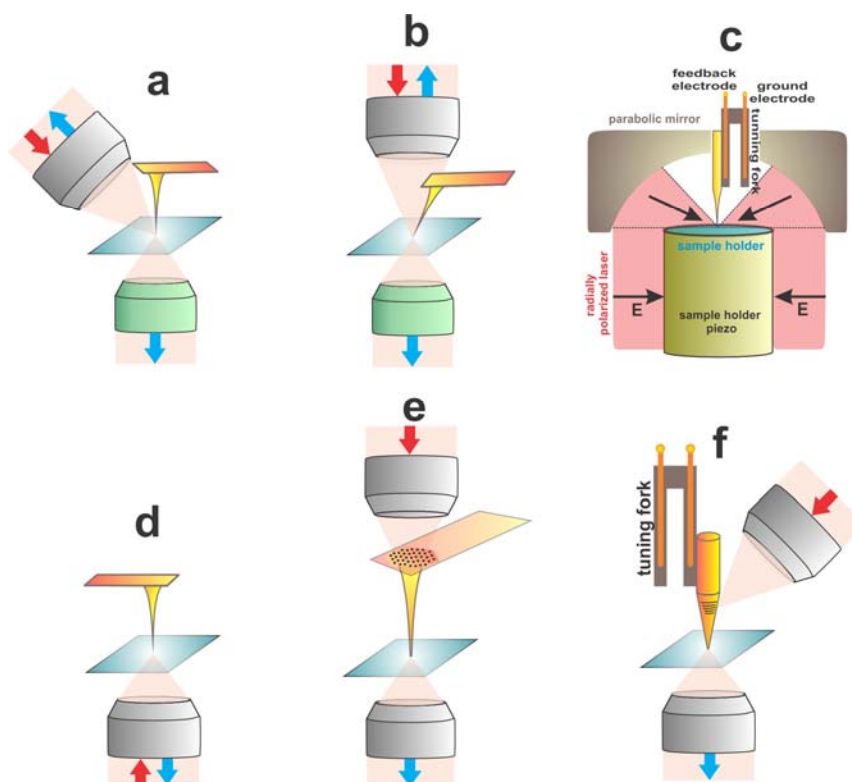


Figure 3.2 TERS optical configurations (a) side illumination, the back-scattered light can be collected either by the illuminating microscope objective or a different one in transmission geometry. The two objectives are depicted in grey and green respectively (b) top illumination, the back-scattered light can be collected either by the illuminating microscope objective or by a different one in transmission geometry. The two objectives are depicted in grey and green respectively (c) illustration of parabolic mirror-based top illumination configuration. Radially polarized laser is focused by a parabolic mirror onto an etched gold tip connected to tuning fork (d) bottom illumination geometry where both incident and back-scattered light is collected by the same microscope objective (e) plasmonic TERS tip nanofabricated through creating waveguides on the tip cantilever (f) etched gold tip with FIB fabricated grating on its shaft. The tip is mounted on the tuning fork of a shear force AFM.

3.1.2.2 Top Axial Illumination

In top illumination configuration, axial illumination from the top is perpendicular to the sample surface and is aligned along the apex of the tip.^{34,35} The non-angled illumination in this configuration makes the focal point symmetric and therefore tighter focus is achieved compared to side illumination. In addition, the reflecting illumination in top setup allows for working on both transparent and opaque samples and it also is beneficial for thick samples where the loss of light in transmission is high. With regards to polarization considerations, as it would be discussed in section 3.3 and further in Chapter 4, radially polarized light with an electric field z-component along the tip axis are beneficial for this illumination orientation. Top illumination is illustrated in **Figure 3.2b**.

In top illumination setup, the tip is located between the objective and the focal region; therefore, the tip blocks a part of the incident light and a part of the detected signal. For this reason, the focal dimensions of the laser and numerical aperture of the microscope objective should be suitable for seeing the area around the tip and to collect the back-scattered light more efficiently. A parabolic mirror-based setup is typically used in top illumination configurations and has been illustrated in **Figure 3.2c**. In these setups, a radially polarized laser is focused by a parabolic mirror onto the tip. The numerical aperture of these reflection objectives is between that of the side and bottom illumination geometries and can be as high as 0.7.^{27,36,37}

3.1.2.3 Bottom Axial Illumination

In bottom illumination geometries, the light is focused by high numerical aperture objectives on the sample and through a transparent substrate. Thin substrates such as thin glass cover slips are generally used and the objectives are generally corrected with respect to the thickness of the substrate. Indium tin oxide (ITO), quartz³⁸ or transparent gold plates³⁹ are other alternatives for glass substrates as long as the thicknesses are compatible with a given microscope objective. In top illumination configuration, the TERS tip is placed over the sample surface and inside the focal region of the Raman excitation laser. Since the substrate and the sample are required to be transparent, AFM

and shear force feedback systems are suitable for this optical geometry. In terms of the choice for the microscope objective, if glass substrates are used, short working distance microscope objectives can be utilized. Short working distance is usually the characteristic of microscope objectives with high numerical apertures of 1.4. High numerical aperture focuses the light more tightly into a smaller area which results in a decrease of background signal. Oil and water immersion microscope objectives are from this category. The same objective is usually used to collect the back-scattered light for detection.^{21,40,41}

In bottom axial illumination, the largest excitation of the plasmon resonances occurs when the incident laser has a polarized component along the tip apex. Therefore, longitudinal waves^{42,43} or higher order laser modes such as radially polarized laser⁴⁴ are mostly beneficial to this optical configurations. Bottom illumination configuration has been illustrated in **Figure 3.2d**.

3.1.2.4 Advanced Optical Configurations

Beside the fundamental illumination configurations that are discussed above, other setups are developed through optically manipulating the TERS tip.

Fabrizio *et al.*³⁴ suggested that an adiabatic compression of the surface plasmon is employed to conduct TERS measurements. Their approach is based on fabrication of TERS tips with trapped waveguides which acts as a photonic-plasmonic device. The waveguide is created on commercially available Si₃N₄ tips by using focused ion beam (FIB) milling. The design of the waveguide on the tip, which is fully compatible with an AFM system, is done in a way that the surface plasmon is focused towards the apex of the tip cone. The operating principle of this device is illustrated on **Figure 3.2e** and the SEM image of these tips is presented in **Figure 3.3a**. The geometric constrains of this cantilever-based design, does not allow its application for opaque samples when bottom illumination is applied.

Raschke *et al.*⁴⁵ proposed that adiabatic plasmon focusing is used through creation of a grating on the shaft of an etched gold tip. In their setup an electromagnetically etched tip

is mounted on an AFM tuning fork and the grating is generated on that via FIB milling. In this configuration, the incident light gets focused onto the grating from the side and the enhanced Raman scattered light gets collected from the apex of the tip in transmission configuration. The schematic of this setup is depicted in **Figure 3.2f** and the SEM image of these tips is presented in **Figure 3.3b**.

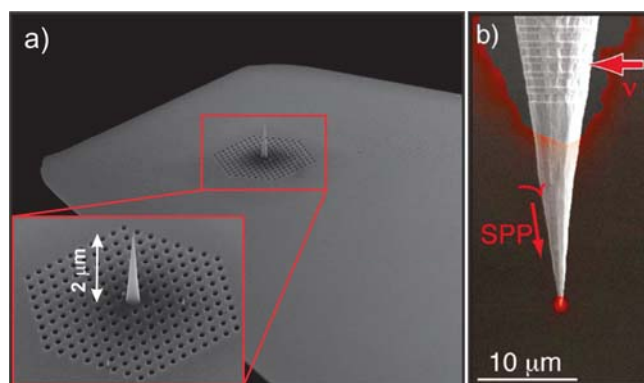


Figure 3.3 (a) SEM image of a trapped waveguide on Si_3N_4 AFM cantilever. The radius of the tip apex is 5 nm. The image is obtained from reference 34 with permission from Nature publications.³⁴ (b) SEM image of an electrochemically etched gold tip with FIB-cut grating on its shaft. The image is adapted from reference 45 with permission from American Chemical Society.⁴⁵

Despite the fact that the adiabatic tips have been successfully tested to study monolayer of malachite green dye molecules⁴⁵ and silicon nanocrystals,³⁴ the time consuming and costly fabrication methods restrict their applications.

3.1.3 TERS Experimental Setup

In the present thesis, the TERS setup is based on a commercial Raman spectrometer (600 gr/mm grating, HR LabRam, Horiba-Jobin-Yvon, Kyoto, Japan) connected to an inverted optical microscope (IX71, Olympus, Tokyo, Japan) and interfaced with a 5 axis atomic force microscope system (AFM, NanoWizard II Bioscience, JPK Instruments Inc., Berlin, Germany) to perform measurements in the bottom illumination configuration and back-scattering collection geometry as shown in **Figure 3.4**.

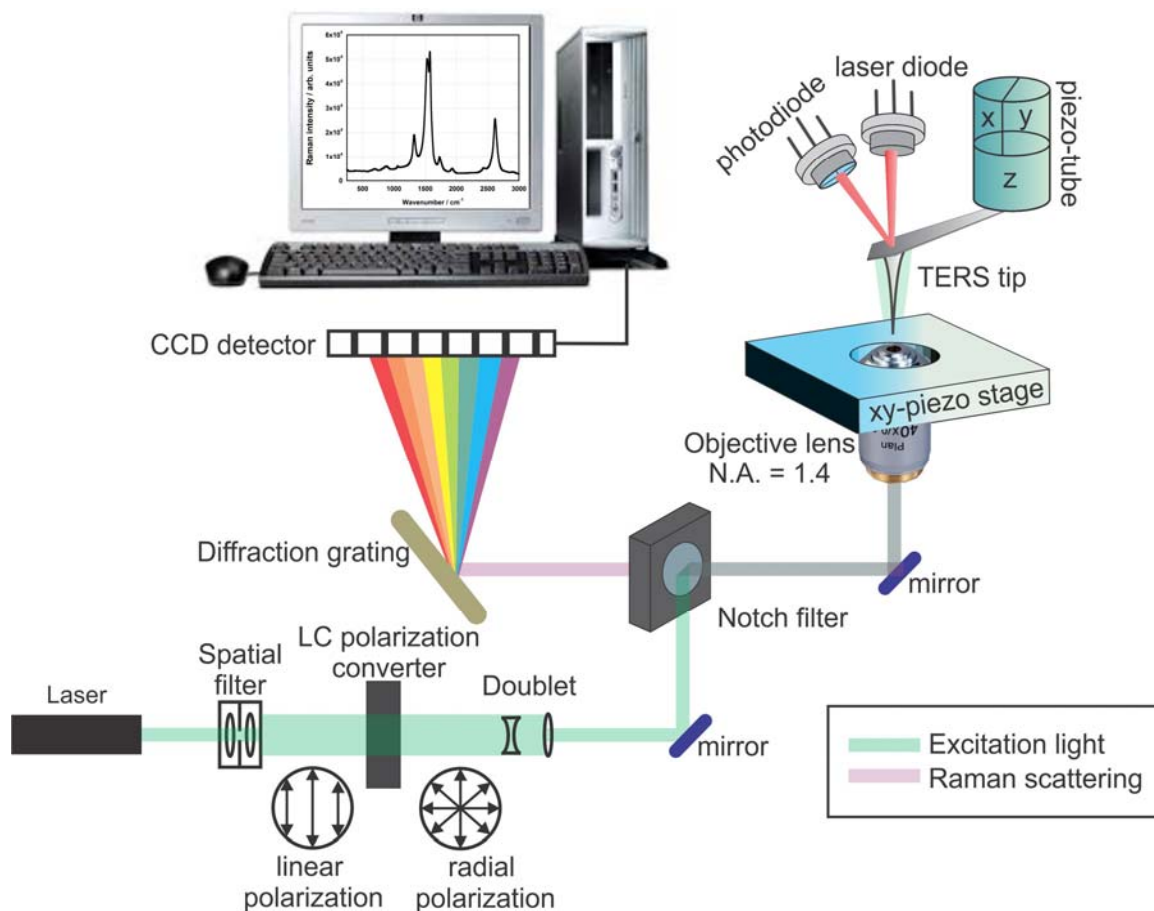


Figure 3.4 Scheme of the TERS setup used in this thesis. The linearly polarized laser passes through a spatial filter to yield a homogeneous Gaussian spatial distribution and then gets converted into a radially polarized light by a liquid crystal (LC) polarization converter. The diameter of the radially polarized laser gets minimized by means of a pair of convex-concave lenses before entering the microscope objective. Next, the radially polarized laser gets focused onto the apex of the TERS tip to excite the Raman scattering of the sample in proximity of the TERS tip. The backscattered light from the sample gets collected using the same microscope objective, passes through the notch filter to reject the incident wavelength and then enters the spectrometer. Inside the spectrometer, a diffraction grating disperses the light spatially, separating the distinct wavelengths. The dispersed light is then detected by a CCD detector. A signal will be sent from the CCD to computer software where the Raman spectrum is created.

The AFM is equipped with a high resolution piezoelectric xy sample scanner as well as an independent xyz piezoelectric actuator to independently control the tip position and to hold the tip a few nanometers above the sample surface during TERS measurements. The Raman signal of the sample is filtered from reflected laser or Rayleigh scatterings by using a notch filter located prior to the spectrometer. With regards to the detection system, a 0.8 m spectrometer equipped with a 600 gr/mm grating disperses the collected light spectrally prior to detection. The spectral resolution achieved with this spectrometer is typically 3-4 cm^{-1} . Alternatively, a 1800 gr/mm grating can be used to increase the spectral resolution and diffraction efficiency; nevertheless the detected intensities will be lower. A liquid nitrogen-cooled charge coupled device (CCD 1024x1600 pixels, Symphony Horiba) with close to single photon counting capacity and high efficiency in the visible range is also attached to this setup. When 600 gr/mm grating is used, the obtained Raman spectra extends roughly over 1100 cm^{-1} spectral range.

3.2 Fabrication of TERS Probes

The major challenge in performing successful TERS is to fabricate efficient and reproducible TERS active probes. Two main factors should be considered when TERS probes are designed. First, the required conditions to excite localized surface plasmon should be fulfilled by choosing the right material with respect to the excitation wavelength, second, the shape and size of the tip apex should be optimized to improve the accessible spatial resolution.^{14,46} The following sections discuss these issues in more details.

3.2.1 Tip Material of TERS Probes

As discussed in Chapter 2, the localized surface plasmon resonance (LSPR) at the metal interface gives rise to a field enhancement at the tip apex. The first factors to be optimized are indeed the nature of the material that forms the tip and the dielectric properties of the surrounding environment.⁴⁷ To do this optimization, the dielectric constant of the tip material, the dielectric constant of the medium surrounding the tip or the material underlying the metal coating⁴⁸ on the tip must be properly selected according

to the excitation wavelength. Polarization of the light^{43,49} has also a critical effect on excitation of the LSPR which will be discussed later in section 3.3.

According to Le Ru *et al.*⁵⁰ the ratio E_{enhanced}/E_0 , with E_{enhanced} being the amplitude of the enhanced electric field and E_0 being the amplitude of the incident electric field, becomes very large if $\varepsilon(\omega) \approx -2\varepsilon_{\text{medium}}$. $\varepsilon(\omega)$ denotes the dielectric function of the TERS tip at frequency ω and $\varepsilon_{\text{medium}}$ shows the dielectric function of the medium. This condition is fulfilled when $\text{Im}(\varepsilon(\omega)) \approx 0$ and $\text{Re}(\varepsilon(\omega)) \approx -2\varepsilon_{\text{medium}}$. $\text{Im}(\varepsilon(\omega))$ and $\text{Re}(\varepsilon(\omega))$ are the imaginary and real part of the dielectric function of the tip, respectively. $\text{Im}(\varepsilon(\omega)) \approx 0$ guarantees that the dissipation losses are minimal and hence the imaginary part determines the actual magnitude of the plasmon resonance. $\text{Im}(\varepsilon(\omega)) \approx 0$ happens only in materials with $-20 \leq \text{Re}(\varepsilon(\omega)) \leq -1$ in the frequency range of interest.⁵⁰ Therefore, to excite a strong optical response at a certain frequency, the dielectric function of different material should be evaluated. To further discuss this effect, the real and imaginary part of the dielectric function for gold, silver, copper and aluminum are presented in **Figure 3.5**. The dielectric function values for these four metals are adapted from experimental values reported in the literature.^{51,52}

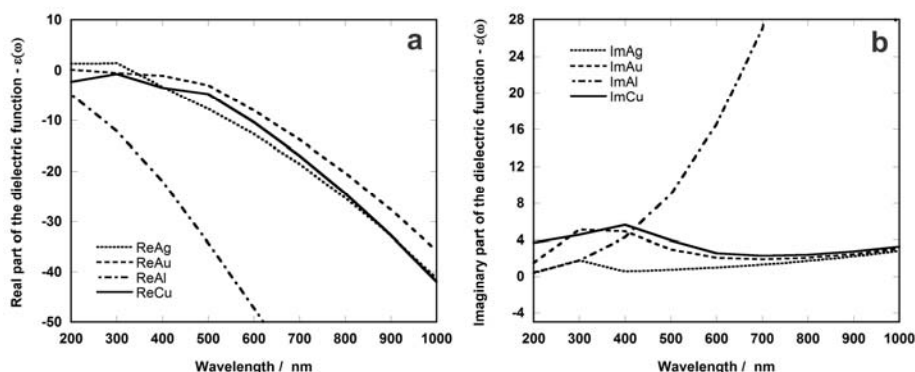


Figure 3.5 (a) Real and (b) imaginary part of complex dielectric function for some noble metals. The two charts are plotted based on the dielectric constant values reported by Johnson & Christy for gold, silver and copper.⁵¹ Dielectric constants of aluminum matches the values reported by Rakie.⁵²

The evaluation of dielectric functions, which are available in many textbooks^{50,53,54} along with absorption/emission behavior of different metals and stability under ambient conditions leads to the conclusion that silver and gold are expected to be the most useful metals in visible range of light. However, it should be noted that the dielectric functions of the two metals show significant difference within UV-visible region.⁴⁸ The imaginary part of the dielectric function for gold (similar to copper) has large values below 600 nm wavelength and therefore, it significantly absorbs light in this region. Above 600 nm, gold exhibits considerable plasmon resonance. Meanwhile, silver shows plasmonic resonances over the whole visible range. Aluminum absorbs strongly over the whole visible range while it is resonant in UV range and has low absorption down to a wavelength of 200 nm. In the deep UV region, the dielectric function of aluminum shows reasonably small imaginary part, whereas the real part stays negative.^{55,56}

Additionally, $\text{Re}(\varepsilon(\omega)) \approx -2\varepsilon_{\text{medium}}$ implies that the underlying material below the metal coating could be altered to tune the plasmon resonance frequency of a tip.⁴⁸ Materials with high refractive index as well as silicon ($n=4.4$) shift the surface plasmon towards higher wavelengths. This has negative effect on overlapping of the excitation laser and the surface plasmon in the TERS tip.⁵⁷ Substituting silicon tips with SiO_2 ($n=1.5$) or Si_3N_4 ($n=2.05$) tips are useful for reaching higher enhancement in blue/green wavelength ranges.⁵⁸ Coating silicon tips with a low refractive index material such as AlF_3 or SiO_2 ^{58,59} below silver coating is an alternative way to change the plasmon resonance frequency of silver tips towards blue/green spectral range. The effect of additional layers on optical properties of coated tips has also been numerically predicted.^{60,61}

In this thesis, the choice of the material for coating TERS probes is limited to gold with excitation of 632.8 nm and silver with 532 nm. AFM tips are chosen to be commercially available silicon tips for the majority of the work while nanocrystalline diamond tips are utilized for the specific case study of silicon nanowires presented in Chapter 6.

3.2.2 TERS Tip Geometry

The size, shape and the roughness of the metal coating deposited over the tip are parameters that also strongly influence the enhancement of the electric field around the apex. Since in TERS the spectral measurements originate from the tip apex, smaller tip apex results in investigation of a smaller volume on the sample surface and therefore increased spatial resolution.^{2,62,63} Additionally, sharper apexes experience larger charge density which leads to larger local enhancement of the electric field. On the other hand, since the tip dimensions are comparable with the oscillation wavelength of the electrons inside the locally confined electric field, defects as small as the grain boundaries within the metal thin film can change substantially the plasmon frequency. The amount of defects and hence the sharpness of the apex could be controlled during the tip preparation process only to some extent.¹¹ This explains the low reproducibility of TERS active tips and variation of LSPR for the tips of similar dimensions that are prepared using similar procedures. This could be problematic since only stable plasmonic activity gives reliable and reproducible enhancement of the Raman scattering and consequently a well resolved chemical imaging.⁶²

Two different tip geometries are used in the current thesis depending on the experimental requirement. The majority of the TERS measurements are conducted using tapping mode NCL-silicon tips from NanoworldTM. The SEM image of these tips is shown in **Figure 3.6a**. These tips are shaped like a polygon based pyramid with height of 10-15 μm . The radius of the tip apex is in the 20 nm range. For TERS study of silicon nanowires ND-DTIRL all diamond tips from Advanced Diamond TechnologiesTM were used. Diamond tips were used to prevent the interference of the Raman signal of the silicon cantilever with the signal of silicon nanowires. These tips have a 3-sided pyramid structure with pyramid height of 5-7 μm and an opening angle wider than the one from the NCL tips. The apex diameter is in 20 nm range. The large opening angle of TERS probes promote the enhancement of the signal from the walls of the tip which leads to poor imaging resolution as it will be discussed in Chapter 6 of this thesis. An SEM image of these tips is shown in **Figure 3.6b**.

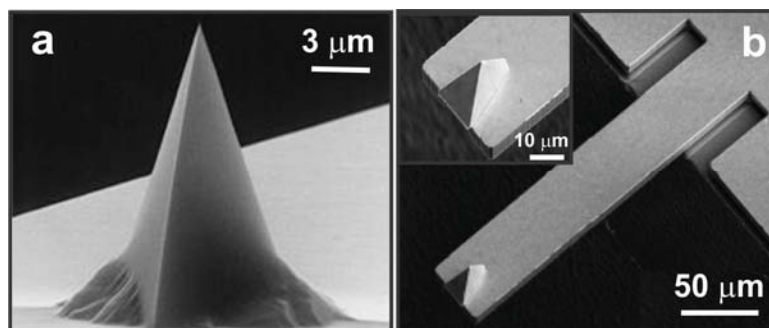


Figure 3.6 SEM images of (a) silicon NCL tapping mode AFM tip (b) ND-DTIRL nanocrystalline all diamond AFM tips

3.2.3 Fabrication Methods

Several approaches were proposed for the fabrication of TERS probes. Electrochemical etching of metallic nanowires is often used for homemade setups or setups based on a STM feedback or tuning fork based systems. Another approach is to deposit a thin layer of metal by sputtering or electron beam induced metal vapor deposition on commercially available AFM tips.⁶⁴ The two methods are briefly reviewed in the following sections.

3.2.3.1 Electrochemical Etching

For TERS probe preparation, gold or silver wires are materials that are generically sharpened using electrochemical etching. To prepare gold tips, a voltage is applied between the gold wire (typically 100 μm diameter) and a gold ring electrode that surrounds the wire, while both wire and the ring are immersed in concentrated hydrochloric acid and ethanol (1:1 V/V) electrolyte. In a procedure proposed by Ren *et al.*⁶⁵ a gold ring of about 8 mm diameter made of 1 mm thickness gold wire is placed on the surface of the etchant solution in a way that $\frac{3}{4}$ height of the ring is immersed in the solution. Other than gold,⁶⁶ platinum⁶⁷⁻⁶⁹ or carbon⁷⁰ rings are also widely used in etching of gold wires. A gold wire of 0.25 mm thickness is then immersed in the center of the gold ring so that 2-3 mm of the wire is inside the etchant solution. Schematic of the etching reaction is presented in **Figure 3.7**. Upon applying the voltage, a large surface tension is formed between the ring and the gold wire which creates a meniscus on the surface⁶⁴ as is depicted in **Figure 3.7**. The etching proceeds more quickly within this

meniscus region. During etching, a downward flow of AuCl_4^- occurs along the wire which results in a partial ion concentration gradient that decelerates the etching of the lower portion of the wire. This leads into the necking of the wire near the meniscus as shown in **Figure 3.7**.⁷¹

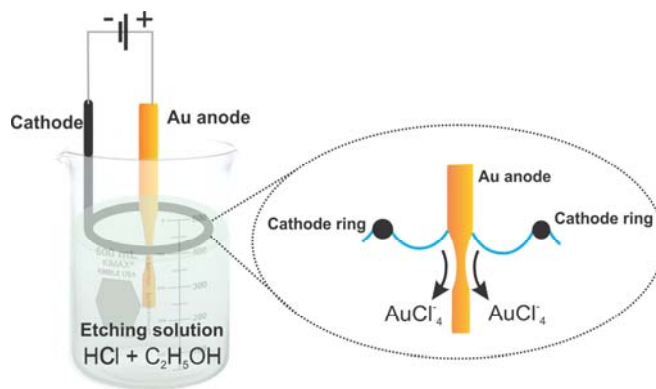
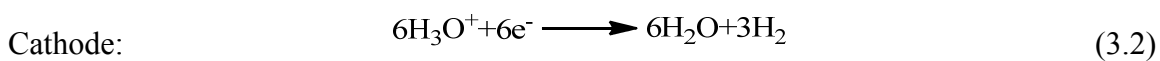
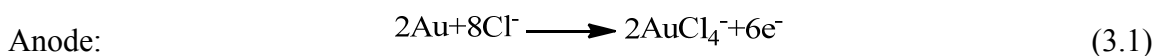


Figure 3.7 The schematic diagram of the etching process for fabricating the gold tips. The gold wire is immersed through a floating cathode ring into the etching solution of HCl and ethanol. The anode (gold wire) and the cathode ring are connected to an AC/DC current supply.

The mechanism of etching, which leads to dissolving of gold in concentrated HCl is shown in the following half cell reactions:



Near the interface between the gold wire and the etching solution, the half reactions in anode results in consumption of a large amount and the depletion of Cl^- . Simultaneously, gold oxides will be formed on the wire, which passivates the gold surface and decreases the reaction current consequently. However, more Cl^- migrates from the bulk solution towards the gold wire, which enforces the dissolution of gold oxide as AuCl_4^- . This would expose the bare gold surface to HCl and thus increases the reaction current. For this reason the reaction current shows periodic changes upon the etching process. As the

etching proceeds, the gold wire becomes thinner at a position below the meniscus until it breaks and the lower part of the wire falls down. The voltage should be shut off at this point.

Fabrication of ideal TERS tip requires that a proper voltage is applied to the etching reaction. Proper voltage causes a stable reaction current oscillation and higher etching quality. Ren *et al.*⁶⁵ proposed that a voltage more positive than 1.4 V with respect to a standard calomel electrode should be applied. Nevertheless, higher voltages would accelerate the reaction rates and lead to formation of O₂ and Cl₂ side products. Gaseous species cause bubbling which roughens the surface of the tip. Addition of ethanol however, decreases the chance of bubbling⁷⁰ because of the ethanol's low surface tension (22.27 mN/m, for water this value is 71.97 mN/m) and results in formation of smoother gold surfaces.⁷²

It should be noted that the utilization of a metal ring as counter electrode may cause some technical problems during the etching process.⁷⁰ If AC voltage with frequencies higher than 1 kHz is used, porous by-products will cover the ring as the etching precedes which contaminates the tip. AC voltages with frequencies as low as 10 Hz should be applied to avoid this problem.⁶⁸ If the ring is placed inside the etching solution, it also produces bubbles which may deform the shape of the tip. For this reason the ring should be kept on the surface to help the bubbles evaporate into the air.⁶⁸ In addition, the position of the ring with respect to the wire may result in asymmetric etched tip. For the reason of these difficulties, some researchers conduct the etching reaction in absence of any cathode ring. Richards *et al.*⁷⁰ position the gold nanowire inside the etching solution in the center of a bottomless beaker with holes on its walls to ensure an even distribution of ion flow during the etching.

For silver tips two main etching methods are usually used. In the first method, the 0.25 mm diameter silver wire is immersed by 6 mm in 10-35% aqueous ammonia electrolyte and a stainless steel plate is utilized as counter electrode. Etching reaction occurs when a current flows through the electrolyte. No metal rings are required in this method. Here the silver wire is manually removed with a 0.2 mm/min steps to form a cone on the body of

the wire. After 10 min the removal is stopped and the etching continues until the lower part of the silver wire inside the etching solution drops. Tip apex radius of 50-100 nm can be achieved by this method.⁷³ In the second method, 60% aqueous solution of perchloric acid and ethanol (1:2 V/V) mixture is used. The silver wire is immersed at the centre of a silver ring that acts as cathode and as soon as a voltage of 1.5 V is applied the etching reaction would begin. The apex size in this method ranges from 50 to 100 nm too.⁷⁴

The electrochemical etching of the tips can be performed by using alternating (AC) or direct current (DC).^{65,67,69,70,75-77} When DC voltage is applied, the electrochemical potential gradient around the tip controls the etching process through controlling the ionic motion of the electrolyte. Under DC voltage, mass transfer from the vicinity of the tip is controlled by convection and electrochemical potential gradient such as diffusion and migration.⁷⁸ This process can however be haphazard and slow and therefore, sharpening of the tip may not necessarily occur in a clear and directional manner. On the contrary, under AC voltage a bubble will form during one half cycle which will be directionally forced upward by buoyancy. The etching rate is indeed controlled by the flow of this driving stream which removes the etched material from the vicinity of the tip. As opposed to normal etching where the bubble flow moves towards the tip shank, the flow moves away from the etched part of the tip which provides better conditions for formation of the tip. The presence of this bubbling flow has been evidenced through optical microscopy.⁷⁹ Nevertheless, when gold rings are used, AC voltages can be problematic due to the potential etching of the ring.⁷⁰

SEM image of a gold tip fabricated through AC and DC electrochemical etching of gold nanowires done by Marion Bouchet, a former member in our research group, is presented in **Figure 3.8**. The gold tip produced through applying 2.4 V AC voltage with 3 kHz frequency and 70 μ sec/impulsion pulse rates is shown in **Figure 3.8a**. The method however yielded low reproducibility. Electrochemical etching of a gold wires using 2.4 V DC voltage resulted in fabrication of gold tip similar to the one shown in **Figure 3.8b** with good reproducibility. (1:1 V/V) mixture of HCl (37%) and ethanol (96%) was utilized as the etching solution in these series of experiments.

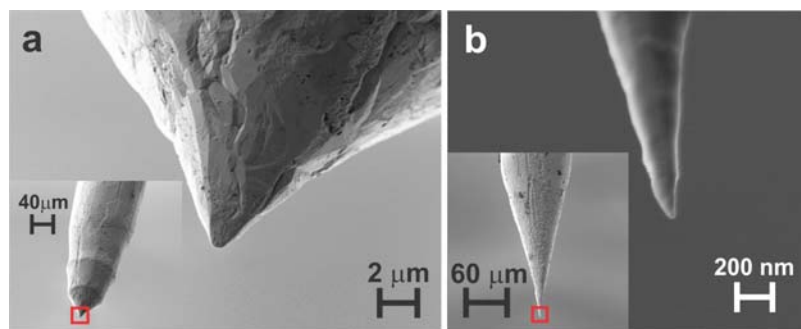


Figure 3.8 SEM image of gold tip etched inside the etching solution of (1:1 V/V) HCl and ethanol using (a) DC and (b) AC voltage

Despite the fact that the etching process could be controlled through optimizing the voltage and etchant mixture, it is not easy to combine these tips with the commercial AFM microscopes. The etched tip should be mounted to a tuning fork or dither piezoelectric in a way that the total added mass of the tip and the glue is minimal. Additional mass could potentially cause damping of the tuning fork (or dither piezoelectric) resonance frequency and influence the maintenance of the feedback sensitivity.⁷⁴ Electron beam induced vapor deposition or sputtering of metal onto the commercially available AFM tips is a widely used alternative for fabrication of TERS active tips, which will be described in the following section.

3.2.3.2 Metal Vapor Deposition

Using this approach metal islands are created on the tip through thermal evaporation of the metal, which is induced by an electron beam inside a vacuum chamber.⁴⁰ Metal islands are essential for creating the proper hotspots at tip apex, which are necessary for TERS activity. Nevertheless, it has been shown that the presence of one metallic grain on the tip end may not guarantee the TERS activity and a cluster of nanoparticles might be necessary.⁴⁶ However, if the cluster is too large it would have negative effects on the resolution of the TERS measurements even though the tips are TERS active. As a result there should be a balance between the thickness of the evaporated metal and the effort to get metallic islands at the tip end. 30 nm thicknesses have repeatedly resulted in good

yield of producing active probes with proper apex sizes of sub-50 nm.⁸⁰⁻⁸³ The deposition rate however should be experimentally tuned in accordance with the deposition conditions and more specifically the distance between the metal source and the tip inside the deposition chamber. This is because the source temperature could have a significant effect on morphology and quality of the resulting film through inducing annealing of the coating.

In the current thesis, electron beam vapor deposition was utilized to coat the non-contact tapping mode AFM probes with gold or silver. The vapor deposition was done in the nanofabrication laboratory at the university of western Ontario. The coating of the tips was conducted by electron beam induced thermal vapor deposition of around 5 nm titanium used as an adhesion layer followed by 30 nm of gold or silver inside a vacuum chamber. The deposition rate was set to 0.1 Å/sec to acquire a homogeneous layer of metallic grains .

Figure 3.9 shows the SEM images of the resulting coated tips.

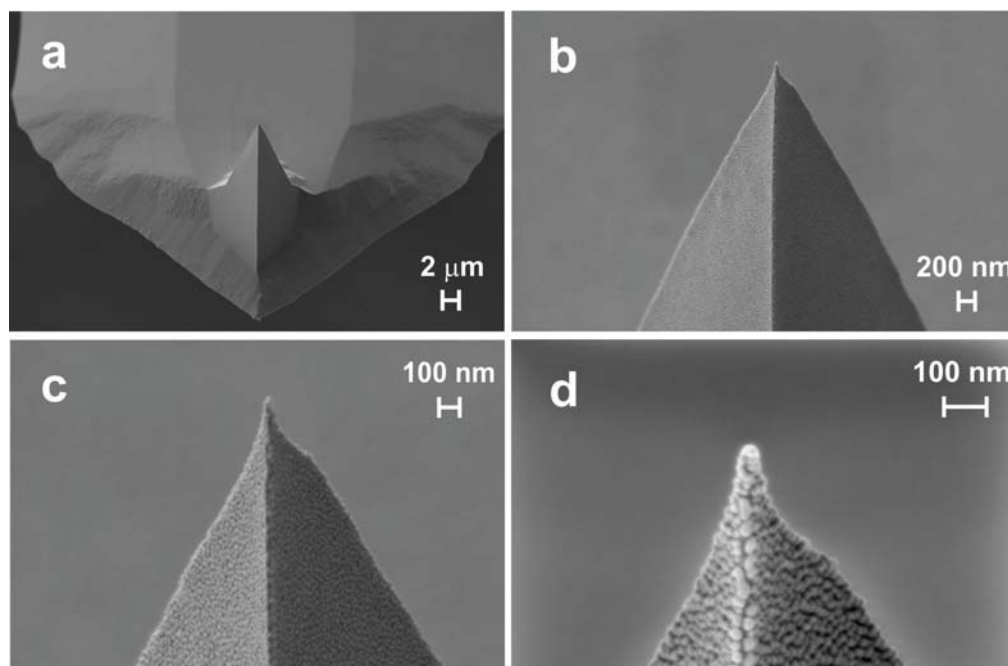


Figure 3.9 SEM images of silver coated silicon tips (NCL tapping mode tips, NanoWorldTM). The coated layer includes 5 nm of titanium and 30 nm of silver. (a)-(d) present different magnification of the same image. A metal island of around 30 nm diameters is formed at the tip apex as presented in (d).

As shown in **Figure 3.9d**, thermal vapor deposition provides a single silver island at the tip apex when optimized deposition conditions are applied. The silver grain size at the tip apex has a diameter of around 30 nm.

Typically one out of every five tips that got metal coated for the TERS measurements of this thesis exhibited TERS activity. This is despite the fact that they are all prepared simultaneously and under the same conditions. The yield is however acceptable when compared to the previously reported results in literature.^{46,62,84,85}

3.2.3.3 Advanced Fabrication methods

There are some alternative techniques to electrochemical etching and vapor deposition. One of these methods includes attaching a gold nanoparticle to the end of an AFM tip and further tailoring of the particle by ion beam milling.^{86,87} Bow-tie antennas^{88,89} and tip-on-aperture techniques^{90,91} are developed based on this method, however, they are expensive and time consuming and hence not practical.⁷⁰ SEM images of these two tips are presented in **Figure 3.10**.

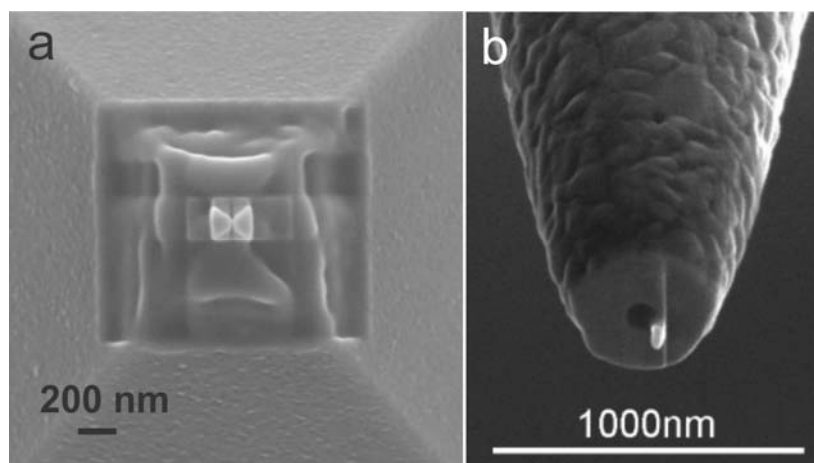


Figure 3.10 (a) Top view SEM image of bow-tie optical antenna at the apex of an AFM tip. The image is obtained from reference 89 with permission from American Physical Society.⁸⁸ (b) Side view SEM image of a tip-on aperture nanoantenna. The image is obtained from reference 92 with permission from American Chemical Society.⁹¹

In a different method, colloidal particles as isolated metal islands are formed at the tip apex through immersing the tip inside a colloidal solution of the metal.^{92,93} A nanoparticle of diameter in range of 20-80 nm is deposited onto the tip apex. Enhancement of the Raman signal in using the mentioned tips were evaluated by TERS study of Rhodamine 6G⁹³ and p-aminothiophenol monolayer adsorbed on 20 nm silver thick films.⁹² In general, picking and attaching the nanoparticle to the tip makes the fabrication method challenging.

Sculpturing the metal nanowires by focused ion beam (FIB) milling is also an alternative method for fabrication of smooth tips;⁹⁴ however the method is slow and costly and could result in unwanted ion implantation.⁹⁵ An example of FIB fabricated tips is illustrated in **Figure 3.11a**.

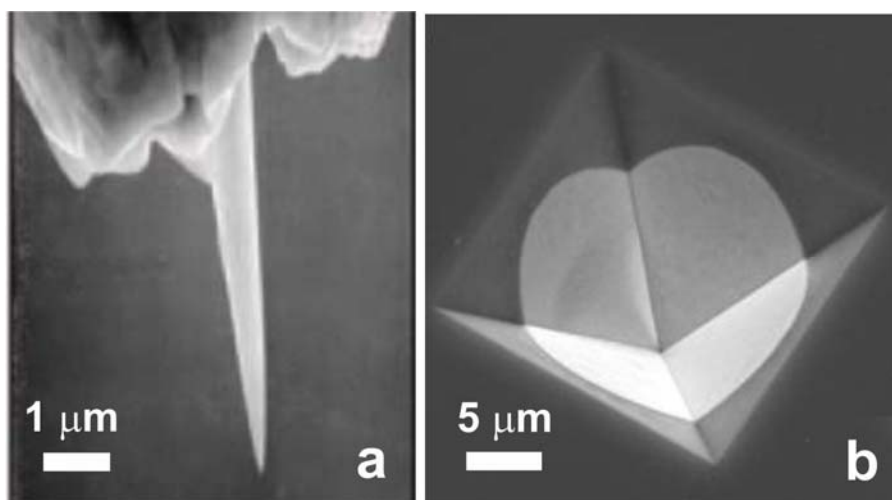


Figure 3.11 (a) SEM image of a TERS gold tip fabricated by focused ion beam (FIB) method. The image is obtained from reference 95 with permission from Annual Reviews.⁹⁴ (b) SEM image of a template-stripped gold tip. The image is obtained from reference 97 with permission from American Chemical Society.⁹⁶

Template-stripped gold pyramids are another way for fabricating TERS tips with sub-20 nm resolution.⁹⁶ The template basis of the method enables mass production of uniform tips. Using a 100 nm thick Si₃N₄ mask on a silicon wafer, large openings (tens of μm's) are created in the silicon nitride with standard photolithography exposure, development and etching. This opening defines the area of further etching in silicon. A subsequent

chemical etch in potassium hydroxide creates inverted pyramids.⁹⁷ Coating the inside of the inverted pyramid by thin metals layer produces pyramidal tip apexes of sub-10 nm diameter and 70.52° opening angle. The pyramids are then attached to a thin tungsten wire to be used in AFM setups. A sample SEM image of these tips is shown in **Figure 3.11b**.

3.2.4 Reproducibility and Lifetime of TERS tip

Chemical degradations such as oxidation or adsorption of molecules or mechanical wear damages are two main sources that limit the lifetime of the TERS tips. Chemical degradation is usually caused through reaction of ambient gases with the metal coating of the tip. For example, silver coated tips are very reactive under ambient condition due to their reaction with the oxygen and sulphur from atmosphere. Formation of oxides and sulphides on the silver layer alters the plasmon resonance which results in the loss of the enhancing properties within 24 h after the coating process.⁹⁸ Gold tips have longer lifetimes and could remain active for weeks; however, due to higher absorption they exhibit less enhancement of electric field in visible light range. To avoid chemical degradations, all the coated tips (silver or gold) used in current thesis were used within 24 h of preparation. In addition, after removal of the coated tips from the deposition chamber, the tips were stored in desiccators that were purged with nitrogen to minimize contact with more reactive ambient gases.

Mechanical wear damages are typically caused upon usage and result in removal of the metal coating from the tip apex.⁹⁸ Mechanical degradations can significantly alter the shape of the tip apex. An example is shown in **Figure 3.12**.

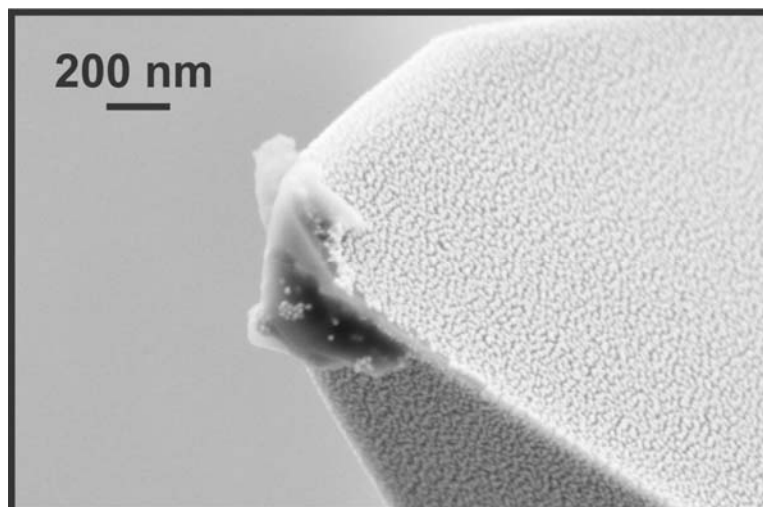


Figure 3.12 Mechanical damage of the silver coating layer after several scans with non-optimized feedback parameters

The peeling of the metallic coat is usually due to the fact that the coating does not stick properly to the tip which results in the loss of sensitivity in TERS tip after conducting a few scans. Mechanical resistance of the tips could be enhanced upon coating with an additional thin layer of alumina or silicon oxide as reported in literature.⁹⁹ However such protective layer may be detrimental to local enhancement as it will be discussed in chapter 4.

To decrease the chance of mechanical damages in the current thesis, AFM scans were conducted using certain parameters which minimize the tip-sample interaction. The AFM scan prior to TERS measurements were performed with low scan rates (~ 0.2 Hz/line) and low driving forces. Since these settings typically have negative influence on the resolution of the acquired AFM scans, higher quality AFM images were in some cases collected after the TERS measurements were completed. Overall, the TERS parameters must be adapted to the type of sample under investigation and spatial resolution may be affected by the type of sample as much as the type of tip used.

It is also noteworthy that pollution of the tip during scanning can lead to artifacts in AFM and Raman imaging and therefore, must be avoided. These artifacts are usually caused through picking up a piece of the sample by the tip upon scanning. Clearly, a

contaminated tip will result in observation of Raman spectra that do not correspond to the probed spot on the sample. To avoid misinterpretation of the Raman spectra, a single spectrum should be acquired on a clean spot where no sample is present.

3.3 Laser Polarization

The dominant contribution towards the enhancement in tip-enhanced Raman spectroscopy arises from a large enhancements in electric field strengths, as the external electromagnetic field couples to localized surface plasmon resonance (LSPR) of the metal tip with dimensions smaller than the wavelength of the light.¹⁰⁰ The enhancement magnitude meanwhile, depends strongly on the polarization of the incident laser with respect to the tip axis.^{43,49} In a light source such as laser beam, the electric field, \vec{E} , and magnetic field, \vec{H} , oscillate perpendicular to each other and perpendicular to the propagation direction, \vec{k} . Electric field interactions with the TERS tip in backscattering configuration are summarized in **Figure 3.13** for both a transverse mode and a radially polarized mode of light.

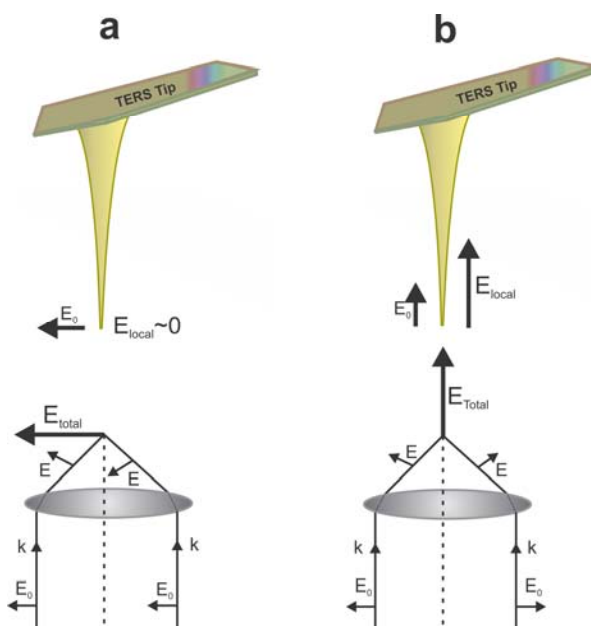


Figure 3.13 (a) Interaction between a metalized tip and Gaussian transverse polarized mode creates no component along the tip axis (b) interaction between a metalized tip and radially polarized mode generates a field component along the tip axis

When a transversely polarized laser is focused using low numerical aperture microscope objectives, the output laser is approximately a Gaussian beam with electric and magnetic field transverse to the propagation direction. By using high numerical aperture objectives, the focus is tight and limited by the diffraction limit to about $\lambda/2$ and the resulting electric field predominantly keeps original transverse polarization. However, a more careful observation of the individual polarization components of the focused electric field shows some weaker components polarized along the tip axis and along the propagation direction. As developed in Chapter 4, these z components localized in two main lobes around the tip are weak but can be used effectively to enhance the field at the apex of the tip as long as the tip is located in one of these two lobes. However, since most of the electric field component are polarized transversally, it will drive the free electron of the metal tip from left to right (**Figure 3.13a**) resulting in a net field close to zero at the center of the tip apex.¹⁰¹ In this case, diametrically opposed points on the tip surface have opposite charges and the apex of the tip remains uncharged and no field enhancement would occur.¹⁰² In the present thesis, whenever a linearly polarized light has been utilized, the TERS tip has been located inside one of the two charge accumulation lobes located at the opposite sides of the tip. The detailed description of the two charge density lobes is discussed in Chapter 4 of this thesis.

3.3.1 Experimental Setup to Generate Radial Polarization

Several approaches have been used to generate a radially polarized mode. Quabis *et al.*¹⁰³ used four segmented half waveplates to generate a radially polarized beam. Each of these four half waveplates are orientated in a way that their optical axis rotates the incoming electric field to the points in the radial direction. Saito *et al.*¹⁰⁰ employed a radial waveplate which was made by orienting eight segmented half waveplates with optical axes in different directions in order to generate radial polarization. These approaches however, suffer from the complexity of fabrication including the cutting and assembly of the waveplate segments. More importantly, the resulting waveplate is effective at a single wavelength which restricts the application of the setup. Recently a liquid crystal (LC) modulator was developed (ArcoptixTM, Switzerland) to generate a radially polarized beam that can be tuned for a wide range of wavelengths between 350 to 1700 nm. The general configuration of LC modulators is shown in **Figure 3.14**. LC modulators consist of a polarization convertor (θ -cell), a phase compensator that allows $\lambda/2$ phase step between the upper and the lower half of the θ -cell and

a twisted nematic cell to rotate the entrance polarization by 90° and permit to switch between the azimuthal and the radial polarization for the output light (**Figure 3.14**).

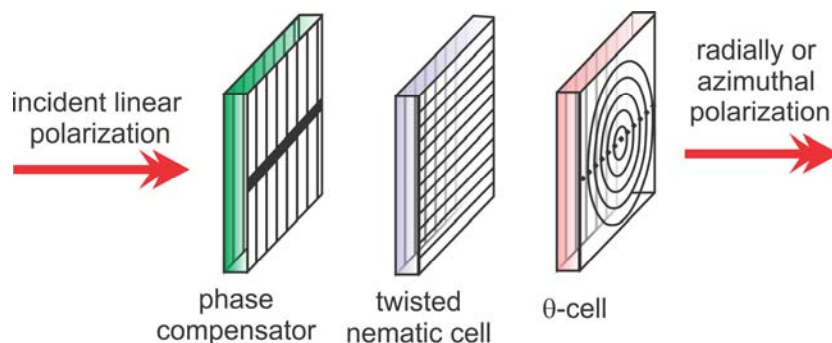


Figure 3.14 Liquid crystal polarization modulator configurations. Linearly polarized light enters from the left first into the phase compensator. The electric field vectors might be rotated by the nematic cell and the light will exit with a radially or azimuthally polarization from the θ -cell.

The top half of the phase compensator (black line across the phase compensator in **Figure 3.14**) has an electrode that permits changing of the inclination angle of its liquid crystal molecules, which changes its extraordinary refraction index. By applying a bias on the electrode the retardance is reduced compared to the bottom half where the retardance stays constant. As a result, the light phase in lower half of the compensator is different from the upper half by a $\lambda/2$ step.

The function of the twisted nematic is also based on the precisely controlled realignment of liquid crystal molecules between different ordered molecular configurations under the action of operating voltages. When the nematic cell is switched off, light does not experience any polarization rotation. A switched-on nematic cell however, rotates the polarization by 90° angle.¹⁰⁴

In θ -cell, the entrance and the exit plates are linearly and circularly rubbed, respectively, and the cell axis is at the direction of the linearly rubbed entrance plate (see θ -cell in **Figure 3.14**). A linearly polarized beam that enters the θ -cell has an electric field parallel or perpendicular to the cell axis. The polarization conversion for each of the two inputs is summarized in **Figure 3.15**. Light with polarization perpendicular to the cell axis will be

radially polarized when it exits the cell (**Figure 3.15a**).¹⁰⁵ If the polarization of the input light is parallel to the cell axis, the output light will be azimuthally polarized (**Figure 3.15b**).

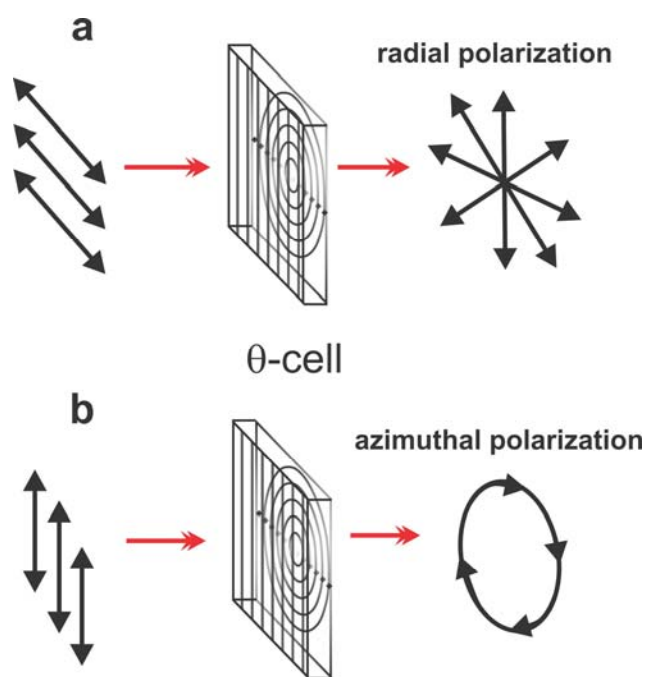


Figure 3.15 (a) radially (b) azimuthally polarized light generated by θ -cell.

The experimental setup used in this thesis to generate radial and azimuthal polarization consists in the following elements. A liquid crystal convertor along with other optical elements such as mirrors, pinholes, lenses and optical spatial filters are utilized. An optical spatial filter is a combination of a microscope objective and a pinhole. The relative position of the objective and the pinhole should be optimized to create a homogeneous Gaussian and parallel beam. Any convergence or divergence of the laser beam must be corrected in the light path. A pair of converging and diverging lenses (convex and concave lenses) is utilized to downsize the beam diameter by a factor of two. Smaller beam cross sections are more easily matched with the entrance aperture of high numerical aperture microscope objectives in TERS setup. Adjustable diaphragms are used to homogenize the beam by cutting out the interferences of back reflected light from the various optical elements. Additional lenses and pinholes might be necessary in order to minimize the size of the beam diameter before it enters the microscope. A CCD camera can be used to evaluate the quality of the laser beam during installation of the setup. An optical image of the radially polarized output of the above setup at the CCD camera and also at the focal point of 1.4 numerical aperture

oil immersion objective is presented in **Figure 3.16**. These images correspond to a radially polarized 632.8 nm red laser (**Figure 3.16a** and **c**) and 532 nm green laser (**Figure 3.16b** and **d**).

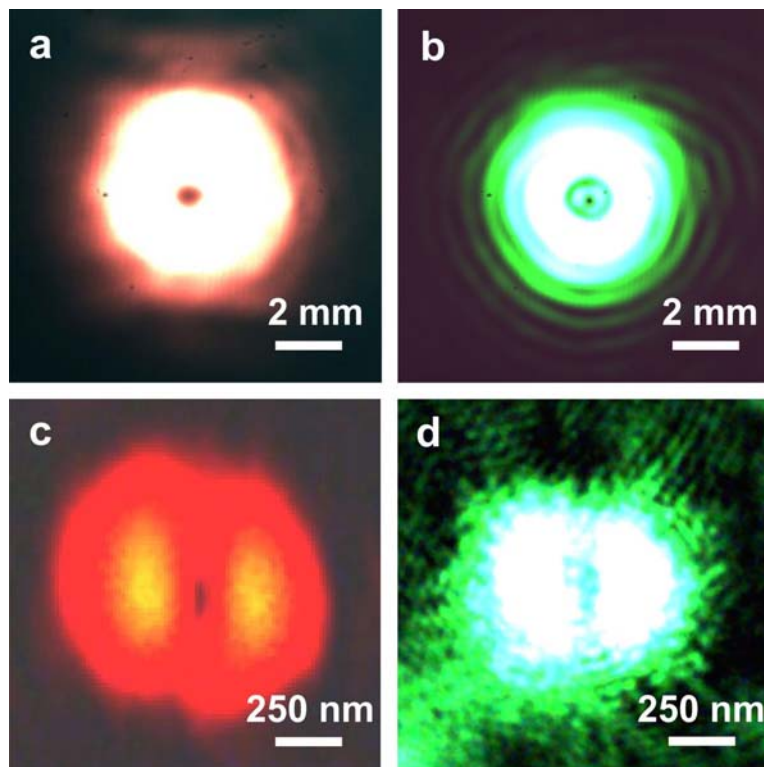


Figure 3.16 Radially polarized (a) 632.8 nm laser projected at a CCD camera before reaching the microscope objective (b) 532 nm laser projected at a CCD camera before reaching the microscope objective (c) 632.8 nm laser focused by a x100 oil immersion objective with $N.A.=1.4$ (d) 532 nm laser focused by a x100 oil immersion objective with $N.A.=1.4$

As shown in **Figure 3.16c** and **d**, a high numerical aperture microscope objective could decrease the beam diameter at focal point to around $1\ \mu\text{m}$. Imperfections in the shape of the beam (more specifically in **Figure 3.16d**) is due to phase imperfections caused by the multiple optical elements located on the optical path. It is noteworthy that the middle part of the doughnut which appears black in **Figure 3.16c** (dark in **Figure 3.16d**) contains the z component of the polarization. Although the intensity of this component is less than the xy components (bright areas in same image), it would get magnified by several orders of magnitude once the TERS tip interacts with the center of this doughnut mode.

3.3.2 Polarization Sensitive Raman Spectroscopy Experiment

Focusing a radially polarized light by a high numerical aperture microscope objective generates a polarization component in z direction. Meanwhile, azimuthally polarized light would only have polarization components in xy plane. As a result, performance of the LC polarization modulator in generating radial and azimuthal polarization can be evaluated through z polarization sensitive Raman spectroscopy. Z polarization sensitive Raman components are barely detectable in conventional measurements by linearly polarized laser due to the absence of significant polarization component in z direction at the focal point.¹⁰⁰

For z polarization sensitive Raman measurements, α -quartz plate¹⁰⁰ was utilized as a test sample. α -quartz is a piezoelectric crystal with D_3 symmetry. Group theory predicts 27 normal modes for this symmetry group from which four would be totally symmetric (A_1 modes) and eight would be doubly generate (E modes). Four A_2 modes are infrared-active. The remaining three are acoustic modes. E modes are simultaneously infrared and Raman active with peak frequency and intensities proportional to the sample orientation with respect to the laser polarization. Out of 27 normal modes, two A_1 and two E modes are typically detectable by Raman in the UV-visible region.¹⁰⁰ the Raman tensor for these modes has the following forms:¹⁰⁶

$$\begin{array}{ccc}
 A_1 & E_x & E_y \\
 \begin{bmatrix} a & 0 & 0 \\ 0 & a & 0 \\ 0 & 0 & b \end{bmatrix} & \begin{bmatrix} c & 0 & 0 \\ 0 & -c & d \\ 0 & d & 0 \end{bmatrix} & \begin{bmatrix} 0 & -c & -d \\ -c & 0 & 0 \\ -d & 0 & 0 \end{bmatrix}
 \end{array} \quad (3.3)$$

Incident polarization in z direction influences the tensor components $\alpha_{zx}(E_y)$, $\alpha_{zy}(E_x)$ and $\alpha_{zz}(A_1)$. On the other hand, the expected Raman signal intensity of each vibrational mode is determined by the multiplication of three factors: the incident light intensities, the corresponding Raman tensors and the detection efficiencies.¹⁰⁷ Therefore, the three Raman modes would have different intensities due to various contributions from z component and a difference in detection efficiencies between α_{zx} , α_{zy} and α_{zz} . For

example, A_I is the most intense Raman peak of α -quartz at 464 cm^{-1} while the peaks at 359 cm^{-1} , 394 cm^{-1} and 450 cm^{-1} with contribution from α_{zz} , α_{zx} and α_{zy} , respectively, have much lower intensities. For the current measurements, z -cut α -quartz sourced from AGopticsTM, was polished to a size of $20\times 20\text{ mm}^2$ with a thickness of $200\text{ }\mu\text{m}$. In z -cut crystals, the z axis of the crystal is along the thickness of the plate. The sample was mounted on the sample stage in a way that the z axis of the crystal was parallel to the propagation direction of the incident light. To collect the Raman signal of the α -quartz, $\lambda=632.8\text{ nm}$ He-Ne laser was used as the excitation source. The sample was set on a xy piezoelectric stage above a x60 water-immersion microscope objective with $N.A.=1.20$ which also collected the back-scattered light. The signal was guided to a spectrometer equipped with 600 gr/mm grating and was detected using a liquid nitrogen-cooled CCD detector.

The pure z polarization components of the Raman spectra of α -quartz can be extracted from polarized Raman measurements. On the basis of the calculations done by Y. Saito *et.al.*,¹⁰⁰ the Raman intensity generated by a radially polarized light, contains 36% transverse polarization contribution (I_x+I_y) at the focal point, which should be removed from the Raman spectra to extract the contribution of the z polarization components. This is based on the fact that Raman intensities are proportional to the intensity of the incident light. The values for I_x and I_y which are the incident light polarization intensities at the sample plane can be found in reference 109 (Kano *et. al.*).¹⁰⁸

To experimentally extract the z component contribution, the Raman spectrum of α -quartz was obtained through illumination by azimuthally polarized light. 36% of the Raman intensities in the collected spectra were subtracted from the Raman spectrum collected after illuminating the α -quartz by radially polarized light. **Figure 3.17a** shows the Raman spectra of α -quartz obtained with radially and azimuthally polarized laser. The spectrum in **Figure 3.17b** shows the z component contribution. The results of **Figure 3.17** are in good agreement with previously published studies on polarization sensitive Raman allowing one to confirm that the setup developed is functioning well with an efficient radially polarized beam.

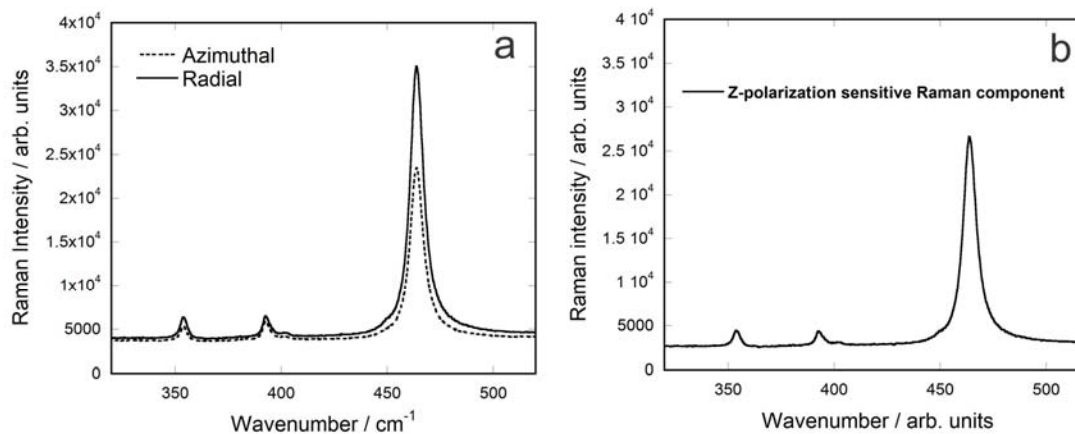


Figure 3.17 (a) Raman spectra of the α -quartz obtained with radially and azimuthally polarized laser (b) z component of α -quartz Raman spectra

3.4 TERS Experimental Procedure

To conduct TERS measurements in the described TERS setup, the sample should be deposited onto a transparent substrate which also does not absorb significantly the Raman excitation laser used for the study. Thin glass or amorphous quartz cover slips are generally ideal for this purpose due to their compatibility with high numerical aperture oil immersion objectives. The sample should be deposited on the substrate in a way that it is facing upwards. This is the only way that the TERS tip approaching from above could sense the sample surface in bottom illumination TERS configuration. The TERS procedure will be described in detail in the following sections.

3.4.1 Alignment of the TERS Tip to the Laser Focal Region

Since the enhancement of the Raman process in TERS originates from the local excitation of the surface plasmon at the tip apex, the tip must be perfectly centered with respect to the irradiation source. Consequently, it is essential to determine the position of the tip apex on the cantilever in order to align it with respect to the focal point of a tightly focused excitation laser. Two approaches can be used to perform such alignment that is summarized in the following sections.

3.4.1.1 Tip Alignment by Rayleigh Scattering Collection

In this method the TERS tip is scanned over the tightly focused Raman laser while it is in feedback with the sample surface. As the laser illuminates the tip it gets back-scattered. The back-scattered light gets collected by a photodiode which is connected to an input channel on the AFM controller box.¹⁰⁹ This generates an image of the cantilever similar to what is shown in **Figure 3.18**.

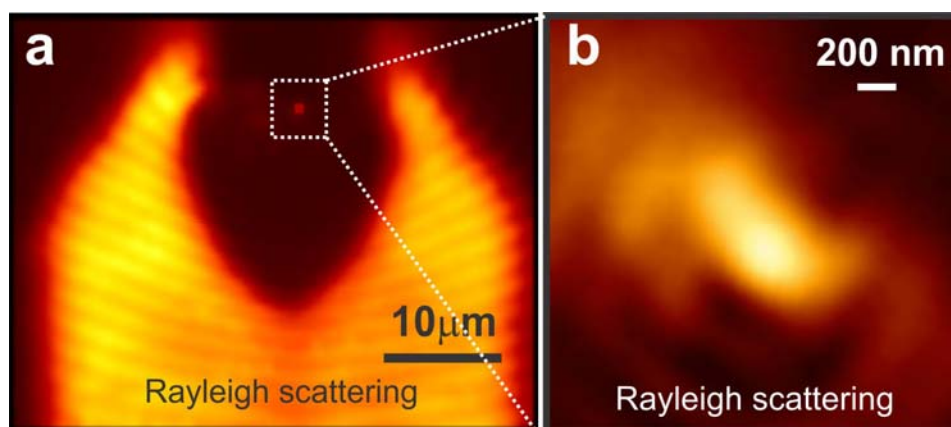


Figure 3.18 Tip alignment based on the collection of the Rayleigh scattering from the cantilever. (a) and (b) are images of an area around the tip apex proximity recorded with different zoom.

As it is shown in **Figure 3.18**, the tip apex position appears as a bright spot on the acquired image reflecting a higher scattering center. Smaller scan area and lower scan rate in general create images with better qualities where the tip apex position is estimated to be at the center of an area with 200 nm diameter (**Figure 3.18b**). It is noteworthy that this bright area indicates the coupling of near-field scatterings into the far-field. Hence, similar spots might be detected simultaneously from other positions on the cantilever that should not be mistaken for the tip position. Since the tip is typically located in a symmetrical distance from the edges of the cantilever, the optical images of a larger area on the cantilever, similar to the image in **Figure 3.18a**, should help to discriminate other bright spots from the tip location. Meanwhile, if the tip position is not determined correctly and it is mistaken by a second bright spot on the Rayleigh scattering image, no TERS activity will be observed.

3.4.1.2 Tip Alignment by Raman Spectra Collection

An alternative method for alignment of the tip with respect to the Raman laser is to collect the Raman spectra of the cantilever. In this method, the vertical deflection image of the cantilever is first collected, which shows the overall shape of the cantilever as well as the approximate tip position (**Figure 3.19a**). Once the rough position of the tip is found, Raman spectra of an area on the cantilever around the tip position are collected. The collected Raman spectra are then used to generate a Raman map of the cantilever (**Figure 3.19b**). The creation of the map is done through integration of the area below a characteristic peak in the Raman spectrum of the cantilever. For example for silicon tips the intense peak at 520 cm^{-1} , corresponding to the first optical phonon mode of silicon, is used. On this color coded map that indicates the variation of intensity of the 520 cm^{-1} mode, the position of the apex appears as a most intense pixel.

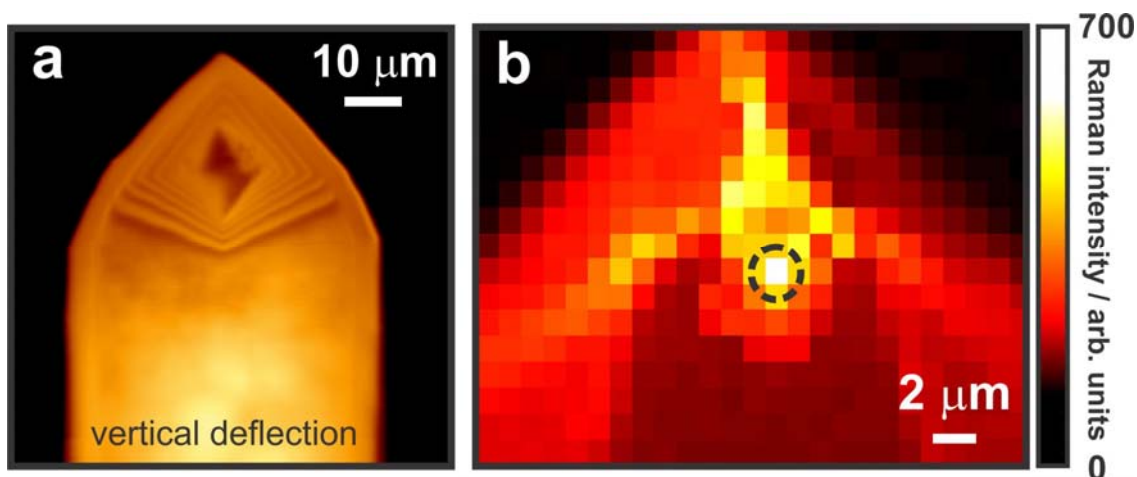


Figure 3.19 Tip alignment by Raman spectra collection (a) image of the cantilever generated by light reflection caused by vertical deflection of the tip upon interacting with the laser (b) Raman map generated by integrating the Raman intensity in the $[515-525]\text{cm}^{-1}$ spectral range. The pixel with the larger intensity indicates the tip location (indicated by a dashed circle in (b)).

This method is more time consuming compared to Rayleigh scattering alignment. However, for some probes such as the diamond tip used in Chapter 6 of this thesis, the tip

alignment is done based on the Raman map of the cantilever due to geometrical restrictions that limit the quality of the Rayleigh scattering image.

Once the tip apex is located, the cantilever is immobilized in the corresponding x and y positions while the z axis is still active to maintain a constant feedback between the tip and the sample. The sample is mounted on its own piezoelectric stage and is scanned to obtain the TERS spectra. It is noteworthy that during the alignment process, the position of the cantilever in z direction also gets optimized. For this purpose the thickness of the sample must be taken into account. If the thickness of the sample is more than 50 nm, the alignment process could not be done on the substrate because the z position of the tip during the TERS measurements on the sample surface would be different from the alignment process. For this reason, when working with thicker samples, tip alignment must be carried out on top of the sample surface. However, for thinner samples, doing the alignment on the sample surface or on the substrate should not cause a significant inaccuracy. Extra care should be taken to ensure that the cantilever position in xy direction does not alter during the experiment. For this reason, mechanical vibrations should be minimized in the room where the TERS measurements are being performed.

3.4.2 TERS Spectra Acquisition

Once tip alignment is performed, the first step of the TERS experiment will be to scan the surface of the sample by AFM. The AFM scans should be done with the proper settings and parameters that minimize the interaction between the tip and the sample. This will decrease the chance of damaging the tip coating or breaking the sharp end of the apex prior to the TERS measurements (see section 3.2.4).

After the AFM image is acquired, selected area or points on the surface can be investigated by TERS. For this purpose, the spot of interest moves to the apex position in a way that it is placed between the apex and the microscope objective inside the focal point of the Raman laser. As the laser reaches the tip, it gets intensified at the apex where the sample is placed few nanometers below it. The Raman scattering is then intensified inside the enhanced electric field and collected in back-reflection mode. Tip-enhanced Raman acquisition on an area over the sample surface creates a Raman image of that

particulate area with high surface sensitivity and high spatial resolution. An illustration for TERS mapping over the sample surface is shown in **Figure 3.20**.

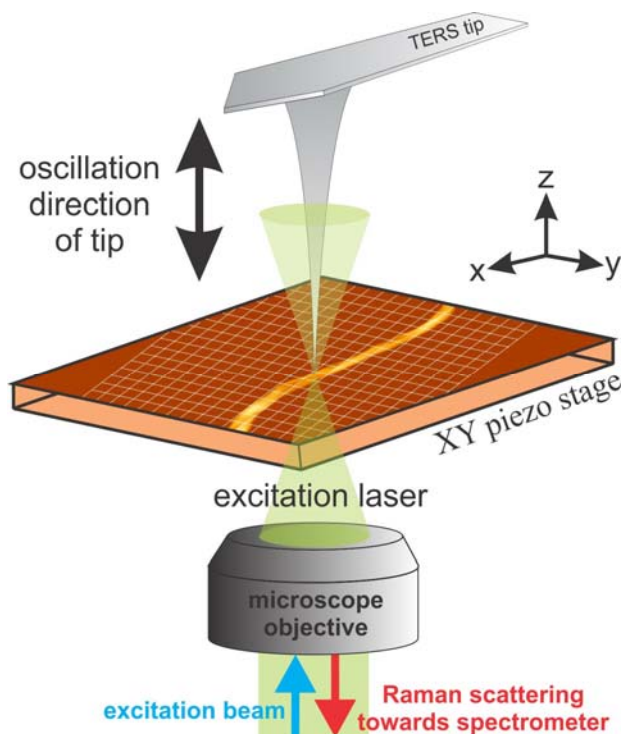


Figure 3.20 Illustration of TERS mapping process. After the AFM image of the sample is collected, an area over the surface will be mapped. The mapping area is divided into small pixels and a Raman spectrum will be collected from each pixel as it moves to the close proximity of the TERS tip apex. The mapped area is shown by a white dashed mesh in this figure.

3.4.3 General Considerations

To guarantee that the tip maintains its activity upon TERS measurements, the near-field nature of the observed Raman spectra must ideally be checked. As it was discussed in Chapter 2, the intensity of the enhanced signal should decrease as the tip-sample distance increases. Within a few nanometers distance from the surface the near-field contribution should rapidly vanish. Since the z position of the tip is well controlled, Raman measurements can be done for distinct tip-sample distances. This feature is suitable for tracking the signal decay.

More AFM scans of the sample can be performed by the same tip after the TERS measurements are finished. Since the nanoscale damages on the tip apex no longer cause a concern, scanning parameters can be optimized to acquire higher quality AFM images of the exact area, which is investigated by TERS. Under optimal conditions, the oscillation amplitude of the tip does not need to be minimal.

At the end of the measurements, a Raman spectrum should be obtained as the tip approaches a clean spot on the glass substrate. This is to guarantee that the tip is not contaminated by the sample. No Raman peaks should be observed in the acquired Raman spectrum at this stage.

Ideally the tip should be characterized by scanning electron microscopy to evaluate the quality of the coating and the apex condition. SEM imaging however, should be avoided prior to the TERS measurements. It is been reported in the literature that hydrocarbon contaminations that are formed on the surface in open air are usually present in the SEM chambers. Silicon oils from the diffusion pump and the grease of vacuum seals and fingerprints are other sources of impurity that might enter the chamber.¹¹⁰ These impurities will not be necessarily removed by ultra vacuum. During electron irradiation, hydrocarbon molecules are cracked and carbon double bonds are form. The double bond carbons undergo polymerization by cross-linking, and a carbon-rich contamination film grows over the tip coating which alters the plasmon resonance of the tip and therefore, should be avoided in TERS measurements.

3.5 Estimation of the Enhancement Factors in TERS

The enhancement factor (EF) of the electric field in TERS is the ratio between the electric field intensity in presence (E_{tip}) and absence (E_0) of the TERS tip:¹⁴

$$EF = \frac{E_{tip}}{E_0} \quad (3.4)$$

The total enhancement in TERS originates from the enhancement of the excitation laser and enhancement of the Raman scattered light. The enhancement factor for each source

will be $EF_{laser} = E_{tip}^{laser} / E_0^{laser}$ and $EF_{Raman} = E_{tip}^{Raman} / E_0^{Raman}$, respectively. E_{tip}^{laser} and E_{tip}^{Raman} are the incident and scattered electric field at the tip apex where E_0^{laser} and E_0^{Raman} are the incident and scattered electric field when the tip is absent.¹¹¹

On the other hand, light intensity is proportional to the square of the electric field strength. Therefore, the magnitude of the enhancement factor for excitation laser and Raman scattered light would be EF_{laser}^2 and EF_{Raman}^2 , respectively. As a result, the total enhancement in TERS would be:

$$EF_{TERS} = EF_{laser}^2 \times EF_{Raman}^2 \quad (3.5)$$

Equation (3.5) is especially useful to determine the enhancement factor obtained in numerical simulations.¹¹² To calculate the enhancement factor achieved in an experiment, two factors should be determined. On the one hand, the spectroscopic contrast C which is a comparison between the Raman peak intensities when the tip is in contact (in near-field of the sample) and the intensities when tip is retracted (in far-field of the sample). This contrast is often described as:⁴⁸

$$C = \frac{I_{nearfield}}{I_{farfield}} = \frac{I_{incontact} - I_{retracted}}{I_{retracted}} \quad (3.6)$$

The second factor is the geometry factor that is critical to evaluate the contributions of the far-field and near-field scattering volumes. Due to the relatively large dimensions of laser cross-section, even when high numerical objectives are used, the investigated area in far-field is much larger than the area that is illuminated by the tip in near-field. For this reason the difference between the illuminated volumes in near-field and far-field should be considered for the estimation of the experimental enhancement factor. In case of very thin samples the volume could be replaced with area of the illumination. The far-field scattering originate from the entire focal region of the laser therefore, $A_{farfield} = r_{laser}^2 \times \pi$ with r_{laser}^2 being the radius of the laser cross-section. The area from where the near-field signal arises can be estimated as $A_{nearfield} = r_{tip}^2 \times \pi$ with r_{tip}^2 being the radius of the tip.¹⁴

By considering the source volume, the enhancement factor of TERS can be defined through the following equation:

$$EF_{TERS} = C \frac{A_{farfield}}{A_{nearfield}} \quad (3.7)$$

A wide range of TERS enhancement factor from 10 to 10^8 has been reported in the literature so far.^{20,26,113,114} Nevertheless, for a reliable comparison of various experiments, the method used for calculation of the enhancement factor should be carefully considered. Since the Raman intensity varies with the scattering cross-section of the sample, this enhancement has to be considered with caution because it is sample dependent.

3.6 Determination of the Spatial Resolution

As mentioned earlier, one of the key strengths of TERS is the ability to provide high lateral resolution beyond the diffraction limit. One of the main experiments that can be conducted to evaluate the effectiveness of a given TERS tip is indeed to estimate the limit of resolution provided by each tip. To do this, the sample surface should be mapped along a few lines. Through mapping shorter lines, more spots can be scanned in a shorter time. In general, a long acquisition period increases the uncertainty of the acquired results due to the possibility of the tip or sample drifting.⁴⁸ Several points on each mapping line are defined in a way that, together with the separation between the lines, the spots separation remains under 10 nm in both x and y direction. A Raman spectrum is then collected from each spot. The intensity of an arbitrary Raman peak in the acquired spectra should then be considered. By averaging the peak intensity from corresponding pixels, a distribution peak similar to the Boltzmann distribution will be generated. Full width at half maximum height of such peak is typically taken as the resolution limit of the conducted measurement.¹¹¹ An example of this is presented in Chapter 5 where TERS measurements on single walled carbon nanotubes have been performed.

3.7 TERS Peak Assignment

TERS peaks are commonly compared to conventional Raman peaks; however, presence or absence of peaks as well as their intensities should be closely investigated. Although the positions of the Raman bands are usually similar in TERS and conventional Raman, the intensity of the individual bands can vary significantly.¹¹⁵

3.7.1 Polarization Considerations

The main consideration for interpretation of the observed peaks is related to the change in Raman selection rules due to the local polarization of the confined electric field. Local polarization components which occur upon tip-laser interaction are the source for observed alteration of the selection rules. For Raman modes that are sensitive to the polarization direction, depolarization of the light at the tip apex is an important source for intensity variation or sometimes absence of the peak in TERS spectra. Electric field gradient in Raman (EFGR) spectroscopy explains this phenomenon. Raman spectra of a sample that experiences a strong electric field gradient exhibit different selection rules and intensities as compared to regular Raman. This effect is more likely when a sample is placed near a metallic structure. In such a case where the electric field changes along the length of an atomic bond, the generated Raman signal depends on the polarizability times the field gradient rather than the polarizability times the field magnitude.¹¹⁶ Gradient field induced Raman requires that the vibration has a component along a direction where the electric field gradient is the largest. This the case for the z component of the electric field enhanced at the apex of the TERS tip.⁴³ Raman modes with components along the z direction should show a change of intensity as the tip-sample distance changes. Therefore, the vibration cross-section for these modes should be enhanced in accordance with the local strength of the z component of the electric field and should not be observed in far-field detection where the z component is absent.¹¹⁷

3.7.2 Tip Contamination

Tip contamination is also misleading for the interpretation of the TERS spectra. As mentioned in section 3.4.3, a control TERS spectrum should always be acquired on a

clean substrate after the TERS measurements are done. This would ensure that the tip has not picked up any molecules during the measurements.

3.7.3 Local Annealing and Heating

Since in TERS the laser is focused onto a very small area on the sample surface, it is very likely that the temperature increases within this area. This has been experimentally¹¹⁸⁻¹²² and numerically^{123,124} investigated. Sample heating could cause sample degradation and the appearance of Raman signal of carbon species. Raman spectra of carbon show two broad peaks at 1350 cm^{-1} (D band) and 1580 cm^{-1} (G band).^{7,125} However, the temporal, spatial and thermal extent of heating is not clear yet. Also, in contrast to conventional Raman microscopy, measurement of the anti-Stokes/Stokes scattering might not necessarily lead to a precise temperature control in TERS experiments. The reason for this is that the TERS enhancement might not be always the same for the Stokes and anti-Stokes measurements especially if they are measured in two separate steps and therefore the enhanced signals in two cases are not necessarily compatible.¹⁴ Overall, TERS measurements should be conducted with minimum laser intensity and short acquisition times to avoid possible thermal damages on the sample.

3.7.4 Other Sources of Misleading Peaks

For some specific samples there is often a broad band background in TERS spectra whose origin is not completely determined. Inelastic scattering from metallic tip and enhanced fluorescence and other plasmon dependent photoluminescence from the rough metal surface are among the potential origins of the mentioned background.⁷¹ As a source of misleading Raman peaks, two peaks in the range of $220\text{-}240\text{ cm}^{-1}$ are also reported and assigned to molecular oxygen chemisorbed on defect sites of silver coated tips.^{126,127}

3.8 Conclusion

In summary, combining scanning near-field optical microscopy with vibrational spectroscopy has provided a high spatial resolution along with spectroscopic fingerprints which makes TERS a unique method for investigating the nanoworld. Nevertheless, the

high resolution and sensitivity would not be guaranteed unless technical details are closely considered. Polarization of the excitation laser, the material of the metal tip, the nature of the environment surrounding the tip and the material underlying the metal coating along with experimental precautions considering the relative position of the tip-laser and tip-sample are among the factors that strongly influence the success of the any TERS measurement. Meanwhile, TERS still faces challenges with respect to the tip fabrication process. The magnitude and reproducibility of the enhancement, lateral resolution and the lifetime of the TERS tip are among the issues that remain problematic. A universal and inclusive application of the method suffers from the lack of reliable tip fabrication methods with the goal to increase the tip's TERS activity and the yield of tip-to-tip reproducibility. This low reproducibility restricts the direct comparison between the TERS studies that are performed in different research works unless the Raman contrast and the lateral resolution are considered. In addition, interpretation of the results requires careful assignment of the observed peaks, as it is discussed in section 3.7 of this Chapter. With this regard, a TERS database would be of great value; however the variability of the different TERS setup makes this possibility rather difficult. Despite all the challenges, TERS has shown great potential for chemical imaging of the surfaces of a large variety of the samples. If the measurements are conducted under the same condition using the same tip, quantitative experiments are also possible in TERS. The large enhancement of the Raman process, which is accessible in TERS explains several companies' efforts to build integrated TERS systems that are applicable for less experienced users. Horiba Scientific, Renishaw, Bruker, AIST-NT, NT-MDT and Nanonics are among these companies. The present research work in following Chapters is focused on the application of TERS in material and biomaterial research.

3.9 References

- (1) Sun, M.; Fang, Y.; Yang, Z.; Xu, H. *Phys. Chem. Chem. Phys.* **(2009)**, *11*, 9412.
- (2) Yang, Z.; Aizpurua, J.; Xu, H. *J. Raman Spectrosc.* **(2009)**, *40*, 1343.
- (3) Pettinger, B.; Domke, K. F.; Zhang, D.; Picardi, G.; Schuster, R. *Surf. Sci.* **(2009)**, *603*, 1335.

- (4) Pettinger, B.; Domke, K. F.; Zhang, D.; Schuster, R.; Ertl, G. *Phys. Rev. B* (2007), 76, 113409.
- (5) Zhang, W.; Yeo, B. S.; Schmid, T.; Zenobi, R. *J. Phys. Chem. C* (2007), 111, 1733.
- (6) Boehme, R.; Richter, M.; Cialla, D.; Roesch, P.; Deckert, V.; Popp, J. *J. Raman Spectrosc.* (2009), 40, 1452.
- (7) Domke, K. F.; Zhang, D.; Pettinger, B. *J. Am. Chem. Soc.* (2007), 129, 6708.
- (8) Hermann, P.; Fabian, H.; Naumann, D.; Hermelink, A. *J. Phys. Chem. C* (2011), 115, 24512.
- (9) Paulite, M.; Blum, C.; Schmid, T.; Opilik, L.; Eyer, K.; Walker, G. C.; Zenobi, R. *ACS Nano* (2013), 7, 911.
- (10) Hoppener, C.; Novotny, L. *Nanotechnol.* (2008), 19, 3840121.
- (11) Roy, D.; Williams, C. M.; Mingard, K. *J. Vac. Sci. Technol., B: Nanotechnol. Microelectron.: Mater., Process., Meas., Phenom.* (2010), 28, 631.
- (12) Eaton, P. J.; West, P. *Atomic force microscopy*; Oxford University Press New York, 2010.
- (13) Ichimura, T.; Fujii, S.; Verma, P.; Yano, T.; Inouye, Y.; Kawata, S. *Phys. Rev. Lett.* (2009), 102, 186101.
- (14) Stadler, J.; Schmid, T.; Zenobi, R. *Nanoscale* (2012), 4, 1856.
- (15) Seine, G.; Coratger, R.; Carladous, A.; Ajustron, F.; Pechou, R.; Beauvillain, J. *Phys. Rev. B* (1999), 60, 11045.
- (16) Sandoz, P.; Friedt, J. M.; Carry, E. *Rev. Sci. Instrum.* (2008), 79, 0861021.
- (17) Bosma, E.; Offerhaus, H. L.; van, d. V. J. T.; Segerink, F. B.; van, W. I. M. *Am. J. Phys.* (2010), 78, 562.
- (18) Lipiec, E.; Sekine, R.; Bielecki, J.; Kwiatek, W. M.; Wood, B. R. *Angew. Chem., Int. Ed.* (2014), 53, 169.
- (19) Verma, P.; Yamada, K.; Watanabe, H.; Inouye, Y.; Kawata, S. *Phys. Rev. B Condens. Matter Mater. Phys.* (2006), 73, 0454161.
- (20) Cancado, L. G.; Hartschuh, A.; Novotny, L. *J. Raman Spectrosc.* (2009), 40, 1420.
- (21) Yu, J.; Saito, Y.; Ichimura, T.; Kawata, S.; Verma, P. *Appl. Phys. Lett.* (2013), 102, 1231101.
- (22) Kharintsev, S. S.; Hoffmann, G. G.; Dorozhkin, P. S.; de With, G.; Loos, J. *Nanotechnol.* (2007), 18, 3155021.
- (23) Zhang, M.; Wang, J.; Tian, Q. *Opt. Express* (2013), 21, 9414.
- (24) Saito, Y.; Hayazawa, N.; Kataura, H.; Murakami, T.; Tsukagoshi, K.; Inouye, Y.; Kawata, S. *Chem. Phys. Lett.* (2005), 410, 136.
- (25) Neacsu, C. C.; van, A. B. B.; Fiebig, M.; Raschke, M. B. *Phys. Rev. B: Condens. Matter Mater. Phys.* (2009), 79, 1001071.

- (26) Pettinger, B.; Ren, B.; Picardi, G.; Schuster, R.; Ertl, G. *Phys. Rev. Lett.* (2004), 92, 0961011.
- (27) Stadler, J.; Schmid, T.; Zenobi, R. *Nano Lett.* (2010), 5, 1530.
- (28) Anderson, M. S.; Pike, W. T. *Rev. Sci. Instrum.* (2002), 73, 1198.
- (29) Mehtani, D.; Lee, N.; Hartschuh, R. D.; Kisliuk, A.; Foster, M. D.; Sokolov, A. P.; Maguire, J. F. *J. Raman Spectrosc.* (2005), 36, 1068.
- (30) Roth, R. M.; Panoiu, N. C.; Adams, M. M.; Osgood, R. M.; Neacsu, C. C.; Raschke, M. B. *Opt. Express* (2006), 14, 2921.
- (31) Saito, Y.; Motohashi, M.; Hayazawa, N.; Iyoki, M.; Kawata, S. *Appl. Phys. Lett.* (2006), 88, 1431091.
- (32) Berweger, S.; Raschke, M. B. *Anal. Bioanal. Chem.* (2010), 396, 115.
- (33) Nieman, L. T.; Krampert, G. M.; Martinez, R. E. *Rev. Sci. Instrum.* (2001), 72, 1691.
- (34) De, A. F.; Das, G.; Candeloro, P.; Patrini, M.; Galli, M.; Bek, A.; Lazzarino, M.; Maksymov, I.; Liberale, C.; Andreani, L. C.; Di, F. E. *Nat. Nanotechnol.* (2010), 5, 67.
- (35) Wang, P.; Zhang, D.; Li, L.; Li, Z.; Zhang, L.; Fang, Y. *Plasmonics* (2012), 7, 555.
- (36) Bek, A.; De Angelis, F.; Das, G.; Di Fabrizio, E.; Lazzarino, M. *Micron* (2011), 42, 313.
- (37) Chan, K. L. A.; Kazarian, S. G. *Nanotechnol.* (2011), 22, 175701.
- (38) Pettinger, B.; Picardi, G.; Schuster, R.; Ertl, G. *Single Mol.* (2002), 3, 285.
- (39) Deckert-Gaudig, T.; Deckert, V. *Small* (2009), 5, 432.
- (40) Rasmussen, A.; Deckert, V. *J. Raman Spectrosc.* (2006), 37, 311.
- (41) Wood Bayden, R.; Bailo, E.; Khiavi Mehdi, A.; Tilley, L.; Deed, S.; Deckert-Gaudig, T.; McNaughton, D.; Deckert, V. *Nano Lett.* (2011), 11, 1868.
- (42) Novotny, L.; Bian, R. X.; Xie, X. S. *Phys. Rev. Lett.* (1997), 79, 645.
- (43) Novotny, L.; Sanchez, E. J.; Xie, X. S. *Ultramicroscopy* (1998), 71, 21.
- (44) Steidtner, J.; Pettinger, B. *Phys. Rev. Lett.* (2008), 100, 236101.
- (45) Berweger, S.; Atkin, J. M.; Olmon, R. L.; Raschke, M. B. *J. Phys. Chem. Lett.* (2010), 1, 3427.
- (46) Asghari-Khiavi, M.; Wood, B. R.; Hojati-Talemi, P.; Downes, A.; McNaughton, D.; Mechler, A. *J. Raman Spectrosc.* (2012), 43, 173.
- (47) Stadler, J.; Oswald, B.; Schmid, T.; Zenobi, R. *J. Raman Spectrosc.* (2013), 44, 227.
- (48) Schmid, T.; Opilik, L.; Blum, C.; Zenobi, R. *Angew. Chem., Int. Ed.* (2013), 52, 5940.
- (49) Novotny, L. *Phys. Today* (2011), 64, 47.
- (50) Le Ru, E.; Etchegoin, P. *Principles of Surface-Enhanced Raman Spectroscopy: and related plasmonic effects*; Elsevier: New York, 2009.

- (51) Johnson, P. B.; Christy, R. W. *Phys. Rev. B* (1972), 6, 4370.
- (52) Rakic, A. D. *Appl. Opt.* (1995), 34, 4755.
- (53) Bohren, C. F.; Huffman, D. R. *Absorption and Scattering of Light by Small Particles*; John Wiley & Sons: New York, 1983.
- (54) Palik, E. D.; Ghosh, G. *Handbook of optical constants of solids* 2nd ed.; Academic press: London, 1998; Vol. II.
- (55) Taguchi, A.; Hayazawa, N.; Furusawa, K.; Ishitobi, H.; Kawata, S. *J. Raman Spectrosc.* (2009), 40, 1324.
- (56) Yang, Z.; Li, Q.; Fang, Y.; Sun, M. *Chem. Commun.* (2011), 47, 9131.
- (57) Kelly, K. L.; Coronado, E.; Zhao, L. L.; Schatz, G. C. *J. Phys. Chem. B* (2003), 107, 668.
- (58) Yeo, B.-S.; Zhang, W.; Vannier, C.; Zenobi, R. *Appl. Spectrosc.* (2006), 60, 1142.
- (59) Hayazawa, N.; Yano, T.-a.; Kawata, S. *J. Raman Spectrosc.* (2012), 43, 1177.
- (60) Cui, X.; Erni, D.; Zhang, W.; Zenobi, R. *Chem. Phys. Lett.* (2008), 453, 262.
- (61) Cui, X.; Zhang, W.; Yeo, B.-S.; Zenobi, R.; Hafner, C.; Erni, D. *Opt. Express* (2007), 15, 8309.
- (62) Deckert-Gaudig, T.; Deckert, V. *Phys. Chem. Chem. Phys.* (2010), 12, 12040.
- (63) Zhang, W.; Cui, X.; Martin, O. J. F. *J. Raman Spectrosc.* (2009), 40, 1338.
- (64) Bailo, E.; Deckert, V. *Chem. Soc. Rev.* (2008), 37, 921.
- (65) Ren, B.; Picardi, G.; Pettinger, B. *Rev. Sci. Instrum.* (2004), 75, 837.
- (66) Kharintsev, S. S.; Hoffmann, G. G.; Fishman, A. I.; Salakhov, M. K. *J. Phys. D: Appl. Phys.* (2013), 46, 145501.
- (67) Lopes, M.; Toury, T.; de La Chapelle, M. L.; Bonaccorso, F.; Gucciardi, P. G. *Rev. Sci. Instrum.* (2013), 84, 0737021.
- (68) Park, J.; Hong, T. S.; Lee, N. S.; Kim, K. B.; Seo, Y. *Curr. Appl. Phys.* (2011), 11, 1332.
- (69) Williams, C.; Roy, D. *J. Vac. Sci. Technol. B* (2008), 26, 1761.
- (70) Eligal, L.; Culfaz, F.; McCaughan, V.; Cade, N. I.; Richards, D. *Rev. Sci. Instrum.* (2009), 80, 0337011.
- (71) Neacsu, C. C.; Berweger, S.; Raschke, M. B. *NanoBiotechnol.* (2009), 3, 172.
- (72) Lehmann, V. In *Electrochemistry of Silicon: Instrumentation, Science, Materials and Applications*; Wiley-VCH: Weinheim, 2002; Vol. 1.
- (73) Dickmann, K.; Demming, F.; Jersch, J. *Rev. Sci. Instrum.* (1996), 67, 845.
- (74) Zhu, L.; Atesang, J.; Dudek, P.; Hecker, M.; Rinderknecht, J.; Ritz, Y.; Geisler, H.; Herr, U.; Geer, R.; Zschech, E. *Mater. Sci.-Pol.* (2007), 25, 19.
- (75) Gingery, D.; Buhlmann, P. *Rev. Sci. Instrum.* (2007), 78, 1137031.

- (76) Nicklaus, M.; Nauenheim, C.; Krayev, A.; Gavriluk, V.; Belyaev, A.; Ruediger, A. *Rev. Sci. Instrum.* **(2012)**, *83*, 0661021.
- (77) Xu, G.; Liu, Z.; Xu, K.; Zhang, Y.; Zhong, H.; Fan, Y.; Huang, Z. *Rev. Sci. Instrum.* **(2012)**, *83*, 1037081.
- (78) Fotino, M. *Rev. Sci. Instrum.* **(1993)**, *64*, 159.
- (79) Fotino, M. *Appl. Phys. Lett.* **(1992)**, *60*, 2935.
- (80) Bailo, E.; Deckert, V. *Angew. Chem., Int. Ed.* **(2008)**, *47*, 1658.
- (81) Schmid, T.; Burkhard, J.; Yeo, B.-S.; Zhang, W.; Zenobi, R. *Anal. Bioanal. Chem.* **(2008)**, *391*, 1899.
- (82) Stöckle, R. M.; Suh, Y. D.; Deckert, V.; Zenobi, R. *Chem. Phys. Lett.* **(2000)**, *318*, 131.
- (83) Watanabe, H.; Ishida, Y.; Hayazawa, N.; Inouye, Y.; Kawata, S. *Phys. Rev. B Condens. Matter Mater. Phys.* **(2004)**, *69*, 1554181.
- (84) Schmid, T.; Yeo, B. S.; Zhang, W.; Zenobi, R. In *Tip Enhancement*; Kawata, S., Shalaev, V. M., Eds.; Elsevier: Amsterdam, 2007.
- (85) Yeo, B.-S.; Schmid, T.; Zhang, W.; Zenobi, R. *Anal. Bioanal. Chem.* **(2007)**, *387*, 2655.
- (86) Gan, Y. *Rev. Sci. Instrum.* **(2007)**, *78*, 081101.
- (87) Kalkbrenner, T.; Ramstein, M.; Mlynek, J.; Sandoghdar, V. *J. Microsc.* **(2001)**, *202*, 72.
- (88) Farahani, J. N.; Pohl, D. W.; Eisler, H. J.; Hecht, B. *Phys. Rev. Lett.* **(2005)**, *95*, 0174021.
- (89) Weber-Bargioni, A.; Schwartzberg, A.; Schmidt, M.; Harteneck, B.; Ogletree, D. F.; Schuck, P. J.; Cabrini, S. *Nanotechnol.* **(2010)**, *21*, 0653061.
- (90) Frey, H. G.; Keilmann, F.; Kriele, A.; Guckenberger, R. *Appl. Phys. Lett.* **(2002)**, *81*, 5030.
- (91) Taminiau, T. H.; Moerland, R. J.; Segerink, F. B.; Kuipers, L.; van Hulst, N. F. *Nano Lett.* **(2007)**, *7*, 28.
- (92) Sinjab, F.; Lekprasert, B.; Woolley, R. A. J.; Roberts, C. J.; Tandler, S. J. B.; Nottingher, I. *Opt. Lett.* **(2012)**, *37*, 2256.
- (93) Wang, J. J.; Saito, Y.; Batchelder, D. N.; Kirkham, J.; Robinson, C.; Smith, D. A. *Appl. Phys. Lett.* **(2005)**, *86*, 263111.
- (94) Novotny, L.; Stranick, S. J. *Annu. Rev. Phys. Chem.* **(2006)**, *57*, 303.
- (95) Lindquist, N. C.; Nagpal, P.; McPeak, K. M.; Norris, D. J.; Oh, S.-H. *Rep. Prog. Phys.* **(2012)**, *75*, 0365011.
- (96) Johnson, T. W.; Lapin, Z. J.; Beams, R.; Lindquist, N. C.; Rodrigo, S. G.; Novotny, L.; Oh, S.-H. *ACS Nano* **(2012)**, *6*, 9168.

- (97) Henzie, J.; Kwak, E.-S.; Odom, T. W. *Nano Lett.* (2005), 5, 1199.
- (98) Barrios, C. A.; Malkovskiy, A. V.; Kisliuk, A. M.; Sokolov, A. P.; Foster, M. D. *J. Phys. Chem. C* (2009), 113, 8158.
- (99) Agapov, R. L.; Sokolov, A. P.; Foster, M. D. *J. Raman Spectrosc.* (2013), 44, 710.
- (100) Saito, Y.; Kobayashi, M.; Hiraga, D.; Fujita, K.; Kawano, S.; Smith, N. I.; Inouye, Y.; Kawata, S. *J. Raman Spectrosc.* (2008), 39, 1643.
- (101) Novotny, L.; Beversluis, M. R.; Youngworth, K. S.; Brown, T. G. *Phys. Rev. Lett.* (2001), 86, 5251.
- (102) Martin, Y. C.; Hamann, H. F.; Wickramasinghe, H. K. *J. Appl. Phys.* (2001), 89, 5774.
- (103) Dorn, R.; Quabis, S.; Leuchs, G. *Phys. Rev. Lett.* (2003), 91, 2339011.
- (104) Schadt, M.; Helfrich, W. *Appl. Phys. Lett.* (1971), 18, 127.
- (105) Stalder, M.; Schadt, M. *Opt. Lett.* (1996), 21, 1948.
- (106) Masso, J. D.; She, C. Y.; Edwards, D. F. *Phys. Rev. B* (1970), 1, 4179.
- (107) Bremard, C.; Dhamelincourt, P.; Laureyns, J.; Turrell, G. *Appl. Spectrosc.* (1985), 39, 1036.
- (108) Kano, H.; Mizuguchi, S.; Kawata, S. *J. Opt. Soc. Am. B* (1998), 15, 1381.
- (109) Pashae, F.; Hou, R.; Gobbo, P.; Workentin, M. S.; Lagugné-Labarthe, F. *J. Phys. Chem. C* (2013), 117, 15639.
- (110) Reimer, L. *Scanning Electron Microscopy*; 2nd ed.; Springer, 1998.
- (111) Hartschuh, A. *Angew. Chem., Int. Ed.* (2008), 47, 8178.
- (112) Zhang, W.; Fischer, H.; Schmid, T.; Zenobi, R.; Martin, O. J. F. *J. Phys. Chem. C* (2009), 113, 14672.
- (113) Budich, C.; Neugebauer, U.; Popp, J.; Deckert, V. *J. Microsc.* (2008), 229, 533.
- (114) Hennemann, L. E.; Meixner, A. J.; Zhang, D. *Spectroscopy* (2010), 24, 119.
- (115) Blum, C.; Schmid, T.; Opilik, L.; Weidmann, S.; Fagerer, S. R.; Zenobi, R. *J. Raman Spectrosc.* (2012), 43, 1895.
- (116) Ayars, E. J.; Hallen, H. D.; Jahncke, C. L. *Phys. Rev. Lett.* (2000), 85, 4180.
- (117) Ayars, E. J.; Hallen, H. D. *Appl. Phys. Lett.* (2000), 76, 3911.
- (118) Grafstroem, S.; Kowalski, J.; Neumann, R.; Probst, O.; Woertge, M. *J. Vac. Sci. Technol., B* (1991), 9, 568.
- (119) Latini, G.; Downes, A.; Fenwick, O.; Ambrosio, A.; Allegrini, M.; Gucciardi, P. G.; Patané, S.; Daniel, C.; Silva, C.; Daik, R.; Feast, W. J.; Cacialli, F. *Synthetic Met.* (2004), 147, 165.
- (120) Malkovskiy, A. V.; Malkovsky, V. I.; Kisliuk, A. M.; Barrios, C. A.; Foster, M. D.; Sokolov, A. P. *J. Raman Spectrosc.* (2009), 40, 1349.

- (121) McCarthy, B.; Zhao, Y.; Grover, R.; Sarid, D. *Appl. Phys. Lett.* **(2005)**, *86*, 1119141.
- (122) Smith, D. A.; Owens, R. W. *Appl. Phys. Lett.* **(2000)**, *76*, 3825.
- (123) Downes, A.; Salter, D.; Elfick, A. *Opt. Express* **(2006)**, *14*, 5216.
- (124) Zhang, M.-L.; Peng, K.-Q.; Fan, X.; Jie, J.-S.; Zhang, R.-Q.; Lee, S.-T.; Wong, N.-B. *J. Phys. Chem. C* **(2008)**, *112*, 4444.
- (125) Kudelski, A.; Pettinger, B. *Chem. Phys. Lett.* **(2000)**, *321*, 356.
- (126) Pieczonka, N. P. W.; Aroca, R. F. *Chem. Phys. Chem.* **(2005)**, *6*, 2473.
- (127) Waterhouse, G. I. N.; Bowmaker, G. A.; Metson, J. B. *Appl. Sur. Sci.* **(2001)**, *183*, 191.

Chapter 4

4 Localized Enhancement of Electric Field in Tip-enhanced Raman Spectroscopy Using Radially and Linearly Polarized Light¹

In the present Chapter, finite-difference time-domain (FDTD) calculations are used to characterize the distribution of the electric field in the vicinity of a sharp silver or gold cone with an apex diameter of 10 nm. The simulations are utilized to predict the intensity and the distribution of the localized enhancement of electric field that occurs in tip-enhanced Raman spectroscopy. A comprehensive comparison of the enhanced electric field induced by a radially and a linearly polarized light in both gap mode and conventional TERS setup is performed. For this purpose, a radially polarized source is created and integrated into the FDTD simulation software. For the linear polarization, both axial and side illuminations geometries are considered whereas radial polarization is investigated only in axial illumination. In addition, the optical effect of a thin protective layer of alumina on the enhancement of the electric field has been investigated.

4.1 Introduction

The enhancement of the electric field in TERS depends critically on various parameters such as the polarization of the excitation beam,¹ the metallic nature and the geometry of the metallic tip^{2,3} as well as the sample substrate.⁴ So far, finite-difference time-domain modeling of the electromagnetic field has been applied successfully to optimize TERS parameters such as the length and the radius of the tip, the material of the tip and the tip-sample distance.⁵⁻⁷ Here, we use FDTD to precisely estimate the impact of both radially and linearly polarized sources on the enhancement of the electric field. While linearly

¹ A version of this chapter has been published in [*Opt. Express*, (2013), 21, 25271.]. Reproduced with permission of the Optical Society of America

polarized source is commonly used for TERS,⁸⁻¹¹ radially polarized modes are of great interest to conduct TERS experiments in axial illumination geometry.¹²⁻¹⁵

Laser beams with radial polarization provide unique focusing properties including a strong electric field component along the tip axis generated at the focal point.^{16,17} In TERS, a polarization component of the incident light along the tip axis induces a strong surface charge density at the sharp apex of the metallic tip which is a prerequisite for local enhancement of the electric field.¹ To conduct the presented calculation, a radially polarized source is designed and integrated into the FDTD modeling. The choice of the material for simulated tip and substrate is limited to silver and gold as they are the two popular metals that were successfully tested for TERS measurements in UV-visible range.^{11,18-20} The presented simulations are performed at two distinct wavelengths of 532 and 632.8 nm, in order to excite the LSPR of silver and gold tips, respectively. These parameters also match our practical TERS experimental conditions.^{21,22} Furthermore, we analyze how a thin protective layer of alumina alters the confinement of the enhanced electric field. Although such protective layer extends the lifetime of the metallic tip by preventing the rapid oxidation and mechanical wear under ambient conditions, it also interferes with the local enhancement.²³⁻²⁵

4.2 Finite-Difference Time-Domain Method

Different models have been developed to numerically and theoretically investigate the enhancement of the electric field around metallic nanostructure. In general in order to calculate the enhanced electric field around a metallic nanoparticle or the TERS tip, either Maxwell's or Helmholtz's equations have to be solved which could be done by using the following classified methods.²⁶

i. Semi-analytical methods; where the field equations are solved exactly within certain domains. The adjustment of the boundary conditions takes place through approximated solutions by discretization of boundary points and minimization of the errors. The multiple multipole program (MMP) is among these methods. In MMP, electric and magnetic fields within individual homogeneous domains are developed by a series

expansion in spherical wavelength vectors, called multipoles, using known analytical solutions of Maxwell's equations. The amplitude of these fields is then solved by a generalized point matching method (GPMM). In general, the scattering problem is described as a set of linear differential equations.^{27,28}

ii. Semi-numerical methods are another approach where the boundary conditions are exactly determined and field equations within a domain are solved approximately. In this method the area is discretized. FDTD and finite element (FE) methods are two examples. In FDTD²⁹⁻³¹ method Maxwell's equations are discretized directly in time and space. The boundary conditions between the discretizing elements for space are exactly adjusted and each rectangular block in the interior of the domain is interpolated. In FE^{32,33} which is a frequency domain method, Helmholtz's equations are discretized in the space domain. This method uses continuous domain which is divided into polygons that are called sub-domains.

As mentioned earlier, finite-difference time-domain approach is employed in this thesis to conduct the presented calculations of this Chapter. So far, FDTD has performed as a reliable method for solving Maxwell's equations in complex geometries.³⁴⁻³⁶ Maxwell's equations describe the situations where the variation of the electric field with time depends on spatial variation of the magnetic field. An electromagnetic field in a medium can be described by four vectors of the electric field strength, \vec{E} , the electric displacement, \vec{D} , the magnetic field strength, \vec{H} and the magnetic flux density, \vec{B} . These vectors are differentiable over the radius vector of any given point position in 3D space, \vec{R} , and time, t . These differential equations indeed form the basis of the Maxwell's equations:

$$-\frac{\partial \vec{D}}{\partial t} + \nabla \times \vec{H} = \vec{J}(t, \vec{R}) \quad (4.1)$$

$$\frac{\partial \vec{B}}{\partial t} + \nabla \times \vec{E} = 0 \quad (4.2)$$

$$\nabla \cdot \vec{D} = \rho(t, \vec{R}) \quad (4.3)$$

$$\nabla \cdot \vec{B} = 0 \quad (4.4)$$

$\rho(t, \vec{R})$ is the volume density of electric charge in a medium and $\vec{J}(t, \vec{R})$ is the volume density of electric current that shows the density of charges that pass in unit time through a unit area. $(\nabla \times)$ is the curl operator and can be applied to a vector in order to measure its degree of local spinning (also known as *rot* or rotation function) in 3D space, as it is shown in the following definition:

$$\nabla \times \vec{V} \sim \hat{i} \left(\frac{\partial \vec{V}_3}{\partial y} - \frac{\partial \vec{V}_2}{\partial z} \right) + \hat{j} \left(\frac{\partial \vec{V}_1}{\partial z} - \frac{\partial \vec{V}_3}{\partial x} \right) + \hat{k} \left(\frac{\partial \vec{V}_1}{\partial y} - \frac{\partial \vec{V}_2}{\partial x} \right) \quad (4.5)$$

$\vec{V} = (\vec{V}_1, \vec{V}_2, \vec{V}_3)$ is an arbitrary vector with components which are each a function of the variables x and y and z . \hat{i} , \hat{j} and \hat{k} are the unit vectors in x , y and z direction respectively.

$(\nabla \cdot)$ denotes the divergence function that shows the presence of a source or a sink for a three dimensional vector at a given point. In Cartesian coordinates divergence has the following definition:

$$\nabla \cdot \vec{V} = \frac{\partial \vec{V}_1}{\partial x} + \frac{\partial \vec{V}_2}{\partial y} + \frac{\partial \vec{V}_3}{\partial z} \quad (4.6)$$

Similarly, the Maxwell equations describe how variation of the magnetic field with time depends on spatial variation of the electric field. This could be summarized in the following six equations:³¹

$$\frac{\partial \vec{E}_x}{\partial t} = -\frac{1}{\varepsilon} \left(\frac{\partial \vec{H}_z}{\partial y} - \frac{\partial \vec{H}_y}{\partial z} \right) \quad (4.7)$$

$$\frac{\partial \vec{E}_y}{\partial t} = -\frac{1}{\varepsilon} \left(\frac{\partial \vec{H}_x}{\partial z} - \frac{\partial \vec{H}_z}{\partial x} \right) \quad (4.8)$$

$$\frac{\partial \vec{E}_z}{\partial t} = -\frac{1}{\varepsilon} \left(\frac{\partial \vec{H}_y}{\partial x} - \frac{\partial \vec{H}_x}{\partial y} \right) \quad (4.9)$$

$$\frac{\partial \vec{H}_x}{\partial t} = -\frac{1}{\mu} \left(\frac{\partial \vec{E}_z}{\partial y} - \frac{\partial \vec{E}_y}{\partial z} \right) \quad (4.10)$$

$$\frac{\partial \vec{H}_y}{\partial t} = -\frac{1}{\mu} \left(\frac{\partial \vec{E}_x}{\partial z} - \frac{\partial \vec{E}_z}{\partial x} \right) \quad (4.11)$$

$$\frac{\partial \vec{H}_z}{\partial t} = -\frac{1}{\mu} \left(\frac{\partial \vec{E}_y}{\partial x} - \frac{\partial \vec{E}_x}{\partial y} \right) \quad (4.12)$$

\vec{H} and \vec{E} are the magnetic and electric fields and ε and μ denote the dielectric constant (permittivity) and magnetic constant (permeability) of the medium, respectively. (H_x, H_y, H_z) and (E_x, E_y, E_z) are the three components of the magnetic and electric field in Cartesian coordinates, respectively. The partial derivatives in these equations are solved through central difference method in FDTD.

$$f'(x) = \lim_{h \rightarrow 0} \frac{f(x+h) - f(x-h)}{2h} \approx \frac{f(x+h) - f(x-h)}{2h} \quad (4.13)$$

Therefore, partial derivatives in Maxwell's equations in time t could be rewritten as general forms of:

$$\frac{\partial f'(i, j, k)}{\partial x} = \frac{f' \left(i + \frac{\Delta x}{2}, j, k \right) - f' \left(i - \frac{\Delta x}{2}, j, k \right)}{\Delta x} \quad (4.14)$$

$$\frac{\partial f'(i, j, k)}{\partial y} = \frac{f' \left(i, j + \frac{\Delta y}{2}, k \right) - f' \left(i, j - \frac{\Delta y}{2}, k \right)}{\Delta y} \quad (4.15)$$

$$\frac{\partial f'(i, j, k)}{\partial z} = \frac{f' \left(i, j, k + \frac{\Delta z}{2} \right) - f' \left(i, j, k - \frac{\Delta z}{2} \right)}{\Delta z} \quad (4.16)$$

Similarly, for temporal derivatives at time $t + 1/2$:

$$\frac{\partial f^{t+1/2}(i, j, k)}{\partial t} = \frac{f^{t+1}(i, j, k) - f^t(i, j, k)}{\Delta t} \quad (4.17)$$

It is through solving equations (4-1) to (4-12) that FDTD provides time-domain information, offering insight into electrodynamics of the system.³⁴ In FDTD, the electromagnetic field and structural materials of interest are described on a discrete mesh composed of so-called Yee cells as demonstrated in **Figure 4.1**. Maxwell's equations are solved discretely in time, where the time step used is related to the mesh size through the stability criterion. This technique is an exact representation of Maxwell's equations in the limit that the spacing mesh goes to zero.

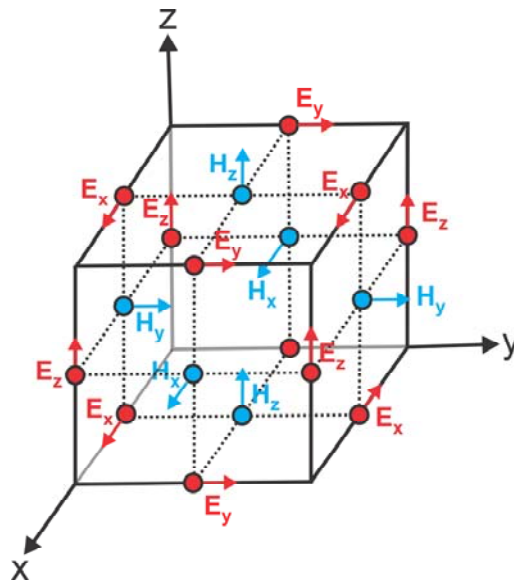


Figure 4.1 Illustration of standard Cartesian Yee cell used for FDTD. The electric (E_x, E_y, E_z) and magnetic (H_x, H_y, H_z) field components are distributed about this cell. The electric field components originate from the edges of the cube and the magnetic field components come out of the faces.

To simulate the TERS tip, a silver or gold rounded-tip cone with the tip diameter of 10 nm, and a cone angle of 25° is utilized. These parameters are estimated based on SEM images of typical tips that are used in TERS measurements (See Chapter 3). To illustrate

gap-mode geometries, a film of silver or gold with 5 nm thickness is introduced inside the simulation area and located 1 nm below the cone apex. The simulation area is set up as a 3D system of $100 \times 100 \times 126 \text{ nm}^3$ surrounded by the perfectly matched layer (PML) boundary, wide enough in order to limit its impact on the resonance of the system. A spatial mesh of 0.15 nm and a temporal mesh of $2.8 \times 10^{-16} \text{ sec}$ are set which guaranteed numerical convergence of the results. The optical constants of alumina are described by Palik,³⁷ the one of silver and gold are obtained from CRC.³⁸ All the calculated and reported intensities are normalized with respect to the intensity of the incident light. The calculation of the total electric field intensity ($|E|^2$) and its distribution was obtained from the sum of its polarized components ($|E_x|^2 + |E_y|^2 + |E_z|^2$). All the calculated and reported intensities are normalized with respect to the intensity of the incident light.

4.3 Results and Discussion

4.3.1 Polarization Modulation for FDTD Simulations

As mentioned earlier, the polarization of the incident laser plays an essential role in the intensity and the distribution of the enhanced electric field at the tip apex.¹ To further investigate this impact, linearly and radially polarized light in different TERS configurations have been considered in this section.

4.3.1.1 Radial Polarization

A radially polarized light has polarization vectors oriented radially in the transverse plane with respect to the propagation direction as it is shown in **Figure 4.2a**. Under a tight focusing of a radially polarized light by a high numerical aperture lens, the focal longitudinal electric field (E_z) and the focal transverse electric field (E_{tr}) could be expressed by the following equations in polar coordinate:³⁹

$$E_z(\rho, z) = 2i \int_0^\alpha P(\theta) \cos^{1/2}(\theta) \sin^2(\theta) J_0(\kappa \rho \sin \theta) \exp(i\kappa z \cos \theta) d\theta \quad (4.18)$$

$$E_r(\rho, z) = \int_0^\alpha P(\theta) \cos^{1/2}(\theta) \sin(2\theta) J_1(\kappa \rho \sin \theta) \exp(i\kappa z \cos \theta) d\theta \quad (4.19)$$

ρ is the transverse size of the beam which is usually defined by the value of $\rho^2 = x^2 + y^2$, α is the maximum focusing angle and could be calculated by $\alpha = \sin^{-1}(N.A./n)$, n is the index of refraction. $\kappa = 2\pi/\lambda$, θ is an angle between ρ and z at each point in space and J_0 and J_1 denote the Bessel functions of the first kind with the orders of zero and one. $P(\theta)$ is the pupil function of a Bessel Gaussian beam:

$$P(\theta) = J_1(2\beta_0 \sin \theta / \sin \alpha) \exp(-\beta_0^2 \sin^2 \theta / \sin^2 \alpha) \quad (4.20)$$

Where $\beta_0 = 3/2$ is the ratio of the pupil radius to the beam waist.⁴⁰

Herein, a script that solved the equations (4.18) and (4.19) was created to describe a focused radially polarized light inside the simulation area. The script was written in Matlab programming language and integrated into FDTD. This light source has been utilized for the corresponding calculations that are reported here. The transverse and longitudinal electric field components of the described beam are shown in **Figure 4.2a** and **Figure 4.2b** in 3D and 2D presentations.

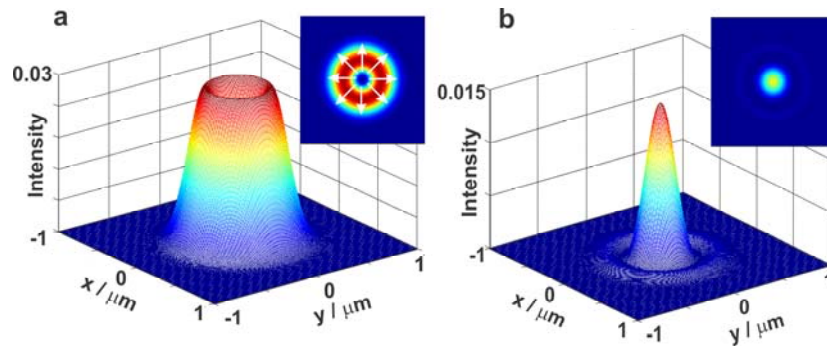


Figure 4.2 (a) Transverse component of a focused radially polarized beam (b) longitudinal component of a focused radially polarized beam in 3D and 2D presentations

The transverse component of a radially polarized beam consists of several concentric rings with variable intensities and a minimum intensity at the middle (**Figure 4.2a**). The

longitudinal component (**Figure 4.2b**) of this beam is another set of concentric rings with overall intensities lower than the transverse component and with a maximum intensity at the center. The enhancement phenomenon that occurs in TERS originates from the interaction of the longitudinal component of the focused light with the apex of the sharp metallic tip.

It is noteworthy that the integration of a radially polarized light for calculation of the electric field distribution around a silver nanosphere at 532 nm was previously done by Du *et al.* in 2011. Using Full-Wave software, they created a homemade radially polarized light by the superposition of a left hand circularly polarized beam with a right hand one.⁴¹ They focused the radially polarized beam by setting an initial equivalent phase function of lens in the source file instead of the objective lens to save computational memory. However, this approach requires the integration of circularly polarized light which is not provided in the Lumerical software that is used in this thesis for conducting FDTD simulations.

4.3.1.2 Linear Polarization

In a linearly polarized electromagnetic wave, the electric field vectors are oriented along a single direction inside a plane perpendicular to the propagation direction of the wave. The top and side view of the total electric field of a focused linearly polarized light along with their corresponding longitudinal components are shown in **Figures 4.3a, 4.3b and 4.3c, 4.3d** respectively. Here the Gaussian light has been focused by passing a 1 mm diameter beam consisting of 1500 plane waves through a thin lens of 5 mm diameter and 1.2 numerical aperture. For the presented simulations where the structures of a few nanometers (less than 20 nm) are studied, a focused Gaussian beam was replaced with a plane wave that is provided in the FDTD software. Here, a special case of a plane wave known as total field scattered field (TFSF) was used to prevent the possible couplings with the boundaries of the simulation area. TFSF separates the computation region into two distinct regions; one contains the total field which is the sum of the incident field and the scattered field while the second region contains only the scattered field.

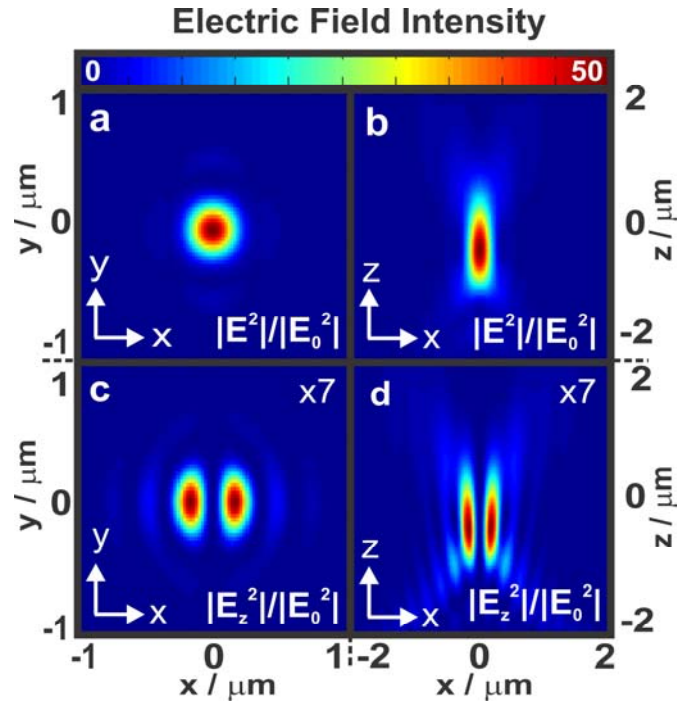


Figure 4.3 Electric energy density of the total field of a focused linearly x polarized light in (a) top and (b) side view (c) longitudinal field of a linearly x polarized light in top and (d) side view.

The top view of a focused Gaussian beam consists of several concentric rings in xy plane with a maximum intensity in the middle (**Figure 4.3a**). From the side view, the beam would be relatively elongated in the direction of propagation along z (**Figure 4.3b**). The z component of the electric field in a focused Gaussian beam has two lobes in the direction of propagation with zero intensity in the middle (**Figure 4.3c and 4.3d**). This minimum intensity results in the absence of significant excitation of plasmon resonances at the tip apex if the tip is located in the center of the focal region. However, tip-enhanced Raman should be observed more significantly in case the tip is located inside one of the two lobes of the excitation laser.

4.3.2 Normalization of the Electric Field Intensity

All of the intensities that are reported in coming sections are normalized with respect to the intensity of the incident light. For simulations where a plane wave has been utilized, the intensity of the source is by default equal to 1 as a presumption in FDTD program.

Therefore, for all the simulations performed by a linearly polarized light, the FDTD output for intensities is already normalized to the intensity of the source. In case of radially polarized sources however, the intensity of the source should be determined in accordance with the FDTD output after the source is created. After the source intensity, $|E_0|^2$, is determined, the estimated electric field magnitude for each simulation, $|E|^2$, was normalized to the source intensity through $|E|^2/|E_0|^2$.

4.3.3 FDTD Calculation of the Electric Field

4.3.3.1 Effect of Polarization on the Enhancement of the Electric Field

The effect of different polarizations of the excitation beam on the magnitude of enhancement and the quality of the distribution of the electric field in TERS measurements has been investigated. This is done through comparison of the electric field at the tip apex as the tip is illuminated by linear and radial polarizations. A linearly polarized source was set to propagate once along the tip axis and once perpendicular to it. In TERS experimental geometries, the former is known as axial illumination while the latter is termed as side illumination. In side illumination the light propagates perpendicular to the tip axis and consequently it will be polarized along the tip axis while the polarization of light in axial illumination is perpendicular to the tip axis. Similar simulations have been performed using the described radially polarized beam. The results of the linear axial illumination, linear side illumination and radial axial illumination are represented in **Figures 4.4a** and **4.4d**, **Figures 4.4b** and **4.4e**, **Figures 4.4c** and **4.4f**, respectively. These results correspond to simulation of a silver tip illuminated by a 532 nm wavelength and gold tip illuminated by 632.8 nm wavelength light.

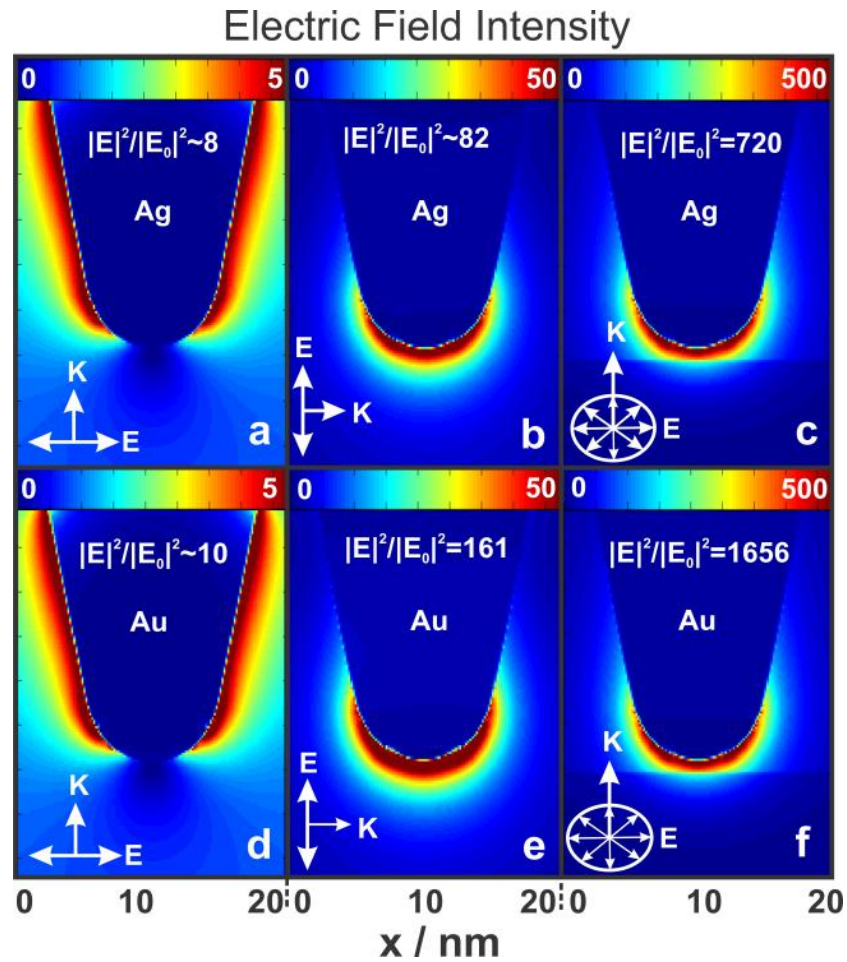


Figure 4.4 Electric field distribution at the 10 nm apex of (a) a silver tip illuminated at 532 nm by linearly polarized light along the tip axis (b) a silver tip illuminated at 532 nm by linearly polarized light perpendicular to the tip axis (c) a silver tip illuminated at 532 nm by radially polarized light along the tip axis (d) gold tip illuminated at 632.8 nm by linearly polarized light along the tip axis (e) gold tip illuminated at 632.8 nm by linearly polarized light perpendicular to the tip axis (f) gold tip illuminated at 632.8 nm by radially polarized light along the tip axis

As shown in **Figure 4.4a and 4.4d**, axial illumination of the tip by linearly polarized beam results in an overall electric field intensity of zero at the center of the apex. Here, the electric field is intensified in two areas located on two sides of the tip with respect to the tip symmetry axis. When the tip is illuminated from the side with a linearly polarized light, (**Figure 4.4b and 4.4e**) the electric field is confined at the tip apex. Side illumination is specifically useful when opaque samples are of interest. However, only

microscope objectives with long working distances and therefore low focusing power could be used in such setups. The creation of an intensified electric field at the tip apex can also be obtained through axial illumination with a tightly focused radially polarized light. The longitudinal component of the electric field in this case is significantly enhanced at the tip apex position. (**Figure 4.4c and 4.4f**)

It is noteworthy that the horizontal line that appears below the tip in **Figure 4.4c** and **Figure 4.4f** should not be confused with an external object. In fact the radial source is imposed in a plane whose position appears as a line in final images. The radial source must be focused so that a longitudinal component appears at tip apex. The longitudinal focal volume therefore is extended along the z direction and the focal plane is located at the horizontal line. Clearly, this line is not observed in all simulations where none focused beam has been utilized (**Figure 4.4 a, 4.4b, 4.4d and 4.4e**).

4.3.3.2 Gap Mode Tip-enhanced Raman Spectroscopy

To compare the gap mode TERS to the conventional TERS measurements, the near-field optical effects of a thin metallic substrate on the electric field distribution has been investigated. In gap mode TERS the electric field experiences an additional enhancement inside the gap that is formed between the metallic tip and a thin metallic substrate.⁴² To illustrate the gap mode, a metal film of 5 nm thickness was placed 1 nm below the tip apex and was extended through the side and bottom walls of the simulation area. Total field scattered field source was used as a source of linearly polarized Gaussian beam while the radially polarized beam was generated externally. The results of these simulations have been presented in **Figure 4.5**. **Figures 4.5a-4.5d** show the results for axial illumination by linear polarization, **Figures 4.5e-4.5h** present the side illumination by linear polarization and **Figures 4.5I-4.5L** correspond to the axial illumination by the radially polarized light. The tip and the metal substrate were set to be either gold or silver. The illumination wavelength was chosen with regards to the tip material.

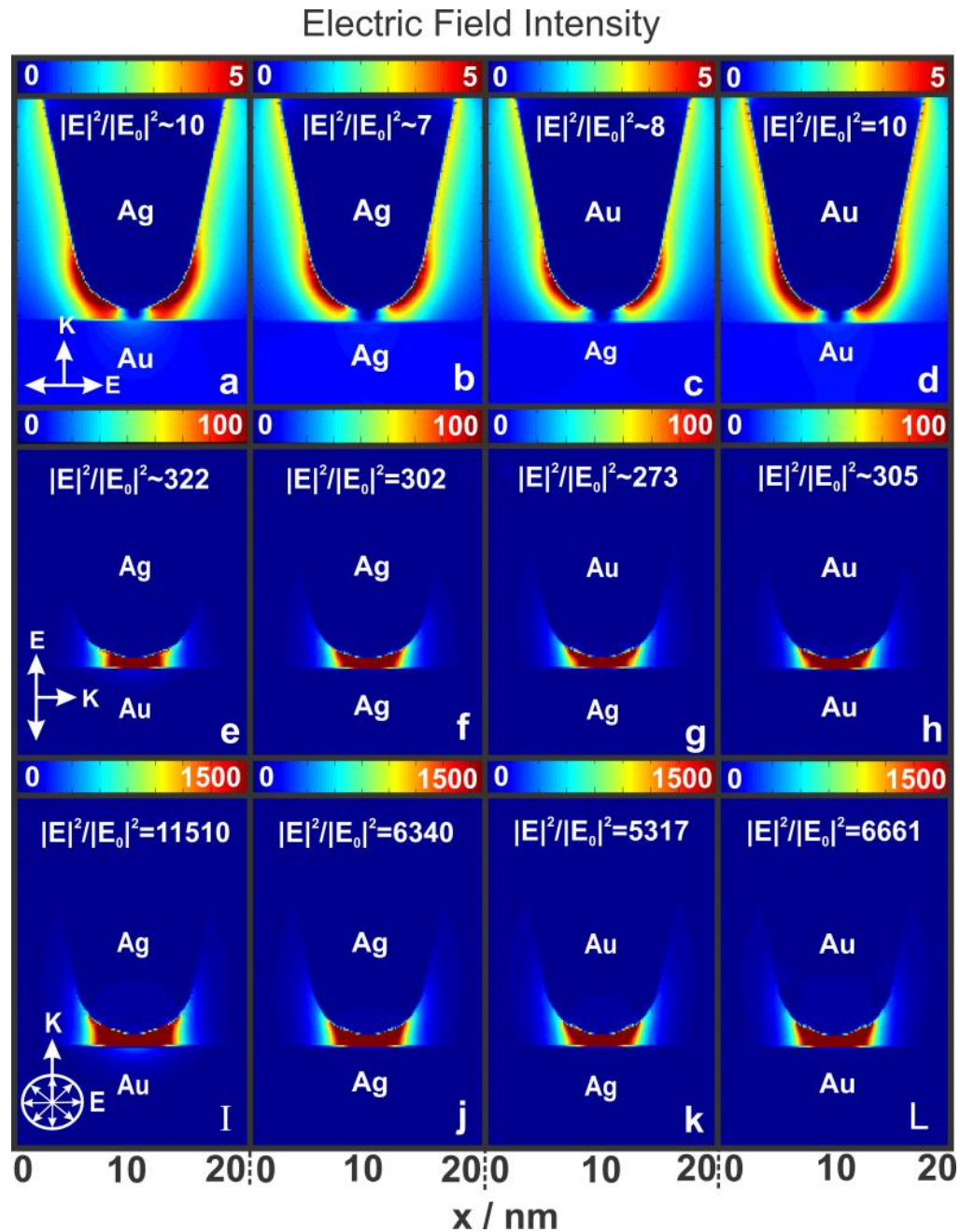


Figure 4.5 Electric field distribution at the 10 nm apex of a silver or gold tip illuminated at 532 or 632.8 nm, respectively, (a)-(d) by linearly polarized light along the tip axis in 1 nm separation from a gold or silver substrate (e)-(h) by linearly polarized light perpendicular to the tip axis in 1 nm separation from a gold or silver substrate (I)-(L) by radially polarized light along the tip axis in 1 nm separation from a gold or silver substrate

Noticeably, the presence of thin layer of metal gives rise to a more localized confinement area around the tip apex (**Figure 4.5**) when compared to the conventional TERS setup (**Figure 4.4**). In addition, the simulations show an increase of the intensity of the electric field concentrated around the tip apex in the gap between the tip and the metal substrate. A closer look at these results reveals that the simulations predict a larger enhancement factor inside the gap generated between a silver tip and a gold substrate rather than the one created between the silver tip and the silver substrate. This phenomenon might be related to the fact that silver, which has extinction coefficient of 3.5 at 532 nm wavelength, adsorbs a larger part of the incident light rather than gold with extinction coefficient of 2.1 at the same wavelength. This absorption weakens the excitation beam that reaches the tip apex. The absorption of the light by the silver substrate can be quite high that breaks the observed trend for the confinement factor of the electric field. An example of this exception is the silver tip illuminated in axial illumination geometry where the enhancement factor decreases from 8 in conventional TERS geometry (**Figure 4.4a**) to 7 within the gap produced between the silver tip and the silver substrate (**Figure 4.5b**). A similar effect is observed for gold tip in vicinity of a silver substrate. The enhancement factor decreases from 10 in conventional TERS geometry (**Figure 4.4d**) to 8 within the gap produced between the gold tip and the silver substrate (**Figure 4.5c**). Silver has larger absorption of 632.8 nm light with extinction coefficient of 4.02 at this wavelength. Gold has an extinction coefficient of 3.02 at 632.8 nm wavelength which decreases the amount of light that reaches the gold tip in gap-mode. Also, the absorption of 632.8 nm light by gold restricts the expected additional enhancement due to the presence of a gold nanoplate in close proximity of the gold tip. The enhancement factor for the illumination of a gold tip by 632.8 nm light in conventional and gap-mode TERS show the same value of 10 in the conducted simulations. However, this phenomenon was observed only for axial illumination with linearly polarized light therefore this could also be due to the direction of the polarization with respect to the tip axis. The simulation results for different combination of gold and silver tip and substrate in various illumination geometries are summarized in **Table 4.1**.

Table 4.1 Comparison of the electric field enhancement at the apex of silver or gold tip in 1 nm distance from thin gold or silver substrate

Tip	Sub.	λ/nm	Config.	$ E^2 / E_0^2 $	Tip	Sub.	λ/nm	Config.	$ E^2 / E_0^2 $
Ag	-	532	axial-radial	720	Au	-	633	axial- radial	1656
Ag	Au	532	axial- radial	11510	Au	Ag	633	axial- radial	5317
Ag	Ag	532	axial- radial	6340	Au	Au	633	axial- radial	6661
Ag	-	532	Side-linear	82	Au	-	633	Side-linear	161
Ag	Au	532	Side-linear	322	Au	Ag	633	Side-linear	273
Ag	Ag	532	Side-linear	302	Au	Au	633	Side-linear	305
Ag	-	532	axial-linear	8	Au	-	633	axial-linear	10
Ag	Au	532	axial-linear	10	Au	Ag	633	axial-linear	8
Ag	Ag	532	axial-linear	7	Au	Au	633	axial-linear	10

4.3.3.3 Impact of Alumina Protective Layer on the Electric Field Enhancement

The effect of a protective layer was investigated by adding a 1 nm thick alumina to the surface of the metallic cone. The thickness of the protective layer has been estimated according to the previously published studies.²⁴ Other than aluminum oxide, silicon dioxide has also been experimentally utilized as a protective layer.²⁴ For the experimental point of view, both aluminum and silicon oxide layers can be easily generated.

Aluminum layer can be created through deposition of metal vapor at very low pressures (10^{-7} Torr) using a single conventional vacuum chamber designed for evaporation of metal.²³ Oxidation of this layer under ambient condition will generate the alumina layer later. SiO_2 layers are deposited by vapor coating technique such as plasma enhanced chemical vapor deposition (PECVD).²⁴ Other dielectrics with high mechanical resistance properties can also be used as protective layer. The impact of a protective layer has been studied in three different geometries where the alumina coated silver tip was brought to a 1 nm distance from the gold substrate and illuminated using a linearly polarized beam in axial and side illumination as well as a radially polarized beam in axial geometry.

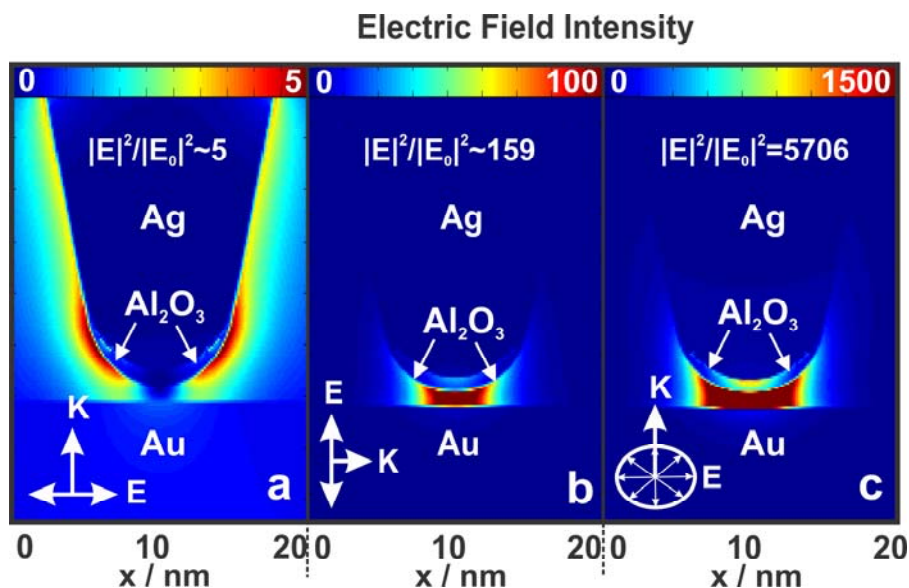


Figure 4.6 Electric field distribution at the 10 nm apex of a silver tip protected with 1 nm Al_2O_3 layer and illuminated at 532 nm by (a) linearly polarized light along the tip axis (b) linearly polarized light perpendicular to the tip axis (c) radially polarized light along the tip axis, in 1 nm separation from a gold substrate

According to **Figure 4.6**, adding 1 nm of dielectric protective layer decreases the intensity of the enhanced electric field by 50%. The observed decrease could originate from a shift in the frequency of the surface plasmon resonance as discussed in Chapters 2 and 3. This shift in the plasmon resonance of the tip/substrate junction reduces the enhancement of the local electric field at a certain wavelength. Therefore, if protective layers are deposited, the plasmon resonance frequency should be tuned accordingly prior to any TERS measurement. Additionally, the presence of the alumina dielectric layer can cause destructive interference of the incident light and the scattered electric field from the different interfaces. However, experiments have proven that for both alumina and silicon dioxide protected TERS tip, the improvement of the lifetime of the tips does in general compensate for the loss of the TERS enhancement. A protective layer increases the lifetime of the tip by protecting it against oxidation and mechanical wear damages. It is noteworthy that as far as the protective layer does not alter the morphology of the tips, it has no negative impact on the spatial resolution of the measurements.²⁴

4.4 Conclusion

The influence of the incident laser polarization, choice of the tip material and the presence of a thin metallic substrate in distinct configurations for tip-enhanced Raman spectroscopy was investigated in this Chapter. We conclude that by utilizing a thin film of transparent gold or silver as a substrate for TERS measurements, a considerable increase in the detection sensitivity can be achieved. Regarding the polarization of the incident light, we conclude that for a linear input polarization, a side illumination is preferable with polarization axis oriented along the tip axis. Meanwhile, axial illumination by radial polarization promotes a significant confinement of the electric field which is ideal for tip-enhanced Raman measurements. However, the exaltation depends on the optical properties of the junction formed by the metallic tip and substrate. A hetero-metallic junction formed by a silver tip and a gold thin film appears to be very efficient. These investigations are in good agreement with a recent study in our research group where the impact of a thin film of gold as substrate along with radially polarized Raman laser is experimentally investigated in TERS detection of a monolayer of molecules.²² Additionally, we demonstrate that adding a thin protective layer to the TERS tip to reduce oxidation and mechanical wear decreases the intensity of the electric field by 50%.

4.5 References

- (1) Novotny, L.; Sanchez, E. J.; Xie, X. S. *Ultramicroscopy* (1998), 71, 21.
- (2) Nottingher, I.; Elfick, A. *J. Phys. Chem. B* (2005), 109, 15699.
- (3) Stadler, J.; Oswald, B.; Schmid, T.; Zenobi, R. *J. Raman Spectrosc.* (2013), 44, 227.
- (4) Deckert-Gaudig, T.; Deckert, V. *Small* (2009), 5, 432.
- (5) Demming, A. L.; Festy, F.; Richards, D. *J. Chem. Phys.* (2005), 122, 1847161.
- (6) Sukharev, M.; Seideman, T. *J. Phys. Chem. A* (2009), 113, 7508.
- (7) Treffer, R.; Bailo, E.; Deckert-Gaudig, T.; Deckert, V. *Beilstein J. Nanotechnol.* (2011), 2, 628.
- (8) Boehme, R.; Richter, M.; Cialla, D.; Roesch, P.; Deckert, V.; Popp, J. *J. Raman Spectrosc.* (2009), 40, 1452.

- (9) Hermann, P.; Hermelink, A.; Lausch, V.; Holland, G.; Moeller, L.; Bannert, N.; Naumann, D. *Analyst* (2011), 136, 1148.
- (10) Kurouski, D.; Deckert-Gaudig, T.; Deckert, V.; Lednev, I. K. *J. Am. Chem. Soc.* (2012), 134, 13323.
- (11) Stadler, J.; Schmid, T.; Zenobi, R. *Nano Lett.* (2010), 5, 1530.
- (12) Hayazawa, N.; Saito, Y.; Kawata, S. *Appl. Phys. Lett.* (2004), 85, 6239.
- (13) Hoppener, C.; Beams, R.; Novotny, L. *Nano Lett.* (2009), 9, 903.
- (14) Steidtner, J.; Pettinger, B. *Phys. Rev. Lett.* (2008), 100, 236101.
- (15) Roy, D.; Williams, C. *J. Vac. Sci. Technol., A* (2010), 28, 472.
- (16) Dorn, R.; Quabis, S.; Leuchs, G. *Phys. Rev. Lett.* (2003), 91, 2339011.
- (17) Quabis, S.; Dorn, R.; Eberler, M.; Glockl, O.; Leuchs, G. *Opt. Commun.* (2000), 179, 1.
- (18) Cancado, L. G.; Hartschuh, A.; Novotny, L. *J. Raman Spectrosc.* (2009), 40, 1420.
- (19) Deckert-Gaudig, T.; Deckert, V. *Phys. Chem. Chem. Phys.* (2010), 12, 12040.
- (20) Paulite, M.; Blum, C.; Schmid, T.; Opilik, L.; Eyer, K.; Walker, G. C.; Zenobi, R. *ACS Nano* (2013), 7, 911.
- (21) Kazemi-Zanjani, N.; Chen, H.; Goldberg, H. A.; Hunter, G. K.; Grohe, B.; Lagugné-Labarhet, F. *J. Am. Chem. Soc.* (2012), 134, 17076.
- (22) Pashaei, F.; Hou, R.; Gobbo, P.; Workentin, M. S.; Lagugné-Labarhet, F. *J. Phys. Chem. C* (2013), 117, 15639.
- (23) Agapov, R. L.; Sokolov, A. P.; Foster, M. D. *J. Raman Spectrosc.* (2013), 44, 710.
- (24) Barrios, C. A.; Malkovskiy, A. V.; Kisliuk, A. M.; Sokolov, A. P.; Foster, M. D. *J. Phys. Chem. C* (2009), 113, 8158.
- (25) Cui, X.; Erni, D.; Zhang, W.; Zenobi, R. *Chem. Phys. Lett.* (2008), 453, 262.
- (26) Bailo, E.; Deckert, V. *Chem. Soc. Rev.* (2008), 37, 921.
- (27) Novotny, L.; Bian, R. X.; Xie, X. S. *Phys. Rev. Lett.* (1997), 79, 645.
- (28) Renger, J.; Grafström, S.; Eng, L. M.; Deckert, V. *J. Opt. Soc. Am. A* (2004), 21, 1362.
- (29) Festy, F.; Demming, A.; Richards, D. *Ultramicroscopy* (2004), 100, 437.
- (30) Krug Ii, J. T.; Sanchez, E. J.; Xie, X. S. *J. Chem. Phys.* (2002), 116, 10895.
- (31) Taflove, A.; Hagness, S. C. *Computational Electrodynamics: The Finite - Difference Time - Domain Method*; Artech House: Boston, MA, 2005.
- (32) Martin, Y. C.; Hamann, H. F.; Wickramasinghe, H. K. *J. Appl. Phys.* (2001), 89, 5774.
- (33) Micic, M.; Klymyshyn, N.; Suh, Y. D.; Lu, H. P. *J. Phys. Chem. B* (2003), 107, 1574.

- (34) Galarreta, B. C.; Rugar, I.; Young, A.; Lagugné-Labarthe, F. *J. Phys. Chem. C* **(2011)**, *115*, 15318.
- (35) Yang, Z.; Aizpurua, J.; Xu, H. *J. Raman Spectrosc.* **(2009)**, *40*, 1343.
- (36) Ye, J.; Van Dorpe, P. *Nanoscale* **(2012)**, *4*, 7205.
- (37) Palik, E. D.; Ghosh, G. *Handbook of optical constants of solids* 2nd ed.; Academic press: London, 1998; Vol. II.
- (38) Lide, D. R. *CRC handbook of chemistry and physics*; 90th ed.; CRC press: New York, 2009.
- (39) Lu, F.; Zheng, W.; Huang, Z. *Opt. Lett.* **(2009)**, *34*, 1870.
- (40) Youngworth, K.; Brown, T. *Opt. Express* **(2000)**, *7*, 77.
- (41) Du, L.; Yuan, G.; Tang, D.; Yuan, X. *Plasmonics* **(2011)**, *6*, 651.
- (42) Deckert-Gaudig, T.; Kaemmer, E.; Deckert, V. *J. Biophotonics* **(2012)**, *5*, 215.

Chapter 5

5 Tip-enhanced Raman Spectroscopy of Single Walled Carbon Nanotubes; Imaging beyond the Diffraction Limit

In this Chapter the spatial resolution of the TERS setup is estimated using isolated single wall carbon nanotubes (SWCNT) as a reference object. Carbon nanotubes are of critical and specific interest to determine the spatial resolution of the TERS setup due to their large Raman scattering cross-section, which makes them ideal nanostructure for Raman studies. Near-field Raman images of isolated carbon nanotubes are collected and utilized for the estimation of the lateral resolution. In addition, the near-field nature of the collected Raman signals is evaluated through measuring the Raman signal decay with respect to the tip-sample separation.

5.1 Introduction

Since their discovery in 1993,^{1,2} carbon nanotubes have been intensively studied in many research fields due to their unique mechanical and electronic properties and their potential use in nanotechnology.^{3,4} Depending on their diameter and chirality,^{3,5} carbon nanotubes exhibit metallic or semiconductor properties which makes them a material of interest in many optical and electronic applications. Metallic nanotubes have applications as molecular quantum wires⁶ or single electron transistors.⁷ Semiconducting properties of carbon nanotubes are useful for creating field-effect transistors.⁸ Carbon nanotube have also found applications as scanning probes,⁹ hydrogen storage material,¹⁰⁻¹² as a carrier for drug delivery^{13,14} and have been utilized as transducers for biosensing applications.¹⁵

The building block of carbon nanotube is a single layer graphene sheet that has been rolled up into a cylinder. Graphene itself is composed of carbon-carbon bond with sp^2 hybridization with two atoms per unit cell as it has been demonstrated in **Figure 5.1**:

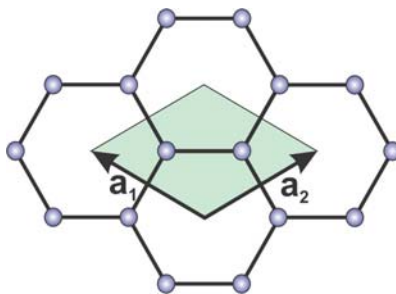


Figure 5.1 Illustration of the unit cell in single layer graphene. There are two sp^2 carbons in each unit cell and the overall structure consists of unsaturated hexagonal carbon cycles with carbon-carbon double bonds. \mathbf{a}_1 and \mathbf{a}_2 are the unit vectors.

Each single walled carbon nanotube is defined by two geometrical integers that are typically denoted by (n,m) and contain information about how the graphene sheet has been rolled up.⁴ The relation between (n,m) and the axis around which rolling of graphene occurs has been illustrated in **Figure 5.2**. The main axis of the product cylinder is determined by a certain combination of n and m . If $m=0$ the final nanotube will have zigzag structure, if $n=m$ armchair nanotubes are formed. Other combinations of the two integers will result in chiral carbon nanotubes. An example of the chiral structure has been illustrated in **Figure 5.2**. In this case the graphene sheet is rolled in the direction of X with the resulting nanotube having its main axis perpendicular to X .

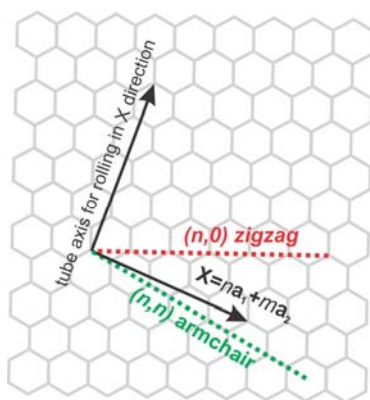


Figure 5.2 Correlation between the n and m integers and the structure of carbon nanotube. Rolling of the single layer graphene in the direction of X or any combination of the two integers results in unique structural and physical properties

In addition to the structural impacts, n and m determine whether the nanotube has metallic or semiconductor properties. If $n=m$ the nanotube is metallic, otherwise it shows semiconducting behavior.⁴

So far, extensive experimental and theoretical studies have been performed to acquire thorough understanding of the electronic, optical, vibrational and mechanical properties of carbon nanotubes.^{3,4} In this context, Raman spectroscopy,¹⁶⁻¹⁹ SERS²⁰ and more specifically TERS²¹ has appeared unrivalled due to their sensitivity and spatial resolution. This is due to the fact that in sp^2 carbon compounds as well as three dimensional graphite, two dimensional graphene or one dimensional carbon nanotube, Raman scattering gets coupled with an optical absorption to and emission from an excited electric state when proper excitation energy is used. The coupling is termed as resonance Raman scattering which is described in details in Chapter 2 of this thesis. The resonant nature of Raman scattering from carbon nanotubes makes their scatterings detectable even if one single nanotube is present. The intense Raman signals from carbon nanotubes in addition to their well defined cylindrical structure makes them ideal for the estimation of the spatial resolution in TERS measurements. So far, lateral resolution better than 1.7 nm is reported in literature for TERS study of carbon nanotubes specifically.²² High resolution imaging of TERS enables nanoscale investigations such as the tracking of semiconductor to metal transition at the junction of two crossing carbon nanotubes,²³ or detection of the defects along a single carbon nanotube.²⁴

The most intense Raman mode of carbon nanotube is known as G band which consists of longitudinal optical (LO) and transverse optical (TO) phonon modes. LO causes vibrations along the cylinder main axis and TO occur along the circumference of hexagonal rings where both happen on the outer surface of the cylinder. LO and TO peaks appear in the range of 1550-1605 cm^{-1} with TO modes appearing in lower frequencies, however their position change with the diameter and metallicity of the tubes.^{25,26} The other source of the Raman peaks for carbon nanotube is referred to as radial breathing mode (RBM). RBM is related to the cylindrical shape of the tubes and involves vibrations along the radial direction. The energy required for these vibrations are related to the cylinder diameter and the (n,m) indices,¹⁸ therefore, RBM related Raman

peaks typically appear in a range of 120-350 cm^{-1} depending on geometrical properties.²⁶ Defects or disorders in carbon nanotubes are the sources for Raman peaks that are known as D bands which appear in 1250-1450 cm^{-1} range depending on the excitation laser energy. The defects are in general caused by in-plane heteroatoms, vacancies or grain boundaries and in general they lower the crystalline symmetry of the tubes. D bands show second order overtones at frequencies around twice the frequency of D bands which are referred to as G' bands.²⁷

The close dependency of the Raman signals on the structure of carbon nanotubes can be used as a useful characterization method. Frequency shifts of the RBM modes for example, provide information about the diameter of the tubes through $\omega_{RBM} = 227.0/d$ where ω_{RBM} is the frequency of the RBM Raman shift and d denote the tube diameter.²⁸ (n,m) integers can also be determined through the frequency of the RBM mode in Raman spectra of carbon nanotubes.¹⁸ D band at around 1350 cm^{-1} can be used as a sign for the presence of defects in the structure.²⁹ The shape of the transverse stretching G band at around 1590 cm^{-1} demonstrates the metallic or semiconductor properties of the carbon nanotubes.³⁰ According to the reported studies, G⁻ peak is assigned to TO and G⁺ to LO phonon modes of metallic nanotubes where the opposite is true for semiconductors. In addition, the G' band at around 2700 cm^{-1} is highly influenced by electron energy dispersion of carbon nanotubes and therefore, can be used for detecting possible dopants across the nanotube's structure.³¹

In this Chapter, we make use of isolated SWCNT to test the potential of our TERS setup for high resolution Raman imaging and to determine the resolution limit of our measurements on a reference object, as suggested in the previous studies.^{21,32-34}

5.2 Experimental Section

5.2.1 Sample Preparation

The raw single walled carbon nanotubes were purchased from Raymor NanotechTM (Lot no. raw RN-020) and purified based on the procedure suggested by S. Giordani *et al.*³⁵ The procedure involves three steps which are described in the following section.

5.2.1.1 Nitric Acid Treatment

200 mg of the raw-SWCT were dispersed into 680 mL of 7 M HNO₃ by sonication for 20 min. The reaction mixture was then put into a 1 L round bottom flask equipped with a condenser and the system was heated to 100 °C for 4 h. Subsequently reaction was quenched with 1000 g of ice. The dispersion was then filtered through a Milipore system (0.2 µm IsoporeTM filter) and washed with distilled water until the filtrate pH became neutral. A further 5 L of distilled water were used to wash the sample after the neutralization while the SWCNTs were never allowed to dry. Within this step a large percentage of possible metallic catalyst residues that were used for the synthesis of the carbon nanotubes will be removed.³⁶ Depending on the synthesis method the catalysts can range from MgO³⁷ to Al₂O₃³⁸ or nickel cobalt yttrium.³⁹

5.2.1.2 Hydrogen Peroxide Treatment

The nitric acid treated SWCNT's were dispersed into 400 mL of 10% H₂O₂ by sonication for 5 min inside a 1 L round bottom flask. The flask equipped with condenser was heated to 100 °C for 1 h; subsequently the reaction was quenched with 1600 g of ice and stand for 12 h. The SWCNTs were then washed with 2 L of distilled water and filtered over 0.2 µm IsoporeTM filter. Again it is essential to not let the solid dry. During oxidation by hydrogen peroxide, a part of carbonaceous impurities will be etched away and the majority of the oxygenated defects on the walls of the SWCNTs will be converted into carboxylic acid moieties.³⁵ It is been reported in literature that the oxygenated groups are created by treatment of SWCNTs with nitric acid³⁶ and are mostly located on carbonaceous fragments adsorbed onto the SWCNTs rather than on the side walls of the nanotube.⁴⁰

5.2.1.3 Sodium Hydroxide Treatment

The oxidized SWCNTs were dispersed in 400 mL of 2 M NaOH by sonication for 5 min. The reaction mixture was heated to 100 °C overnight in a 1 L round bottom flask equipped with a condenser. The day after, the reaction mixture was cooled to room temperature and the SWCNTs were washed with 200 ml of 2 M NaOH and filtered through 0.2 µm IsoporeTM filter. After the filtrate pH became neutral, 2 L of distilled

water, 400 mL of 1 M HCl followed by extra 2 L of distilled water were used for further washing of the SWCNTs. The solid was dried at 40 °C under vacuum for 2 days; a 26% yield was obtained. During this step, the carboxylated part of the carbonaceous impurities would be converted into more soluble salts and get removed.

After the carbon nanotubes were purified, they were dispersed in water and the resulting mixture got homogenized ultrasonically for about 15 min. A few droplets of the homogenized mixture were transferred onto clean glass cover slip. After the water was evaporated the samples were washed by quick dipping of the glass cover slip into clean distilled water.

5.2.2 TERS Experimental Details

The TERS setup that is used in the present study is described in detail in Chapter 3. The polarization of a linearly polarized laser beam ($\lambda=632.8$ nm, He-Ne laser) was first modified to generate radially polarized light using the optical setup that is also described in Chapter 3. The radial beam was focused on the sample by a high numerical aperture oil immersion microscope objective (PlanAPO Olympus, $N.A.=1.4$, x100). The backscattered light was collected by the same microscope objective. To minimize the thermal effects the power of the laser at the focal spot was limited to about 300 μ W. Topographic images and TERS spectra were acquired in non-contact AFM mode using gold coated AFM tips (NCL50 Nanoworld Inc.; resonance frequency 170 kHz, force constant 48 N/m). Gold coating was done inside a vacuum chamber through electron beam thermal evaporation of 25 nm of gold. Prior to gold, a 5 nm titanium adhesion layer was deposited on the AFM tip inside the same chamber. At the end of each TERS measurement, a TERS spectrum was acquired on clean glass cover slip to test for possible contamination of the tip. In addition, an AFM scan was carried out on the same spot where TERS measurements were performed. This was done to evaluate any thermal or physical damages on the sample surface.

5.3 Results and Discussion

Carbon nanotube sample on glass cover slip were first characterized by conventional Raman spectroscopy and AFM microscopy prior to TERS measurements. AFM image and Raman spectra acquired through illuminating the sample by radially polarized $\lambda=632.8$ nm laser are presented in **Figure 5.3**.

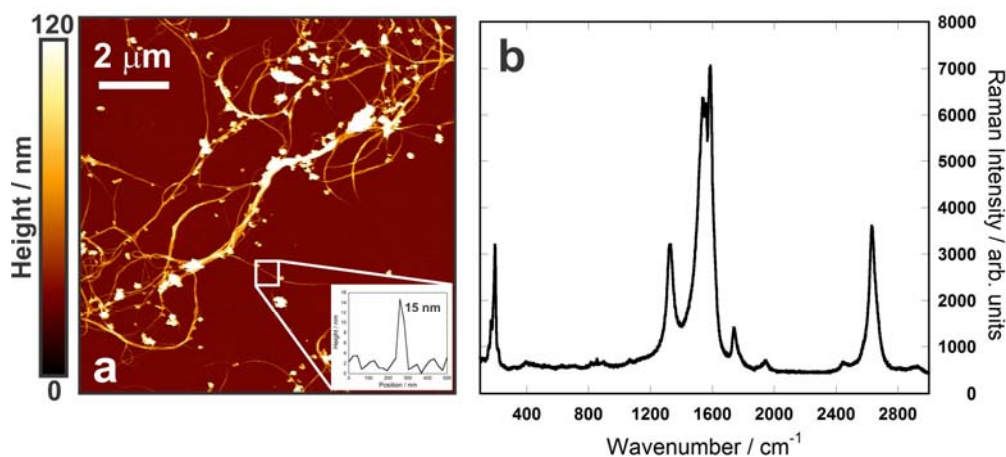


Figure 5.3 (a) AFM image of carbon nanotubes on glass cover slip. Evidenced by the inset cross-section curve, carbon nanotubes with sub-15 nm diameter are perfectly resolved (b) Raman spectrum of carbon nanotubes in far-field configuration

As the diameter of the nanotubes in AFM image in **Figure 5.3a** suggests the sample consists nearly mono dispersed carbon nanotubes on glass substrate. The peak assignment for the observed Raman spectrum in **Figure 5.3b** is in accordance with the information provided in section 5.1. The peak series at around 200 cm^{-1} correspond to the radial breathing mode bands (RBM). 1322 cm^{-1} is the D band of single walled carbon nanotubes. The two intense peaks at 1541 and 1591 cm^{-1} originate from the two G bands (TO and LO respectively). 2632 cm^{-1} is the G' band which is the overtone of D band.

5.3.1 Estimation of Lateral Resolution

The lateral resolution of the TERS measurements was evaluated through near-field mapping of the nanotubes. **Figure 5.4a** shows the near-field Raman map of a SWCNT that is created by integrating the G band in the collected spectra using the $[1400\text{--}1684\text{ cm}^{-1}]$

¹] spectral range. An area of 120x120 nm² has been mapped with a step size of 12 nm in both x and y direction, Acquisition time was set to 10 sec per pixel. Three sample spectra corresponding to three pixels inside the Raman map is presented in **Figure 5.4b**. The AFM topographic image of the mapped nanotube along with a topographic cross-section curve that indicates the height of the nanotube is presented in **Figures 5.4c** and **Figures 5.4e** respectively. **Figure 5.4d** shows average Raman intensity profile which is generated from the map in **Figure 5.4a**.

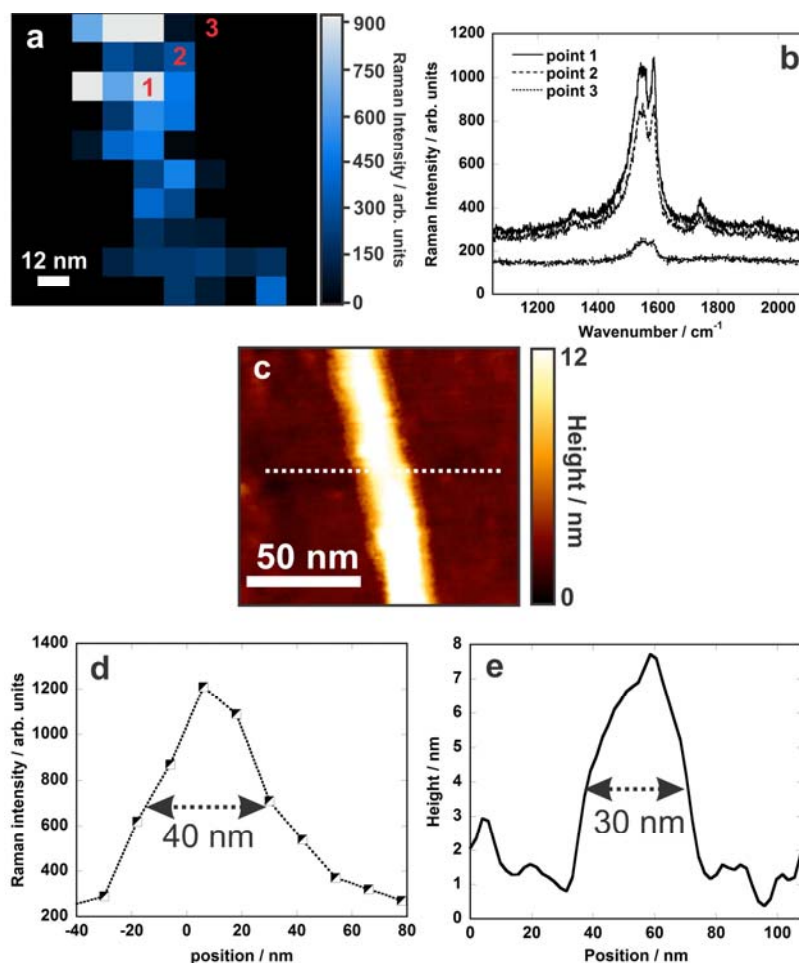


Figure 5.4 (a) Near-field Raman intensity map of SWCNT (b) TERS spectra of three arbitrary points on the TERS map (c) AFM topographic image of the SWCNT (d) averaged Raman cross-section obtained from the Raman map in (a), (e) topographic cross section obtained over the dashed line in (c)

The estimated width in AFM image of **Figure 5.4e** shows about 50% deviation from the height of the studied nanotube due to a convolution by the tip shape. Nevertheless, comparison of the widths (FWHM) of the SWCNT in AFM image of **Figure 5.4c** (30 nm) and an average width from the Raman map (40 nm) indicates high lateral resolution far beyond the diffraction limit and consequently the near-field nature of the Raman signals. Despite the fact that the estimated width in AFM image is convoluted by the tip shape⁴¹ while the dimensions estimated in Raman map is chemical signature, AFM is showing higher resolution in this measurements. We believe that unfavourable scattering effects at the edges of the SWCNT and nanometer drifting of the sample during the mapping process cause deviation from the results that are estimated by AFM topography. Similar Raman map was acquired after the tip was retracted from the sample, however, it was lacking Raman contrast because same signal intensities was recorded everywhere inside the mapped area. Considering the size of the mapping area and the similar Raman intensity observed at the mapped pixels, the resolution obtained in far-field measurements most definitely exceeds 120 nm (10 pixels, 12 nm each) which indicated the diffraction limit of conventional spectroscopy.

To avoid the potential drifting of our AFM system and more accurately estimate the limit of resolution in TERS measurements, we decreased the measurement duration by limiting the Raman spectroscopy to a single line that crosses the carbon nanotube. Consequently more spots with smaller step sizes can be measured within a shorter time range while the unfavourable scattering from the edges of the nanotubes will be reduced. The resulting Raman spectra collected along the white dashed line in **Figure 5.5a** were used to generate the Raman cross-section curve in **Figure 5.5b**. The separation between the consequent spots along the dashed line was as small as 1 nm and the acquisition time for each spot was set to 30 sec. A polynomial fit is used to more accurately estimate the half width at maximum height of the intensity peak in **Figure 5.5b**.

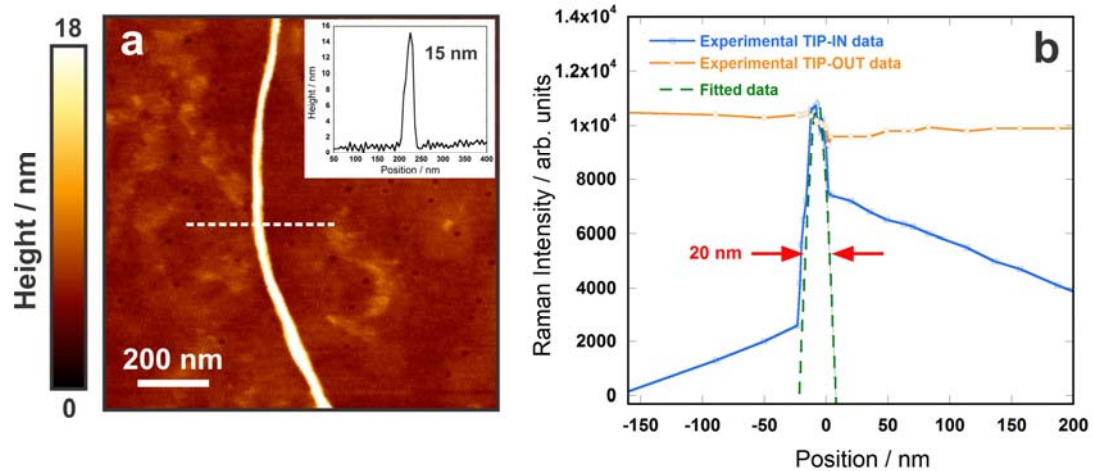


Figure 5.5 (a) AFM image of an isolated carbon nanotube with 15 nm diameter as shown in the inset topographic cross-section curve (b) Raman intensity profile along the dash line in orthogonal direction to the SWCNT's main axis while the tip is approached to (TIP-IN) and retracted from (TIP-OUT) the sample. The lateral resolution is estimated to be around 20 nm according to the fitted curve.

The collected spectra and the resulting cross-section curve in **Figure 5.5b** suggest a lateral resolution of ~ 20 nm for TIP-IN measurements where the TERS tip has approached the surface of the sample. This is in good agreement with the estimated height by AFM image of **Figure 5.5a**, therefore, an improvement of the resolution is achieved when compared to the results of **Figure 5.4**. As it is shown in **Figure 5.4b**, the Raman contrast along the mapped line was completely lost as soon as the tip was retracted from the surface of the carbon nanotube (TIP-OUT measurements). However, a constant large far-field distribution is observed with intensities close to the highest intensity that was detected in near-field measurements. This large far-field contribution can be explained by resonant behavior of SWCNT but at the same time can originate from undefined background carbon impurities or neighboring carbon compounds. In addition, the TIP-IN data show a non-symmetric shape on one side of the SWCNT, the exact source of which is not known at the moment. Similar to the previous discussion, the presence of carbon impurities or neighboring carbon compounds is a possible reason for this observation.

A similar experiment was performed on a different carbon nanotube using a different gold coated AFM tip to check the reproducibility of the results. Here the separation between the spots along the mapping line (white dashed line in **Figure 5.6a**) was set to 1 nm and the Raman spectrum from each point was acquired within 30 sec. The Raman intensity profile obtained from this measurement is presented in **Figure 5.6b**. Similar to **Figure 5.5**, a polynomial fit is used to more accurately estimate the half width at maximum height of the intensity peak in **Figure 5.6b**.

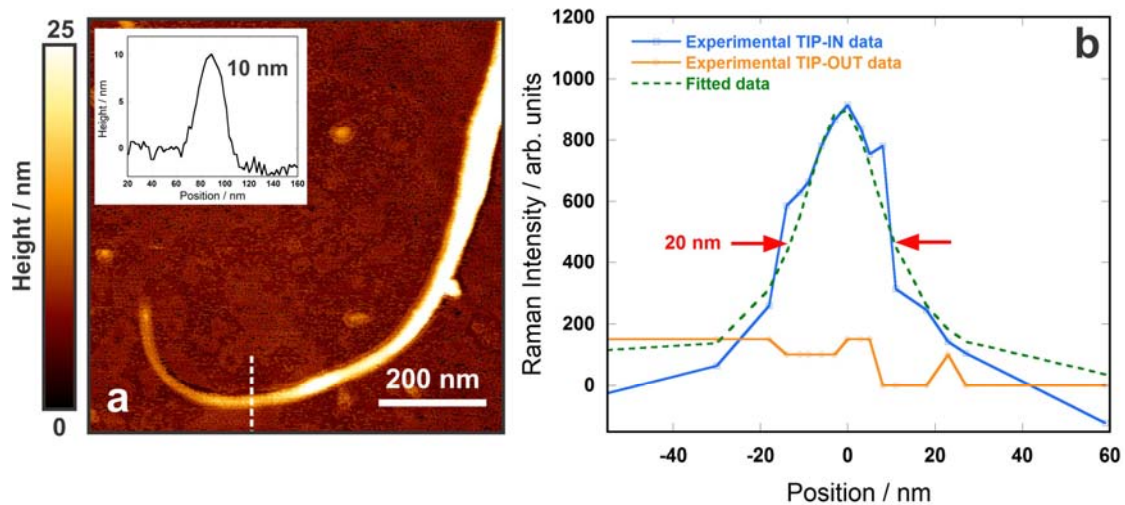


Figure 5.6 (a) AFM image of a nearly isolated carbon nanotube with 10 nm diameter as shown in the inset topographic cross-section curve **(b)** Raman intensity cross-section along the dash line in orthogonal direction to the SWCNT's main axis while the tip is approached to (TIP-IN) and retracted from (TIP-OUT) the sample. The lateral resolution is estimated to be around 20 nm according to the fitted curve.

As estimated by the AFM image in **Figure 5.6a** the diameter of the carbon nanotube along the mapped line is around 10 nm. TERS Raman cross-section however estimates the diameter to be around 20 nm and the Raman contrast was lost as soon as the tip was retracted as it has been shown in **Figure 5.6b**. Despite the fact that the lateral resolution is still well beyond the diffraction limit, the difference between the results of **Figure 5.5** and **Figure 5.6** demonstrate the influence of the tip quality on the limit of accessible resolution in similar measurements. Low reproducibility of the tip coating process results in TERS tips with variable apex sizes and consequently different performances.

Nevertheless, similar resolutions in both measurements of **Figure 5.5** and **Figure 5.6** along with the SEM image of the coated tip which was presented in Chapter 3 (**Figure 3.9**) estimates an average 20-30 nm diameter for the TERS tips that are utilized in this thesis. Therefore, spatial resolutions higher than 20 nm cannot be expected in TERS measurements conducted using such tips. On the other hand, the diameter of a single walled carbon nanotube is expected to be less than 2 nm, therefore according to the height of the studied carbon nanotubes in **Figures 5.4, 5.5** and **5.6**, the three measurements should have been performed on a bundle of SWCNT's. This suggests that the lateral resolution could reach a limit beyond 20 nm if a completely isolated carbon nanotube is present. This however is not easy to achieve when the sample is prepared by drop casting of SWCNT solution on glass and more sophisticated sample preparation methods are needed.

5.3.2 Near-Field Origin of the Enhanced Raman Signals

The near-field origin of the observed Raman signal in TIP-IN measurements was evaluated by measuring the decrease of the enhanced Raman signal as a function of tip-sample distance. As the theoretical discussions in Chapter 2 predict, it is expected that the Raman intensities decay quickly as the tip-sample distance increases. In this experiment the tip was positioned over an arbitrary spot on carbon nanotube and a Raman spectra was collected first as the tip was in approach position (TIP-IN) with the sample. The separation between the tip and the sample was then increased with the step sizes of a few nanometers and a Raman spectrum was collected for each position. The distance between the sample and the tip varied between 0 to 1000 nm. The results of this measurement are presented in **Figure 5.7**. The intensity of the G band is utilized for generating this curve.

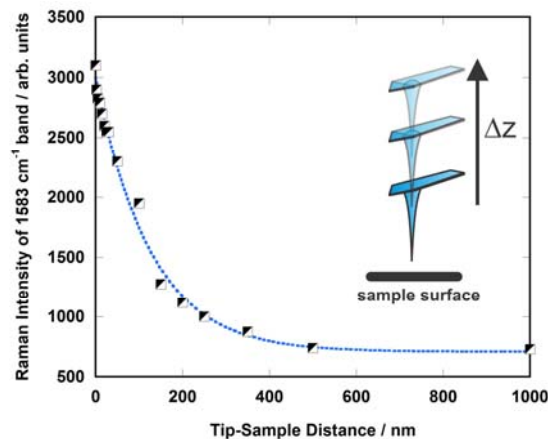


Figure 5.7 Dependence of the Raman intensity of the G band on the longitudinal tip-sample separation. The squared points show the experimental data and the dashed line shows a fitted line over these data.

According to the resulted curve presented in **Figure 5.7**, for tip-sample separations below 150 nm the signal decays quit rapidly with the distance increase. At around 150 nm half of the Raman intensities are lost and 500 nm distance from the sample surface all the near-field contributions disappear. Much shorter decay rates of 11 nm has been reported in a TERS study of CdSe nanowire done by A. Hartschuh *et al.*⁴² where at distanced above 30 nm the near-field signal was no longer detectable. Generally, it is expected that the longitudinal confinement be consistent with lateral resolution of the TERS measurements and the tip radius. Nevertheless, the low reproducibility of the TERS tips do not allow to acquire similar resolution through different TERS tips even though they are produced under the same condition. Therefore, we believe that the slow decay rate of the enhancement originates from poor quality of the TERS tip that was utilized for this specific measurement. The influence of the far-field contributions should also play a considerable role.

5.3.3 Estimation of the Enhancement Factor

To estimate the enhancement factor for the G band and the conducted experiments in general, the intensity of the Raman band in TIP-IN and TIP-OUT position should not only be compared but also corrected with respect to the illuminated area in each of the

two cases. For the mapping of **Figure 5.4**, the Raman intensity of TIP-IN case is around 9 times larger than the results acquired from TIP-OUT measurements. To normalize the intensities with respect to the ratio of the detected area, the method suggested in reference 22 is used.³² The carbon nanotubes are generally longer than the focus area; therefore, the area probed for far-field measurements can be estimated as a product of the tube diameter (~ 9 nm) and the focus diameter ($\sim 1\mu\text{m}$) to be 9000 nm^2 . The probed area in near-field will be then the product of the tube diameter and the tip apex diameter (~ 20 nm) to be 180 nm^2 . Similar to the discussion of section 3.5 from Chapter 3, the following equation can be used for calculation of the enhancement factor:

$$EF_{TERS} = \frac{I_{TIP-IN}}{I_{TIP-OUT}} \times \frac{A_{farfield}}{A_{nearfield}} \quad (5.1)$$

Where I_{TIP-IN} and $I_{TIP-OUT}$ denote the Raman intensities in TIP-IN and TIP-OUT measurements and $A_{nearfield}$ and $A_{farfield}$ show the probed areas in two cases. This results in an enhancement factor of ~ 450 for the conducted measurement in **Figure 5.4**. This value are comparable to enhancement factors reported in the literature for similar TERS experiments, ranging from 10 to 10^8 but most recent studies converge towards a normalized enhancement factor in the 10^2 range.^{32,43-46}

5.4 Conclusion

We conclude that TERS provides a powerful method for nanoscale Raman imaging with around 20 nm lateral resolution. The achievable resolution however, is strongly sensitive to the TERS activity and apex size of the tip utilized for the measurements. The high resolution chemical maps along with AFM topographic images opens up new possibilities in characterization of nanoscale feature on carbon nanotubes such as structural strains,⁴⁶ intertube junctions²³ or the adsorption position of molecules along the surface of the tubes.⁴⁵ Nevertheless, reproducibility of the TERS experiment is tip-dependent and sharper tips would presumably lead to a better lateral resolution with our setup and similar excitation conditions.

5.5 References

- (1) Bethune, D. S.; Kiang, C. H.; de, V. M. S.; Gorman, G.; Savoy, R.; Vazquez, J.; Beyers, R. *Nature* (1993), 363, 605.
- (2) Iijima, S.; Ichihashi, T. *Nature* (1993), 363, 603.
- (3) Dresselhaus, M. S.; Dresselhaus, G.; Eklund, P. C.; Editors *Science of Fullerenes and Carbon Nanotubes*; Academic Press: San Diego, 1996.
- (4) Saito, R.; Dresselhaus, G.; MS., D. *Physical Properties of Carbon Nanotubes*; Imperial Coll. Press: London, 1998.
- (5) Saito, R.; Fujita, M.; Dresselhaus, G.; Dresselhaus, M. S. *Appl. Phys. Lett.* (1992), 60, 2204.
- (6) Tans, S. J.; Devoret, M. H.; Dal, H.; Thess, A.; Smalley, R. E.; Geerligs, L. J.; Dekker, C. *Nature* (1997), 386, 474.
- (7) Bockrath, M.; Cobden, D. H.; McEuen, P. L.; Chopra, N. G.; Zettl, A.; Thess, A.; Smalley, R. E. *Science* (1997), 275, 1922.
- (8) Tans, S. J.; Verschueren, A. R. M.; Dekker, C. *Nature* (1998), 393, 49.
- (9) Dai, H.; Hafner, J. H.; Rinzler, A. G.; Colbert, D. T.; Smalley, R. E. *Nature* (1996), 384, 147.
- (10) Dillon, A. C.; Jones, K. M.; Bekkedahl, T. A.; Kiang, C. H.; Bethune, D. S.; Heben, M. J. *Nature* (1997), 386, 377.
- (11) Liu, C.; Fan, Y. Y.; Liu, M.; Cong, H. T.; Cheng, H. M.; Dresselhaus, M. S. *Science* (1999), 286, 1127.
- (12) Ye, Y.; Ahn, C. C.; Witham, C.; Fultz, B.; Liu, J.; Rinzler, A. G.; Colbert, D.; Smith, K. A.; Smalley, R. E. *Appl. Phys. Lett.* (1999), 74, 2307.
- (13) Bielicka, A.; Wisniewski, M.; Terzyk, A. P.; Gauden, P. A.; Furmaniak, S.; Roszek, K.; Kowalczyk, P.; Bieniek, A. *J. Phys.: Condens. Matter* (2013), 25, 355002.
- (14) Lee, Y. K.; Choi, J.; Wang, W.; Lee, S.; Nam, T.-H.; Choi, W. S.; Kim, C.-J.; Lee, J. K.; Kim, S.-H.; Kang, S. S.; Khang, D. *ACS Nano* (2013), 7, 8484.
- (15) Baldacchini, C.; Chamorro, M. A. H.; Prato, M.; Cannistraro, S. *Adv. Funct. Mater.* (2011), 21, 153.
- (16) Duesberg, G. S.; Loa, I.; Burghard, M.; Syassen, K.; Roth, S. *Phys. Rev. Lett.* (2000), 85, 5436.
- (17) Jorio, A.; Pimenta, M. A.; Souza, F. A. G.; Saito, R.; Dresselhaus, G.; Dresselhaus, M. S. *New J. Phys.* (2003), 5, 1.
- (18) Jorio, A.; Saito, R.; Hafner, J. H.; Lieber, C. M.; Hunter, M.; McClure, T.; Dresselhaus, G.; Dresselhaus, M. S. *Phys. Rev. Lett.* (2001), 86, 1118.
- (19) Yu, Z.; Brus, L. *J. Phys. Chem. B* (2001), 105, 1123.

- (20) Kneipp, K.; Kneipp, H.; Corio, P.; Brown, S. D. M.; Shafer, K.; Motz, J.; Perelman, L. T.; Hanlon, E. B.; Marucci, A.; Dresselhaus, G.; Dresselhaus, M. S. *Phys. Rev. Lett.* **(2000)**, *84*, 3470.
- (21) Hartschuh, A.; Sanchez, E. J.; Xie, X. S.; Novotny, L. *Phys. Rev. Lett.* **(2003)**, *90*, 0955031.
- (22) Chen, C.; Hayazawa, N.; Kawata, S. *Nat. Commun.* **(2014)**, *5*, 43121.
- (23) Okuno, Y.; Saito, Y.; Kawata, S.; Verma, P. *Phys. Rev. Lett.* **(2013)**, *111*, 2161011.
- (24) Anderson, N.; Hartschuh, A.; Cronin, S.; Novotny, L. *J. Am. Chem. Soc.* **(2005)**, *127*, 2533.
- (25) Dresselhaus, M. S.; Dresselhaus, G.; Jorio, A.; Souza Filho, A. G.; Saito, R. *Carbon* **(2002)**, *40*, 2043.
- (26) Saito, R.; Gruneis, A.; Samsonidze, G. G.; Brar, V. W.; Dresselhaus, G.; Dresselhaus, M. S.; Jorio, A.; Cancado, L. G.; Fantini, C.; Pimenta, M. A.; Souza, F. A. G. *New J. Phys.* **(2003)**, *5*, 1.
- (27) Brown, S. D. M.; Jorio, A.; Dresselhaus, M. S.; Dresselhaus, G. *Phys. Rev. B: Condens. Matter Mater. Phys.* **(2001)**, *64*, 0734031.
- (28) Araujo, P. T.; Maciel, I. O.; Pesce, P. B. C.; Pimenta, M. A.; Doorn, S. K.; Qian, H.; Hartschuh, A.; Steiner, M.; Grigorian, L.; Hata, K.; Jorio, A. *Phys. Rev. B: Condens. Matter Mater. Phys.* **(2008)**, *77*, 2414031.
- (29) Maultzsch, J.; Reich, S.; Thomsen, C. *Phys. Rev. B: Condens. Matter Mater. Phys.* **(2001)**, *64*, 1214071.
- (30) Piscanec, S.; Lazzeri, M.; Robertson, J.; Ferrari, A. C.; Mauri, F. *Phys. Rev. B: Condens. Matter Mater. Phys.* **(2007)**, *75*, 0354271.
- (31) Maciel, I. O.; Anderson, N.; Pimenta, M. A.; Hartschuh, A.; Qian, H.; Terrones, M.; Terrones, H.; Campos-Delgado, J.; Rao, A. M.; Novotny, L.; Jorio, A. *Nat. Mater.* **(2008)**, *7*, 878.
- (32) Cancado, L. G.; Hartschuh, A.; Novotny, L. *J. Raman Spectrosc.* **(2009)**, *40*, 1420.
- (33) Hartschuh, A.; Anderson, N.; Novotny, L. *Int. J. Nanosci.* **(2004)**, *3*, 371.
- (34) Nicklaus, M.; Nauenheim, C.; Krayev, A.; Gavriluk, V.; Belyaev, A.; Ruediger, A. *Rev. Sci. Instrum.* **(2012)**, *83*, 0661021.
- (35) Flavin, K.; Kopf, I.; Del, C. E.; Navio, C.; Bittencourt, C.; Giordani, S. *J. Mater. Chem.* **(2011)**, *21*, 17881.
- (36) Hu, H.; Zhao, B.; Itkis, M. E.; Haddon, R. C. *J. Phys. Chem. B* **(2003)**, *107*, 13838.
- (37) Fu, X.; Cui, X.; Wei, X.; Ma, J. *Appl. Surf. Sci.* **(2014)**, *292*, 645.
- (38) Nguyen, M. A.; Ngo, D. T.; Le, V. T.; Cao, D. V. *Adv. Nat. Sci.: Nanosci. Nanotechnol.* **(2013)**, *4*, 0350181.
- (39) Lekgoathi, M. D. S.; Augustyn, W. G.; Heveling, J. *J. Nanosci. Nanotechnol.* **(2011)**, *11*, 7001.

- (40) Salzmann, C. G.; Llewellyn, S. A.; Tobias, G.; Ward, M. A. H.; Huh, Y.; Green, M. L. H. *Adv. Mater.* **(2007)**, *19*, 883.
- (41) Eaton, P. J.; West, P. *Atomic force microscopy*; Oxford University Press New York, 2010.
- (42) Boehmler, M.; Hartschuh, A. *Chem. Phys. Chem.* **(2012)**, *13*, 927.
- (43) Budich, C.; Neugebauer, U.; Popp, J.; Deckert, V. *J. Microsc.* **(2008)**, *229*, 533.
- (44) Pettinger, B.; Ren, B.; Picardi, G.; Schuster, R.; Ertl, G. *Phys. Rev. Lett.* **(2004)**, *92*, 0961011.
- (45) Yan, X.; Suzuki, T.; Kitahama, Y.; Sato, H.; Itoh, T.; Ozaki, Y. *Phys. Chem. Chem. Phys.* **(2013)**, *15*, 20618.
- (46) Yano, T.-a.; Ichimura, T.; Kuwahara, S.; H'Dhili, F.; Uetsuki, K.; Okuno, Y.; Verma, P.; Kawata, S. *Nat. Commun.* **(2013)**, *4*, 3592.

Chapter 6

6 Tip-enhanced Raman Imaging and Nanospectroscopy of Etched Silicon Nanowires²

In this Chapter, TERS is used to investigate the influence of strain in isolated and overlapping silicon nanowires prepared by chemical etching of a (100) silicon wafer. An AFM tip made of nanocrystalline diamond and coated with a thin layer of silver is used in conjunction with an excitation wavelength of 532 nm in order to probe the first order optical phonon mode of the isolated [100] silicon nanowires. The frequency shift and the broadening of the silicon first order phonon are analyzed for distinct nanowires that are disposed in straight, bent or overlapping configuration over a microscope cover slip. The TERS spatial resolution is close to the topography provided by the nanocrystalline diamond tip and subtle spectral changes are observed for different nanowire configurations.

6.1 Introduction

Owing to their superior electronic, optical, mechanical, thermal and chemical properties, silicon nanowires (SiNW) have been investigated for a wide range of potential applications. Silicon nanowires exhibit excellent photo-catalytic activity,¹ and due to their direct path of charge transfer,² they can be used as anode materials and improve the storage capacity of lithium ion batteries.³ In the field of photovoltaics, SiNW-based solar cells can achieve efficient absorption of sunlight by using only 1% of the active material required in conventional solar cells.⁴ Also because of their poor thermal conductance, silicon nanowires could act as efficient thermoelectric materials.⁵ However, these physical properties are sensitive to the nanoscale variations in the crystalline structure of the nanowires. For example, it has been reported that surface roughness influences the

² A version of this chapter has been published in [*Sensors* (2013), 13, 12744.]. Reproduced with permission from the Multidisciplinary Digital Publishing Institute

thermoelectric performance of silicon nanowires.⁶ Therefore it is essential to develop characterization techniques that provide insight into the structure of the nanowires on a nanometer scale. In this context, Raman spectroscopy serves as a powerful characterization technique with sensitivity to the crystal lattice structure. The shape and the frequency shift of the Raman peaks may reveal useful information about the crystallinity, the amorphicity, the induced mechanical strain and even about the diameter of nanoscale silicon nanowires.^{7,8} Therefore, Raman spectra of silicon nanowires are of great value for understanding the properties of isolated nanowires.⁹

Despite the fact that previous studies provide very useful information about the silicon nanowires, they all lack specificity due to their limited spatial resolution. Measurements acquired from far-field conventional measurements are an average of the bulk properties that results in the loss of the spatial information and the knowledge of the distribution of defects.¹⁰ In an attempt to surpass this problem, TERS opens up many new possibilities, including better spatial resolution and better surface sensitivity.¹¹

TERS is not limited by the diffraction limit of light¹² and it has reached 1.7 nm lateral spatial resolution, which provides significantly sharpened optical details of the sample.^{13,14} In addition, due to a localized surface plasmon resonance which is confined at the apex of the metallic tip, TERS can provide detailed spectroscopic information from a functionalized surface or an interface with a high specificity. Nevertheless, due to the enhancement of the longitudinal field by the metal tip¹⁵ and the possible depolarization effects from the TERS probe, polarized TERS measurements are limited as opposed to conventional confocal Raman spectroscopy where full polarization measurements are accessible for both excitation and scattered signals.^{10,16,17}

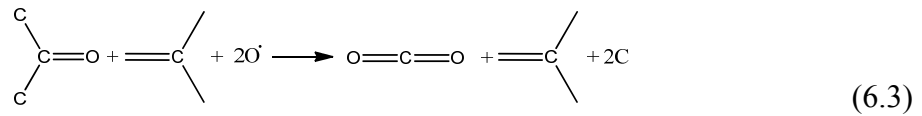
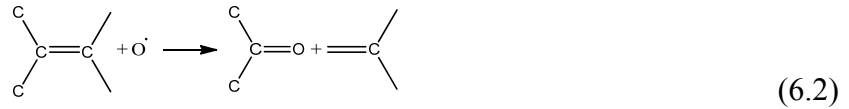
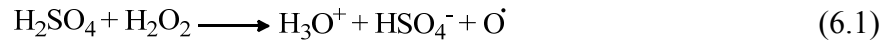
In this Chapter, isolated [100] nanowires have been dispersed onto glass cover slip and studied under the TERS setup using a silver coated nanocrystalline diamond AFM tip. The spatial and spectral resolution accessible in the TERS setup allows for the precise assignment of the vibrational frequency shifts and the change of FWHM (full width at half maximum) in silicon Raman signal to the strain induced in silicon nanowires due to the structural variations. In this study we have made use of nanocrystalline diamond tips

to prevent the interference between the silicon signal of nanowires and the silicon signal from the most common silicon based AFM tips. Alternatively, other tips made of Si_3N_4 , oxidized silicon or modified glass tips can be used in similar studies.¹⁸

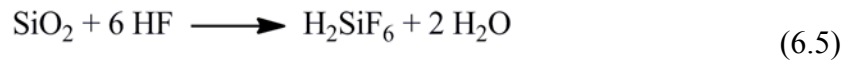
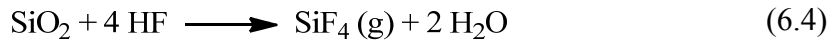
6.2 Experimental Section

6.2.1 Sample Preparation

Silicon nanowires were synthesized following the method proposed by Zhang *et al.*¹⁹ N-type (phosphorous doped) silicon wafers with a thickness of 525 μm , a resistivity of 1.5 Ohm.cm and a (100) orientation were cut into smaller pieces and then cleaned with acetone, ethanol and water in a subsonic device to remove a part of the organic impurities. Next, the silicon pieces were cleaned at room temperature by immersing them for 10 min in a 3:1 (v/v) Piranha mixture of H_2SO_4 (98%) and H_2O_2 (35%) followed by immersion in a 5% HF solution for about 3 min. The mechanism of action for Piranha for removing carbon impurities is summarized in equations (6.1) to (6.3):

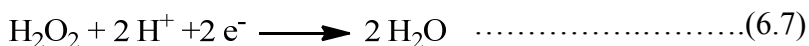


The mechanism of action for HF to remove silicon dioxide is shown in equations (6.4) and (6.5)



The surface of the silicon pieces will be hydrogen terminated in HF aqueous solution. Such surfaces have enhanced stability under ambient condition and can be handled in air for a longer time.

On the next step, silver nanoparticles were deposited on the wafer pieces by dipping the silicon wafers into silver coating solution of 4.8 M HF and 0.005 M of AgNO₃ for one min. After a uniform layer of silver nanoparticles were formed, the silicon pieces were washed with water to remove extra Ag⁺ ions. The silicon pieces with the uniform layer of nanoparticles were then etched in an etchant solution composed of 4.8 M HF and 0.4 M H₂O₂ for 40 min. 4.8 M HF acts as a strong oxidizer to initiate the electroless oxidation of silicon. In an exchange reaction, silicon is oxidized to form soluble hexafluoride complex and silver ions are reduced by electron transfer from the valence band of silicon. Reduction of silver creates nanoclusters of silver that forms a galvanic cell with uncovered silicon areas. The corresponding half reactions are summarized in equations 6.6 to 6.8:²⁰



The nanoclusters of silver catalyze the etching reaction, sink below the surface and leave behind columns of one-dimensional silicon nanostructures. After the etching step, the samples were washed with water and the Ag catalyst clusters were removed by immersion in a 1:1 (v/v) solution of HNO₃ and H₂O followed by an immersion in 5% HF solution. Finally the wafers were washed with water to remove remaining corrosive HF from the wires. This procedure results in formation of nanowires oriented normal to the surface of the (100) wafer, with [100] direction, diameters ranging from 40 to 200 nm and lengths varying from 10 to 50 μm. To isolate and disperse the synthesized wires, the surface of the silicon wafer pieces was gently scratched by a razor blade and the scratched powder was transferred into ethanol. The resulting solution got homogenized

ultrasonically for about 10 min and then a drop of this solution was transferred onto a clean glass microscope cover slip.

6.2.2 TERS Setup

The TERS setup used in this study is as described in chapter 3. The linearly polarized incident laser beam ($\lambda = 532$ nm, Compass 315 M laser, Coherent, Santa Clara, CA, USA) was focused on the sample with a high numerical aperture oil immersion microscope objective (PlanAPO Olympus, $N.A.=1.4$, $\times 100$) which collects the backscattered light as well. The power of the laser at the focal spot was set to about 300 μW to rule out temperature induced spectral fluctuation. AFM topography was acquired in non-contact AFM mode using nanocrystalline diamond tips. For TERS experiments nanocrystalline diamond AFM tips were exclusively used (ND-DTIRL-4 All-Diamond tip, typical oscillating frequency of 240 kHz and a force constant of 30 N/m, Advanced Diamond Technologies, Inc., Romeoville, IL, USA) and were coated with 5 nm of titanium followed by 20 nm of silver by means of electron beam thermal evaporation of silver inside a vacuum chamber. The coated tips were used within a day after coating before oxidation degrades the thin silver layer.

6.3 Results and Discussion

6.3.1 Raman Characterization of Silicon Nanowires

Raman spectra of a single silicon nanowire and a bulk (100) silicon wafer were acquired prior to the TERS measurements. The two spectra are shown in **Figure 6.1**.

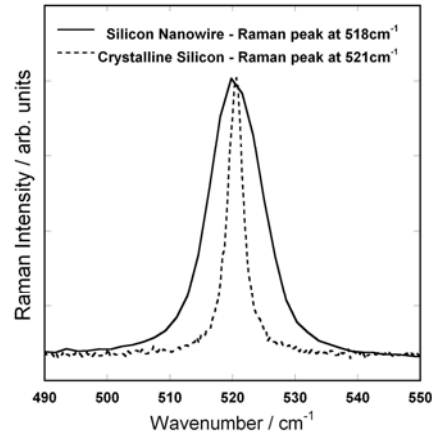


Figure 6.1 First order optical phonon Raman peak of silicon nanowire and (100) silicon wafer

In the absence of internal or external stress, in back scattering geometry, the triply degenerate first order optical phonon modes of silicon (1 LO, 2TO) result in a single Raman peak at 521 cm^{-1} for a silicon wafer while it shifts to 518 cm^{-1} for a 60 nm diameter silicon nanowire. Furthermore, the Raman peak shows a significant broadening with FWHM of 10 cm^{-1} as compared to 2.5 cm^{-1} for bulk silicon wafer. This spectral variations and a qualitative investigation of the phenomena was previously reported in literature.⁸ In brief, when the crystalline sizes decreases, momentum conservation will be relaxed and Raman active modes will no longer be limited to the center of the Brillouin zone.

For silicon sample subject to stress, the characterization of the phonon modes (LO or TO) by Raman spectroscopy depends on the sample crystallinity, the orientation of the crystal with respect to the incident polarization but also the directivity of the stress (uniaxial or biaxial) and its sign (compressive or tensile). For negative uniaxial (compressive) stress along the [111] direction of a silicon wafer, the triply degenerate optical mode split into two Raman peaks with wave vectors parallel (singlet) or perpendicular (doublet) to the strain direction.^{21,22} In backscattering geometry, only the singlet mode can be observed and the optical-phonon frequency can be predicted with respect to the unstrained silicon lattice.²²

6.3.2 TERS Tip Alignment

Similar to the procedure of section 3.4.1.2 of Chapter 3, vertical deflection images (**Figure 6.2a**) and Raman intensity maps of the silver coated nanocrystalline diamond AFM cantilever (**Figure 6.2b**) have been utilized to find the position of the tip apex. Raman intensity map is generated by integration of the Raman signal scattered by the nanocrystalline diamond tip shown in **Figure 6.2c** in $1207\text{-}1653\text{ cm}^{-1}$ spectral ranges.

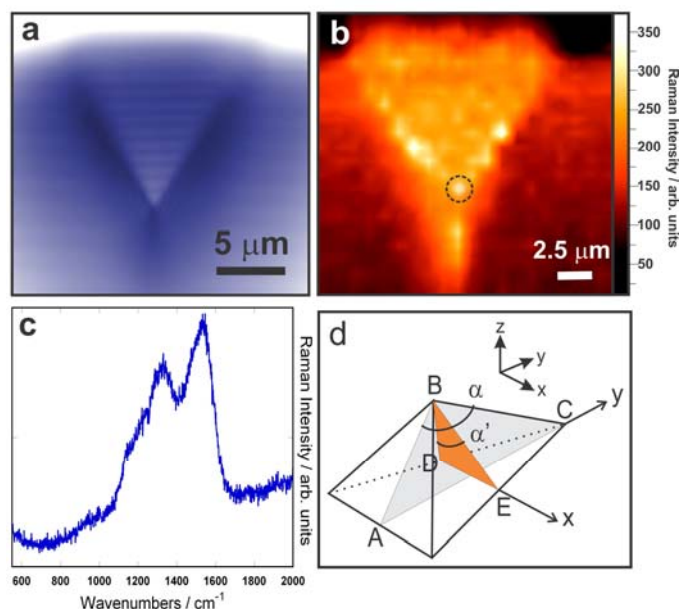


Figure 6.2 (a) Vertical deflection image of the nanocrystalline diamond tip and cantilever coated with 5 nm titanium and 20 nm silver (b) Raman intensity map of the same tip. The three edges of the tetrahedral pyramid can clearly be distinguished (c) Raman spectra of a nanocrystalline diamond tip (d) Geometry of the nanocrystalline tetrahedral diamond tip, $\alpha = 125.24^\circ$ and $\alpha' = 79.34^\circ$

The vertical deflection image (**Figure 6.2a**) and the Raman scattering of the tip (**Figure 6.2b**) both show clearly the tetrahedral structure of the tip. Scans of the tip over smaller area are then performed to optimize the signal and tune the position of the tip.

It is noteworthy that the Rayleigh scattering method was not used for alignment of the TERS tip because of the difficulty in recording sharp scattering images of the

nanocrystalline diamond tip, presumably due to the wide angles formed by the tetrahedral tip of 125.24° and 79.34° along the Y and X axes, respectively. The tetrahedral tip and its wide angles along the X and Y direction are depicted in **Figure 6.2d**.

After the position of the tip was found, the tip cantilever was immobilized at the defined x-y position in **Figure 6.2b** with the highest Raman intensity that corresponds to the tip position and laser focal point simultaneously. In **Figure 6.2b** some intense Raman spectra located along the sharp edges of the tetrahedral pyramid can also be observed. However, the shape of the Raman map together with the vertical deflection image clearly reveals the tip position located at the crossing point of the three edges, allowing one to determine accurately the position of the tip. It should be noted here that the Raman signature of the nanocrystalline diamond would be different from a diamond material containing large diamond grains and rich in graphitic phase.²³ TEM observations on the nanocrystalline diamond have shown agglomeration of nanoscale diamond grains with steep grain boundaries and no amorphous phase between them.

After immobilization of the tip, preliminary AFM images of the nanowire were acquired in order to select the points to be probed. Minimum interaction between the tip and the sample was used in order to avoid any wear of the metallic coating of the tip. This weak interaction may result in poor AFM image qualities. Sharper topographical images of the wire of interest were generally collected using either the same tip or using a non-coated tip once the TERS measurements were finished.

6.3.3 TERS Imaging of Silicon Nanowires

After the AFM image of the silicon nanowires were acquired (**Figure 6.3a**), TERS spectra of various nanowires were collected in non-contact mode by moving the sample in the *xy* plane using a piezoelectric stage. Here the Raman spectra of the each nanowire were collected when the TERS tip was in proximity of the wire (TIP-IN) and when the tip was withdrawn from the sample (TIP-OUT). The Raman spectra were collected by step-scanning the isolated wire with a 250 nm step in the x and y directions. Smaller scan steps were avoided at this stage to prevent the considerable increase of the mapping time duration. By integration of the first order optical phonon silicon Raman signal in the

collected spectra, Raman intensity map of the silicon nanowires were generated for both TIP-IN and TIP-OUT measurements. The maps are presented in **Figure 6.3b** and **Figure 6.3c**, respectively. The acquisition time for collecting the individual Raman spectra was set to 1 sec/spectrum.

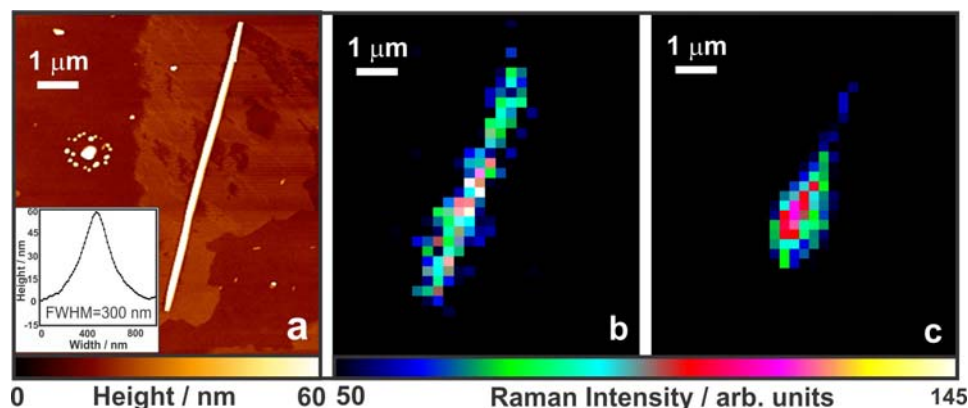


Figure 6.3 (a) AFM image and topographic cross-section of the studied silicon nanowire. The AFM image was recorded with a non-coated tip after the TERS experiments. The lateral resolution of the AFM cross-section is poor compared to the height resolution presumably due to the wide opening angle of the tip apex shown in **Figure 6.2d** (b) near-field (TIP-IN) Raman intensity map of the silicon nanowire showing the variation of the silicon Raman signal intensity (c) far-field (TIP-OUT) Raman intensity map of the silicon nanowire. For (b) and (c) the spectra were integrated over the $511\text{-}534\text{ cm}^{-1}$ spectral range.

According to the Raman map shown in **Figure 6.3b**, the TERS tip has just slightly improved the lateral resolution of the mapping when compared to the Raman map which was generated from the far-field signals in **Figure 6.3c**. We suggest two reasons for this observation: *i.* the wide opening angle of the tip promotes the enhancement of the signals not only from the apex of the tip but also from the side walls which are also coated with silver. This has a negative influence on the lateral resolution of the TERS measurement; *ii.* 250 nm mapping steps increase the chance of undesirable reflections from the edges of the nanowires which makes distinguishing of the boundaries more difficult. Nevertheless, the far-field map in **Figure 6.3c** is less homogeneous implying that the near-field contribution is important to provide a good sensitivity to probe the full wire. With regards

to the AFM image that is presented in **Figure 6.3a**, the estimated height of the nanowire corresponds to the nominal diameter of the single nanowire (~60 nm) while the lateral cross-section of the wire shown as an inset of **Figure 6.3a** is about ~300 nm due to the convolution with the geometry of the AFM tip. This image was acquired after the TERS experiments were performed.

6.3.4 Estimation of Accessible Spatial Resolution

As mentioned above, the relatively large size of the mapping area makes the collection process of the spectra lengthy if the separation between the individual points in the map decreases. On the other hand, thermal effects that might be induced during a long illumination process reduce the reliability of the acquired results. Nevertheless, it is difficult to estimate the spatial resolution reached in the near-field measurements through analyzing the data acquired using 250 nm mapping steps along the nanowire due to the uncertainty caused by reflection of the laser from the edges of the wire. Furthermore the measurements acquired with the tip approached to the sample include the far-field contribution that significantly broadens the spatial resolution especially when the experiment is conducted under by short acquisition time and low signal/noise detection ratio. For this reason, we have scanned three short lines on a random section of a nanowire with smaller step sizes and in the orthogonal direction with respect to the long axis of the wire. The acquisition time was set to 15 sec/spectrum. The lines are shown in **Figure 6.4a**. Each of the three lines were 3 μm long and the step between each individual spectra was set to 30 nm in both x and y direction along the lines. By integrating the silicon peak intensity for each pixel of the map and averaging the intensity values for corresponding pixels in these three lines, the spatial resolution limit of our experiment was estimated. **Figure 6.4a** shows the AFM image of the corresponding nanowire along with the topographic cross-section curve. Variations in the intensity of the silicon Raman signal with TIP-IN and TIP-OUT averaged along three lines are presented in **Figure 6.4b** and **Figure 6.4c**. The two dashed curves in these figures present the experimentally measured Raman intensities of the total field (TIP-IN) and far-field (TIP-OUT) while the solid curves are the Gaussian model which is fitted on the experimental data points. In this experiment, when the tip is close to the sample the signal is significantly higher

(6000 counts) compared with the case when the tip is retracted (250 counts). The optical contrast defined by $C = (I_{TIP-IN} - I_{TIP-OUT}) / I_{TIP-OUT}$ in this case will be around 20. The spatial resolution for this experiment was estimated by taking the average silicon peak intensity values in corresponding pixels of the three lines.

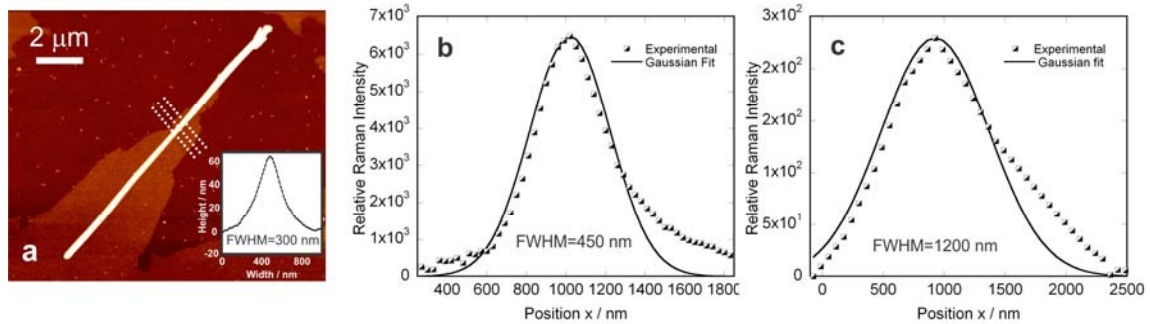


Figure 6.4 (a) AFM image of a single silicon nanowire and the topography cross-section of the same nanowire (b) total Raman signal when the metal tip approaches the sample. The full width at half maximum indicates a spatial resolution of ~450 nm as compared to a topographical cross-section of ~300 nm provided by the AFM. (c) the optical cross-section obtained in far-field measurements provides a full width at half maximum of 1200 nm and significantly lower Raman intensities.

As it could be observed in **Figure 6.4b**, ~450 nm resolution was obtained for near-field that matches the dimensions of the wire predicted by the topographic cross section curve (~300 nm) more closely. Note that due to the difference of signal between the two experiments (TIP-IN *versus* TIP-OUT), the removal of the far-field contribution from the experiment where the tip has approached the sample does not improve the spatial resolution. We believe that any variation from the actual size of the wire is due to the geometry of the tip (wide opening angle) and possible inhomogeneities of the metal coating of the TERS tip. As shown in **Figure 6.4c**, the far-field spectra predict a resolution of ~1200 nm which corresponds roughly to the dimension of the laser focal spot.

6.3.5 Estimation of Enhancement Factor

The determination of the local enhancement factor is more delicate since it implies a good knowledge of the volume of the tip that participates to the enhancement. To estimate the TERS contrast of the current experiment, a series of Raman spectra were acquired at selected locations on the surface of the SiNW with an acquisition time of 10 sec/spectrum. The TERS spectrum of the silicon nanowires along with the Raman spectra obtained with TIP-IN and TIP-OUT of the [100] nanowire are shown in **Figure 6.5**.

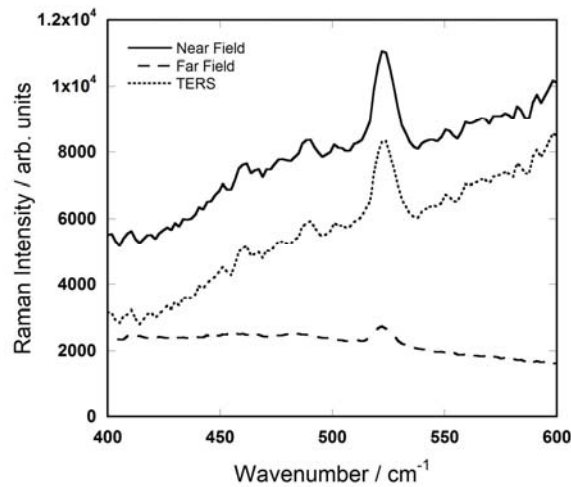


Figure 6.5 Raman spectra with metalized tip positioned in the optical near-field and in the optical far-field of the sample. The difference of the two spectra indicates the enhancement induced by the metallic tip.

Here, the TERS spectrum is obtained by calculating the difference between the two experiments conducted with the tip close and far from the sample. In addition to the improvement of the spatial resolution, a contrast ratio ($C = (I_{TIP-IN} - I_{TIP-OUT}) / I_{TIP-OUT}$) of $C \sim 3-4$ was achieved. This value differs from $C \sim 20$ obtained in the previous experiment (**Figure 6.4**). Such variation may arise from the difference of activity between the different tips used in this study. The observed enhancement originates from the LSPR of the TERS tip which is highly sensitive to the shape of the tip and the quality of the metal coating.²⁴

6.3.6 Lattice Strain Influence on Spectral Fingerprints of Nanowires

The influence of the lattice strain on vibrational frequency shift and FWHM of silicon Raman signal was studied by TERS. Bending is a source of lattice strain and previous studies have revealed a conductance enhancement in bent nanowires.²⁵ We studied the effect of this strain on the first order optical phonon Raman peak of silicon nanowires by collecting the TERS spectra at selected positions over a bent silicon nanowire. The AFM image of this bent structure is presented in **Figure 6.6a**, while **Figure 6.6b** shows the TERS spectra obtained from different locations on this structure assigned to the nanostructure variations.

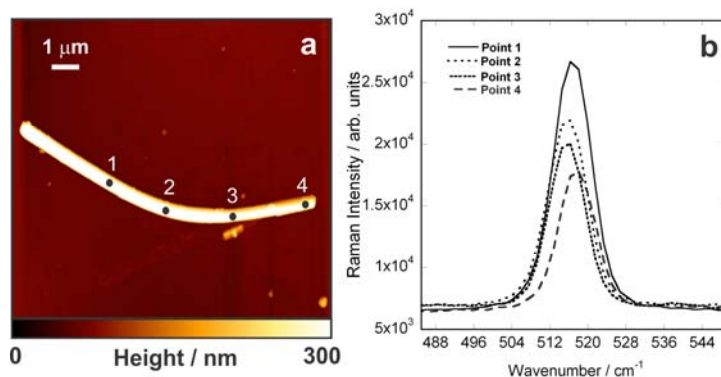


Figure 6.6 (a) AFM image of a bent silicon nanowire (b) TERS spectra collected along the nanowire in position 1-4

In **Figure 6.6b** the TERS Raman spectra show over 2 cm⁻¹ shift towards lower frequencies and a slight broadening for the bent portion of the nanowire (points 2,3) as compared to the straight portions of the wire (points 1,4). The broadening effect originates from the fact that nanowires experience compressive strain on the inner side of curvature and tensile strain on the outer side.²⁶ Compression leads to a positive frequency shift of phonon modes, whereas tension induces a negative shift and together, the two produce a broadening.²⁶ The broadening effect disappears as towards the straight ends of the bent wire and the Raman peak appears at 518 cm⁻¹ again. This bending strain that causes lattice strain is proportional to the ratio between the diameter of the nanowire and

the radius of the curvature of the bent nanowire.^{9,25} Therefore, our results indicate that a simultaneous tensile and a compressive strain not only causes a frequency shift of the silicon molecular vibrations, but also it results in broadening of the corresponding Raman peak. Similar observations are also reported for ZnO nanowires.²⁷ For ZnO nanocrystals the compressive and tensile stress are shifting the LO phonon to higher and lower frequencies, respectively. These results could also be compared with high resolution transmission electron microscopy investigations of Zheng *et al.*²⁶ In their work it has been reported that the neutral-strain axis was shifted from the compressive zone to the tensile region and that significant strain variation along the bending axial direction in the compressive region was revealed. The measured TERS spectra however, did not show significant changes along the bending direction which could be due to insufficient spatial resolution.

Finally the spectral variations due to potential strains induced by crossing were investigated. Crossed nanowires play an important role in fabrication of the nanodevices and it has been shown that overlapping crossed silicon nanowires make good electrical contact with each other and create electrical junctions which exhibit good diode behaviour.²⁸ To investigate the presence of strain in the nanowires, the AFM image of two arbitrary crossed nanowires was first obtained (**Figure 6.7a**). The TERS spectra of different spots on the crossed wires were then collected. The results are shown in Figure **6.7b**. The acquisition time was 10 s for each of the acquired spectra.

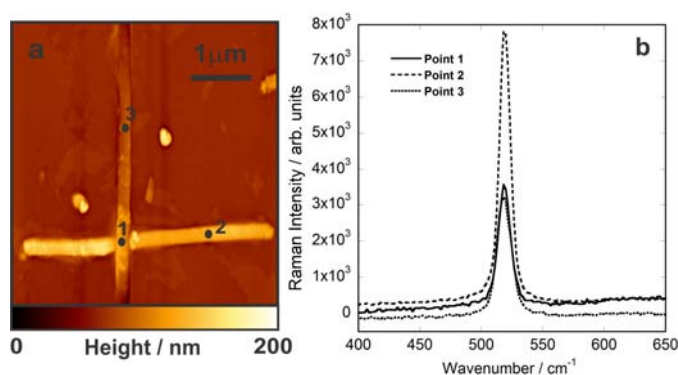


Figure 6.7 (a) AFM image of two crossed silicon nanowires (b) TERS spectra measured on points 1-3

As it is shown in **Figure 6.7b**, the Raman signal of silicon, which appears at around 518 cm^{-1} for a single silicon nanowire, does not experience significant spectral shift or a change in FWHM, suggesting that no significant strain is necessarily induced in the nanowires as a result of crossing.

6.4 Conclusion

In this Chapter, TERS of isolated nanowires were investigated using a nanocrystalline diamond tip coated with silver. Despite the low aspect ratio of the AFM tip used in this study, the TERS results show a lateral resolution close to the AFM cross section. We believe that higher aspect ratio AFM tips should lead to higher spatial resolution which correlate better with the diameter of a single nanowire estimated by AFM. Since the mechanical, electrical, optical and thermal properties of silicon nanowires are sensitive to the structure of the wires, the TERS technique could provide reliable insights into the influence of morphology on any of these properties.

References

- (1) Liao, F.; Liu, S.; Shao, M.; Lee, S.-t. *Appl. Phys. Lett.* **(2009)**, *100*, 0931141.
- (2) Tsakalakos, L.; Balch, J.; Fronheiser, J.; Korevaar, B. A.; Sulima, O.; Rand, J. *Appl. Phys. Lett.* **(2007)**, *91*, 2331171.
- (3) Ge, M.; Rong, J.; Fang, X.; Zhou, C. *Nano Lett.* **(2012)**, *12*, 2318.
- (4) Zhu, J.; Cui, Y. *Nat. Mater* **(2010)**, *9*, 183.
- (5) Boukai, A. I.; Bunimovich, Y.; Tahir-Kheli, J.; Yu, J.-K.; Goddard, W. A., III; Heath, J. R. *Nature* **(2008)**, *451*, 168.
- (6) Hochbaum, A. I.; Chen, R.; Delgado, R. D.; Liang, W.; Garnett, E. C.; Najarian, M.; Majumdar, A.; Yang, P. *Nature* **(2008)**, *451*, 163.
- (7) Piscanec, S.; Cantoro, M.; Ferrari, A. C.; Zapien, J. A.; Lifshitz, Y.; Lee, S. T.; Hofmann, S.; Robertson, J. *Phys. Rev. B: Condens. Matter Mater. Phys.* **(2003)**, *68*, 2413121.
- (8) Li, B.; Yu, D.; Zhang, S.-L. *Phys. Rev. B: Condens. Matter Mater. Phys.* **(1999)**, *59*, 1645.
- (9) Chen, Y.; Peng, B.; Wang, B. *J. Phys. Chem. C* **(2007)**, *111*, 5855.
- (10) Tarun, A.; Hayazawa, N.; Balois, M. V.; Kawata, S.; Reiche, M.; Moutanabbir, O. *New J. Phys.* **(2013)**, *15*, 053042.
- (11) Bailo, E.; Deckert, V. *Angew. Chem., Int. Ed.* **(2008)**, *47*, 1658.

- (12) Cancado, L. G.; Hartschuh, A.; Novotny, L. *J. Raman Spectrosc.* (2009), 40, 1420.
- (13) Chen, C.; Hayazawa, N.; Kawata, S. *Nat. Commun.* (2014), 5, 43121.
- (14) Stadler, J.; Schmid, T.; Zenobi, R. *Nanoscale* (2012), 4, 1856.
- (15) Bouhelier, A.; Beversluis, M. R.; Novotny, L. *Appl. Phys. Lett.* (2003), 82, 4596.
- (16) Pauzauskie, P. J.; Talaga, D.; Seo, K.; Yang, P.; Lagugné-Labarthe, F. *J. Am. Chem. Soc.* (2005), 127, 17146.
- (17) De, W. I. *Semicond. Sci. Technol.* (1996), 11, 139.
- (18) Lee, N.; Hartschuh, R. D.; Mehtani, D.; Kisliuk, A.; Maguire, J. F.; Green, M.; Foster, M. D.; Sokolov, A. P. *J. Raman Spectrosc.* (2007), 38, 789.
- (19) Zhang, M.-L.; Peng, K.-Q.; Fan, X.; Jie, J.-S.; Zhang, R.-Q.; Lee, S.-T.; Wong, N.-B. *J. Phys. Chem. C* (2008), 112, 4444.
- (20) Hutagalung, S. D.; Tan, A. S. Y.; Tan, R. Y.; Wahab, Y. *Proc. SPIE* (2010), 7743, 7743051.
- (21) Anastassakis, E.; Pinczuk, A.; Burstein, E.; Pollak, F. H.; Cardona, M. *Solid State Commun.* (1970), 8, 133.
- (22) Lockwood, D. J.; Baribeau, J. M. *Phys. Rev. B* (1992), 45, 8565.
- (23) Birrell, J.; Gerbi, J. E.; Auciello, O.; Gibson, J. M.; Johnson, J.; Carlisle, J. A. *Diamond Relat. Mater.* (2005), 14, 86.
- (24) Asghari-Khiavi, M.; Wood, B. R.; Hojati-Talemi, P.; Downes, A.; McNaughton, D.; Mechler, A. *J. Raman Spectrosc.* (2012), 43, 173.
- (25) Han, X.; Jing, G.; Zhang, X.; Ma, R.; Song, X.; Xu, J.; Liao, Z.; Wang, N.; Yu, D. *Nano Res.* (2009), 2, 553.
- (26) Zheng, K.; Han, X.; Wang, L.; Zhang, Y.; Yue, Y.; Qin, Y.; Zhang, X.; Zhang, Z. *Nano Lett.* (2009), 9, 2471.
- (27) Yan, B.; Chen, R.; Zhou, W.; Zhang, J.; Sun, H.; Gong, H.; Yu, T. *Nanotechnol.* (2010), 21, 4457061.
- (28) Cui, Y.; Lieber, C. M. *Science* (2001), 291, 851.

Chapter 7

7 Label-free Mapping of Osteopontin Adsorption to Calcium Oxalate Monohydrate Crystals by Tip-enhanced Raman Spectroscopy³

In the ectopic biomineralization of calcium oxalate kidney stones, the competition between calcium oxalate monohydrate (COM) formation and its inhibition by the phosphoprotein osteopontin (OPN) plays a key role in COM stone forming processes. To get more insights into these processes, tip-enhanced Raman spectroscopy is used to provide surface-specific information about the adsorption of OPN to faces of COM crystals. As TERS works label-free and non-invasively, it is an excellent technique to study the distribution of adsorbed proteins on crystal faces at the sub-micrometer scale. In this Chapter, we generated Raman intensity maps indicating high surface specificity and a distinct variation in relative peak intensities. The collected TERS spectra show that the OPN preferentially adsorbs to edges and faces at the ends of COM crystals (order: $\{121\}$ edge $>$ $\{100\}$ face $>$ $\{100\}/\{010\}$ edge \approx $\{121\}/\{010\}$ edge $>$ $\{010\}$ face) providing also relevant information on the inhibition of crystal growth.

7.1 Introduction

The use of TERS in the biochemical and biophysical sciences is particularly attractive as, unlike other techniques (e.g., fluorescence spectroscopy and microscopy), it allows for sensitive analyses of very small areas of a sample at a high spatial resolution and in the absence of any label. As mentioned earlier, labelling could lead to undesired artifacts and misinformation, and sometimes requires the synthesis of endogenous fluorophores, which could perturb the native organization of the biosystem of interest.²

³ A version of this chapter has been published in [*J. Am. Chem. Soc.* (2012), 134, 17076.]. Reproduced with permission from the American Chemical Society

So far TERS has been successfully tested to open insights into many biological systems such as RNA³ and DNA strands^{4,5} isolated cells⁶⁻⁸ and viruses.⁹ The present Chapter focuses on the use of TERS to study the interactions of the phosphoprotein osteopontin (OPN) with calcium oxalate monohydrate (COM) crystals. The latter is the most common mineral phase of kidney stones ($\approx 75\%$), while OPN is believed to be a potent inhibitor of kidney stone formation.¹⁰ A perspective view of a COM penetration twin (main habit in physiological environments) is shown in **Figure 7.1**.

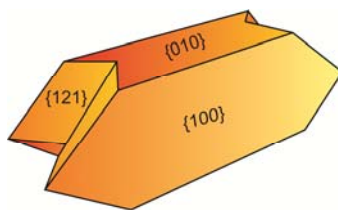


Figure 7.1 Perspective view of a faceted COM penetration twin depicting the main crystal faces of calcium oxalate monohydrate

The formation of oxalate stones in the urinary system involves the nucleation, growth, and aggregation of these crystals; a complex process that depends on many parameters such as the diet and water intake of the subject.¹¹ However, low molecular weight (e.g., citrate) and macromolecular inhibitors play an important role in regulating these calcification processes. Members of the latter category are the Tamm-Horsfall protein (THP) and OPN.^{12,13} OPN, which is part of the body's defence mechanism against pathological calcification,¹⁴ is proposed to be a potent inhibitor of stone formation.

To test this hypothesis, effects of a variety of OPN peptides and the parent protein on COM growth inhibition were analyzed.¹⁵⁻¹⁸ In vitro, OPN is adsorbed onto COM crystals,^{11,19,20} inhibits their growth,²¹⁻²³ and prevents crystal aggregation.²⁴ Atomic force microscopy of growth steps, for instance, has shown that OPN adsorption to {010} faces is more selective than adsorption to {100} faces.²³ Very recently, the adsorption pattern of OPN isoforms to COM crystals was studied using a combination of confocal fluorescence and scanning electron microscopy.^{17,18,25} These investigations have shown that fluorescent-labelled OPN preferentially adsorbs to the edges between the {100} and {121} faces, and, after longer adsorption times, to {100} faces. Adsorption to {010} and

{121} faces was not evident. The preliminary structure of OPN is summarized in **Table 7.1**.

Table 7.1 Preliminary structure of OPN

Amino acid	Class	R side-chain group	/backbone
Glycine	Hydrocarbon	H-	6
Alanine	Hydrocarbon	CH ₃ -	21
Valine	Hydrocarbon	(CH ₃) ₂ CH-	15
Isoleucine	Hydrocarbon	(CH ₃) ₂ CH ₂ CH ₂ -	6
Leucine	Hydrocarbon	(CH ₃) ₂ CH ₂ CH ₂ -	19
Serine	Alcohol	HOCH ₂ -	55
Threonine	Alcohol	HOCH(CH ₃)-	12
Methionine	Sulfur	H ₃ CSCH ₂ CH ₂ -	2
Asparagine	Amide	H ₂ NCOCH ₂ -	7
Glutamine	Amide	H ₂ NCOCH ₂ CH ₂ -	15
Arginine	Basic	HN=C(NH ₂)NH(CH ₂) ₃ -	9
Lysine	Basic	H ₂ N(CH ₂) ₄ -	18
Histidine	Basic	HN=CHNH-	15
Phenylalanine	Aromatic	C ₆ H ₅ CH ₂ -	6
Tyrosine	Aromatic	HOC ₆ H ₅ CH ₂ -	5
Tryptophan	Aromatic	C ₆ H ₄ HNHC=CH ₂ -	1
Proline	Secondary amine	H ₂ CCH ₂ CH ₂ -	15
Aspartic acid	Acidic	HOOCCH ₂ -	42
Glutamic acid	Acidic	HOOCCH ₂ CH ₂ -	33

We demonstrate for the first time that a tip-enhanced chemical fingerprint of adsorbed OPN to COM faces results in a detailed, semi-quantitative and complete adsorption profile of the phosphoprotein (phosphorylated recombinant rat bone osteopontin, p-OPN) to COM crystal faces. This is carried out in non-contact AFM mode and without the requirement of fluorescent label. The findings of this Chapter demonstrate the utility of this novel approach to study protein mineral interactions, and provide important insights into the adsorption behaviour of OPN, which could be used to develop new strategies for therapeutic intervention of pathological calcification.

7.2 Experimental Section

7.2.1 Chemicals and Solution Preparation

For crystallization of calcium oxalates, reagent grade sodium oxalate ($\text{Na}_2\text{C}_2\text{O}_4$; J. T. Baker), calcium nitrate tetra-hydrate ($\text{Ca}(\text{NO}_3)_2 \cdot 4\text{H}_2\text{O}$; J. T. Baker), sodium chloride (NaCl ; J. T. Baker) and sodium acetate (CH_3COONa , anhydrous; Sigma) were used to prepare calcium and oxalate stock solutions as previously described.²⁶ Recombinant full-length rat osteopontin (recOPN) was expressed as an N-terminal His-tagged protein following a protocol used for recombinant bone sialoprotein.²⁷ The purified protein was analyzed by MALDI-TOF mass spectrometry (MALDI-TOF MS; Bruker Reflex III) and a molecular weight of 36 050 g/mol determined. Phosphorylation of recOPN occurred by treating recOPN with protein kinase $\text{CK2}\alpha$ expressed as a GST-tagged protein following a protocol by Saad *et al.*²⁸ MALDI-TOF MS revealed that the molecular weight of phosphorylated recOPN (p-OPN) is 36 694 g/mol. The mass difference between recOPN and p-OPN (644 g/mol) corresponds to 8.05 phosphate groups. To verify identity, protein content and purity, SDS-PAGE and amino acid analysis (Alberta Peptide Institute, Edmonton, Canada) were used. For adsorption experiments, an aqueous stock solution of 2 mg/mL (54.5 μM) p-OPN was prepared.

7.2.2 Crystallization and Adsorption Experiments

COM formation was initiated by modifying a method previously established.¹⁷ In brief, custom-made Teflon block (**Figure 7.2**) containing three bottomless reaction wells (diameter, 9 mm; height, 10 mm) was sealed by o-rings (Viton) with optical cover glass (Fisher, 22 \times 22 mm, No. 1) and clamped using a microscopic slide as bottom cover.

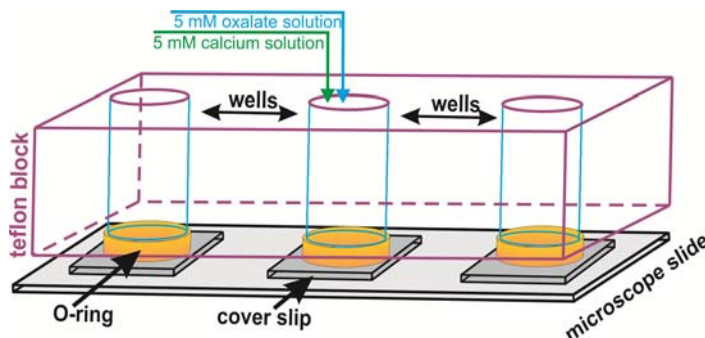


Figure 7.2 Schematic (not to scale) of a reaction well-containing Teflon block for the growth of COM crystals

Before assembly, the cover glass was treated in 7 wt % NaOH solution at 60 °C for 20 min to increase negative charge and pit densities of the substrate surfaces in order to have the crystals stick better to the surface of the glass cover slip.²⁹⁻³¹ This treatment was necessary to prevent crystals from moving during atomic force microscopy scans. All components of the assembly were thoroughly rinsed in doubly distilled H₂O with sonication for 5 min before use. For crystallization, the reaction assembly and all reaction solutions were preheated to 37 ± 0.2 °C. Thereafter, oxalate solution was added to the wells followed by water and calcium solutions (total volume of 500 μL) and the assembly incubated (Ultra Tec WJ 501 S) at 37 ± 0.2 °C for 3 h. The final concentrations were [Ca²⁺]=[C₂O₄²⁻]=1 mM, sodium acetate 10 mM and sodium chloride 150 mM. For some reactions, pH measurements were carried out immediately after mixing the solutions; the pH was always between 6.65 and 6.75. For adsorption experiments, crystal growth solutions were exchanged by low-supersaturated calcium oxalate solutions ([Ca²⁺]=[C₂O₄²⁻]=0.06 mM, preheated to 37 °C ± 0.2 °C) followed by the addition of 0.4 mg/mL p-OPN to the wells containing preformed crystals. The total volume was again 500 μL. After allowing adsorption to the crystals for a period of 60 min (37 ± 0.2 °C), cover glass samples were rinsed with deionized water, air-dried and stored in a desiccators until further use.

7.2.3 TERS Experimental Details

The TERS setup used in this study is described in Chapter 3. To conduct the Raman measurements, linearly polarized coherent laser beam ($\lambda = 532$ nm, Compass 315 M laser, Coherent, Santa Clara, CA, USA) was focused on the sample using an objective with a high numerical aperture (Olympus PlanAPO, $NA=0.95$, $\times 100$). The same objective was used to collect the backscattered light. The laser intensity at the sample was adjusted to $300\mu\text{W}$. AFM scans were conducted in non-contact mode using silver coated AFM tips (NCL20 NanoWorld Inc.; resonance frequency 170 kHz, force constant 48 N/m). Silver coating (30 nm layer) was carried out by electron beam thermal evaporation of the metal in a vacuum chamber. The coated tips were used within the day of coating. 5-10 coated tips were used for each face of crystals, whereas an average of 1 in 5 tips provided large enhancement. At the end of each experiment, a TERS experiment with the tip in proximity to the glass surface was performed to test for a possible contamination of the tip.

7.3 Results and Discussion

At first Raman reference spectra of both the phosphoprotein and the calcium oxalate crystals were acquired which is shown in **Figure 7.3**.

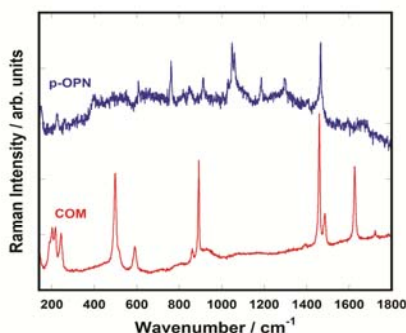


Figure 7.3 Raman spectra of the phosphoprotein p-OPN and COM crystals. The acquisition times were 120 sec for p-OPN and 20 sec for the COM crystal using similar irradiation conditions. The spectrum of the protein is multiplied by a factor of 10.

The most intense Raman peak of p-OPN appears at 1465 cm^{-1} which overlaps with a main peak of COM at 1464 cm^{-1} . The presence of OPN could however be distinguished from COM by monitoring the intensity ratio for the wavenumbers 1464 cm^{-1} and 1487 cm^{-1} . The latter Raman peak is assigned to COM only. Therefore, the larger the ratio I_{1464}/I_{1487} is, the larger is the amount of proteins adsorbed onto the crystal surface. The peak assignments for both OPN and COM are shown in **Table 7.2**.

Table 7.2 Raman peak assignment for p-OPN and COM crystals

p-OPN (cm^{-1})	COM (cm^{-1})	intensity	band assignment
	503-595	w	O-C-O bending ³²
608		w	C-O bending of amide VI band ³³
761		m	Indole systematic breathing mode of Trp, ³⁴ systematic stretching of O-P-O ³⁵
800–900		m	Systematic C-N-C stretching ³³
	850-950	m	C-C stretching ³²
915		m	C-C stretching of side chains ³⁴
1050		s	C-C stretching of side chains ³⁴
1062		m	Systematic P-O stretching vibration, ³⁶ C-N stretching of side chains ³⁴
1187		w	CO-OC stretching mode, ³⁷ Amide III ³⁸
1250-1350		w	Amide III bending and stretching of backbone ³⁹
	1300-1500	s	Systematic C-O stretching ³²
1425-1475		s	CH ₂ scissoring or CH ₃ systematic stretching ³⁹
1550-1750	1550-1750	m	Asymmetric C-O stretching, ³² Amide I in OPN ^{37,40}

To investigate the adsorption pattern of OPN on the surface of the COM crystals, we collected TERS maps of both p-OPN adsorbed to $\{100\}$ faces and p-OPN adsorbed to $\{010\}$ faces. The mapping was performed first within selected areas of $10 \times 10\ \mu\text{m}^2$ near the extremities of the crystals. The lateral separation between adjacent pixels inside the mapping region was set to be 250 nm. For each crystal face, collection of Raman signals was carried out sequentially keeping the metallic AFM tip in feedback with the surface of the sample. Prior to scanning, the TERS tip was aligned to the focused excitation beam for each crystal face analyzed. Spectra for maps were acquired using a laser power of $300\ \mu\text{W}$ at the sample plane for 1 sec. Once all spectra were collected, two sets of maps were generated by integrating the Raman peaks at 1464 cm^{-1} (of COM and p-OPN; **Figure 7.4b** and **Figure 7.4c**) and the peaks at 1487 cm^{-1} (of COM only; **Figure 7.4e** and

Figure 7.4f). We then evaluated the p-OPN distribution on the $\{100\}$ and $\{010\}$ crystal faces by calculating the intensity ratios of 1464 cm^{-1} and 1487 cm^{-1} peaks for four selected points on each of the two crystal faces. The four points (black dots) are shown in **Figure 7.4b** and **Figure 7.4c**, while the spectra and associated ratios are shown in **Figure 7.4g** and **Figure 7.4h**.

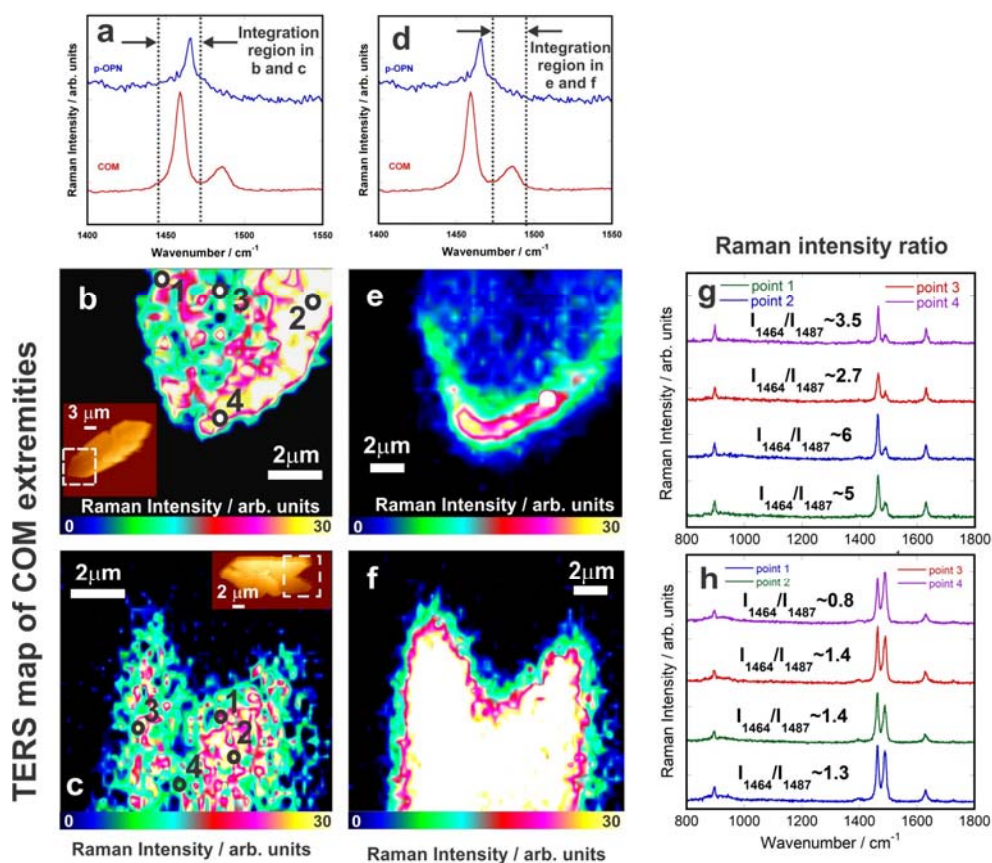


Figure 7.4 TERS maps of p-OPN adsorbed to $\{100\}$ and $\{010\}$ crystal faces. The color bars represent Raman intensity. Blue and white colors indicate weak and strong Raman signals, respectively. (a and d) Integration area used to generate the maps in (b and c) and (e and f), respectively. (b and c) Maps resulting from the integration of the 1465 cm^{-1} peak on $\{100\}$ and $\{010\}$ faces (signal of COM and p-OPN), respectively. (e and f) Raman intensity maps resulting from the integration of the 1487 cm^{-1} peak of $\{100\}$ and $\{010\}$ faces (COM only), respectively. (g and h) Raman spectra of four spots (see (b) and (c)) selected from maps on $\{100\}$ and $\{010\}$ faces, respectively.

In these maps, each collected signal includes both the near-field contribution from the crystal surface together with the far-field bulk signal from the crystal. TERS of {121} faces was not performed, as these faces are not accessible for the tuned AFM/Raman laser setup. **Figure 7.4b** and **Figure 4.7c** shows variations in intensities of the Raman peak at 1464 cm^{-1} for {100} and {010} faces as well as the crystal edges. Other bands of OPN such as 761 cm^{-1} and 1062 cm^{-1} were too weak to be exploited. The measurements indicate the presence of p-OPN and slight changes in thickness of the adsorbed protein layer, which also results in changes of COM intensities. Comparing the TERS spectra of the two maps shown in **Figure 7.4 b** and **Figure 7.4c** indicates, by variations in intensity, that the phosphoprotein tends to adsorb more to the extremities of the crystal. From these data, it is apparent that p-OPN adsorbs preferentially to the edges between {100} and {121} faces and, rather marginally, to the {010}/{121} edges. In addition, more intense Raman signals at {100} faces suggest that p-OPN adsorbs more selectively to {100} than to {010} faces. This outcome confirms recent findings by Hunter and co-workers, who report that high Ca^{2+} densities on {100} faces promote the adsorption of the acidic phosphoprotein.^{16,25} Moreover, adsorption of p-OPN to the edges might be an effect of surface energies.^{16,17} To provide additional evidence for the presence and selectivity of adsorbed p-OPN on COM faces, single spot TERS measurements (four at each crystal face) and calculations of intensity ratios (I_{1464}/I_{1487}) were carried out for each spot. On the {100} face, these ratios were between 2.7 and 6, and for the spots on the {010} face, ratios between 0.4 and 1.4 were calculated (the higher the ratio the higher the OPN concentration, see above). Particularly for the {100} face (**Figure 7.4g**), large ratios near the crystal edges were measured (points 1,2,4). For the face itself (point 3), a ratio of 2.7 was received. This value is relatively high compared to those measured for the {010} face (**Figure 7.4h**). In addition, the {010}-ratios are more homogeneous and show a lower affinity for p-OPN to {010} faces. In general, the adsorption profile found for p-OPN is in good agreement with results achieved in previous studies using confocal fluorescence microscopy.¹⁷ There is, however, one important difference. The semi-quantitative results derived in the present study clearly show that p-OPN does not only adsorb relatively strong to {100}/{121} edges, a fact also reported by Taller *et al.*,¹⁷ but also to {100} and (marginally) to {010} faces. In contrast, confocal fluorescence

microscopy used by Taller *et al.* showed very weak (if at all) and undistinguishable binding to {100} and {010} faces.¹⁷ Indeed, Hunter *et al.* have reported slight OPN adsorption to {100} faces but no protein binding to {010} faces, as well.²⁵ Therefore, using the sensitivity of TERS allowed us to specify the selectivity of OPN adsorption with very high accuracy, finally indicating an order of adsorbed p-OPN of {100}/{121} edges > {100} faces > {010} faces. On the basis of the p-OPN concentration used (0.4 mg/mL) in the present study and the treatment of the samples after adsorption (rinsing the crystals and removing excess of p-OPN [desorption of physisorbed protein]), it is proposed that the p-OPN layers detected by TERS are strongly bound (chemisorbed) protein. In contrast, Taller *et al.* used very low concentration (1 µg/mL) to study the selectivity (chemisorption) of OPN binding in situ.¹⁷ Both methods reveal binding affinities to COM edges and faces which are quite comparable, with the obvious difference that TERS is more sensitive. The fact that Hunter *et al.* found more OPN bound to {100} faces than Taller *et al.* suggests an effect of the adsorption time.^{17,25} Using the same in situ method, Hunter *et al.* adsorbed for ≥90 min, whereas Taller *et al.* used 60 min, like the present study. It is assumed that these longer treatments applied by Hunter *et al.* resulted in higher adsorption rates of (physisorbed) OPN to {100} faces.²⁵ Moreover, the adsorption profile found in the present study directly mirrors the growth inhibition profile reported in recent studies.^{17,18,25} These studies indicated strong interactions of the protein with {100}/{121} edges, weaker OPN effects on {100} faces and marginally affected {010} faces when COM was grown in the presence of higher concentrations (5 µg/mL). Another advantage of TERS (compared to conventional fluorescence microscopy) is the possibility to highly resolve variations in surface roughness, ability similar to that of AFM (**Figure 7.6e** and **Figure 7.6f**). Using the 1487 cm⁻¹ peak of COM investigations indicates that the {010} face shows more homogeneity rather than the {100} face.

To clearly demonstrate the TERS effect, Raman spectra were collected at several locations on both crystal faces using an acquisition time of 600 sec per point (**Figure 7.5**). For these measurements, the tip was either kept in the near-field position of the surface (typically 1-10 nm) or in the far-field above the surface (~ 1 µm). After measurements, TERS spectra (blue color) were derived by calculating the difference

between the Raman spectra acquired in near-field (green color) and the far-field (red color). The three spectra of one spot over the surface of a random crystal (**Figure 7.5b**) is shown in **Figure 7.5a**. As the TERS spectra represent Raman signals originating from the crystal surface rather than the bulk, they contain a high contribution of signals from the adsorbed p-OPN.

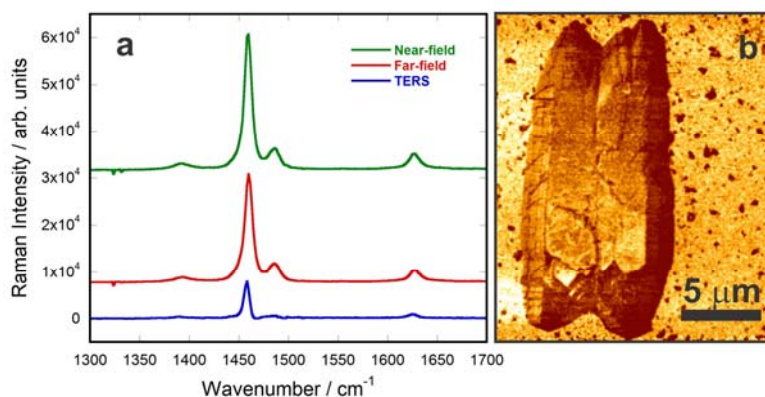


Figure 7.5 (a) Raman spectra of adsorbed p-OPN on COM faces along with (b) AFM images of {010} face of COM. The green, red, and blue spectra correspond to the near-field, far-field, and TERS spectra, respectively.

Figure 7.5 shows that a spectrum with higher intensity is obtained (green spectra) when the AFM tip is in near-field position also indicating a higher sensitivity of the near-field mode. The adsorption pattern found by TERS is therefore extractable by performing both near-field and far-field maps. The resulting TERS (blue spectra) is, in turn, the intensity difference between the spectra collected in far-field and in near-field, respectively. This method provides qualitative insights into features of the crystal surface and gives an idea of the tip enhancement factor. In the following, we would have a brief look at this effect.

According to the mechanism introduced in Chapter 3 for estimation of the TERS enhancement factor, the optical contrast can be calculated as the ratio between the intensities of the near-field and far-field.⁴¹ To consider the geometrical dimension of the focal point and the AFM tip, the ratio between the area of the diffraction-limited focal spot, $A_{farfield} = r_{laser}^2 \pi$ with r_{laser} being the radius of the focused laser⁴¹ and the area from which the near-field signal is generated $A_{nearfield} = r_{tip}^2 \pi$ where r_{tip} is the radius of the

tip^{37,38} should be calculated. The TERS enhancement factor can then be calculated according to $EF_{TERS} = (I_{nearfield}/I_{farfield})(A_{farfield}/A_{nearfield})$. Considering a laser spot diameter of 275 nm and a tip diameter of 20 nm, we obtain $A_{farfield} \sim 0.06 \mu\text{m}^2$ and $A_{nearfield} \sim 3 \times 10^{-4} \mu\text{m}^2$, respectively. At the best, a spectroscopic contrast factor of 1.5 can be determined from the difference of intensities between the near-field and the far-field Raman spectra (**Figure 7.5a**, peak at 1464 cm^{-1}). This yields to an enhancement factor of $EF \sim 300$. This value could be compared to enhancement factors reported in the literature for similar TERS experiments, covering a wide range from $EF = 14$ to 10^8 (using comparable setups and experimental conditions, but different samples).^{5,38,42,43}

To further investigate the TERS enhancement effect and distribution patterns of p-OPN on surfaces of crystal faces (rather than the edges), we performed mapping of $20 \times 5 \mu\text{m}^2$ areas on the crystal surface using the conditions described above (acquisition time, 1 sec; laser power $300 \mu\text{W}$ at the crystal surface). For the final maps, integration of the 1464 cm^{-1} peak was carried out. The maps shown in **Figure 7.6** correspond to a region in the middle of the crystal with the tip either in the near-field of the sample (**Figure 7.6b**, **Figure 7.6e**) or in the far-field ($\sim 1 \mu\text{m}$ above the sample; **Figure 7.6c**, **Figure 7.6f**).

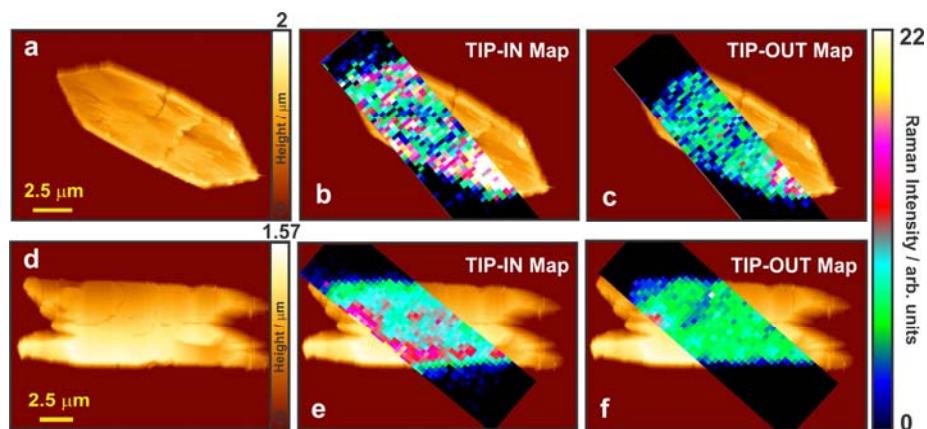


Figure 7.6 (a,d) AFM images of $\{100\}$ and $\{010\}$ faces. Raman intensity maps of p-OPN adsorbed to an $\{100\}$ face: (b) in TERS, (c) in standard Raman mode. Raman intensity maps of OPN adsorbed to an $\{010\}$ face (e) in TERS and (f) in Raman mode. For both modes, the scanned area was set to be $20 \times 5 \mu\text{m}^2$, using 330 nm steps along both directions. This results in a total of 900 measuring points.

Intensity maps of larger areas measured in near- and far-field (**Figure 7.6**) provide more information about the overall distribution of p-OPN adsorbed to crystal faces. In general, these maps validate the results and the data that was described earlier (**Figure 7.4**). It is, however, important to note that OPN also shows tendencies to adsorb to the edges between $\{100\}$ and $\{010\}$ faces of COM (**Figure 7.6b**, **Figure 7.6e**), a result not detected in previous fluorescence studies.

7.4 Conclusion

In summary, we have demonstrated for the first time that tip-enhanced Raman spectroscopy could provide valuable insights into the adsorption behaviour of OPN on calcium oxalate monohydrate crystals without any need to label the protein. Despite the fact that some factors such as the quality of the metal coating of the TERS tip could influence the spatial resolution of this technique, our findings provide valuable insights into the adsorption pattern of the phosphoprotein to COM crystal faces. On the basis of the results of this study, OPN tends to adsorb preferentially to $\{100\}/\{121\}$ edges at the ends of the crystal and, less preferentially, to $\{100\}$ faces. We also observed some adsorption to $\{010\}/\{121\}$ and $\{100\}/\{010\}$ edges. The final adsorption pattern found shows the preference: $\{100\}/\{121\}$ edge $>$ $\{100\}$ face $>$ $\{100\}/\{010\}$ edge \approx $\{121\}/\{010\}$ edge $>$ $\{010\}$ face. The fact that the $\{100\}$ face exhibited more adsorbed OPN than the $\{010\}$ face is presumably related to the higher Ca^{2+} ions density on the $\{100\}$ face. Adsorption to the edges might be a result of higher surface energies in these regions. In general, it was shown that TERS is a label-free, highly sensitive and non-invasive technique, which is able to show detailed information of the adsorption pattern of proteins, a method also useful for studying other systems such as self-assembled, layered or arrayed structures.

7.5 References

- (1) Adrian, F. J. *J. Chem. Phys.* **(1982)**, *77*, 5302.
- (2) Deckert-Gaudig, T.; Deckert, V. *Phys. Chem. Chem. Phys.* **(2010)**, *12*, 12040.
- (3) Bailo, E.; Deckert, V. *Angew. Chem., Int. Ed.* **(2008)**, *47*, 1658.

- (4) Lipiec, E.; Sekine, R.; Bielecki, J.; Kwiatek, W. M.; Wood, B. R. *Angew. Chem., Int. Ed.* (2014), 53, 169.
- (5) Hennemann, L. E.; Meixner, A. J.; Zhang, D. *Spectroscopy* (2010), 24, 119.
- (6) Boehme, R.; Mkandawire, M.; Krause-Buchholz, U.; Roesch, P.; Roedel, G.; Popp, J.; Deckert, V. *Chem. Commun.* (2010), 47, 11453.
- (7) Wood Bayden, R.; Bailo, E.; Khiavi Mehdi, A.; Tilley, L.; Deed, S.; Deckert-Gaudig, T.; McNaughton, D.; Deckert, V. *Nano Lett.* (2011), 11, 1868.
- (8) Richter, M.; Hedegaard, M.; Deckert-Gaudig, T.; Lampen, P.; Deckert, V. *Small* (2011), 7, 209.
- (9) Cialla, D.; Deckert-Gaudig, T.; Budich, C.; Laue, M.; Moeller, R.; Naumann, D.; Deckert, V.; Popp, J. *J. Raman Spectrosc.* (2009), 40, 240.
- (10) Bushinsky, D. A. *Adv. Intern. Med.* (2001), 47, 219.
- (11) Khan, S. R.; Kok, D. J. *Front. Biosci.* (2004), 9, 1450.
- (12) Giachelli, C. M. *Orthod. Craniofac. Res.* (2005), 8, 229.
- (13) Kumar, V.; Lieske, J. C. *Curr. Opin. Nephrol. Hypertens.* (2006), 15, 374.
- (14) Kleinman, J. G.; Wesson, J. A.; Hughes, J. *Nephron* (2004), 98, 43.
- (15) Grohe, B.; O'Young, J.; Ionescu, D. A.; Lajoie, G.; Rogers, K. A.; Karttunen, M.; Goldberg, H. A.; Hunter, G. K. *J. Am. Chem. Soc.* (2007), 129, 14946.
- (16) Hug, S.; Grohe, B.; Langdon, A.; Jalkanen, J.; Rogers, K. A.; Goldberg, H. A.; Karttunen, M.; Hunter, G. K. *Langmuir* (2012), 28, 12182.
- (17) Taller, A.; Grohe, B.; Rogers, K. A.; Goldberg, H. A.; Hunter, G. K. *Biophys. J.* (2007), 93, 1768.
- (18) Grohe, B.; Taller, A.; Vincent, P. L.; Tieu, L. D.; Rogers, K. A.; Heiss, A.; Sorensen, E. S.; Mittler, S.; Goldberg, H. A.; Hunter, G. K. *Langmuir* (2009), 25, 11635.
- (19) Kok, D. J. *World J. Urol.* (1997), 15, 219.
- (20) Wesson, J. A.; Worcester, E. M.; Wiessner, J. H.; Mandel, N. S.; Kleinman, J. G. *Kidney Int.* (1998), 53, 952.
- (21) Shiraga, H.; Min, W.; VanDusen, W. J.; Clayman, M. D.; Miner, D.; Terrell, C. H.; Sherbotie, J. R.; Foreman, J. W.; Przysiecki, C.; et al. *Proc. Natl. Acad. Sci. U. S. A.* (1992), 89, 426.
- (22) Worcester, E. M.; Blumenthal, S. S.; Beshensky, A. M.; Lewand, D. L. *J. Bone Miner. Res.* (1992), 7, 1029.
- (23) Qiu, S. R.; Wierzbicki, A.; Orme, C. A.; Cody, A. M.; Hoyer, J. R.; Nancollas, G. H.; Zepeda, S.; De Yoreo, J. J. *Proc. Natl. Acad. Sci. U. S. A.* (2004), 101, 1811.
- (24) Wesson, J. A.; Ganne, V.; Beshensky, A. M.; Kleinman, J. G. *Urol. Res.* (2005), 33, 206.

- (25) Hunter, G. K.; Grohe, B.; Jeffrey, S.; O'Young, J.; Sorensen, E. S.; Goldberg, H. A. *Cells Tissues Organs* (2009), 189, 44.
- (26) Grohe, B.; Rogers, K. A.; Goldberg, H. A.; Hunter, G. K. *J. Cryst. Growth* (2006), 295, 148.
- (27) Tye, C. E.; Hunter, G. K.; Goldberg, H. A. *J. Biol. Chem.* (2005), 280, 13487.
- (28) Saad, F. A.; Salih, E.; Wunderlich, L.; Flueckiger, R.; Glimcher, M. J. *Biochem. Biophys. Res. Commun.* (2005), 333, 443.
- (29) Behrens, S. H.; Grier, D. G. *J. Chem. Phys.* (2001), 115, 6716.
- (30) Mellott, N. P.; Brantley, S. L.; Hamilton, J. P.; Pantano, C. G. *Surf. Interface Anal.* (2001), 31, 362.
- (31) Meyer, P.; Jouffroy, M.; Membrey, F.; Fromm, M.; Chambaudet, A. *Radiat. Prot. Dosim.* (1997), 74, 75.
- (32) Frost, R. L.; Weier, M. L. *Thermochim. Acta* (2004), 409, 79.
- (33) Socrates, G. *Infrared and Raman Characteristic Group Frequencies: Tables and Charts, 3rd Edition*, 2004.
- (34) Stewart, S.; Fredericks, P. M. *Spectrochim. Acta, Part A* (1999), 55A, 1615.
- (35) Hermann, P.; Fabian, H.; Naumann, D.; Hermelink, A. *J. Phys. Chem. C* (2011), 115, 24512.
- (36) Zhang, D.; Ortiz, C.; Xie, Y.; Davisson, V. J.; Ben-Amotz, D. *Spectrochim. Acta A* (2005), 61A, 471.
- (37) Boehme, R.; Richter, M.; Cialla, D.; Roesch, P.; Deckert, V.; Popp, J. *J. Raman Spectrosc.* (2009), 40, 1452.
- (38) Budich, C.; Neugebauer, U.; Popp, J.; Deckert, V. *J. Microsc.* (2008), 229, 533.
- (39) Matthaus, C.; Chernenko, T.; Newmark, J. A.; Warner, C. M.; Diem, M. *Biophys. J.* (2007), 93, 668.
- (40) Kurouski, D.; Deckert-Gaudig, T.; Deckert, V.; Lednev, I. K. *J. Am. Chem. Soc.* (2012), 134, 13323.
- (41) Stadler, J.; Schmid, T.; Zenobi, R. *Nanoscale* (2012), 4, 1856.
- (42) Cancado, L. G.; Hartschuh, A.; Novotny, L. *J. Raman Spectrosc.* (2009), 40, 1420.
- (43) Pettinger, B.; Ren, B.; Picardi, G.; Schuster, R.; Ertl, G. *Phys. Rev. Lett.* (2004), 92, 0961011.

Chapter 8

8 Conclusion and Outlook

In this thesis, we have investigated tip-enhanced Raman vibrational spectroscopy on both theoretical and experimental aspects as a potential technique to probe nanostructures. The main emphasis was directed towards the optimization of the TERS setup with the goal to conduct a higher spatial resolution spectroscopic investigation of the nanoscale features along with a better surface specificity. Improved sensitivity and specificity of TERS makes it a unique approach with unprecedented spatially resolved optical measurements that can be applicable to a large variety of materials and biomaterials.

Theoretical analysis of the plasmonic confinement at the vicinity of the metallic apex of the TERS nanotip in Chapter 4 was conducted by finite-difference time-domain simulations. The simulation results revealed a strong dependence of the electric field confinement to the polarization of the incident laser. The intensified electric field is larger if the nanotip is illuminated by a radially polarized laser when compared to illumination by a linearly polarized light. In addition, thin metallic substrates with plasmonic properties at the wavelength region of interest showed to have significant impact on the magnitude of the field enhancement and the local confinement of the electric field around the tip apex. Protection of the TERS tip through a thin alumina coating on top of the metal surface was found to occur to the detriment of a decrease in plasmonic responses of the tip. The next logical step with this regard would be to study the influence of the protective coating on the dielectric function of the TERS tip and the consequent tuning of the excitation wavelength.

The TERS mapping of carbon nanotubes in Chapter 5 was an important step in estimating the limit of the accessible spatial resolution in a TERS setup where a radially polarized laser illuminates a gold coated silicon tip in transmission bottom illumination configuration. Sub-20 nm resolution was obtained upon these measurements but yet the reproducibility of these experiments was dependent on the tip activity. Such tip activity suffers strongly from the low tip-to-tip coating reproducibility in general. In addition in the case of carbon nanotubes, the resonant behavior of the nanotubes with respect to the

incident light generates a large far-field contribution to the total detected Raman signal. Hence, we suggest that the efficiency of TERS benefits significantly from two strategies:

i. A universal method for preparation of effective TERS tips since thermal evaporation suffers from random coating process with low chance of creating metal nano-islands at the apex of the tip. Electrochemical etching of metal wire appears to be a method of choice for the production of metallic tips. Nevertheless, the attachment of the etched nanowires to a tuning fork makes the method more vulnerable to reproducibility. Modification of commercially available AFM tips in terms of the tip material seems to be the straightest forward way of providing access to TERS tips with relatively consistent TERS activity. The mechanical resistance of such metallic tips might be addressed through utilizing plasmonic alloys for the entire AFM probe. Meanwhile, focused ion milling of the TERS probe seems to be a promising approach provided that new instrumentations allow for rapid and less costly operations.

ii. The detection sensitivity of TERS measurements could be improved through employing a lock-in method in order to discriminate the far-field contribution from the near-field at the frequency of the tip oscillation. It was mentioned in Chapter 3 that synchronizing a pulsed laser with the time duration while the TERS tip is in near-field of the sample in addition to the employment of fast detectors that solely collect the near-field signal is a promising method to enhance the chemical sensitivity. The instrumentation of such fast and efficient setups is however the major challenge. From these observations, we believe that integrated TERS setup as a commercially available instrument is inevitable if broad applications of TERS are of interest. Nevertheless TERS setups will most probably never be fully turnkey instruments and must be designed for a specific range of applications. A TERS setup for biological investigation will be different from a TERS setup dedicated to nanostructures located onto a non-transparent surface. However the greatest feature of these setups is the possibility of conducting simultaneous AFM and Raman spectroscopy which yields simultaneous topographic images and tip-enhanced Raman spectra.

The work in Chapter 6 illustrated an application of TERS spectroscopy in studying the impact of structural strains on the molecular vibrations of nanostructures such as silicon nanowire. This allows distinguishing the local properties of individual spots on the surface of a sample from the bulk properties; a feature which could open new ways into the engineering of nanodevices and nanocircuits. The application of TERS to the chemical and biochemical analyses is also of great value. The study of kidney stone microcrystals in Chapter 7 was an important demonstration of TERS potential in nanoscale mapping of microscale surfaces with nanosteps without requiring further manipulating and labeling of the species that are present. This application along with all the great examples of TERS high performance in life sciences seem to offer TERS as a powerful complementary technique to medical diagnosis methods such as NMR and MRI scanning. Nevertheless, the shortcoming of TERS as a surface restricted method remains unresolved.

As a natural extension of the work, beyond all the critical issues mentioned above, conducting TERS measurements inside an isolated and more controlled environment can be of interest to push the limit of detection and to better understand some fundamentals. Not only the thermal and mechanical isolation of the TERS setup provide protection against positional drifts of the tip-sample junction, but also the tip and the sample can be isolated from the ambient substances under vacuum conditions. In this context, ultrahigh vacuum TERS (UHV-TERS) appears to be the next logical step towards efficient spectroscopy down to single molecule detection preventing oxidation of the tip or the sample, and eliminating the presence of residual water layer at the surface. All sample preparation and tip cleaning process occurs in-situ and inside an ultrahigh vacuum chamber yielding atomically clean surfaces. The development of UHV-TERS is still in its early stages and an example of it is the recent work from J. G. Hou (University of Science and Technology, China) where the doubly-resonance enhancement of the excitation laser and the Raman scattering is employed to achieve sub-1 nm resolution in TERS mapping of single *meso*-tetraakis (3,5-di-tertiarybutylphenyl)-prophyrin (H_2TBPP) molecule on the Ag(111) surface. In their recent work published in Nature,¹ STM-controlled TERS experiments are done by exciting the plasmon resonances of a electrochemically etched silver tip by p-polarized 532 nm wavelength laser in side

illumination configuration inside an ultrahigh vacuum (10^{-10} Torr) and low temperature (80 K) chamber. In this setup, the resonance of the nanocavity plasmon formed inside the tip-substrate gap, is spectrally matched to the molecular vibronic transitions. The doubly-resonant process involves efficient resonant excitation through spectral overlap between the nanocavity plasmon, the Raman laser and the molecular vibronic excitation in addition to significant scattering enhancement by spectral matching between the nanocavity plasmon resonance and the molecular vibronic scattering. The doubly-resonant conditions allowed Hou and his coworkers to excite large plasmonic enhancement of the single molecule Raman signal even when very small photon flux (0.8 mW laser power) was used. The TERS map and TERS spectra of single H_2TBPP molecules are shown in **Figure 8.1**.

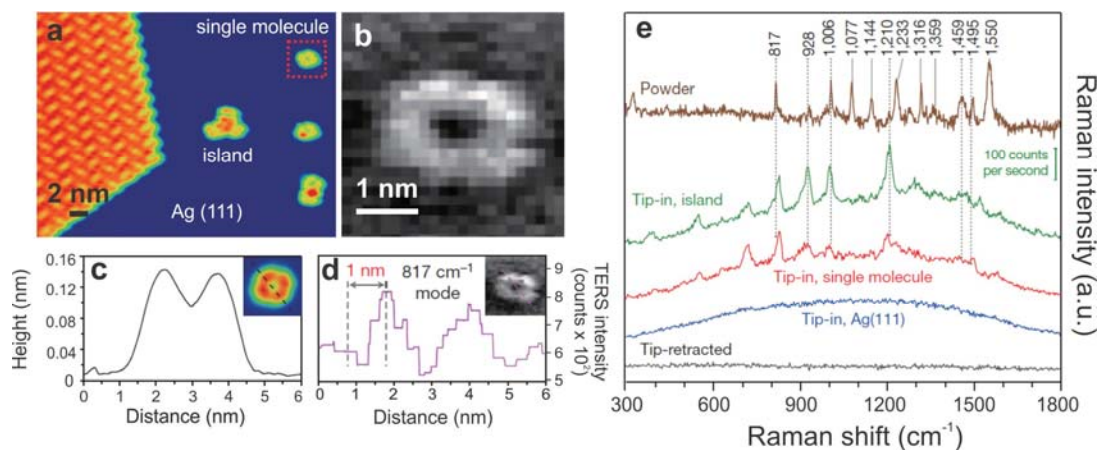


Figure 8.1 (a) STM image of sub-monolayer of H_2TBPP molecules on $Ag(111)$. Two isolated single molecules on the right, three-molecule cluster at the center and a densely packed monolayer island on the left are observed. The blue area in this image shows the $Ag(111)$ surface (b) Experimental TERS mapping of single molecule generated through intensity variation of the 817 cm^{-1} Raman peak (c) Height profile of a line trace in the inset STM image (d) TERS intensity profile of the same line trace in the inset TERS map (e) TERS spectra of different spots on the STM image presented in (a). The acquisition time was 3sec for all the recorded spectra. The images are adapted from reference 1 with permission from Nature publications.

Similar methodology was recently utilized in R. Van Duyne's research group (Northwestern University, USA) in an effort to acquire molecular resolution information of site-specific binding of copper phthalocyanine (CuPc) adlayer on Ag(111) surfaces. In their setup UHV-TERS measurements are conducted in room temperature using an electrochemically etched silver tip in combination with 632.8 nm wavelength laser which is polarized along the tip axis in side illumination configuration. A recent manuscript published in Nano Letters² summarizes their work and the future directions of UHV-TERS. Each TERS spectrum obtained in their study however originate from a monolayer of the adsorbent which contains 2.3×10^4 CuPc molecules according to the authors. It is noteworthy that the first concurrent STM topography and TERS spectroscopy under UHV condition was reported by J. Steidtner and B. Pettinger in 2007-2008.^{3,4} The authors report single molecule sensitivity however the TERS spectra acquired in their work shows only one or two Raman peaks which is not sufficient for the full characterization of the molecules. In their work, sample preparation was done outside the UHV chamber which might have negative influence on the results due to possible surface contaminations. With further technical improvements in future, the ultrahigh sensitivity and spatial resolution of UHV-TERS method can provide insight into interfacial phenomena such as the catalysis processes, surface functionalization and organization and can also bring new information about the electric field gradient effect at the tip-sample junction.

Finally, plasmonic couplings seem to be compatible with other analytical optical methods ranging from vibrational Raman and infrared spectroscopy to fluorescence⁵ and photo luminescence.⁶ The local enhancement of the light-matter interaction expands the detection sensitivities of these methods far beyond the conventional limits. In the field of infrared spectroscopy, tip-enhanced infrared nanospectroscopy has emerged as an alternative and complementary analytical method providing nanoscale resolution along with the molecular fingerprints. A great example of this is the method was recently proposed by M. A. Belkin.⁷ Their method is based on the fact that the absorption of a p-polarized mid-infrared laser pulses by a sample monolayer deposited onto a gold surface with side illumination configuration causes microscopic volume increases due to the molecular vibrations. The expansion of the monolayer (polyethylene glycol) causes

forces acting on a gold coated AFM tip positioned in contact with the molecules. This applied force causes a small cantilever deflection which gets amplified by a lock-in amplifier connected to the AFM system. The detection mechanism for the cantilever deflections relies on the matching of the repetition frequency of IR laser pulses with the bending resonant frequency of the cantilever. As a result of this synchronization which is possible with quantum cascade lasers, a plot of the amplified cantilever deflection signals versus the wavelength of the laser will be generated. The produced peak in these spectra represents the vibrational fingerprints of the sample under mid-infrared illumination. The authors report a spatial resolution of about 25 nm under ambient conditions which corresponds to the setup detection sensitivity of around 30 molecules. Recently developed on the same basis, ANASYS Instruments Company has combined the capabilities of AFM with the ones from nanoscale infrared technique using optical parametric oscillator (OPO) as a tunable laser source in the mid-infrared range. In the new Lorentz Contact Resonance (LCR) instrument that they have designed, differentiation between multiple compounds through simultaneous AFM microscopy and compositional nanoscale infrared mapping is made possible.

In conclusion, integrated instruments capable of conducting simultaneous topographic and chemical analysis of the various substances with detection resolutions comparable to their sub-nanometre building blocks appears to be the future for a variety of applications ranging from material science to catalysis and surface chemistry. All these techniques involve the use, the tunability and the tailoring of surface plasmon which appears to be the key element for further improvement in high resolution optical microscopy.

8.1 References

- (1) Zhang, R.; Zhang, Y.; Dong, Z. C.; Jiang, S.; Zhang, C.; Chen, L. G.; Zhang, L.; Liao, Y.; Aizpurua, J.; Luo, Y.; Yang, J. L.; Hou, J. G. *Nature* (2013), 498, 82.
- (2) Jiang, N.; Foley, E. T.; Klingsporn, J. M.; Sonntag, M. D.; Valley, N. A.; Dieringer, J. A.; Seideman, T.; Schatz, G. C.; Hersam, M. C.; Van Duyne, R. P. *Nano Lett.* (2012), 12, 5061.
- (3) Steidtner, J.; Pettinger, B. *Rev. Sci. Instrum.* (2007), 78, 1031041.
- (4) Steidtner, J.; Pettinger, B. *Phys. Rev. Lett.* (2008), 100, 236101.

- (5) Volkov, I. L.; Ramazanov, R. R.; Ubyivovk, E. V.; Rolich, V. I.; Kononov, A. I.; Kasyanenko, N. A. *Chem. Phys. Chem.* **(2013)**, *14*, 3543.
- (6) Ogawa, Y.; Katayama, K.; Minami, F. *J. Nanosci. Nanotechnol.* **(2011)**, *11*, 11055.
- (7) Lu, F.; Jin, M.; Belkin, M. A. *Nat. Photonics* **(2014)**, doi: 10.1038/nphoton.2013.373, ahead of print.

Appendix A.

Copyrights



RightsLink®

Home

Account
Info

Help

ACS Publications Title:
High quality. High impact.Label-Free Mapping of
Osteopontin Adsorption to
Calcium Oxalate Monohydrate
Crystals by Tip-Enhanced Raman
SpectroscopyLogged in as:
nastaran kazemi zanjani
Account #:
3000723370

LOGOUT

Author: Nastaran Kazemi-Zanjani,
Honghong Chen, Harvey A.
Goldberg, Graeme K. Hunter,
Bernd Grohe, and François
Lagugné-Labarhet**Publication:** Journal of the American
Chemical Society**Publisher:** American Chemical Society**Date:** Oct 1, 2012

Copyright © 2012, American Chemical Society

PERMISSION/LICENSE IS GRANTED FOR YOUR ORDER AT NO CHARGE

This type of permission/license, instead of the standard Terms & Conditions, is sent to you because no fee is being charged for your order. Please note the following:

- Permission is granted for your request in both print and electronic formats, and translations.
- If figures and/or tables were requested, they may be adapted or used in part.
- Please print this page for your records and send a copy of it to your publisher/graduate school.
- Appropriate credit for the requested material should be given as follows: "Reprinted (adapted) with permission from (COMPLETE REFERENCE CITATION). Copyright (YEAR) American Chemical Society." Insert appropriate information in place of the capitalized words.
- One-time permission is granted only for the use specified in your request. No additional uses are granted (such as derivative works or other editions). For any other uses, please submit a new request.

BACK

CLOSE WINDOW

Copyright © 2014 Copyright Clearance Center, Inc. All Rights Reserved. [Privacy statement](#).
Comments? We would like to hear from you. E-mail us at customercare@copyright.com

https://iwc.uwo.ca/iwc_static/layout/shell.html?lang=en&2-4.01_114059

Subject: RE: copyright permission request
To: Nastaran Kazemi Zanjani

Date: 11/25/13 02:03 PM
From: pubscopyright

image001.png (3kB)

Dear Nastaran,

Thank you for contacting The Optical Society.

Because you are the author of the source paper which you wish to reproduce, OSA considers your requested use of its copyrighted materials to be permissible within the author rights granted in the Copyright Transfer Agreement submitted by the requester on acceptance for publication of his/her manuscript. It is requested that a complete citation of the original material be included in any publication. This permission assumes that the material was not reproduced from another source when published in the original publication.

Please let me know if you have any questions.

Best,

Hannah

Hannah Bembia

November 25, 2013

Authorized Agent, The Optical Society

OSA Light in Focus

From: Nastaran Kazemi Zanjani
Sent: Monday, November 25, 2013 11:30 AM
To: pubscopyright

Subject: copyright permission request

Hello,

I am Nastaran Kazemi-Zanjani, PhD student at Western University, London Ontario, Canada. My article titled as "Localized enhancement of electric field in tip-enhanced Raman spectroscopy using radially and linearly polarized light" got recently published in Optics Express journal (Kazemi-Zanjani, Nastaran; Vedrairie, Sylvain; Lagugné-Labarthe, François, Optics Express, Vol. 21 Issue 21, pp.25271-25276 (2013)).

This email is to acquire permission for using a version of this article in my PhD thesis. A modified version of the figures 1 to 3 would be used in one chapter of my thesis.

I appreciate if you could guide me with this regard.

Kind Regards
Nastaran Kazemi-Zanjani

MDPI Journals A-Z For Authors For Editors For Librarians About Open Access Policy Submit My Manuscript Login Register

 OPEN ACCESS

Title / Keyword	Journal	all	Volume	
Author	Section	--	Issue	<input type="text"/>
Article Type	Special Issue	--	Page	<input type="text"/>

Standard Business Terms and Conditions MDPI AG

[Standard Terms and Conditions of Business of MDPI AG \(pdf\)](#)

Website Terms and Conditions of Use

- Extend of the Terms and Conditions of Use.** General Use of the websites mdpi.com, mdpi.org, mdpi.net, and all subdomains of these domains (hereinafter referred to as "website") are subject to the following terms and conditions. By browsing, linking to, or making any other use of the website you agree to these terms and conditions, which form a binding contract between MDPI AG, registered at Klybeckstrasse 64, 4057 Basel, Switzerland (hereinafter referred to as "MDPI") and you as the user (hereinafter referred to as "user").
- Copyright of the Website and Website Content.** Unless otherwise stated, the website and the website content are the property of MDPI. The copyright belongs to MDPI or its licensors. Unless explicitly indicated, and as described in §3 and §4 of these terms and conditions, the reproduction, redistribution, or collection of material from this website is prohibited. Permission to reproduce or redistribute parts of the website may be obtained by the user in written form from MDPI.
- Open Access License.** Articles labeled as "Open Access" are licensed by its copyright holder to be further distributed or reused by the user subject to attribution and correct citation of the original source and to the limitations described in §4 of these terms and conditions.
- Limitations to the Open Access License.** Some articles published on this website (especially articles labeled as "Review" or similar) may make use of copyrighted material for which the author(s) have obtained a reprint permission from the copyright holder. Usually such reprint permissions do not allow author(s) and/or MDPI to further license the copyrighted material. The licensing described in §3 of these terms and conditions are therefore not applicable to such kind of material enclosed within articles. It is the user's responsibility to identify reusability of material provided on this website, for which he may directly enter in contact with the authors of an article.
- Privacy Policy.** The user confirms to have read and to accept the Privacy Policy applicable to the website.
- Website Access Restriction.** MDPI reserves the right to block or to terminate the user's access to the website at any time and without prior notice.
- Linking to the Website.** The user may link to the website or to the content on the website provided that the linking does not imply any endorsement of any kind of MDPI. MDPI reserves the right to force the user to remove any link pointing to this website.
- Advertising.** The website may contain advertising. MDPI does not endorse any responsibility of any kind for the content of the advertisement or sponsorship or the advertised product or service, which is the responsibility of the advertiser or sponsor, unless the advertised product or service is offered by MDPI.
- Disclaimer of Warranty.** THERE IS NO WARRANTY FOR THE WEBSITE AND ITS CONTENT, TO THE EXTENT PERMITTED BY APPLICABLE LAW. MDPI, THE COPYRIGHT HOLDERS AND/OR OTHER PARTIES PROVIDE THE WEBSITE AND ITS CONTENT "AS IS" WITHOUT REPRESENTATIONS OR WARRANTIES OF ANY KIND, EITHER EXPRESSED OR IMPLIED, INCLUDING, BUT NOT LIMITED TO, THE IMPLIED WARRANTIES OF MERCHANTABILITY, SATISFACTORY QUALITY AND FITNESS FOR A PARTICULAR PURPOSE RELATING TO THIS WEBSITE, ITS CONTENT OR ANY WEBSITE TO WHICH IT IS LINKED. NO REPRESENTATIONS OR WARRANTIES ARE GIVEN AS TO THE ACCURACY OR COMPLETENESS OF THE INFORMATION PROVIDED ON THIS WEBSITE, OR ANY WEB SITE TO WHICH IT IS LINKED.
- Limitation of Liability.** IN NO EVENT UNLESS REQUIRED BY APPLICABLE LAW SHALL MDPI, ITS EMPLOYEES, AGENTS, SUPPLIERS, CONTRACTORS OR ANY OTHER PARTY, BE LIABLE TO THE USER FOR ANY DAMAGES OF ANY NATURE, INCLUDING ANY GENERAL, SPECIAL, INCIDENTAL OR CONSEQUENTIAL DAMAGES, LOSS, COST, CLAIM OR ANY EXPENSE OF ANY KIND ARISING OUT OF THE USE, INABILITY TO USE, OR IN CONNECTION WITH THE USE OF THE WEBSITE, ITS CONTENT AND INFORMATION, EVEN IF THE USER HAS BEEN ADVISED OF THE POSSIBILITY OF SUCH DAMAGES.
- Changes to the Terms and Conditions of Use.** MDPI reserves the right to change these Terms and Conditions of Use at any time by posting changes to this page of the website. The user will be considered to have accepted such changes in case the user should continue the use of the website after MDPI has published changes to this page of the website.
- Place of Jurisdiction.** These Terms and Conditions of Use shall be governed by and construed in accordance with Swiss Law applicable at the place of jurisdiction of MDPI.

Basel, Switzerland, May 2008

Last updated 4 June 2010

[Terms & Conditions](#) [Privacy Policy](#) [Contact MDPI](#) [Payment Information](#) [Jobs at MDPI](#)

© 1996-2014 MDPI AG (Basel, Switzerland) unless otherwise stated



RightsLink®

Home

Account
Info

Help

ACS Publications **Title:**
High quality. High impact.Optical Properties of Silver and
Gold Tetrahedral Nanopyramid
Arrays Prepared by Nanosphere
LithographyLogged in as:
nastaran kazemi zanjani
Account #:
3000723370**Author:** Mohammadali Tabatabaei,
Alexandre Sangar, Nastaran
Kazemi-Zanjani, Philippe
Torchio, Alexandre Merlen, and
François Lagugné-Labarthe

LOGOUT

Publication: The Journal of Physical
Chemistry C**Publisher:** American Chemical Society**Date:** Jul 1, 2013

Copyright © 2013, American Chemical Society

PERMISSION/LICENSE IS GRANTED FOR YOUR ORDER AT NO CHARGE

This type of permission/license, instead of the standard Terms & Conditions, is sent to you because no fee is being charged for your order. Please note the following:

- Permission is granted for your request in both print and electronic formats, and translations.
- If figures and/or tables were requested, they may be adapted or used in part.
- Please print this page for your records and send a copy of it to your publisher/graduate school.
- Appropriate credit for the requested material should be given as follows: "Reprinted (adapted) with permission from (COMPLETE REFERENCE CITATION). Copyright (YEAR) American Chemical Society." Insert appropriate information in place of the capitalized words.
- One-time permission is granted only for the use specified in your request. No additional uses are granted (such as derivative works or other editions). For any other uses, please submit a new request.

If credit is given to another source for the material you requested, permission must be obtained from that source.

BACK

CLOSE WINDOW

Copyright © 2014 Copyright Clearance Center, Inc. All Rights Reserved. [Privacy statement](#).
Comments? We would like to hear from you. E-mail us at customercare@copyright.com



RightsLink®

Home

Account
Info

Help

ACS Publications
High quality. High impact.

Title: Highly Reproducible Near-Field
Optical Imaging with Sub-20-nm
Resolution Based on Template-
Stripped Gold Pyramids

Author: Timothy W. Johnson, Zachary J.
Lapin, Ryan Beams, Nathan C.
Lindquist, Sergio G. Rodrigo,
Lukas Novotny, and Sang-Hyun
Oh

Publication: ACS Nano

Publisher: American Chemical Society

Date: Oct 1, 2012

Copyright © 2012, American Chemical Society

Logged in as:
nastaran kazemi zanjani
Account #:
3000723370

LOGOUT

PERMISSION/LICENSE IS GRANTED FOR YOUR ORDER AT NO CHARGE

This type of permission/license, instead of the standard Terms & Conditions, is sent to you because no fee is being charged for your order. Please note the following:

- Permission is granted for your request in both print and electronic formats, and translations.
- If figures and/or tables were requested, they may be adapted or used in part.
- Please print this page for your records and send a copy of it to your publisher/graduate school.
- Appropriate credit for the requested material should be given as follows: "Reprinted (adapted) with permission from (COMPLETE REFERENCE CITATION). Copyright (YEAR) American Chemical Society." Insert appropriate information in place of the capitalized words.
- One-time permission is granted only for the use specified in your request. No additional uses are granted (such as derivative works or other editions). For any other uses, please submit a new request.

If credit is given to another source for the material you requested, permission must be obtained from that source.

BACK

CLOSE WINDOW

Copyright © 2014 Copyright Clearance Center, Inc. All Rights Reserved. [Privacy statement](#).
Comments? We would like to hear from you. E-mail us at customercare@copyright.com



RightsLink®

[Home](#)[Account Info](#)[Help](#)ACS Publications
High quality. High impact.**Title:** $\lambda/4$ Resonance of an Optical Monopole Antenna Probed by Single Molecule Fluorescence**Author:** Tim H. Taminiau et al.**Publication:** Nano Letters**Publisher:** American Chemical Society**Date:** Jan 1, 2007

Copyright © 2007, American Chemical Society

Logged in as:

nastaran kazemi zanjani

Account #:

3000723370

[LOGOUT](#)**PERMISSION/LICENSE IS GRANTED FOR YOUR ORDER AT NO CHARGE**

This type of permission/license, instead of the standard Terms & Conditions, is sent to you because no fee is being charged for your order. Please note the following:

- Permission is granted for your request in both print and electronic formats, and translations.
- If figures and/or tables were requested, they may be adapted or used in part.
- Please print this page for your records and send a copy of it to your publisher/graduate school.
- Appropriate credit for the requested material should be given as follows: "Reprinted (adapted) with permission from (COMPLETE REFERENCE CITATION). Copyright (YEAR) American Chemical Society." Insert appropriate information in place of the capitalized words.
- One-time permission is granted only for the use specified in your request. No additional uses are granted (such as derivative works or other editions). For any other uses, please submit a new request.

If credit is given to another source for the material you requested, permission must be obtained from that source.

[BACK](#)[CLOSE WINDOW](#)

Copyright © 2014 Copyright Clearance Center, Inc. All Rights Reserved. [Privacy statement](#).
Comments? We would like to hear from you. E-mail us at customercare@copyright.com



RightsLink®

Home

Account
Info

Help

ACS Publications
High quality. High impact.**Title:** Adiabatic Tip-Plasmon Focusing
for Nano-Raman Spectroscopy**Author:** Samuel Berweger, Joanna M.
Atkin, Robert L. Olmon, and
Markus B. Raschke**Publication:** Journal of Physical Chemistry
Letters**Publisher:** American Chemical Society**Date:** Dec 1, 2010

Copyright © 2010, American Chemical Society

Logged in as:
nastaran kazemi zanjani
Account #:
3000723370

LOGOUT

PERMISSION/LICENSE IS GRANTED FOR YOUR ORDER AT NO CHARGE

This type of permission/license, instead of the standard Terms & Conditions, is sent to you because no fee is being charged for your order. Please note the following:

- Permission is granted for your request in both print and electronic formats, and translations.
- If figures and/or tables were requested, they may be adapted or used in part.
- Please print this page for your records and send a copy of it to your publisher/graduate school.
- Appropriate credit for the requested material should be given as follows: "Reprinted (adapted) with permission from (COMPLETE REFERENCE CITATION). Copyright (YEAR) American Chemical Society." Insert appropriate information in place of the capitalized words.
- One-time permission is granted only for the use specified in your request. No additional uses are granted (such as derivative works or other editions). For any other uses, please submit a new request.

If credit is given to another source for the material you requested, permission must be obtained from that source.

BACK

CLOSE WINDOW

Copyright © 2014 Copyright Clearance Center, Inc. All Rights Reserved. [Privacy statement](#).
Comments? We would like to hear from you. E-mail us at customercare@copyright.com



RightsLink®

Home

Account
Info

Help



ACS Publications

High quality. High impact.

Title: Full Spectroscopic Tip-Enhanced Raman Imaging of Single Nanotapes Formed from β -Amyloid(1-40) Peptide Fragments

Author: Melissa Paulite, Carolin Blum, Thomas Schmid, Lothar Opilik, Klaus Eyer, Gilbert C. Walker, and Renato Zenobi

Publication: ACS Nano

Publisher: American Chemical Society

Date: Feb 1, 2013

Copyright © 2013, American Chemical Society

Logged in as:

nastaran kazemi zanjani

Account #:

3000723370

LOGOUT

PERMISSION/LICENSE IS GRANTED FOR YOUR ORDER AT NO CHARGE

This type of permission/license, instead of the standard Terms & Conditions, is sent to you because no fee is being charged for your order. Please note the following:

- Permission is granted for your request in both print and electronic formats, and translations.
- If figures and/or tables were requested, they may be adapted or used in part.
- Please print this page for your records and send a copy of it to your publisher/graduate school.
- Appropriate credit for the requested material should be given as follows: "Reprinted (adapted) with permission from (COMPLETE REFERENCE CITATION). Copyright (YEAR) American Chemical Society." Insert appropriate information in place of the capitalized words.
- One-time permission is granted only for the use specified in your request. No additional uses are granted (such as derivative works or other editions). For any other uses, please submit a new request.

If credit is given to another source for the material you requested, permission must be obtained from that source.

BACK

CLOSE WINDOW

Copyright © 2014 Copyright Clearance Center, Inc. All Rights Reserved. [Privacy statement](#).
Comments? We would like to hear from you. E-mail us at customercare@copyright.com



RightsLink®

Home

Account
Info

Help

ACS Publications
High quality High impact.

Title: Tip-Enhanced Raman Scattering (TERS) from Hemozoin Crystals within a Sectioned Erythrocyte

Author: Bayden R. Wood, Elena Bailo, Mehdi Asghari Khiavi, Leann Tilley, Samantha Deed, Tanja Deckert-Gaudig, Don McNaughton, and Volker Deckert

Logged in as:
nastaran kazemi zanjani
Account #:
3000723370

LOGOUT

Publication: Nano Letters
Publisher: American Chemical Society
Date: May 1, 2011
Copyright © 2011, American Chemical Society

PERMISSION/LICENSE IS GRANTED FOR YOUR ORDER AT NO CHARGE

This type of permission/license, instead of the standard Terms & Conditions, is sent to you because no fee is being charged for your order. Please note the following:

- Permission is granted for your request in both print and electronic formats, and translations.
- If figures and/or tables were requested, they may be adapted or used in part.
- Please print this page for your records and send a copy of it to your publisher/graduate school.
- Appropriate credit for the requested material should be given as follows: "Reprinted (adapted) with permission from (COMPLETE REFERENCE CITATION). Copyright (YEAR) American Chemical Society." Insert appropriate information in place of the capitalized words.
- One-time permission is granted only for the use specified in your request. No additional uses are granted (such as derivative works or other editions). For any other uses, please submit a new request.

If credit is given to another source for the material you requested, permission must be obtained from that source.

BACK

CLOSE WINDOW

Copyright © 2014 Copyright Clearance Center, Inc. All Rights Reserved. [Privacy statement](#).
Comments? We would like to hear from you. E-mail us at customercare@copyright.com



RightsLink®

Home

Account
Info

Help

ACS Publications **Title:**
High quality. High impact.Structure and Composition of
Insulin Fibril Surfaces Probed by
TERSLogged in as:
nastaran kazemi zanjani
Account #:
3000723370**Author:** Dmitry Korouski, Tanja Deckert-
Gaudig, Volker Deckert, and
Igor K. Lednev

LOGOUT

Publication: Journal of the American
Chemical Society**Publisher:** American Chemical Society**Date:** Aug 1, 2012

Copyright © 2012, American Chemical Society

PERMISSION/LICENSE IS GRANTED FOR YOUR ORDER AT NO CHARGE

This type of permission/license, instead of the standard Terms & Conditions, is sent to you because no fee is being charged for your order. Please note the following:

- Permission is granted for your request in both print and electronic formats, and translations.
- If figures and/or tables were requested, they may be adapted or used in part.
- Please print this page for your records and send a copy of it to your publisher/graduate school.
- Appropriate credit for the requested material should be given as follows: "Reprinted (adapted) with permission from (COMPLETE REFERENCE CITATION). Copyright (YEAR) American Chemical Society." Insert appropriate information in place of the capitalized words.
- One-time permission is granted only for the use specified in your request. No additional uses are granted (such as derivative works or other editions). For any other uses, please submit a new request.

If credit is given to another source for the material you requested, permission must be obtained from that source.

BACK

CLOSE WINDOW

Copyright © 2014 Copyright Clearance Center, Inc. All Rights Reserved. [Privacy statement](#).
Comments? We would like to hear from you. E-mail us at customercare@copyright.com

**NATURE PUBLISHING GROUP LICENSE
TERMS AND CONDITIONS**

Mar 06, 2014

This is a License Agreement between nastaran kazemi zanjani ("You") and Nature Publishing Group ("Nature Publishing Group") provided by Copyright Clearance Center ("CCC"). The license consists of your order details, the terms and conditions provided by Nature Publishing Group, and the payment terms and conditions.

All payments must be made in full to CCC. For payment instructions, please see information listed at the bottom of this form.

License Number	3343400042542
License date	Mar 06, 2014
Licensed content publisher	Nature Publishing Group
Licensed content publication	Nature Communications
Licensed content title	A 1.7 nm resolution chemical analysis of carbon nanotubes by tip-enhanced Raman imaging in the ambient
Licensed content author	Chi Chen, Norihiko Hayazawa, Satoshi Kawata
Licensed content date	Feb 12, 2014
Volume number	5
Type of Use	reuse in a dissertation / thesis
Requestor type	academic/educational
Format	electronic
Portion	figures/tables/illustrations
Number of figures/tables /illustrations	1
High-res required	no
Figures	I wish to use the STM image and TERS map of the carbon nanotubes in Figure 4 as an example of TERS applications in high resolution measurements.
Author of this NPG article	no
Your reference number	
Title of your thesis / dissertation	Tip-enhanced Raman Spectroscopy
Expected completion date	May 2014
Estimated size (number of pages)	200
Total	0.00 USD
Terms and Conditions	

Terms and Conditions for Permissions

Nature Publishing Group hereby grants you a non-exclusive license to reproduce this material for this purpose, and for no other use, subject to the conditions below:

1. NPG warrants that it has, to the best of its knowledge, the rights to license reuse of this material. However, you should ensure that the material you are requesting is original to Nature Publishing Group and does not carry the copyright of another entity (as credited in the published version). If the credit line on any part of the material you have requested indicates that it was reprinted or adapted by NPG with permission from another source, then you should also seek permission from that source to reuse the material.
2. Permission granted free of charge for material in print is also usually granted for any electronic version of that work, provided that the material is incidental to the work as a whole and that the electronic version is essentially equivalent to, or substitutes for, the print version. Where print permission has been granted for a fee, separate permission must be obtained for any additional, electronic re-use (unless, as in the case of a full paper, this has already been accounted for during your initial request in the calculation of a print run). NB: In all cases, web-based use of full-text articles must be authorized separately through the 'Use on a Web Site' option when requesting permission.
3. Permission granted for a first edition does not apply to second and subsequent editions and for editions in other languages (except for signatories to the STM Permissions Guidelines, or where the first edition permission was granted for free).
4. Nature Publishing Group's permission must be acknowledged next to the figure, table or abstract in print. In electronic form, this acknowledgement must be visible at the same time as the figure/table/abstract, and must be hyperlinked to the journal's homepage.
5. The credit line should read:
Reprinted by permission from Macmillan Publishers Ltd: [JOURNAL NAME] (reference citation), copyright (year of publication)
For AOP papers, the credit line should read:
Reprinted by permission from Macmillan Publishers Ltd: [JOURNAL NAME], advance online publication, day month year (doi: 10.1038/sj.[JOURNAL ACRONYM].XXXXX)

Note: For republication from the *British Journal of Cancer*, the following credit lines apply.

Reprinted by permission from Macmillan Publishers Ltd on behalf of Cancer Research UK: [JOURNAL NAME] (reference citation), copyright (year of publication) For AOP papers, the credit line should read:

Reprinted by permission from Macmillan Publishers Ltd on behalf of Cancer Research UK: [JOURNAL NAME], advance online publication, day month year (doi: 10.1038/sj.[JOURNAL ACRONYM].XXXXX)

6. Adaptations of single figures do not require NPG approval. However, the adaptation should be credited as follows:

Adapted by permission from Macmillan Publishers Ltd: [JOURNAL NAME] (reference citation), copyright (year of publication)

Note: For adaptation from the *British Journal of Cancer*, the following credit line applies.

Adapted by permission from Macmillan Publishers Ltd on behalf of Cancer Research UK: [JOURNAL NAME] (reference citation), copyright (year of publication)

7. Translations of 401 words up to a whole article require NPG approval. Please visit <http://www.macmillanmedicalcommunications.com> for more information. Translations of up to a 400 words do not require NPG approval. The translation should be credited as follows:

Translated by permission from Macmillan Publishers Ltd: [JOURNAL NAME] (reference citation), copyright (year of publication).

Note: For translation from the *British Journal of Cancer*, the following credit line applies.

Translated by permission from Macmillan Publishers Ltd on behalf of Cancer Research UK: [JOURNAL NAME] (reference citation), copyright (year of publication)

We are certain that all parties will benefit from this agreement and wish you the best in the use of this material. Thank you.

Special Terms:

v1.1

If you would like to pay for this license now, please remit this license along with your payment made payable to "COPYRIGHT CLEARANCE CENTER" otherwise you will be invoiced within 48 hours of the license date. Payment should be in the form of a check or money order referencing your account number and this invoice number RLNK501244342.

Once you receive your invoice for this order, you may pay your invoice by credit card. Please follow instructions provided at that time.

Make Payment To:
Copyright Clearance Center
Dept 001
P.O. Box 843006
Boston, MA 02284-3006

For suggestions or comments regarding this order, contact RightsLink Customer Support: customercare@copyright.com or +1-877-622-5543 (toll free in the US) or +1-978-646-2777.

Gratis licenses (referencing \$0 in the Total field) are free. Please retain this printable license for your reference. No payment is required.

**NATURE PUBLISHING GROUP LICENSE
TERMS AND CONDITIONS**

Mar 12, 2014

This is a License Agreement between nastaran kazemi zanjani ("You") and Nature Publishing Group ("Nature Publishing Group") provided by Copyright Clearance Center ("CCC"). The license consists of your order details, the terms and conditions provided by Nature Publishing Group, and the payment terms and conditions.

All payments must be made in full to CCC. For payment instructions, please see information listed at the bottom of this form.

License Number	3346530252243
License date	Mar 12, 2014
Licensed content publisher	Nature Publishing Group
Licensed content publication	Nature
Licensed content title	Chemical mapping of a single molecule by plasmon-enhanced Raman scattering
Licensed content author	R. Zhang, Y. Zhang, Z. C. Dong, S. Jiang, C. Zhang, L. G. Chen
Licensed content date	Jun 5, 2013
Volume number	498
Issue number	7452
Type of Use	reuse in a dissertation / thesis
Requestor type	academic/educational
Format	electronic
Portion	figures/tables/illustrations
Number of figures/tables /illustrations	2
High-res required	no
Figures	I would like to show the TERS map of the single H2TBPP molecules as well as the experimental setup for UHV-TERS in my thesis.
Author of this NPG article	no
Your reference number	
Title of your thesis / dissertation	Tip-enhanced Raman Spectroscopy
Expected completion date	May 2014
Estimated size (number of pages)	200
Total	0.00 USD
Terms and Conditions	

Terms and Conditions for Permissions

Nature Publishing Group hereby grants you a non-exclusive license to reproduce this material for this purpose, and for no other use, subject to the conditions below:

1. NPG warrants that it has, to the best of its knowledge, the rights to license reuse of this material. However, you should ensure that the material you are requesting is original to Nature Publishing Group and does not carry the copyright of another entity (as credited in the published version). If the credit line on any part of the material you have requested indicates that it was reprinted or adapted by NPG with permission from another source, then you should also seek permission from that source to reuse the material.
2. Permission granted free of charge for material in print is also usually granted for any electronic version of that work, provided that the material is incidental to the work as a whole and that the electronic version is essentially equivalent to, or substitutes for, the print version. Where print permission has been granted for a fee, separate permission must be obtained for any additional, electronic re-use (unless, as in the case of a full paper, this has already been accounted for during your initial request in the calculation of a print run). NB: In all cases, web-based use of full-text articles must be authorized separately through the 'Use on a Web Site' option when requesting permission.
3. Permission granted for a first edition does not apply to second and subsequent editions and for editions in other languages (except for signatories to the STM Permissions Guidelines, or where the first edition permission was granted for free).
4. Nature Publishing Group's permission must be acknowledged next to the figure, table or abstract in print. In electronic form, this acknowledgement must be visible at the same time as the figure/table/abstract, and must be hyperlinked to the journal's homepage.

5. The credit line should read:
 Reprinted by permission from Macmillan Publishers Ltd: [JOURNAL NAME] (reference citation), copyright (year of publication)
 For AOP papers, the credit line should read:
 Reprinted by permission from Macmillan Publishers Ltd: [JOURNAL NAME], advance online publication, day month year (doi: 10.1038/sj.[JOURNAL ACRONYM].XXXXX)

Note: For republication from the *British Journal of Cancer*, the following credit lines apply.

Reprinted by permission from Macmillan Publishers Ltd on behalf of Cancer Research UK: [JOURNAL NAME] (reference citation), copyright (year of publication) For AOP papers, the credit line should read:
 Reprinted by permission from Macmillan Publishers Ltd on behalf of Cancer Research UK: [JOURNAL NAME], advance online publication, day month year (doi: 10.1038/sj.[JOURNAL ACRONYM].XXXXX)

6. Adaptations of single figures do not require NPG approval. However, the adaptation should be credited as follows:

Adapted by permission from Macmillan Publishers Ltd: [JOURNAL NAME] (reference citation), copyright (year of publication)

Note: For adaptation from the *British Journal of Cancer*, the following credit line applies.

Adapted by permission from Macmillan Publishers Ltd on behalf of Cancer Research UK: [JOURNAL NAME] (reference citation), copyright (year of publication)

7. Translations of 401 words up to a whole article require NPG approval. Please visit <http://www.macmillanmedicalcommunications.com> for more information. Translations of up to a 400 words do not require NPG approval. The translation should be credited as follows:

Translated by permission from Macmillan Publishers Ltd: [JOURNAL NAME] (reference citation), copyright (year of publication).

Note: For translation from the *British Journal of Cancer*, the following credit line applies.

Translated by permission from Macmillan Publishers Ltd on behalf of Cancer Research UK: [JOURNAL NAME] (reference citation), copyright (year of publication)

We are certain that all parties will benefit from this agreement and wish you the best in the use of this material. Thank you.

Special Terms:

v1.1

If you would like to pay for this license now, please remit this license along with your payment made payable to "COPYRIGHT CLEARANCE CENTER" otherwise you will be invoiced within 48 hours of the license date. Payment should be in the form of a check or money order referencing your account number and this invoice number RLNK501249004.

Once you receive your invoice for this order, you may pay your invoice by credit card. Please follow instructions provided at that time.

**Make Payment To:
Copyright Clearance Center
Dept 001
P.O. Box 843006
Boston, MA 02284-3006**

For suggestions or comments regarding this order, contact RightsLink Customer Support: customercare@copyright.com or +1-877-622-5543 (toll free in the US) or +1-978-646-2777.

Gratis licenses (referencing \$0 in the Total field) are free. Please retain this printable license for your reference. No payment is required.

**NATURE PUBLISHING GROUP LICENSE
TERMS AND CONDITIONS**

Mar 06, 2014

This is a License Agreement between nastaran kazemi zanjani ("You") and Nature Publishing Group ("Nature Publishing Group") provided by Copyright Clearance Center ("CCC"). The license consists of your order details, the terms and conditions provided by Nature Publishing Group, and the payment terms and conditions.

All payments must be made in full to CCC. For payment instructions, please see information listed at the bottom of this form.

License Number	3343390928804
License date	Mar 06, 2014
Licensed content publisher	Nature Publishing Group
Licensed content publication	Nature Nanotechnology
Licensed content title	Nanoscale chemical mapping using three-dimensional adiabatic compression of surface plasmon polaritons
Licensed content author	Francesco De Angelis, Gobind Das, Patrizio Candeloro, Maddalena Patrini, Matteo Galli et al.
Licensed content date	Nov 22, 2009
Volume number	5
Issue number	1
Type of Use	reuse in a dissertation / thesis
Requestor type	academic/educational
Format	electronic
Portion	figures/tables/illustrations
Number of figures/tables /illustrations	1
High-res required	no
Figures	I wish to use the STM image of the adiabatic tip in Figure 1 as an example of various probes that can be used to conduct Tip-enhanced Raman Spectroscopic (TERS) measurements
Author of this NPG article	no
Your reference number	
Title of your thesis / dissertation	Tip-enhanced Raman Spectroscopy
Expected completion date	May 2014
Estimated size (number of pages)	200
Total	0.00 USD

Terms and Conditions

Terms and Conditions for Permissions

Nature Publishing Group hereby grants you a non-exclusive license to reproduce this material for this purpose, and for no other use, subject to the conditions below:

1. NPG warrants that it has, to the best of its knowledge, the rights to license reuse of this material. However, you should ensure that the material you are requesting is original to Nature Publishing Group and does not carry the copyright of another entity (as credited in the published version). If the credit line on any part of the material you have requested indicates that it was reprinted or adapted by NPG with permission from another source, then you should also seek permission from that source to reuse the material.
2. Permission granted free of charge for material in print is also usually granted for any electronic version of that work, provided that the material is incidental to the work as a whole and that the electronic version is essentially equivalent to, or substitutes for, the print version. Where print permission has been granted for a fee, separate permission must be obtained for any additional, electronic re-use (unless, as in the case of a full paper, this has already been accounted for during your initial request in the calculation of a print run). NB: In all cases, web-based use of full-text articles must be authorized separately through the 'Use on a Web Site' option when requesting permission.
3. Permission granted for a first edition does not apply to second and subsequent editions and for editions in other languages (except for signatories to the STM Permissions Guidelines, or where the first edition permission was granted for free).
4. Nature Publishing Group's permission must be acknowledged next to the figure, table or abstract in print. In electronic form, this acknowledgement must be visible at the same time as the figure/table/abstract, and must be hyperlinked to the journal's homepage.
5. The credit line should read:
Reprinted by permission from Macmillan Publishers Ltd: [JOURNAL NAME] (reference citation), copyright (year of publication)
For AOP papers, the credit line should read:
Reprinted by permission from Macmillan Publishers Ltd: [JOURNAL NAME], advance online publication, day month year (doi: 10.1038/sj.[JOURNAL ACRONYM].XXXXX)

Note: For republication from the *British Journal of Cancer*, the following credit lines apply.

Reprinted by permission from Macmillan Publishers Ltd on behalf of Cancer Research UK: [JOURNAL NAME] (reference citation), copyright (year of publication) For AOP papers, the credit line should read:
Reprinted by permission from Macmillan Publishers Ltd on behalf of Cancer Research UK: [JOURNAL NAME], advance online publication, day month year (doi: 10.1038/sj.[JOURNAL ACRONYM].XXXXX)

6. Adaptations of single figures do not require NPG approval. However, the adaptation should be credited as follows:

Adapted by permission from Macmillan Publishers Ltd: [JOURNAL NAME] (reference citation), copyright (year of publication)

Note: For adaptation from the *British Journal of Cancer*, the following credit line applies.

Special Terms:

v1.1

If you would like to pay for this license now, please remit this license along with your payment made payable to "COPYRIGHT CLEARANCE CENTER" otherwise you will be invoiced within 48 hours of the license date. Payment should be in the form of a check or money order referencing your account number and this invoice number RLNK501244332.

Once you receive your invoice for this order, you may pay your invoice by credit card. Please follow instructions provided at that time.

Make Payment To:
Copyright Clearance Center
Dept 001
P.O. Box 843006
Boston, MA 02284-3006

For suggestions or comments regarding this order, contact RightsLink Customer Support: customercare@copyright.com or +1-877-622-5543 (toll free in the US) or +1-978-646-2777.

Gratis licenses (referencing \$0 in the Total field) are free. Please retain this printable license for your reference. No payment is required.



AMERICAN PHYSICAL SOCIETY

One Physics Ellipse, College Park, MD 20740 · <http://www.aps.org>

March 20, 2014

Nastaran Kazemi-Zanjani

Ref # 26162

Thank you for your permission request dated Mar. 7, 2014. We are pleased to grant you a non-exclusive, non-transferable permission, English rights, limited to **print and electronic format**, provided you meet the criteria outlined below. Permission is for a one-time use and does not include permission for future editions, updates, databases, translations, or any other matters. Permission must be sought for each additional use. This permission does not include the right to modify APS material.

Please print the required copyright credit line on the first page that the material appears: "Reprinted (abstract/excerpt/figure) with permission from [FULL REFERENCE CITATION] as follows: authors names, journal title, volume number, page number and year of publication. Copyright (YEAR) by the American Physical Society."

The following language must appear somewhere on the website: "Readers may view, browse, and/or download material for temporary copying purposes only, provided these uses are for noncommercial personal purposes. Except as provided by law, this material may not be further reproduced, distributed, transmitted, modified, adapted, performed, displayed, published, or sold in whole or part, without prior written permission from the American Physical Society."

Provide a hyperlink from the reprinted APS material (the hyperlink may be embedded in the copyright credit line). APS's link manager technology makes it convenient and easy to provide links to individual articles in APS journals. For information, see: <http://link.aps.org/>.

You must also obtain permission from at least one of the authors for each separate work, if you haven't done so already. The author's name and address can be found on the first page of the published Article.

Use of the APS material must not imply any endorsement by the American Physical Society.

Permission is granted for use of the following APS material only:

- Fig. 2, Phys. Rev. Lett. 103, 186101 – Published 26 October 2009
- Fig. 1, Phys. Rev. Lett. 95, 017402 – Published 28 June 2005

Permission is limited to the single title specified of the publication as follows:

A thesis entitled "Tip-enhanced Raman Spectroscopy (TERS)" to be published by Western University.

If you have any questions, please refer to the Copyright FAQ at: <http://publish.aps.org/copyrightFAQ.html> or send an email to assocpub@aps.org.

Sincerely,

Jamie L. Casey
Circulation and Fulfillment Assistant



RightsLink®

[Home](#)[Account Info](#)[Help](#)

Title: NEAR-FIELD OPTICAL
MICROSCOPY AND
SPECTROSCOPY WITH POINTED
PROBES*

Author: Lukas Novotny and Stephan J.
Stranick

Publication: Annual Review of Physical
Chemistry

Publisher: Annual Reviews

Date: Apr 6, 2006

Copyright © 2006, Annual Reviews

Logged in as:
nastaran kazemi zanjani
Account #:
3000723370

[LOGOUT](#)

Permission Not Required

Material may be republished in a thesis / dissertation without obtaining additional permission from Annual Reviews, providing that the author and the original source of publication are fully acknowledged.

[BACK](#)[CLOSE WINDOW](#)

Curriculum Vitae

Name: Nastaran Kazemi-Zanjani

Post-secondary Education and Degrees: University of Tehran
Tehran, Iran
2006-2008 M.Sc. Physical Chemistry.

K. N. Tousi University
Tehran, Iran
2002-2005 B.Sc. Chemistry

Honours and Awards:

- 1- Ontario Graduate/Queen Elizabeth II Scholarship **2013-2014**
- 2- Best Oral Presentation in Surface Science Division at Canadian Chemical Conference (CSC) **2013**
- 3- Graduate Thesis Award (GTRA), **2013**.
- 4- Best Oral Presentation at Canadian Materials Science Conference (MCSC) **2012**
- 5- Second Prize for Poster Presentation in Analytical Chemistry Division at Canadian Chemistry Conference (CSC) **2011**

Related Work Experience Teaching Assistant
University of Western Ontario
2010-2013

Publications:

1. Kazemi-Zanjani, N.; Gobbo, P.; Zhu, Z.; Workentin M. S.; Lagugné-Labarthe, F. *Can. J. Chemistry* (**2014**), submitted.
2. Kazemi-Zanjani, N.; Vedraïne, S.; Lagugné-Labarthe, F. *Opt. Express* (**2013**), *21*, 25271.
3. Kazemi-Zanjani, N.; Kergrene, E.; Liu, L.; Sham, T.-K.; Lagugné-Labarthe, F. *Sensors* (**2013**), *13*, 12744.
4. Tabatabaei, M.; Sangar, A.; Kazemi-Zanjani, N.; Torchio, P.; Merlen, A.; Lagugné-Labarthe, F. *J. Phys. Chem. C* (**2013**), *117*, 14778.
5. Kazemi-Zanjani, N.; Chen H.; Goldberg H. A.; Hunter G. K.; Grohe B.; Lagugné-Labarthe F. *J. Am. Chem. Soc.* (**2012**) *134*, 17076.
6. Gobbo P.; Ghiassian S.; Hesari M.; Stampelcoskie K. G.; Kazemi-Zanjani N.; Lagugné-Labarthe F.; Workentin M. S. *J. Mater. Chem.* (**2012**) *22*, 23971.
7. Kazemi-Zanjani N.; Pashae F.; Lagugné-Labarthe F. *Proc. SPIE* (**2012**) 8412, 8412201.